Trapping fermionic and bosonic helium atoms

VRIJE UNIVERSITEIT

Trapping fermionic and bosonic helium atoms

ACADEMISCH PROEFSCHRIFT

ter verkrijging van de graad van doctor aan
de Vrije Universiteit Amsterdam,
op gezag van de rector magnificus
prof.dr. T. Sminia,
in het openbaar te verdedigen
ten overstaan van de promotiecommissie
van de faculteit der Exacte Wetenschappen
op woensdag 1 juni 2005 om 13.45 uur
in de aula van de universiteit,
De Boelelaan 1105

door

Roland Johannes Wilhelmus Stas

geboren te Eindhoven

promotor: prof.dr. W. Hogervorst
copromotor: dr. W. Vassen

The work described in this thesis was performed with support from the 'Space Research Organization Netherlands' (SRON), and was carried out at the Laser Centre of the Vrije Universiteit Amsterdam.

Cover design: Jaconelle Schuffel, Roland Stas
Printed by PrintPartners Ipskamp BV, Enschede

ISBN 90-9019353-7

Contents

Chapter 1

Introduction

Cold atom research is a typical example of Atomic, Molecular and Optical (AMO) Physics. With experiments directed at the manipulation of atoms with external fields, it characterizes modern AMO Physics, where the aim to *control* the internal and external degrees of freedom of atoms, molecules and light fields plays a key role. Wieman, Pritchard and Wineland [213] have pointed out that the aim for control goes hand in hand with a characteristic approach: in AMO Physics, known physics is used to devise innovative techniques to better isolate and control atomic systems, so that the systems can be explored with higher precision and new physical phenomena may be discovered. This approach, having resulted in an increasingly precise control of atoms and molecules, can be traced back to the work of Rabi [158] on radio-frequency resonance techniques and has recurred in later developments, such as the work of Kastler [22, 75, 94] on optical pumping, the work of Ramsey [160] on atomic frequency standards, and the work of Paul [144] on ion traps. Cold atom research was initiated by the work on laser cooling, a development that fits in perfectly with the preceeding research developments. Control of the degrees of freedom of atoms is central to cold atom research, including the work presented here.[1]

In this thesis, experimental and theoretical work is discussed on samples of laser-cooled metastable ($2\ ^3S_1$) helium atoms (He*). Studies are performed on both helium isotopes, ^{3}He* and ^{4}He*. The experiments and theoretical work concern the interaction of He* atoms with laser light in laser cooling processes, and collisions between laser-cooled He* atoms. An introduction to techniques of laser cooling and trapping is given in Section 1.1 and the work presented in this thesis is further introduced in Section 1.2. Atomic fountains for frequency metrology are an important application of laser cooling and trapping

[1] The dominating role of the aim to control the internal and external degrees of freedom of atoms, molecules and light fields is also discussed by Kleppner [96] and Chu [33].

techniques and the possibilities of an atomic fountain based on ^{3}He* atoms are discussed in Section 1.3. Section 1.4 gives a chapter-by-chapter outline of this thesis.

1.1 Laser cooling and trapping

Techniques of laser cooling and trapping form the basis of cold atom research and have dominated the field of AMO Physics for more than two decades now. The first ideas stem from 1975, when Hänsch and Schwalow [74], and Wineland and Dehmelt [216] suggested that atoms (and ions) can be cooled with laser light. The first experiments (on neutral atoms) have been performed by Balykin, Letokhov and Minogin [4, 5, 11, 12] in Russia and by Metcalf and Phillips [152, 156] in the United States. Subsequent experiments, that have triggered enormous interest, were performed a few years later: in 1985, cooling of atoms in a three-dimensional optical molasses was demonstrated by Chu *et al.* [34], and, in 1987, the confinement of atoms in a magneto-optical trap (MOT) was achieved by Raab *et al.* [157]. In the years following, several review articles have appeared (see e.g. [1]), and recently also a textbook [130]. In 1997, the Nobel Prize for Physics was awarded to three laser cooling pioneers [32, 37, 151].

The cooling mechanism, proposed in 1975 and demonstrated in three dimensions by Chu *et al.* in 1985, is referred to as Doppler cooling and plays an important role in this thesis. The mechanism is named after the Doppler shift that plays a central role: moving atoms, that are illuminated from all directions with laser light tuned to the red from an atomic transition, predominantly scatter photons from counter-propagating beams, as the Doppler shift brings this light closer to resonance. In such a configuration, atoms are cooled to a temperature that is limited by the heating effects associated with the stochastic processes of absorption and spontaneous emission of photons [130]. Doppler cooling is characterized by a large capture velocity and temperatures around 1 mK [130]. Several other cooling mechanisms—sub-Doppler cooling, such as polarization gradient cooling and magnetically induced laser cooling, and sub-recoil cooling, such as velocity-selective coherent population trapping and Raman cooling—have been demonstrated afterwards, and can be used to obtain even lower temperatures. Typically, the capture velocity of these cooling mechanisms is small, so that the cooling mechanisms are used in parallel with Doppler cooling or sequentially. In the present work, only Doppler cooling is applied.

Magneto-optical trapping, as demonstrated by Raab *et al.* in 1987, is another laser cooling and trapping technique that plays an important role in this thesis. In the standard (six-beam) configuration, three orthogonal pairs of counter-propagating laser beams, tuned to the red from an atomic transition, with mutual opposite circular polarizations, are superimposed with a magnetic quadrupole field. Atoms with a sufficiently small velocity are captured in the MOT and confined near the zero point of the magnetic field. The trapped sample also undergoes cooling and the temperature can be derived from Doppler cooling theory [130] (if other cooling mechanisms can be neglected).

Pioneering laser cooling experiments were performed with alkali atoms, for which at that time continuous-wave laser sources were available to drive laser cooling transitions. However, it was soon recognized that laser cooling could also be applied to metastable noble gas atoms by driving a closed transition between a metastable state and a higher-excited state [6, 129, 178].

1.2 Metastable helium

Much effort has been invested in the development and understanding of new laser cooling techniques, and the acquired knowledge has been applied in many experiments, taking advantage of the unique properties of cold atoms. Here, an overview is given of experimental and theoretical work concerning cold He* atoms. First, special features of He* are indicated that provide unique opportunities for cold atoms experiments.

The helium atom, consisting of a nucleus and two electrons, has a relatively simple structure.[2] With one electron excited from the core to a metastable state, the He* atom behaves as a single valence electron atom. However, coupling between the spins of the open s-state core and the excited electron gives rise to states with parallel spins (triplet) and antiparallel spins (singlet), as shown in Fig. 1.1. The metastable $2\,^3S_1$ state has a lifetime of 7.9 ks (Appendix A) and can be regarded as an effective ground state in all experiments discussed in this thesis.

There are two naturally occurring isotopes, ^{3}He which is a fermion, and ^{4}He which is a boson. The isotopes have different level structures due to the mass difference and the fact that ^{3}He has a nuclear spin $I = \frac{1}{2}$. Therefore, the level structure of ^{3}He shows hyperfine structure, which is absent for ^{4}He. The structure differences between the isotopes are not visible on the scale of Fig. 1.1. In the experiments presented in this thesis, laser cooling is performed on transition $2\,^3S_1 \rightarrow 2\,^3P$ (wavelength 1083 nm) in the case of ^{3}He and ^{4}He and also on transition $2\,^3S_1 \rightarrow 3\,^3P$ (wavelength 389 nm) in the case of ^{4}He. A discussion of the (hyper)fine structure and Zeeman effect on states $2\,^3S_1$, $2\,^3P$ and $3\,^3P$ of ^{3}He and ^{4}He is presented in Appendix A, along with a discussion of the optical excitation of the laser cooling transitions.

An important feature of the He* atom for laser cooling experiments is the large amount of internal energy of 19.82 eV stored in the metastable $2\,^3S_1$ state that gives rise to the phenomenon of Penning ionization (PI) [145],

$$\mathrm{He^* + X \rightarrow He + X^+ + } e^- \quad \text{(PI)}. \tag{1.1}$$

where X is any atom with an ionization energy that is smaller than the internal energy of He*; only helium and neon in their ground states have ionization energies that are larger, 24.59 eV and 21.56 eV, respectively. In magneto-

[2] This enables accurate atomic structure calculations, that can be confronted with precision measurements on laser-cooled atoms. The simplest of atoms, hydrogen, cannot be laser-cooled, as a continuous-wave laser to drive the Lyman-α transition (at 121.67 nm) with sufficient intensity is not (yet) available [56].

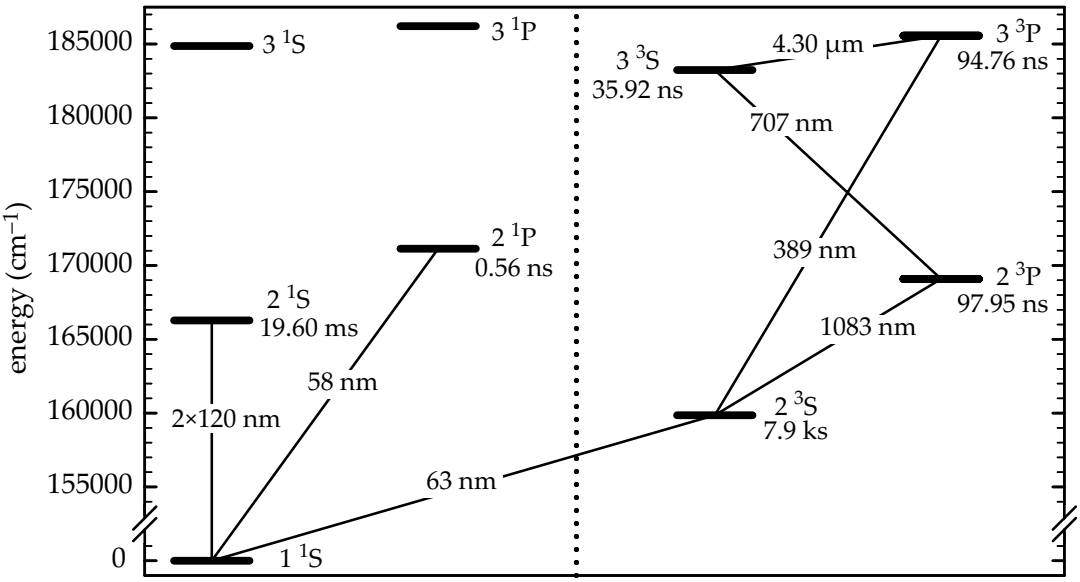

Figure 1.1. Grotrian diagram of the lowest energy levels of the helium atom (adapted from [195]). States 2 ^{1}S and 2 ^{3}S are metastable. The main decay processes are a two-photon electric-dipole transition in the case of 2 ^{1}S, and a single-photon magnetic-dipole transition in the case of 2 ^{3}S. A discussion of the (hyper)fine structure and Zeeman effect on the laser cooling transitions with wavelengths of 1083 nm and 389 nm is presented in Appendix A.

optically trapped samples of He* atoms, collisions between He* atoms are frequent. These collisions can give rise to Penning ionization or, with the formation of a molecular ion, associative ionization (AI)

$$\mathrm{He^* + He^* \rightarrow He + He^+ + e^-} \quad \text{(PI)}, \tag{1.2}$$

$$\mathrm{He^* + He^* \rightarrow He_2^+ + e^-} \quad \text{(AI)}. \tag{1.3}$$

The large internal energy of He* allows the use of charged-particle detectors, such as channel electron multipliers or microchannel plates (MCPs), as diagnostic tools with near unity detection efficiency. Detection of He^+ ions produced in magneto-optically trapped He* samples provides information on collisions between trapped atoms, while detection of He* atoms can be used to determine the temperature or the number of trapped atoms in the samples. A drawback of the large internal energy of He* and the resulting reactivity concerns the production of He* atoms. Plasma sources have a rather small metastable production efficiency, leading to relatively small He* fluxes. This does not have to be a problem, as the He* beam can be collimated with the curved-wavefront technique (see Chapter 2).

Using a Zeeman slower to decelerate the collimated beam (Chapter 2), He* atoms can be captured in a MOT. The resulting magneto-optically trapped samples, typically containing over 10^8 atoms, can be used as a starting point for a wide range of experiments. In the present work, trapping light with a wavelength of 1083 nm is used to trap samples containing either ^{3}He* atoms or ^{4}He* atoms (see Chapter 2). Using two trapping frequencies, the simultaneous

magneto-optical trapping of both isotopes is achieved (see Chapter 6). Using trapping light with a wavelength of 389 nm, magneto-optical trapping of ^{4}He* atoms is demonstrated. The MOT is investigated and it is shown that, although the trap has a limited capture velocity, samples of high phase-space density can be obtained—a result of the reduced two-body loss rate (see Chapter 3).

A drastic increase of phase space density (more than six orders of magnitude) can be achieved if the sample is transferred to a magnetic trap. Using the technique of forced rf-evaporative cooling, Bose-Einstein condensation (phase space density of order one) of a sample of ^{4}He* atoms has been achieved [147, 162, 199]. As magnetically trapped ^{4}He* atoms are (locally) spin-polarized, Penning ionization is suppressed by four orders of magnitude due to spin conservation (Wigner's spin-conservation rule). Since the first reports in 1995 of Bose-Einstein condensation of Rb, Na and Li [3, 20, 21, 44], many groups are studying Bose-Einstein condensates in dilute vapors. A condensate of ^{4}He* atoms provides unique opportunities, as condensed ^{4}He* atoms can be detected with almost unit detection efficiency, allowing the measurement of quantum statistical properties of the condensate with high spatial and temporal resolution.

Techniques of evaporative cooling can also be applied to trapped samples containing a mixture of bosonic ^{4}He* atoms and fermionic ^{3}He* atoms. Although this has not yet been demonstrated, it is expected that this could lead to Fermi degeneracy of ^{3}He* atoms or quantum degeneracy in a mixture of both isotopes. As the interspecies scattering length is expected to be very large, a quantum degenerate mixture could be used to study phase separation (if the scattering length is positive) or stability properties of the mixture (if the scattering length is negative). As a first step, ^{3}He* and ^{4}He* atoms must be simultaneously confined in a MOT. Simultaneous magneto-optical trapping is reported in this thesis: a discussion is presented in Chapter 6, along with a further introduction of experimental and theoretical work on quantum degenerate mixtures.

Magneto-optically trapped samples of He* atoms can also be used to study cold (ionizing) collisions. At low temperatures, the de Broglie wavelength associated with the atomic motion becomes very large leading to quantum threshold behavior where the collision process is dominated by the lowest allowed angular momentum partial waves. With the number of collisional degrees of freedom reduced, it is possible to study quantum mechanical collision effects with high precision. In the present work, ionizing collisions of He* atoms are investigated in the absence of trapping light by monitoring ion production rates in the trapped sample with a charged-particle detector (Chapter 5). Similar studies have been performed with other metastable noble gas atoms [95, 141]. However, in the case of He*, the relatively simple atomic structure allows a clear analysis of the collision process. A theoretical model including quantum threshold behavior, Wigner's spin-conservation rule and quantum statistical symmetry requirements is derived to analyze the experimental result (Chapter 4). The model is complementary to the more complete (and precise) close-coupling theory, developed for ^{4}He* atoms [111, 204, 205], as it provides clear insight into the process of ionizing collisions without requiring heavy numerical calculations.

The presence of near-resonant (trapping) light strongly modifies the dynamics of cold collisions. Due to the small relative velocity, atom pairs absorb and emit photons during the collision, giving rise to an increased collision cross section. These so-called light-assisted collisions (sometimes optical or photoassociative collisions) form the dominant loss process in magneto-optically trapped samples of He* atoms and are studied in this thesis by monitoring loss rates from the trapped samples (see Chapters 2 and 3). Related experiments on photoassociation spectroscopy have been reported, where probe light is used to excite a bound state between two colliding atoms and information on the interatomic potentials is obtained. These experiments have led to the creation of giant (0.5 μm) dimer molecules [112, 113].

Cold He* atoms have been been used in several other experiments.[3] The large stored energy in He* atoms allows an efficient damage of photoresist-coated surfaces. Manipulating a He* beam with laser light, sub-wavelength sized structures can be created in nanolithography experiments [150]. Furthermore, the large recoil velocity of He* has been used to create atomic beamsplitters via Bragg scattering from standing light waves [100] or velocity-selective coherent population trapping [106]. Also laser cooling with a bichromatic force [30] and other schemes involving nonmonochromatic light fields [27–29] have been demonstrated, as well as deceleration by combined optical and electric fields in a Stark slower [174]. Laser cooling techniques have also found application in the field of frequency metrology. In the next section, possibilities of an atomic fountain clock based on ^{3}He* atoms are discussed.

1.3 Laser-cooled frequency standards

Laser cooling techniques have been used to manipulate atomic samples into a perturbation-free environment, where precision measurements can be performed with long interrogation times. With Doppler and pressure broadening effects suppressed, atomic transition frequencies and lifetimes have been measured with high precision [140]. In the field of atomic frequency standards, laser cooling techniques have led to major advances with the development of microwave atomic fountain clocks [35, 93]. The use of Ramsey's method of separated oscillatory fields [159] in a fountain based on cold atoms has resulted in frequency stabilization with unprecedented stability and accuracy [15, 50, 110], and an improvement of the time standard.[4] Nowadays, frequency stabilization and electronic frequency measurements can be performed with such high precision that considerable effort is devoted to realizing standards for other SI base quantities that can be related to a frequency measurement.

It is interesting to consider an atomic fountain clock based on ^{3}He* atoms, as large numbers of ^{3}He* can be confined using laser cooling techniques and the hyperfine transition $2\ ^3\mathrm{S}(F = 3/2) \rightarrow 2\ ^3\mathrm{S}(F = 1/2)$, with a transition

[3] The list of experiments with cold He* atoms given here is not exhaustive.

[4] Data from cesium fountain clocks is included in the calculation of the International Atomic Time (TAI) [15].

frequency of 6.7 GHz, is suitable for the stabilization of a microwave signal using the method of separated oscillatory fields. Compared to the existing fountain clocks, based on ^{133}Cs or ^{87}Rb, a ^{3}He* fountain clock allows the investigation of several innovative aspects. Most importantly, collisions between fermionic atoms (^{133}Cs and ^{87}Rb are bosons) can be studied with high precision [60, 107, 186], and the corresponding contribution to the uncertainty of the accuracy budget can be investigated. Controlling the internal state of the launched atoms, quantum threshold behavior and quantum statistical effects can be observed through the cold collision frequency shift. If an atomic sample is prepared in a single spin state, the collision cross section is expected to be very small compared to the shift in fountain clocks based on ^{133}Cs or ^{87}Rb, where it contributes significantly to the accuracy budget [50]. Another innovative aspect of a ^{3}He* fountain clock is the direct detection of atoms with charged-particle detectors. The detection efficiency of He* atoms with MCP detectors is almost unity, ensuring a high signal-to-noise ratio. Finally, the development of atomic clocks based on new atomic species is interesting for measurements of possible variations of the fine-structure constant,[5] as the dependence of the hyperfine transition frequencies on the fine-structure constant is dependent on the atomic number [155]. The comparison of the output frequencies of atomic frequency standards based on different atomic species provides one of the best ways to perform laboratory tests of the stability of fundamental constants over a timescale of $\sim$1 yr [18].

To investigate the possibilities of an atomic fountain clock based on ^{3}He* and to determine the feasibility of the investigation of these innovative aspects, a theoretical study has been performed, including Monte Carlo simulations of the interrogation of atoms in magnetic fields of limited homogeneity. The study is presented in Chapter 7 and shows that, as a result of the small mass, the relatively high temperature of a laser-cooled ^{3}He* sample and the magnetic field dependence of the clock transition, the ^{3}He* fountain clock has an expected stability and accuracy that is significantly inferior to that of Cs and Rb fountain clocks.[6] It is also shown that the expected visibility of Ramsey fringe patterns is poor and it is concluded that it would not be sensible to perform an experimental study of a ^{3}He* fountain clock at the time being.

[5] Such experiments are motivated by the development of string theory models, that allow for, or even predict, variations of the fine-structure constant α with time and space [201]. A recent analysis of the spectrum of quasars [209] suggests that α may have changed over the cosmological time scale (10^{10} yr), while a second (independent) analysis [187] is not in agreement. An overview of experimental bounds on the variation of the fine-structure constant is given in [201].

[6] At the time of writing (2004), the most accurate atomic clock is a cesium (microwave) atomic fountain clock with an accuracy of $\sigma_\nu/\nu_0 < 4 \times 10^{-16}$, dominated by the uncertainty in the black-body radiation shift (2.5×10^{-16}) and the uncertainty of the cold collision frequency shift (1.5×10^{-16}) [50]. It must be noted that with the introduction of frequency combs [84], that accurately divide optical frequencies into countable microwave frequencies, much effort is devoted to the development of all-optical atomic clocks [51], where ultimate accuracies of 10^{-18} have been predicted [46]. The most accurate optical clock, based on a single $^{88}Sr^+$ ion, has an accuracy of 3.4×10^{-15} [120].

1.4 Outline of thesis

This thesis consists of seven chapters and three appendices. Following the introduction, Chapter 2 presents a discussion of the experimental setup and the characterization of magneto-optically trapped samples containing a single He* isotope, either ^{3}He* or ^{4}He*. Chapter 3 presents an experimental study of a magneto-optical trap utilizing light at 389 nm. Chapter 4 presents a theoretical model for ionizing collisions between laser-cooled He* isotopes and Chapter 5 presents experiments where the ionization rate coefficients for these collisions are measured. Chapter 6 presents the simultaneous trapping of large numbers of both ^{3}He* atoms and ^{4}He* atoms, indicating implications for quantum degeneracy research. Finally, Chapter 7 presents the results of a feasibility study for frequency metrology with ^{3}He* in an atomic fountain clock. Appendix A presents a discussion of the (hyper)fine structure and Zeeman effect on atomic states relevant for the experiments. Also, optical excitation of the laser cooling transitions is reviewed with the help of the electric dipole operator, and tables with atomic data and data concerning the optical excitation and laser cooling parameters are presented. Appendix B presents the derivation of the expression used to analyze TOF signals in Chapter 2. Appendix C presents the calculation of the interatomic potentials for two ^{3}He* atoms in the 2 $^3S_1(F)$ state. These potentials are used in the theoretical model of Chapter 4.

Chapter 2

A magneto-optical trap setup for two metastable helium isotopes

Magneto-optical trapping of ^{4}He* atoms has been reported in several publications with an increasing number of trapped atoms. The first experiments [13, 101], following naturally from the pioneering work performed with alkali atoms, demonstrated the trapping of ^{4}He* atoms with light with a wavelength of 1083 nm, probing transition $2\,^3S_1 \rightarrow 2\,^3P_2$. However, light-assisted ionizing collisions turned out to give rise to large trap loss [13] and the obtained trapped atom numbers were small, about 10^4. For the pursuit of Bose-Einstein condensation in a dilute gas of ^{4}He* atoms, a magneto-optical trap (MOT) operating in a novel regime was developed. With a large detuning of the trapping light from the atomic resonance, $\Delta = -25\,\Gamma$ with Γ the natural linewidth of the laser cooling transition, trap loss due to light-assisted collisions was reduced and up to 3×10^7 atoms were confined [164]. Further optimization has resulted in MOTs containing over 10^9 atoms [148, 196] (and Bose-Einstein condensation has been achieved [147, 162, 199]). Recently, magneto-optical trapping of ^{3}He* atoms has been reported also [102, 103]. In a MOT of tetrahedral configuration [179], up to 10^5 atoms were confined.

In this chapter, a setup is described that allows magneto-optical trapping of large numbers of ^{3}He* and ^{4}He* atoms using light with a wavelength of 1083 nm: up to 4×10^8 ^{4}He* atoms and 3×10^8 ^{3}He* atoms have been confined separately, and up to 1.5×10^8 atoms of both isotopes have been confined simultaneously. The setup is based on an apparatus that was built by Rooijakkers and further extended by Herschbach and Tol, and several parts of the setup are well described in their publications [163, 164] and theses [77, 195]. Here, focus is on the innovating aspects of the setup, which are mainly connected with simultaneous Zeeman slowing and magneto-optical trapping of both isotopes, and

reference is made to the above-mentioned works for details of designs and experimental techniques that were straightforwardly copied. In an early stage, the setup has been used to study the magneto-optical trapping of ^{4}He* atoms with light with a wavelength of 389 nm; these experiments are reported in Chapter 3. Although Chapter 3 provides a complete description of the 389 nm setup, differences with the (final) 1083 nm setup are discussed for the sake of clarity in a separate section of this chapter (Section 2.9).

The current chapter is composed as follows. Section 2.1 presents an overview of the setup and discusses the vacuum system. The following sections present the successive discussions of laser systems (Section 2.2), the beam source and recycling apparatus (Section 2.3), the collimation section (Section 2.4), the Zeeman slower (Section 2.5), the MOT (Section 2.6), diagnostic tools (Section 2.7) and the (computer-controlled) system for experiment control (Section 2.8). Section 2.9 discusses differences with the setup used for the 389 nm experiments. The chapter is concluded with a characterization (temperature and density profile) of trapped samples of single isotopes; these samples constitute the starting point for the collision experiments of Chapter 5. The characterization of the two-isotope MOT is discussed in Chapter 6, with a focus on optical pumping effects and implications for quantum degeneracy experiments.

2.1 Overview of setup and vacuum system

A schematic view of the setup is given in Fig. 2.1. A beam of metastable helium (He*) atoms is extracted from a DC-discharge source, that is cooled with liquid nitrogen to obtain a low beam velocity. The beam is collimated with the curved-wavefront technique to improve brightness, and decelerated in a Zeeman slower to a velocity around 50 m/s. The decelerated atoms are captured, cooled and confined in a MOT, and the resulting sample of trapped atoms can be studied in further experiments, making use of the available diagnostic tools. A microchannel plate (MCP) detector with a negative high voltage on its front

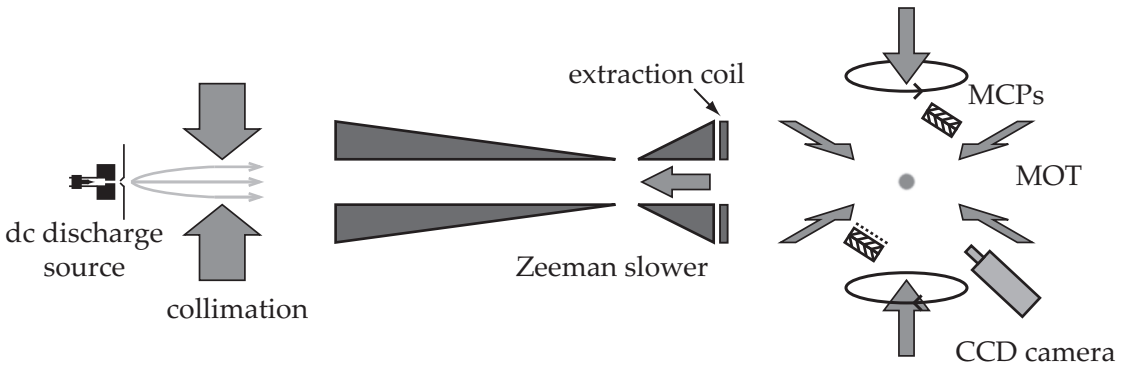

Figure 2.1. Schematic overview of the setup with, going from left to right (down the beam), source, collimation section, Zeeman slower (two parts plus extraction coil) and MOT with diagnostic tools (two MCP detectors and a CCD camera).

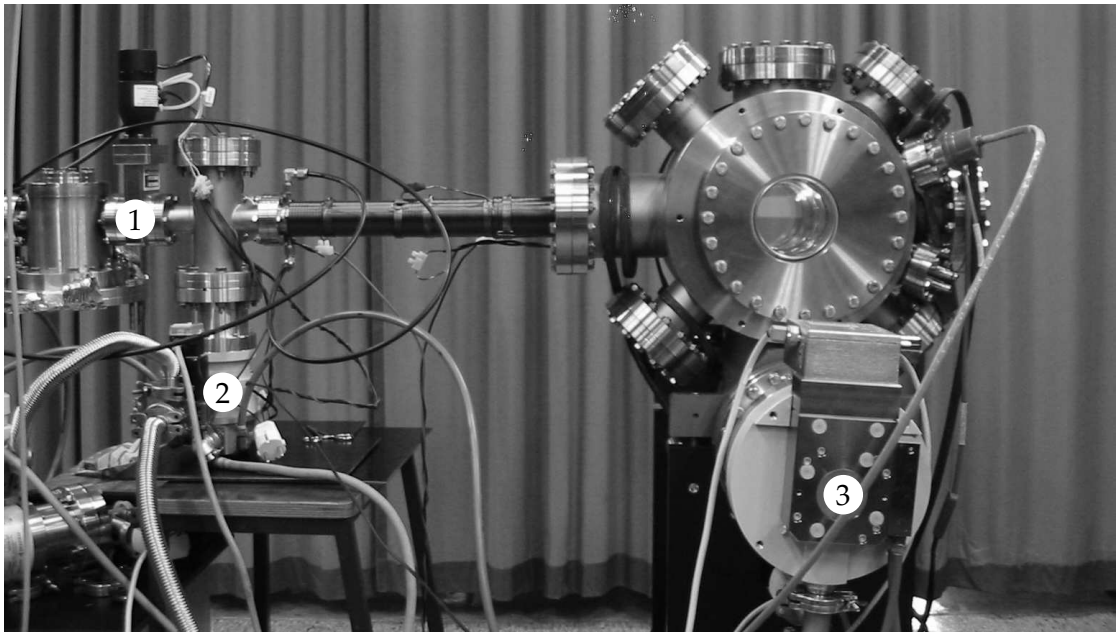

Figure 2.2. Picture of the MOT vacuum chamber and the second part of the Zeeman slower. The first and second part of the Zeeman slower are connected by T-pieces and a (pneumatically operated) valve, indicated by (1). This way, the ultrahigh-vacuum in the MOT chamber can be disconnected from the lower quality vacuum in the first part of the Zeeman slower. The diameter of the MOT chamber is 30 cm. The picture was taken before the mounting of optics and magnetic coils. Characteristics of the turbomolecular pumps indicated by (2) and (3) can be found in Table 2.1.

plate attracts all ions produced in the sample. A second MCP detector that is shielded electrically from the cloud by a grounded grid, measures the flux of He* atoms escaping in its direction (after the trap is switched off). In addition, a CCD camera is used to obtain absorption and fluorescence images of the trapped sample; the images are used to determine the density profile, the number of trapped atoms and the size of the sample. The light used for laser manipulation (collimation, Zeeman deceleration, magneto-optical trapping) and absorption imaging has a wavelength of 1083 nm and is generated with three solid-state laser systems.

Naturally, the He* beam and trapped sample are under vacuum conditions. The vacuum system consists of a series of interconnected chambers, specially designed for the various sections of the setup. The source is housed in a cube-shaped aluminum vacuum chamber with a length of 20 cm (measured along the direction of the beam). The chamber is connected to the collimation section vacuum chamber (made of aluminum, length of 56 cm) by a cone-shaped skimmer with a hole of 1 mm diameter. The collimation section chamber is connected to the Zeeman slower tubes by bellows and a T-piece (length 25 cm). The bellows are connected to the collimation section chamber and incorporate a flow resistance consisting of a tube with a length of 100 mm and an inner diameter of 3 mm. The T-piece joins the bellows and the first Zeeman slower tube

and is pumped by a turbomolecular pump. The two Zeeman slower tubes are made of stainless steel and are electrolytically polished on the inside. The first tube has a length of 197 cm and an inner diameter of 25 mm, while the second tube has a length of 58 cm and an inner diameter of 32 mm. The two tubes are connected by a vacuum piece consisting of two T-pieces, that are pumped by turbomolecular pumps and joined by a pneumatically actuated valve. The total distance from collimation section chamber to the end of the second tube is 291 cm. The second tube is welded onto a reentrant flange that is mounted onto the MOT vacuum chamber. The chamber has a diameter of 30 cm and is constructed from stainless steel (type 316). As shown in Fig. 2.2, it provides good optical access to the trapped samples by way of nine (uncoated) windows. Two windows are reentrant (Larson Electronic Glass, 3 $^3/_4$ -inch outer diameter), allowing MOT coils to be mounted close to the trap center. The chamber is sealed with conflat flanges.

All vacuum sections are pumped by turbomolecular pumps manufactured by Pfeiffer Vacuum. Information on the pumps is given in Table 2.1, along with the pressures measured in the various chambers while the helium beam is present. If the source is shut down, so that the helium load is removed, the pressure in the MOT chamber drops to about 7×10^{-11} mbar. To achieve this pressure, the chamber has been baked for seven days at a temperature of 200 °C.

2.2 Laser systems

To perform laser cooling, light with a wavelength of 1083 nm is needed to excite transition $2\,^3S_1 \rightarrow 2\,^3P_2$ in case of ^{4}He, and $2\,^3S_1(F = \frac{3}{2}) \rightarrow 2\,^3P_2(F = \frac{5}{2})$ in case of ^{3}He. As the isotope shift of the laser cooling transition is 34 GHz, which is too large to bridge with a modulator, two separate fiber lasers are used for the two isotopes. For absorption imaging, a narrow-band diode laser is used. Stabilizing the laser frequency to one of the above-mentioned transitions, absorption imaging has been applied to trapped samples containing a single isotope. The two-isotope MOT (Chapter 6) has been studied with MCP detectors only.

2.2.1 Fiber laser systems

The fiber lasers used in the experiments are commercial systems delivering a high-power, single-mode laser beam with a wavelength that is tunable around 1083 nm. A laser with an output power of 1 W (IPG, model YLD-1BC) is used for the laser manipulation of ^{3}He* atoms and a laser with an output power of about 2 W (IPG, model YLD-2BC) is used for ^{4}He* atoms. The lasers consist of a single-mode fiber, doped with Yb^{3+} ions, that is pumped by multiple 1 W multimode diode lasers. The ytterbium-doped fiber acts as a gain medium, showing very broad absorption and emission bands, with ∼800 nm to ∼1064 nm for absorption and ∼970 nm to ∼1200 nm for emission [143]. The fiber is seeded

Table 2.1. Characteristics of the turbomolecular pumps (Pfeiffer Vacuum) used in the setup and pressures with the helium source present. Sections indicated as Zeeman slower 1, 2 and 3 refer to the T-pieces mounted between the collimation section and the first Zeeman slower tube (1), between the first Zeeman slower tube and the pneumatically actuated valve (2) and between the valve and the second Zeeman slower tube (3).

section of vacuum apparatus	type	pressure (mbar)	volume flow rate (for He) (l/s)	compression ratio (for He)
source chamber	TMH 521[a]	7×10^{-5} [b]	500	5×10^{7}
collimation section	TPH 520[a]	1×10^{-7} [b]	500	5×10^{7}
Zeeman slower 1	TMU 071P[a]	—	55	1×10^{7}
Zeeman slower 2	TMU 521[c]	$< 1 \times 10^{-9}$ [b]	500	5×10^{7}
Zeeman slower 3	TPU 062H[d]	—	49	2.6×10^{8}
MOT chamber	TMU 521[c]	7×10^{-10}	500	5×10^{7}

[a] Backed by a scroll vacuum pump (Varian, type SH-100). For a backing pressure of about 0.1 mbar, the volume flow rate is 0.3 l/s.

[b] Pressure reading is not corrected for the high concentration of helium in the vacuum.

[c] Backed by a turbomolecular pump (Pfeiffer Vacuum, type TMH 064/TMU 064) with a volume flow rate (for He) of 42 l/s and a compression ratio (for He) of 7×10^{4}. This pump maintains a backing pressure $< 5 \times 10^{-4}$ mbar and is backed by a diaphragm pump (Varian, type 949-9452) with a volume flow rate of 1.3 l/s, maintaining a backing pressure of about 1 mbar.

[d] Backed by a diaphragm pump (Varian, type 949-9452) with a volume flow rate of 1.3 l/s, maintaining a backing pressure of about 1 mbar.

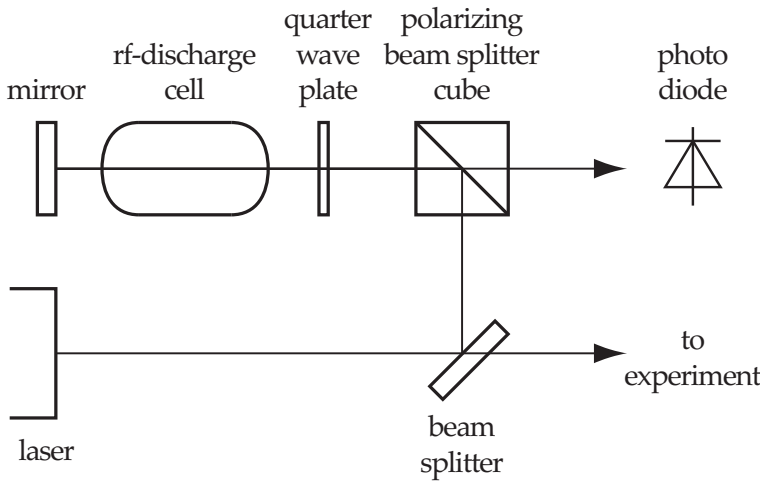

Figure 2.3. Setup for saturated absorption spectroscopy.

by a tunable Distributed Bragg Reflector (DBR) diode laser. The wavelength of the seed laser can be tuned over 2 nm (around 1083 nm) by manual adjustment of the temperature of the laser diode through the control unit. Fine tuning of the wavelength is achieved with a voltage (between 0 V and 5 V) applied to the modulation input of the control unit, that adjusts the current through the seed laser. The modulation range is a few GHz for both fiber laser systems.

The fiber lasers are frequency stabilized to the laser cooling transitions of either isotope using a low-frequency-modulation locking technique. A few mW of laser light is used to perform saturated absorption spectroscopy in an rf-discharge gas cell, filled with either ^{3}He or ^{4}He gas to a pressure of about 0.1 mbar; a schematic setup is shown in Fig. 2.3. Modulating the laser frequency with a low-frequency signal at 8 kHz through the modulation input, an error signal is obtained by demodulating the saturated absorption signal obtained from the photo-diode with a lock-in amplifier. The error signal is applied to a PI controller that is connected to the modulation input of the control unit. The resulting feedback loop stabilizes the laser frequency to the Lamb dip in the saturated absorption spectrum.

The linewidth of the (stabilized) fiber lasers is determined from heterodyne beat experiments against the diode laser discussed in Section 2.2.2, that has a full width at half-maximum (FWHM) linewidth of 0.4 MHz. For laser YLD-1BC, 500 power spectra are recorded over a period of 26 s, and for laser YLD-2BC, 1000 power spectra are recorded over a period of 51 s; the recorded spectra are averaged. The averaged beat note spectrum has a Gaussian shape indicating inhomogeneous broadening usually associated with technical noise. Therefore, the width of the beat note is assumed to be the square root of the sum of squared laser linewidths. Laser YLD-1BC has a FWHM linewidth of 1.6 MHz and laser YLD-2BC has a FWHM linewidth of 3.0 MHz. The specified short-term (1 ms) stability of the lasers is $\sim$ 1 MHz.

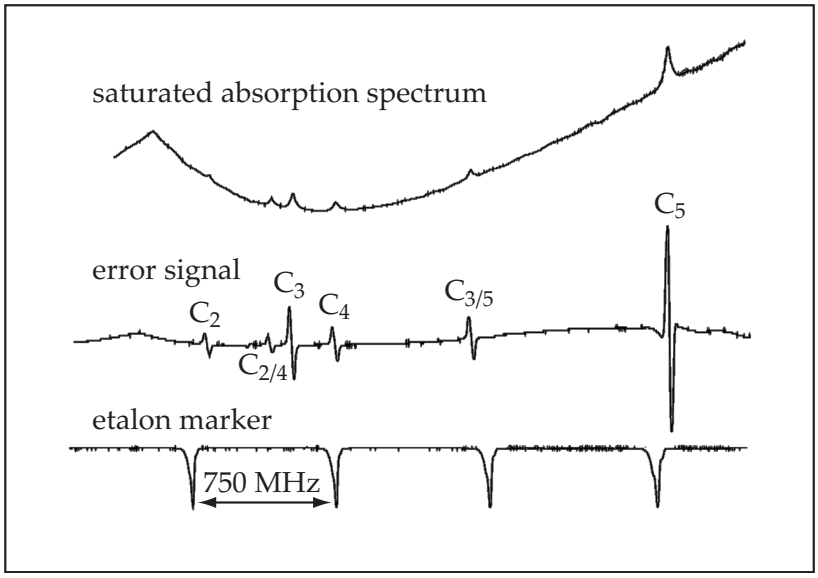

Figure 2.4. Saturated absorption spectrum and error signal after demodulation in the case of ^{3}He*. The Doppler broadened spectrum shows Lamb dips from four transition and two cross-overs. The etalon marker indicates the frequency scale. The transitions $2\,^3S_1(F) \rightarrow 2\,^3P(F')$ in ^{3}He are indicated by C_1–C_9 as defined in Fig. 2.9. Transition C_3 is the laser cooling transition. The graph is taken from [87].

2.2.2 Diode laser

The diode laser system (Toptica, model DL100) is a commercial system delivering a single-mode laser beam with a power of 37 mW in a narrow frequency band tunable around a wavelength of 1083 nm. The system consists of a external-grating extended-cavity diode laser in a temperature-stabilized laser head together with a control unit containing electronics for laser frequency scanning and stabilization, and laser head temperature stabilization. The DL100 system is based on the system presented in [161] and detailed information can be found there. In the following, some aspects concerning the implementation of the laser system in the setup are discussed.

The laser diode is mounted in an external-grating extended-cavity configuration, where a cavity is formed between the laser diode and a reflection grating mounted on a piezo actuator. The grating is mounted in the Littrow configuration, where the first-order diffracted beam is reflected collinear with the incident beam and re-imaged on the diode facet [63]. Setting the laser frequency to the laser cooling transition of either isotope, the laser frequency of the extended cavity system is coarsely tuned by changing the grating angle with a micrometer screw in the laser head. The scanning range is 7 nm around the central wavelength of 1083 nm. For a given angle of the reflection grating, the laser frequency is tuned manually by adjusting the diode temperature and piezo voltage through the control unit electronics. Fine-tuning of the laser frequency is achieved by changing the current through the diode.

To stabilize the frequency to the atomic transition, the diode current is mod-

ulated at a frequency of 20 MHz, through a bias-T connection on the diode. Using a setup as depicted in Fig. 2.3, an error signal is obtained from the photo diode signal using the so-called Pound-Drever-Hall technique [19]. Figure 2.4 shows the saturated absorption signal from the photo diode and the resulting error signal. The laser frequency is stabilized with two feedback signals. To compensate for fast frequency fluctuations, the error signal is applied directly to the diode through a FET-current control with a large bandwidth of 5 MHz. In addition, the error signal is applied to a PID regulator that steers the diode current through the control box (bandwidth of 1 MHz).

A heterodyne beat experiment between the diode laser and an LNA laser with a FWHM linewidth of 0.16 MHz [195] has shown that the linewidth of the diode laser depends slightly on the settings of the control system. For time intervals of several minutes, the FWHM linewidth is 0.4 MHz [87].

The laser beam profile from the diode shows two intensity maxima and deviates strongly from a Gaussian (TEM_{00}) mode. Therefore, the beam is coupled through a polarization-maintaining single-mode fiber; the output beam, with a Gaussian mode, has a power of about 10 mW.

2.3 Source and recycling apparatus

The He* beam is generated with a DC-discharge source with a design based on Fahey *et al.* [57] and a construction identical to Rooijakkers *et al.* [163]. In the source, helium atoms are excited to the metastable $2\,^3S_1$ state by collisions with electrons in an electric DC-discharge that is maintained through a nozzle. The nozzle is a canal with a length of 10 mm and an inner diameter of 0.25 mm in a slab of liquid-nitrogen-cooled boron nitride, a material that combines poor electric conductivity with good thermal conductivity. As collisions lead to de-excitation, only atoms that are excited in the 1 cm expansion region between nozzle and skimmer are likely to survive in the metastable state. The current running through the discharge is set to 8 mA, so that the intensity of the He* beam is 4×10^{14} $s^{-1}sr^{-1}$ and the fraction of He* atoms in the beam is 10^{-4} (see Chapter 5). The velocity distributions of the ^{3}He* beam and ^{4}He* beam have been measured with a time-of-flight (TOF) technique and are shown shown in Fig. 2.5. The differences between the velocity distributions is due to the mass difference between the isotopes. The area with velocity $v < 1375$ is shaded, indicating the fraction of atoms that is decelerated in the Zeeman slower.

If the source is operated with a ^{3}He gas or a ^{3}He$-^4$He gas mixture, a recycling apparatus is used to purify and recycle the gas, as the ^{3}He isotope with its small natural abundance of 1.4×10^{-4} % (see Appendix A) is rather expensive.[1] The apparatus is connected to the source chamber, so that all gas that does not end up in the beam is recycled. The amount of gas that ends up in the beam

[1] The gas consumption of the source (without recycling) is estimated at 0.13 atm l/h, while 1 atm l of ^{3}He gas costs about USD 100 (anno 2004).

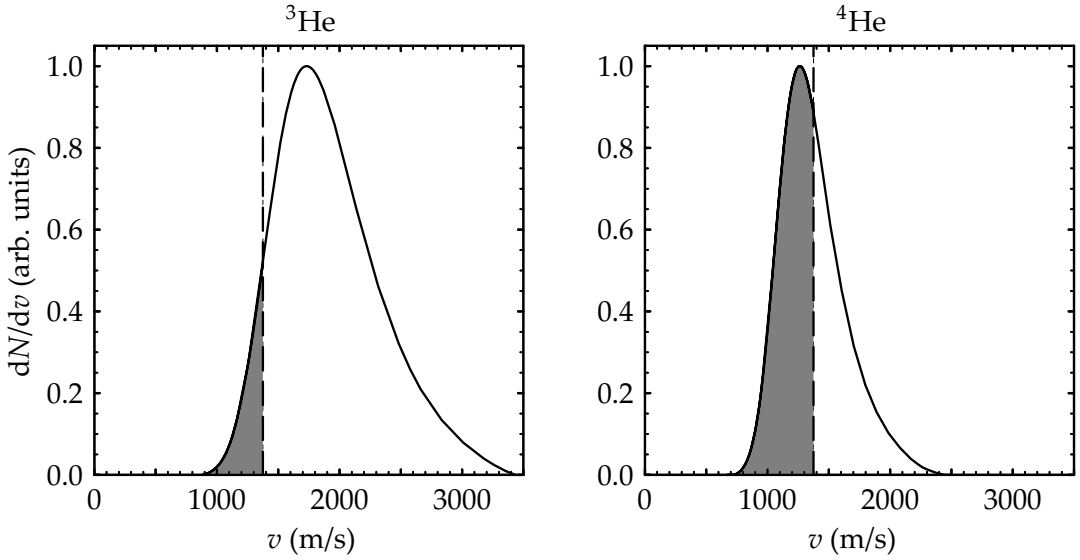

Figure 2.5. Velocity distributions of the ^{3}He* beam and ^{4}He* beam from the source at a discharge current of 8 mA. The fraction captured in the Zeeman slower is shaded. In the case of ^{3}He* (^{4}He*), the fraction amounts to 8% (58%). Furthermore, the most probable velocity is 1724 m/s (1247 m/s), the mean velocity is 1897 m/s (1369 m/s), and the FWHM is 909 m/s (531 m/s). The pressure drop over the nozzle and the resulting gas flow differ by $\sim$ 20% for the presented velocity distributions.

is at most 10^{-3} of the helium consumption of the source. A flowchart of the recycling apparatus is shown in Fig. 2.6.

If the recycling apparatus is in operation, the purification stages containing molecular sieve material (see Fig. 2.6) are cooled with liquid nitrogen and valves 1, 2, 6 and 8 are opened, while the other valves are shut. Helium gas is pumped from the source vacuum chamber into the purification stages by the turbomolecular pump and the scroll pump backing it. The gas is returned to the source through a variable leak valve. To avoid contamination of the recycled helium gas, the recycling loop is interrupted if the source is not in use. Valves 6, 8 and 2 are closed (in that order), and valve 3 is opened to the atmosphere of the laboratory. To start up the recycling, valve 3 is closed and valve 4 is opened until the tubes connecting the backing pump and valves 2, 3 and 4 are evacuated. Then, valves 2, 6 and 8 are opened and the source is ready for use. If valves 2 and 6 are closed, the recycling system can be filled up from the filling cylinder by opening valves 5a and 5b. Finally, with valves 1, 3, 7 and 8 opened the source is operated with ^{4}He gas without recycling.

2.4 Collimation section

In the collimation section, the He* beam is collimated in horizontal and vertical direction applying the curved-wavefront technique [7, 163, 203]. Collimation leads to an increase of brightness of the beam and is based on the interaction of atoms in the beam with two pairs of counter-propagating, convergent laser

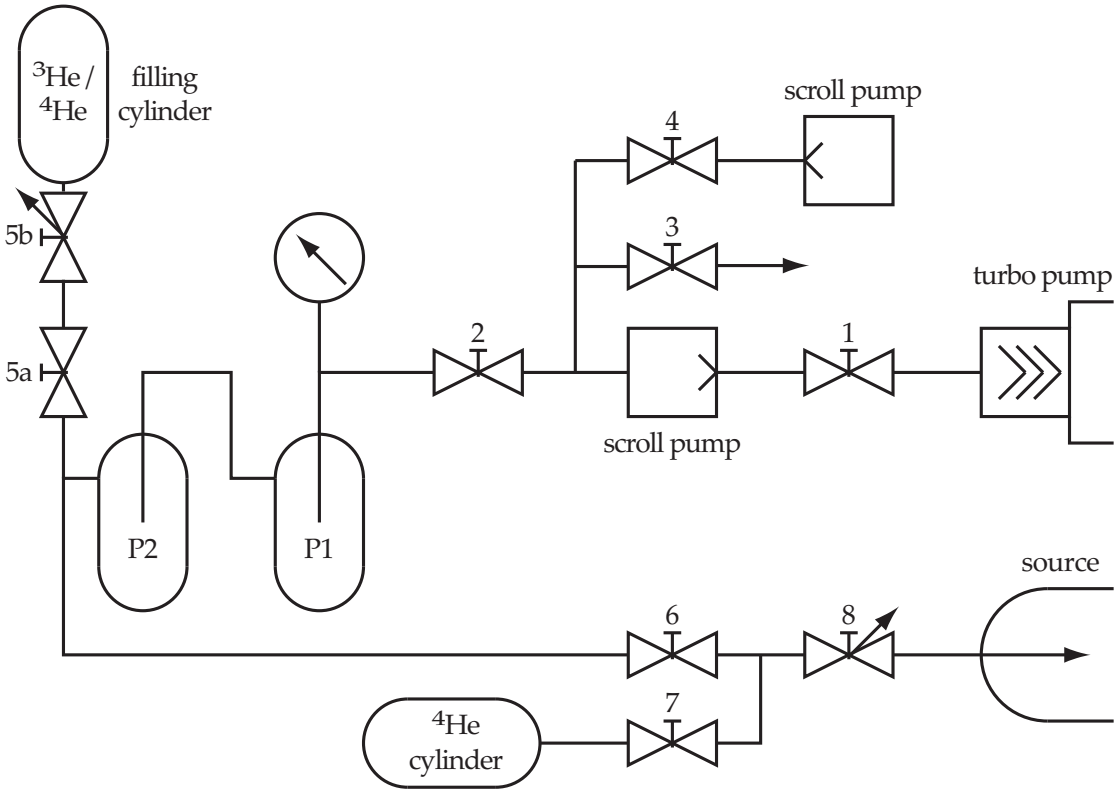

Figure 2.6. Flow chart of the recycling apparatus. Valves 1 and 5a are angle valves (Balzers, KF-25), valves 2–4, 6 and 7 are diaphragm valves (Nupro, SS-DLS6mm), valve 5b is a pressure reduction valve (Messer, Spectron FM62) and valve 8 is a variable leak valve (Granville-Phillips, series 203). All valves are manually actuated. Purification stage P1 is filled with type 4A molecular sieve (sodium zeolite with a pore size of 4 Å) and purification stage P2 is filled with type 13X molecular sieve (sodium zeolite with a pore size of 10 Å). The pressure in the purification stages depends on the amount of helium gas in the system and varies between 100 mbar and 250 mbar. Characteristics of the turbomolecular pump (Pfeiffer Vacuum, TMH 521) and scroll vacuum pumps (Varian, type SH-100) are given in Table 2.1.

beams resonant with the atomic transition. To provide insight in the collimation process, the force exerted by a single laser beam on an atom is considered, neglecting the saturation effects [115] induced by the three other beams.

The force exerted by a laser beam on an atom is referred to as the radiation pressure force and can be written as [195]

$$F_{\text{rad}} = \hbar k \frac{\Gamma}{2} \frac{I/fI_{\text{sat}}}{1 + I/fI_{\text{sat}}} \frac{1 + \gamma/\Gamma}{\left(1 + \gamma/\Gamma\right)\left(1 + \gamma\Gamma/\Gamma'^2\right) + (2\Delta/\Gamma')^2}, \tag{2.1}$$

where $k = 2\pi/\lambda$ is the wave number (with λ the wavelength) and I the intensity of the laser light; the laser lineshape is assumed to be Lorentzian with linewidth γ. The force depends on the line strength of the transition that is driven by the laser light: the corresponding saturation intensity, fI_{sat}, is the product of a relative line strength factor f [195] and the saturation intensity for the transition between stretched magnetic substates, i.e. transition $M_J = 1 \rightarrow M'_J = 2$ in the case of ^{4}He* and $M_F = \frac{3}{2} \rightarrow M'_F = \frac{5}{2}$ in the case of ^{3}He*. It is shown in Appendix A that $I_{\text{sat}} = 0.167\ \text{mW/cm}^2$ for both isotopes. For a single atom, the relative line strength factor is the inverse of the relative strength associated with the excited transition (see Section 2.10.2); in the case of linearly polarized light, used in the collimation section, $f \approx 2$ for either ^{3}He* or ^{4}He* in any magnetic substate. Finally, $\Gamma/2\pi = 1.62$ MHz is the natural linewidth of the transition, $\Gamma' = \Gamma\sqrt{1 + I/fI_{\text{sat}}}$ is the power-broadened linewidth of an atomic transition, $\hbar$ is Planck's constant divided by 2π and Δ is the detuning of the laser frequency with respect to the atomic transition frequency, including the Doppler effect and Zeeman effect.[2]

As the radiation pressure force saturates to

$$F_{\text{rad}}^{(\text{max})} = \lim_{I \rightarrow \infty} F_{\text{rad}} = \hbar k \frac{\Gamma}{2}, \tag{2.2}$$

atoms are captured by the collimating light beams only if their transverse velocity is smaller than $v_{\text{cap}} = (L/R)v_z$, with L the length of the region (measured along the beam) where atoms interact with the light beams, R the radius of curvature of the collimating light beams and v_z the longitudinal velocity of the atom. Then they essentially follow a trajectory with the same radius of curvature R as the wavefront of the laser beam. The force in a convergent wave and the resulting trajectories of atoms are described in detail in [203].

The collimation section is constructed as described by Rooijakkers *et al.* [163]. About 200 mW of resonant light is used. The linearly polarized beams have an elliptical profile with rms radii of 3 mm × 38 mm (long dimension along the atomic beam) and a central intensity of 62 mW/cm^2, corresponding to about 370 I_{sat}. To obtain maximum increase in beam intensity, the interaction range is

[2] The expression for the force differs from the textbook expression [130]

$$F_{\text{rad}} = \hbar k \frac{\Gamma}{2} \frac{I/fI_{\text{sat}}}{1 + I/fI_{\text{sat}} + (2\Delta/\Gamma)^2} = \hbar k \frac{\Gamma}{2} \frac{I/fI_{\text{sat}}}{1 + I/fI_{\text{sat}}} \frac{1}{1 + (2\Delta/\Gamma')^2},$$

where it is assumed that $\gamma \ll \Gamma$.

put as close as possible to the nozzle, starting at a distance of about 3 cm. For a typical radius of curvature $R = 12$ m; with an interaction length $L = 10$ cm, the capture velocity is $v_{\text{cap}} = 10$ m/s.

For a given choice of the radius of curvature R, the collimation depends on the intensity of the laser beams and longitudinal velocities. As the Zeeman slower decelerates atoms with longitudinal velocities $\lesssim 1375$ m/s, the radii of curvature and alignment of the beam pairs are optimized for the number of atoms in the magneto-optical trap, as suggested by Herschbach [77]. An extensive analysis of the curved-wavefront technique, pointing out discrepancies between theoretical predictions and experimental results for collimation of a ^{4}He* beam is given by Tol [195].

2.5 Zeeman slower

Atoms from the collimated beam are decelerated in the Zeeman slower from about 1375 m/s (depending on the slowing light intensity) to a velocity around 50 m/s. The deceleration occurs over a distance of 2.7 m, where the atoms are in resonance with a circularly polarized, counter-propagating laser beam. The changing Doppler shift is compensated by the Zeeman shift in an inhomogeneous magnetic field, a technique applied for the first time by Phillips and Metcalf [152]. By exciting the cycling transition, $M_J = 1 \rightarrow M'_J = 2$ in the case of ^{4}He* and $M_F = 3/2 \rightarrow M'_F = 5/2$ in the case of ^{3}He*, the slowing light exerts a radiation pressure F_{rad} with $f = 1$, as given by Eq. (2.1).

The magnetic field points along the axis of the Zeeman slower and has been measured with a Hall probe. The result is shown in Fig. 2.7, where a positive magnetic field value indicates a field pointing towards the source. The field is generated by two tapered solenoids and an extraction coil and changes direction three times. Deceleration takes place between the positions of maximum magnetic field ($B_{\text{max}} = 540$ G) and minimum magnetic field ($B_{\text{min}} = -317$ G), where atoms and slowing light are resonant and the radiation pressure force provides a deceleration exceeding the acceleration of free fall g by more than four orders of magnitude. The extraction coil generates a positive magnetic field and is designed to exactly compensate the magnetic field from the second solenoid in the center of the MOT around $z = 2.99$ m (see inset of Fig. 2.7). The field B_{max} is chosen to be smaller than 563 G, where a level crossing in the Zeeman diagrams of both the ^{3}He* and the ^{4}He* atom gives rise to optical pumping to nonslowed magnetic substates, if the slowing light is not perfectly σ^+ polarized [164].

To obtain a deceleration from about 1375 m/s to around 50 m/s, the slowing light is detuned to the red of the laser cooling transition by 500 MHz.[3] Using

[3] Due to the large detuning, interaction of slowing light with atoms in the trapped sample is negligible.

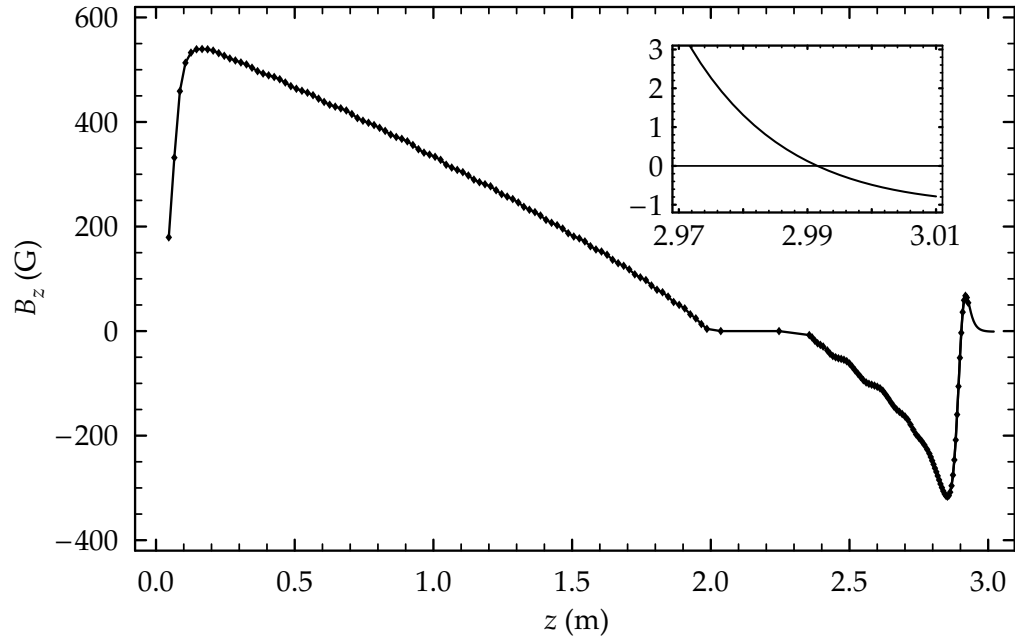

Figure 2.7. Magnetic field component B_z on the axis of the Zeeman slower. The field changes from $B_{\max} = 540$ G to $B_{\min} = -317$ G and has roughly a square root shape along the beam axis. The inset shows an enlarged part at the position of the MOT.

the resonance condition[4]

$$kv(z) = \mu_B B(z)/\hbar - \Delta_{\text{laser}}, \tag{2.3}$$

with $\Delta_{\text{laser}}/2\pi = -500$ MHz, one sees that for a magnetic field $B_{\max}$ an atom velocity $v_{\max} = 1360$ m/s is resonant with the slowing light and for a field $B_{\min}$ velocity $v_{\min} = 61$ m/s is resonant. The capture velocity $v_{\max}$ is significantly larger compared to slowers constructed for a ^{4}He* beam only [164], as a ^{3}He* beam has a significantly larger mean velocity (see Fig. 2.5). The slower presented here can be used for the deceleration of ^{3}He* atoms or ^{4}He* atoms, as well as for the simultaneous deceleration of both ^{3}He* and ^{4}He* atoms with two slowing light frequencies.

To design a Zeeman slower for multiple isotopes, the deceleration process has been analyzed with Newton's equation of motion given by $F_{\text{rad}} = \mathrm{d}p/\mathrm{d}t = m(\mathrm{d}^2z/\mathrm{d}t^2)$. Starting from the magnetic field profile $B(z)$ of Fig. 2.7 and slowing light intensity $I(r,z)$, the equation has been solved numerically, with a solution given by $\zeta(t)$, while incorporating effects of the finite linewidth of the slowing laser and power broadening of the atomic transition. Intensity $I(r,z)$ represents

[4]The resonance condition is easily derived in the reference frame of a decelerating atom. If the atom has a velocity $\boldsymbol{v}(z)$ opposite to the wave vector of the slowing light $\boldsymbol{k}$, the slowing light frequency in the reference frame can be written $\omega_{\text{laser}} = \omega_0 + \Delta_{\text{laser}} + \Delta_{\text{Doppler}}$, where ω_0 is the transition frequency of the unperturbed atom, Δ_{laser} is the detuning of the slowing light from ω_0, and $\Delta_{\text{Doppler}} = -\boldsymbol{k}\cdot\boldsymbol{v} = kv(z)$ is the Doppler shift. In the magnetic field of the Zeeman slower, the atomic transition frequency undergoes a Zeeman shift, $\omega_{\text{atom}} = \omega_0 + \Delta_B$, where $\Delta_B = \mu_B B(z)/\hbar$ is the Zeeman shift [41]. The resonance condition is written $\omega_{\text{laser}} = \omega_{\text{atom}}$, or $kv(z) = \mu_B B(z)/\hbar - \Delta_{\text{laser}}$.

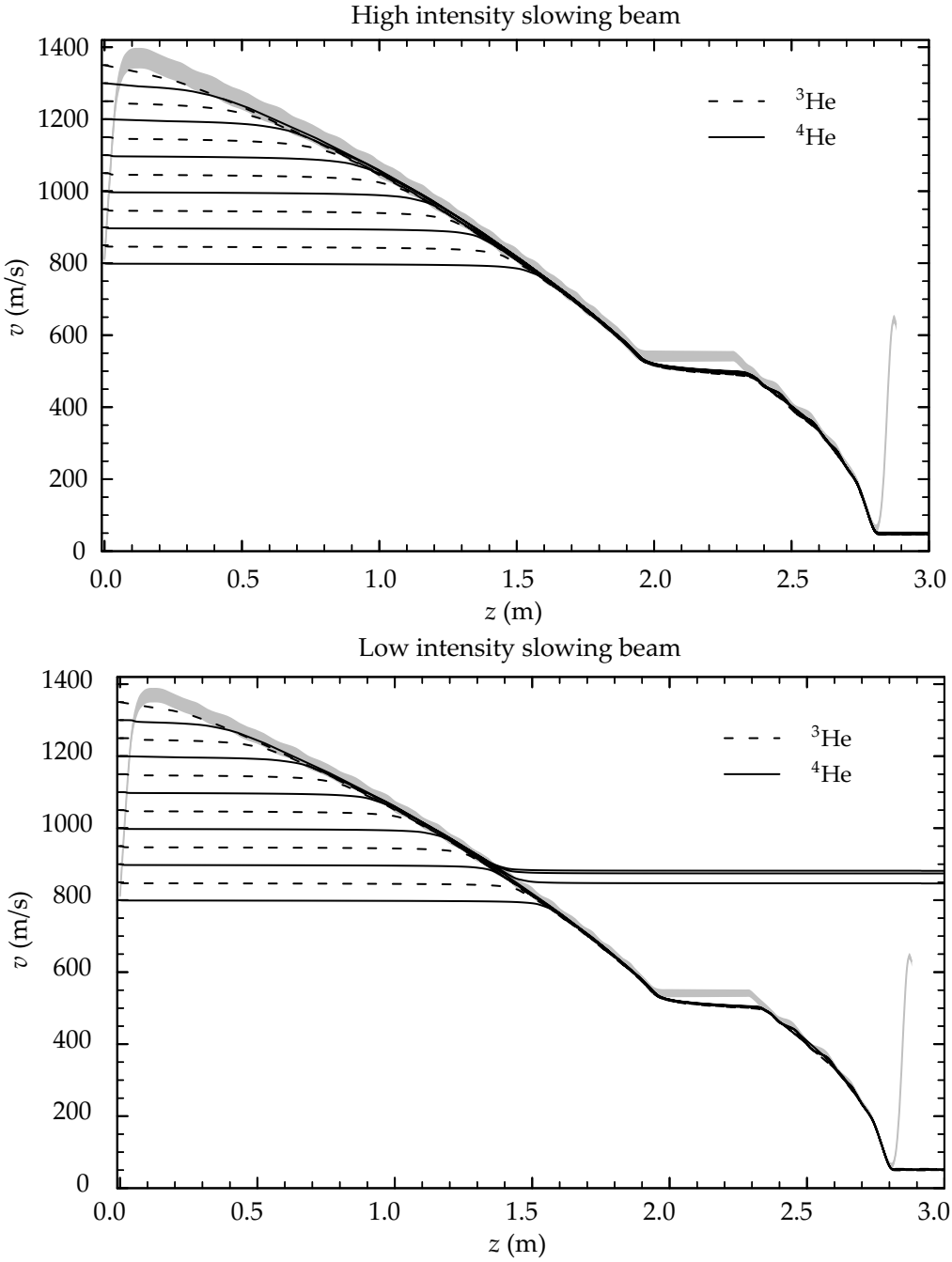

Figure 2.8. Atom velocities $v = \mathrm{d}\zeta(t)/\mathrm{d}t$ as a function of position $z = \zeta(t)$ in the Zeeman slower for a high intensity slowing beam and a low intensity slowing beam. The slowing beams are focussed onto the skimmer. For the high (low) intensity beam, the central intensity is $540 I_{\mathrm{sat}}$ ($270 I_{\mathrm{sat}}$) at the maximum B-field and $100 I_{\mathrm{sat}}$ ($50 I_{\mathrm{sat}}$) at the minimum B-field. The gray band indicates resonant velocities; for atom velocities at the band edges, the deceleration has half the maximum value; the height of the band is given by $(1/2k)[(\gamma+\Gamma)^2 + (\gamma+\Gamma)\Gamma I(0,z)/I_{\mathrm{sat}}]^{1/2}$, reaching a minimum value of 24 m/s (17 m/s) in case of the high (low) intensity beam. Atoms leave the slower at a velocity of about 50 m/s, except ^{4}He* atoms with initial velocities of 1100 m/s, 1200 m/s and 1300 m/s in case of the low intensity slowing beam. The radiation pressure force is too weak and the atoms are lost at velocities of 881 m/s, 874 m/s and 846 m/s, respectively.

a slowing laser beam with an rms diameter of 1.2 cm, that is focussed by a lens ($f = 2.2$ m) onto the skimmer in the collimation section vacuum chamber. The resulting beam profile anticipates the transverse spreading (due to transverse heating) of the decelerated beam given by [90, 195]

$$r_{\mathrm{rms}}(z) = \sqrt{\tfrac{1}{10} v_{\mathrm{rec}} [v_z(0) - v_z(t)]}\, t, \tag{2.4}$$

where $t = \zeta^{-1}(z)$ and $v_{\mathrm{rec}} = \hbar k/m$ is the recoil velocity. Using the slowing light intensity $I\big(r_{\mathrm{rms}}(z), z\big)$, solutions are shown in Fig. 2.8 for two slowing light powers and various initial velocities.[5]

The solutions show significant differences between the two He isotopes as a result of the different masses. With the slowing force equal for both isotopes, ^{3}He* atoms experience a larger deceleration than ^{4}He* atoms. For a large slowing light intensity ($I \geq 100 I_{\mathrm{sat}}$), the effects of the mass difference are small: both isotopes are decelerated from velocities of 1375 m/s to around 50 m/s. However, at small slowing laser intensity ($I \geq 50 I_{\mathrm{sat}}$), simulations show that the deceleration process of ^{4}He atoms with velocities $v \gtrsim 1100$ m/s stops around a velocity of 870 m/s. For ^{3}He* atoms, deceleration to 50 m/s occurs for intensities down to $I \geq 33 I_{\mathrm{sat}}$. As fluctuations in the radiation force are not included in the calculation, the occurrence of longitudinal velocity spreading in the beam is neglected. Solutions $\zeta(t)$ are still expected to provide a good approximation for the deceleration process, as the range of resonant velocities (gray band in Fig. 2.8) is much larger than the recoil velocity, $v_{\mathrm{rec}} = 0.0920$ m/s for ^{4}He* and $v_{\mathrm{rec}} = 0.122$ m/s for ^{3}He* (see Appendix A). Deviations can be expected if recoil kicks accumulate in the forward direction and the absorption rate is too small to compensate for the reduced deceleration. These effects can be taken into account in a Monte Carlo simulation [206], which is outside the scope of the present discussion.

As discussed in Section 2.1, the Zeeman slower is constructed from two double-walled tubes. The outer diameter is 35 mm and cooling water flows between the walls. The first Zeeman slower tube carries the first solenoid and has an inner diameter of 25 mm. The second tube carrying the second solenoid and the extraction coil, has an inner diameter of 32 mm. The distance between the location of the magnetic field minimum and the MOT center is minimized to achieve optimum loading of the MOT. The slowing light is split off from the fiber laser beam and detuned to the red from the laser cooling transition by 500 MHz

[5] Considering the Zeeman deceleration process, Napolitano *et al.* [138] have derived adiabatic following condition $a(z) < a_\infty$, where

$$a(z) = -\frac{\mathrm{d}v}{\mathrm{d}t} = -v\frac{\mathrm{d}v}{\mathrm{d}z} = -v\frac{\mu_{\mathrm{B}}}{\hbar k}\frac{\mathrm{d}B}{\mathrm{d}z} = \frac{\mu_{\mathrm{B}}}{\hbar^2 k^2}(\hbar\Delta_{\mathrm{laser}} - \mu_{\mathrm{B}} B)\frac{\mathrm{d}B}{\mathrm{d}z},$$

is the deceleration at resonance and $a_\infty = F_{\mathrm{rad}}^{(\mathrm{max})}/m = \hbar k\Gamma/(2m)$. The condition is a convenient tool for anyone designing a slower, but does not have to be satisfied along the entire deceleration distance. At points where the solenoids change by one turn, the deceleration is allowed to be larger than a_∞, as long as there are stretches between these points where the field gradient is much smaller [195].

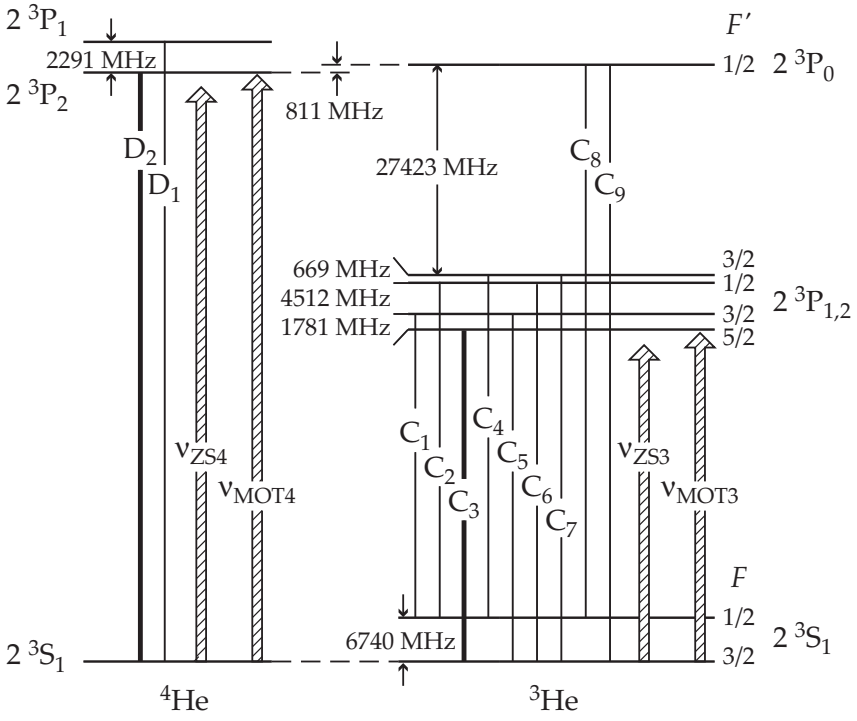

Figure 2.9. Transitions and laser frequencies. Transition $M_F = 3/2 \rightarrow M'_F = 5/2$ of C_3 and transition $M_J = 1 \rightarrow M'_J = 2$ of D_2 are the cycling transitions used for the deceleration of ^{3}He* atoms and ^{4}He* atoms, respectively. Both transitions have a Landé g-factor of 1. Transition C_9 has a Landé g-factor of -1.9.

with a 250 MHz AOM (A.A Opto-Electronic, model AA.MT.250/A0.4-IR) in a double pass configuration.

For the simultaneous deceleration of ^{3}He* and ^{4}He* atoms, the polarization of the slowing light is tuned with a quarter-wave plate (in a rotatable mount) to obtain maximum loading of atoms in the MOT. The polarization of the ^{4}He* slowing light is of critical importance in the case of simultaneous deceleration, as optical pumping effects frustrate the deceleration of ^{3}He* atoms if the light has a significant σ^- component. Figure 2.9 displays the slowing frequencies ν_{ZS3} and ν_{ZS4} and the transitions at 1083 nm, and shows that the isotope shift and fine-structure splitting are of the same order of magnitude, so that transitions C_9 and D_2 are separated by less than a GHz. Calculation of Zeeman diagrams shows that resonant excitation of transition $M_F = 3/2 \rightarrow M'_F = 1/2$ of C_9 by the σ^- component of ν_{ZS4} occurs at a magnetic field of 199 G. Excited ^{3}He* atoms have a high probability of decaying into a nonslowed magnetic substate and escape the slower at a velocity around 843 m/s. These optical pumping effects are observed in the experiments of Chapter 6 as a critical dependence of the loading rate of ^{3}He* atoms on the polarization of the ^{4}He* slowing light.

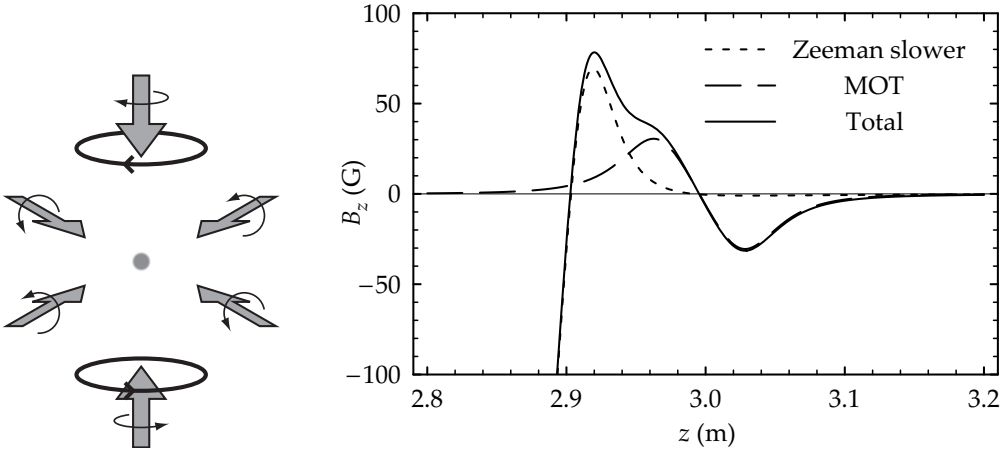

Figure 2.10. MOT configuration (left) and magnetic field component B_z on the axis of the Zeeman slower in the trapping region (right). The magnetic field from the MOT has a (radial) field gradient of 14 G/cm.

2.6 Magneto-optical trap

The decelerated atoms are captured, cooled and confined in a magneto-optical trap of the standard (six-beam) configuration, as suggested by Dalibard [157, in closing remarks] and realized for the first time by Raab *et al.* [157]. Figure 2.10 shows a schematic view of the six-beam MOT configuration: three orthogonal pairs of counter-propagating laser beams with mutual opposite circular polarizations intersect at the zero point of a superimposed magnetic quadrupole field. When the laser frequency is detuned to the red of the laser cooling transition ($\Delta_{\text{laser}} < 0$), atoms experience the cooling effect of a three dimensional optical molasses combined with a confinement by the spatial dependence of the radiation pressure force due to Zeeman shifts in the magnetic field.

An estimate for the force on the axis of a single beam pair (assuming $f = 1$ everywhere) is given by

$$F(x,v) = \hbar k \frac{\Gamma}{2} \left\{ \frac{I_+/I_{\text{sat}}}{1 + I_{\text{tot}}/I_{\text{sat}}} \frac{1+\gamma/\Gamma}{(1+\gamma/\Gamma)(1+\gamma\Gamma/\Gamma'^2) + (2\Delta_+(x,v)/\Gamma')^2} - \frac{I_-/I_{\text{sat}}}{1 + I_{\text{tot}}/I_{\text{sat}}} \frac{1+\gamma/\Gamma}{(1+\gamma/\Gamma)(1+\gamma\Gamma/\Gamma'^2) + (2\Delta_-(x,v)/\Gamma')^2} \right\}, \quad (2.5)$$

where the power-broadened linewidth is $\Gamma' = \Gamma\sqrt{1 + I_{\text{tot}}/I_{\text{sat}}}$ and the detuning is $\Delta_\pm(x,v) = \Delta_{\text{laser}} \mp kv \mp (\mu_B/\hbar)(\partial B/\partial x)x$. The effect of laser beams in other directions is taken into account in the saturation of the transition [115].

The force is different compared to usual MOTs [130], as trapping light detuning is extraordinarily large, $\Delta_{\text{laser}}/2\pi = -25\,(\Gamma/2\pi) = -40$ MHz. As discussed by Herschbach [77], two regimes can be distinguished for the motion of trapped atoms: the capture regime, where atoms with a large velocity of about 50 m/s are captured in the trap, and the molasses regime in which atoms have small velocities and small displacements from the center of the trap. As shown

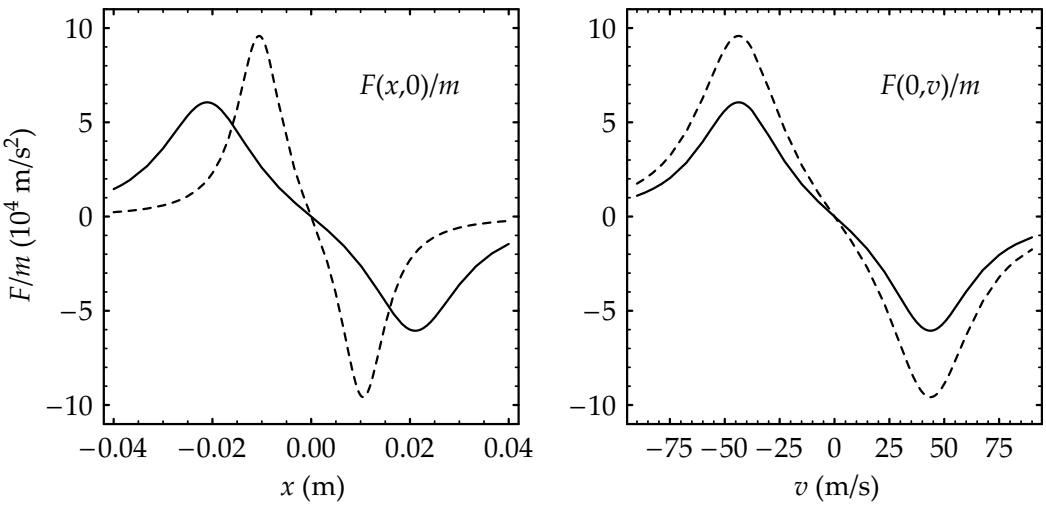

Figure 2.11. Radial (solid line) and axial (dashed line) acceleration due to the radiation pressure force in the MOT. For the radial direction, $I_+ = I_- = 8\ \mathrm{mW/cm^2}$ and $\partial B/\partial x = 14\ \mathrm{G/cm}$. For the axial direction, $I_+ = I_- = 13\ \mathrm{mW/cm^2}$ and $\partial B/\partial x = 28\ \mathrm{G/cm}$. The total trapping intensity $I_{\mathrm{tot}} = 59\ \mathrm{mW/cm^2}$

in Fig. 2.11, force $F(x,v)$ is strong in the capture regime, where $x \approx 0.01$ m and $v \approx 50$ m/s, and weak in the molasses regime, where $x \approx 0.003$ m and $v \approx 1.5$ m/s. Consequently, absorption probabilities are small in the molasses regime, so that the light-assisted ionizing collision rate is small and large numbers of He* atoms can be confined in the MOT [164].

The trapping light is detuned by -40 MHz with an AOM (IntraAction Corp., model 40R) in a single pass configuration. With beam splitter plates, the light is split in six beams that enter the MOT chamber through uncoated windows (see Fig. 2.2). Two beam pairs are at an angle of 45° with the direction of gravity and one pair, entering the chamber through the reentrant windows, is at an angle of 90°. The beams can be aligned independently and have a large rms diameter of 27 mm; the total central intensity is $59\ \mathrm{mW/cm^2}$. The MOT coils are wound with insulated copper wire with a 2 mm × 3 mm rectangular cross-section. Consisting of 24.5 windings, the coils have an inner diameter of 55 mm, outer diameter of 77 mm and a height of 17 mm, and are mounted in water-cooled, cylindrical boxes (with a circular hole in the center) of polyvinyl chloride (PVC) with an inner (outer) diameter of 45 mm (89 mm). The boxes are mounted in the reentrant windows and the coils, in an anti-Helmholtz configuration, produce an axial magnetic gradient of about 1.2 G/cm per ampere. The reentrant windows are separated by a distance of 40 mm. For the two-isotope MOT, laser beams from the two fiber lasers for the two isotopes are overlapped and coupled into a single-mode, polarization-maintaining fiber to achieve perfect overlap at the expense of laser power. To compensate for the loss of laser power, the rms diameter of the trapping beams is reduced and a larger magnetic field gradient is used. Experimental details and the characterization of the two-isotope samples are provided in Chapter 6. The characterization of the trapped samples of single isotopes is presented in Section 2.10.

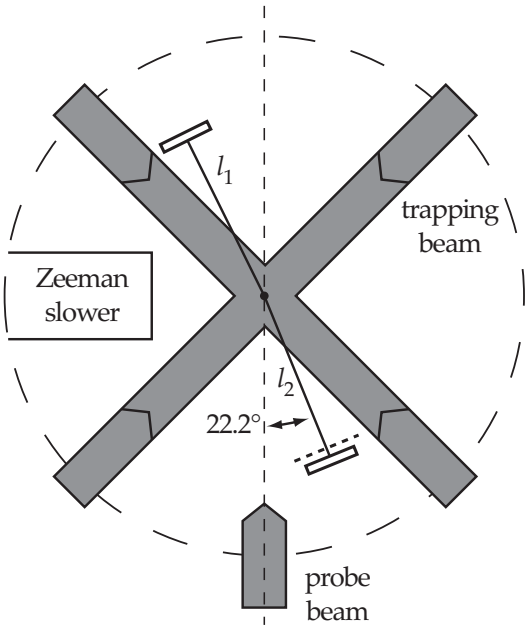

Figure 2.12. Schematic view of the MCP detectors in the MOT vacuum chamber.

2.7 Diagnostic tools

The trapped He* samples are studied with four diagnostic tools. A microchannel plate detector with a negative high-voltage on its front plate attracts all positive ions created in the sample and is used to measure ion production rates in the trapped samples.[6] A second MCP detector is electrically shielded by a grounded grid and is used to perform time-of flight measurements with the trapped samples (see Section 2.10.1). An imaging system based on a charge-coupled device (CCD) camera can be used to obtain fluorescence images of the trapped sample. Also, with an additional probe laser pulse, absorption images can be obtained (see Section 2.10.2).

The MCP detectors are two-stage MCP assemblies (Hamamatsu, model F4655) with an active area diameter of 14.5 mm. The detectors are operated in current mode configuration, i.e. as a DC-current amplifier [219], and the current signal is converted to a voltage, amplified and recorded on a digital oscilloscope. A neutral He* atom can be detected with an MCP detector, because of its large internal energy of 20 eV. If the He* atom hits a MCP channel, the internal energy releases an electron with high probability, initiating an avalanche of electrons in the channel.

The unshielded MCP detector is operated at a voltage of -1620 V and is mounted as shown in Fig. 2.12, at a distance $l_1 = 106(2)$ mm from the MOT center. The detector points towards the MOT center, i.e. the detector surface is perpendicular to the line connecting MOT center and center of the detector surface. The shielded detector is mounted in a similar manner at a distance $l_2 = 106(2)$ mm from the MOT center and is operated at a voltage of -1500 V.

[6] Chapters 3 and 5 present experiments where ion production rates are measured to determine ionization rate coefficients for cold collisions of He* atoms.

The line connecting detector center and MOT center (which is perpendicular to the detector surface) makes an angle of 22.2° with the direction of gravity. As discussed in Appendix B, the orientation of the detector is important for the analysis of the TOF signals. Both detectors are mounted such that He* atoms from the (decelerated) atomic beam cannot directly hit the detector surface.

The imaging system consists of a CCD camera (Cohu, RS-170 monochrome 1/2-inch, model 6312-2001) with a 2/3-inch objective lens mounted in front of a 2-inch magnifier lens. The objective lens is uncoated and has a focal length of 50 mm and a relative aperture of $f/2.8$. The magnifier lens has an anti-reflection coating for 1083 nm and a focal length of 600 mm. The two lenses image the trapped sample with a magnification $M = 0.17$ onto the 786-pixel $\times$ 488-pixel CCD image sensor (Texas Instruments, TC245) that has a pickup area with dimensions 6.4 mm $\times$ 4.8 mm. Background light is blocked by an infrared edge filter. The aperture stop of the imaging is formed by the camera objective and the field stop is formed by the CCD sensor. Consequently, the entrance window of the system is situated in object space and has a rectangular profile with dimensions 37 mm $\times$ 28 mm. The angular aperture is 53 mrad.

2.8 Experimental control

To perform experiments on the trapped samples, various components of the setup are controlled from a standard IBM PC compatible computer extended with a digital I/O card, a frame grabber card and a GPIB card. These interface cards are controlled from a program written in LabVIEW (National Instruments); the program is built from subroutines (subVIs) provided by the manufacturers of the interface cards.

The digital I/O card (Viewpoint Systems, model DIO-128) is used to actuate setup components in a predefined time sequence with high resolution. The card contains a digital signal processor, memory and clock, and has 64 output channels. A timetable with TTL signals for the output channels is loaded into the memory from the LabVIEW program and is executed with a resolution of 1 µs, independent of the processor of the computer host. The card is used to control AOM drivers for the switching of trapping, slowing and probe light on a µs scale, and mechanical shutters (Uniblitz, models LS2T2 and LS6T2) for the switching of trapping and slowing light on a ms scale. Furthermore, it is used to control two current switches (high voltage power MOSFETs), one for the MOT coils and one for the second Zeeman slower coil, and to trigger the frame-grabber card as well as a digital oscilloscope to record signals from the MCP detectors.

The frame-grabber card (Data Translation, model DT3152) is used to record images from the CCD camera. The images can be stored on the hard drive of the computer as bitmaps with the LabVIEW program. A digital oscilloscope (Tektronix, model TDS210) is connected to the computer through the GPIB card (National Instruments, model PCI-GPIB). Oscilloscope traces can be transferred to the computer and stored on the hard drive with the LabVIEW program.

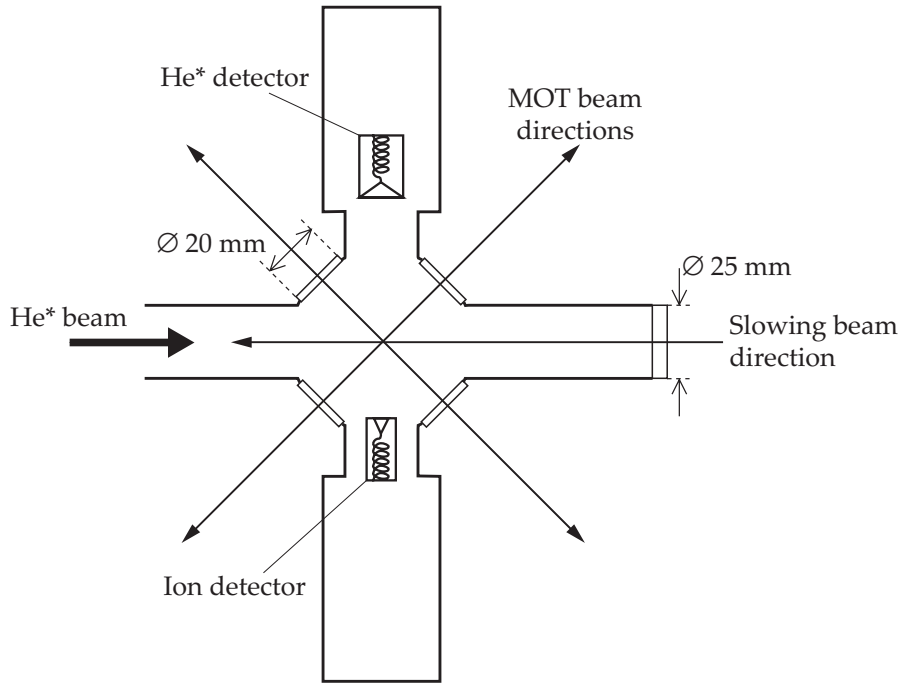

Figure 2.13. Top view of the 389 nm MOT vacuum chamber. The vertical MOT laser beams are not shown. Dimensions are given in mm.

2.9 Setup for 389 nm experiments

In an early stage, the setup has been used to study the magneto-optical trapping of ^{4}He* atoms with 389 nm light. Afterwards, the setup was significantly changed to improve vacuum conditions and to allow trapping beams with a large rms diameter. Differences with the setup discussed so far are presented in the following. The laser system used to produce the 389 nm light is described elsewhere [97, 98].

In the 389 nm setup, the magnetic field in the second Zeeman slower tube has a minimum value of -160 G and the slowing light is detuned to the red of the laser cooling transition by 250 MHz. The maximum magnetic field is 540 G, so that atoms are decelerated from a velocity of about 1100 m/s to a velocity around 30 m/s. (cf. Section 2.5).

The 389 nm MOT vacuum chamber is schematically depicted in Fig. 2.13; a picture is shown in Fig. 3.3. The second Zeeman slower tube is welded onto the chamber and has an inner diameter of 25 mm. The windows in the horizontal plane have an anti-reflection coating for 389 nm and are glued into the stainless steel chamber with epoxy (UHU Plus two-component epoxy adhesive), so that the chamber is bakeable up to 90 °C only. The Zeeman slower is pumped by a single turbomolecular pump (Pfeiffer Vacuum, type TMU 071P, Table 2.1) through a T-piece mounted between the first and second Zeeman slower tubes. The pressure in the MOT chamber, pumped by a turbomolecular pump (Pfeiffer Vacuum, type TPU 062H, Table 2.1), was 2×10^{-9} mbar when the helium beam was absent, and 1×10^{-8} mbar when the beam was present.

A quadrupole magnetic field with the symmetry axis in the vertical direction is produced by two MOT coils that are wound around the vacuum chamber. Each coil consists of 17 windings of water-cooled copper tubing. The trapping beams have an rms diameter of 8 mm and the total central intensity is about 330 mW/cm^2. In the horizontal plane, beams are retro-reflected. Separate vertical beams are used as the corresponding windows are uncoated.

The trapped sample was studied with two channeltron detectors (Dr. Sjuts, model KBL 210 and model KBL 1010). The detectors are used for detection of ion production rates and to perform TOF measurements on the trapped samples. A CCD camera (Pulnix, model TM-6AS) is used for imaging of 707 nm fluorescence, emitted by a steady-state 389 nm MOT. Absorption imaging was not applied in the 389 nm experiment. Further details are provided in Chapter 3.

2.10 Single isotope trapped samples

Trapped samples are characterized by their temperature, number of trapped atoms and effective volume (the samples have a Gaussian density distribution). The temperature is derived from a TOF measurement with the shielded MCP detector, as explained in Section 2.10.1. The number of trapped atoms and effective volume are derived from absorption images recorded with the CCD camera. This detection technique is discussed in Section 2.10.2. Experimental results for trapped samples containing a single isotope, either ^{3}He* or ^{4}He* are presented in Section 2.10.3. Samples containing both isotopes are discussed in Chapter 6.

2.10.1 Time-of-flight measurement

In a TOF measurement, the trap is switched off and atoms from the sample, undergoing a ballistic expansion, hit the unshielded MCP detector and produce a TOF signal. The trap is switched off by blocking the trapping light and slowing light with AOMs and removing the magnetic fields for MOT and Zeeman slower with the corresponding current switches (only the second Zeeman slower solenoid and extraction coil are switched). The TOF signals, that are recorded on a digital oscilloscope, are shown in Fig. 2.14 for samples of both isotopes.

A TOF signal yields information on the velocity distribution of the trapped atoms and, therefore, the temperature of the sample. As the MCP detector is operating in a linear output regime, the signal is proportional to the rate of atoms hitting the detector surface $\mathcal{S}$, given by

$$R_{\mathrm{MCP}} = \iint_{\mathcal{S}} (\boldsymbol{\Phi} \cdot \boldsymbol{n}) \, \mathrm{d}\sigma, \tag{2.6}$$

where $\boldsymbol{n}$ is the unit normal on $\mathcal{S}$ pointing into the detector and

$$\boldsymbol{\Phi}(x, y, z; t) = n(x, y, z; t) \, \boldsymbol{u}(x, y, z; t), \tag{2.7}$$

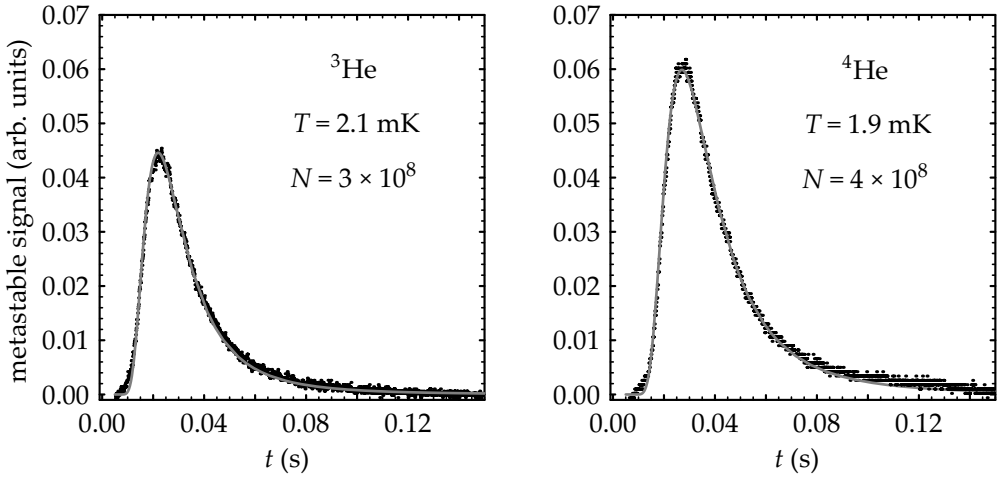

Figure 2.14. Time-of-flight signals. The time at which the TOF signal peaks depends on temperature and mass of the isotope.

is the atom flux associated with the expanding sample, with $\boldsymbol{u}(x, y, z; t)$ the local velocity (see Appendix B). To obtain the temperature of the sample, the signal is analyzed with a least square fitting procedure. In Appendix B, it is shown that for our setup the fitting function can be written as

$$R_{\mathrm{MCP}} = \frac{1}{\sqrt{1+a^2}} \int_{-r}^{r} \int_{x_1}^{x_2} (a\Phi_x(x, y, ax+b; t) - \Phi_z(x, y, ax+b; t))\, \mathrm{d}x\mathrm{d}y \quad (2.8)$$

with $r = 6.43$ mm, $a = 0.408$, $b = -114.5$ mm, $x_1 = 34.1$ mm and $x_2 = 46.0$ mm (defining the dimension, orientation and distance from the MOT center of the MCP detector). Atom flux components $\Phi_x(x, y, z; t)$ and $\Phi_z(x, y, z; t)$ depend on temperature. The initial spatial distribution of the sample can be neglected as the radius of the trapped cloud is small compared to the radius of the ballistically expanded cloud that hits the detector. Detected atoms cover a solid angle of 1.2×10^{-3} sr.

It is conceivable that magnetic field gradients produced by eddy currents disturb the trajectories of the atoms at the start of a TOF measurement. However, the MOT coils are mounted in PVC boxes and placed in reentrant windows, and the steel chamber walls are at a sufficient distance from the trapped sample, so that these effects can be neglected. No evidence of disturbed trajectories was observed.

As the area under a TOF signal is proportional to the number of trapped atoms in a sample N, TOF measurements can be used for the determination of N, if the MCP detector is calibrated. To analyze the two-isotope MOT, the MCP detector operating at the voltage of -1500 V is calibrated with absorption images and TOF signals are used to determine trapped atom numbers. This is discussed in Chapter 6.

2.10.2 Absorption imaging

To determine the density distribution of the trapped sample, absorption images are taken. The trap is switched off and, after 500 µs when magnetic fields have disappeared, a resonant laser beam is sent through the sample, into the CCD camera. The sample is imaged onto the CCD chip, appearing as a shadow in the probe light. To avoid pushing of the atoms by the light, a beam of low intensity ($I \lesssim 0.05 I_{\mathrm{sat}}$) is used, that is switched on for a short time of 100 µs.

The probe light is generated with the Toptica diode laser. Applying a magnetic field to the discharge cell in the saturated absorption spectroscopy setup, the Lamb dips are shifted with the Zeeman effect and the laser frequency is stabilized at 27 MHz from the (unperturbed) atomic transition. A resonant probe beam, switchable at a nanosecond timescale, is obtained with an AOM (Neos Technologies, Q-switch model N33027-50-5-I) operating at 27 MHz, in a single pass configuration.

The interaction between the probe light and the atomic sample can be treated with rate equations [195]. For a low intensity beam, traveling through a sample with density distribution $n(x,y,z)$, along the y-axis in positive direction, the intensity $I(x,y,z,)$ satisfies Lambert-Beer's law[7]

$$\frac{\mathrm{d}I(x,y,z)}{\mathrm{d}y} = -\hbar\omega\frac{\Gamma}{2}\frac{I(x,y,z)}{I'_{\mathrm{sat}}}n(x,y,z), \tag{2.9}$$

[7] As discussed by Tol [195], the intensity of the probe beam satisfies (quantum numbers apply to ^{4}He*; for ^{3}He*, replace J by F, J' by F', M_J by M_F, and M'_J by M'_F)

$$\frac{\mathrm{d}I}{\mathrm{d}y} = -\hbar\omega\frac{\Gamma}{2}\frac{I}{I'_{\mathrm{sat}}}(\textstyle\sum_{M_J} n_{M_J} - \sum_{M'_J} n_{M'_J})$$

with

$$I'_{\mathrm{sat}} = \frac{\sum_{M_J} n_{M_J} - \sum_{M'_J} n_{M'_J}}{\sum_{M'_J}\sum_{M_J} (\Theta_{M'_J M_J}/3)\, C_{M'_J M_J}\, \chi_{M'_J M_J}\, (n_{M_J} - n_{M'_J})}.$$

Here, n_{M_J} and $n_{M'_J}$ are the population of magnetic substates M_J and M'_J, respectively, $\Theta_{M'_J M_J}$ takes into account the polarization of the light, $C_{M'_J M_J} = \left|\langle J\,1; M_J(M'_J - M_J)|J' M'_J\rangle\right|^2$ is the relative strength of electric dipole transition $M_J \rightarrow M'_J$ expressed in terms of Clebsch-Gordan coefficients $\langle j_1 j_2; m_1 m_2 | jm\rangle$, and $\chi_{M'_J M_J}$ is a line-shape factor for the transition.

For samples released from the MOT, all $\chi_{M'_J M_J}$ are the same and the effective saturation intensity can be written as $I'_{\mathrm{sat}} = f I_{\mathrm{sat}}/\chi$, where f is a rational number that depends on the polarization of the light, the population of the magnetic substates and the relative strengths of the transitions between substates. Writing $n = \sum_{M_J} n_{M_J} + \sum_{M'_J} n_{M'_J}$, expressions can be derived for two extreme situations. In the initial state, when the interaction of probe light and atoms has just started, $n_{M'_J} = 0$ and

$$\frac{\mathrm{d}I}{\mathrm{d}y} = -\hbar\omega\frac{\Gamma}{2}\frac{I}{I'_{\mathrm{sat}}}n.$$

After a time of about 50 µs, a steady state is reached, where $\mathrm{d}n_{M'_J}/\mathrm{d}t = 0$ and

$$\frac{\mathrm{d}I}{\mathrm{d}y} = -\hbar\omega\frac{\Gamma}{2}\frac{I/I'_{\mathrm{sat}}}{1 + I/I'_{\mathrm{sat}}}n$$

At small intensities, $I \ll I'_{\mathrm{sat}}$, the two cases are described by the same expression with different values of I'_{sat}. Details can be found in Tol [195].

where

$$I'_{\mathrm{sat}} = \frac{f I_{\mathrm{sat}}}{\chi(T)} \tag{2.10}$$

is an effective saturation intensity ($I_{\mathrm{sat}} = 0.167\ \mathrm{mW/cm^2}$), that accounts for Doppler broadening of the atomic transition and the distribution of atoms over the magnetic substates. It is assumed that $I(x,-\infty,z) \ll I'_{\mathrm{sat}}$. The solution of Lambert-Beer's law is given by

$$I(x,y,z) = I(x,-\infty,z)\ \exp\left[-\sigma_{\mathrm{a}} \int_{-\infty}^{y} n(x,y',z)\,\mathrm{d}y'\right] \tag{2.11}$$

with absorption cross-section

$$\sigma_{\mathrm{a}} = \hbar\omega \frac{\Gamma}{2} \frac{1}{I'_{\mathrm{sat}}} = \frac{3\lambda^2}{2\pi} \frac{\chi(T)}{f}. \tag{2.12}$$

Doppler broadening is included in the line shape factor

$$\chi(T) = \sqrt{\frac{m}{2\pi k_{\mathrm{B}} T}} \int_{-\infty}^{\infty} \frac{1}{1 + 4(\Delta - kv)^2/\Gamma^2}\ \exp[-mv^2/(2k_{\mathrm{B}}T)]\,\mathrm{d}v, \tag{2.13}$$

which is the convolution of the natural Lorentz line shape of the transition and a Maxwell-Boltzmann velocity distribution describing the trapped sample. The laser linewidth of 0.4 MHz ($0.25\,\Gamma/2\pi$) is too small to have a significant effect on the relative absorption.

The distribution over magnetic substates is described by numerical factor f. For an unpolarized sample[8] probed by linearly-polarized light, factor f_{unpol} is the inverse of the mean relative transition strength with $M_J = M'_J$ for ^{4}He* and $M_F = M'_F$ for ^{3}He*. It can be derived from Fig. 2.15, that $f_{\mathrm{unpol}} = 18/10$ for ^{4}He* and $f_{\mathrm{unpol}} = 2$ for ^{3}He* atoms.[9] The interaction between the atoms and the linearly-polarized light leads to polarization of the sample. For experimental conditions, steady state is reached after about 50 µs [195]. The corresponding f factor can be obtained by solving the rate equations. An analytical expression and tabulated values for common two-level systems (including $J = 1 \rightarrow J' = 2$ and $F = 3/2 \rightarrow F' = 5/2$) are given in [66]. For a ^{4}He* sample, $f_{\mathrm{steady}} = 17/10$ and, for a ^{3}He* sample, $f_{\mathrm{steady}} = 25/14$. Consequently, optical pumping leads to a decrease of the f factors by 6% for ^{4}He* and by 11% for ^{3}He*.

As the samples have a Gaussian shape, the density distribution is given by

$$n(x,y,z) = \frac{N}{(2\pi)^{3/2}\sigma_x\sigma_y\sigma_z}\ \exp\left(-\frac{x^2}{2\sigma_x^2} - \frac{y^2}{2\sigma_y^2} - \frac{z^2}{2\sigma_z^2}\right), \tag{2.14}$$

[8] When a sample is released from the trap, magnetic fields are switched off and any polarization is assumed to be washed out.

[9] Tol [195] has shown that, for equally populated magnetic substates n_J (unpolarized samples), f is independent of the polarization of the light and can be written $f_{\mathrm{init}} = 3(2J+1)/(2J'+1)$ in the case of ^{4}He*, and $f_{\mathrm{init}} = 3(2F+1)/(2F'+1)$ in the case of ^{3}He*.

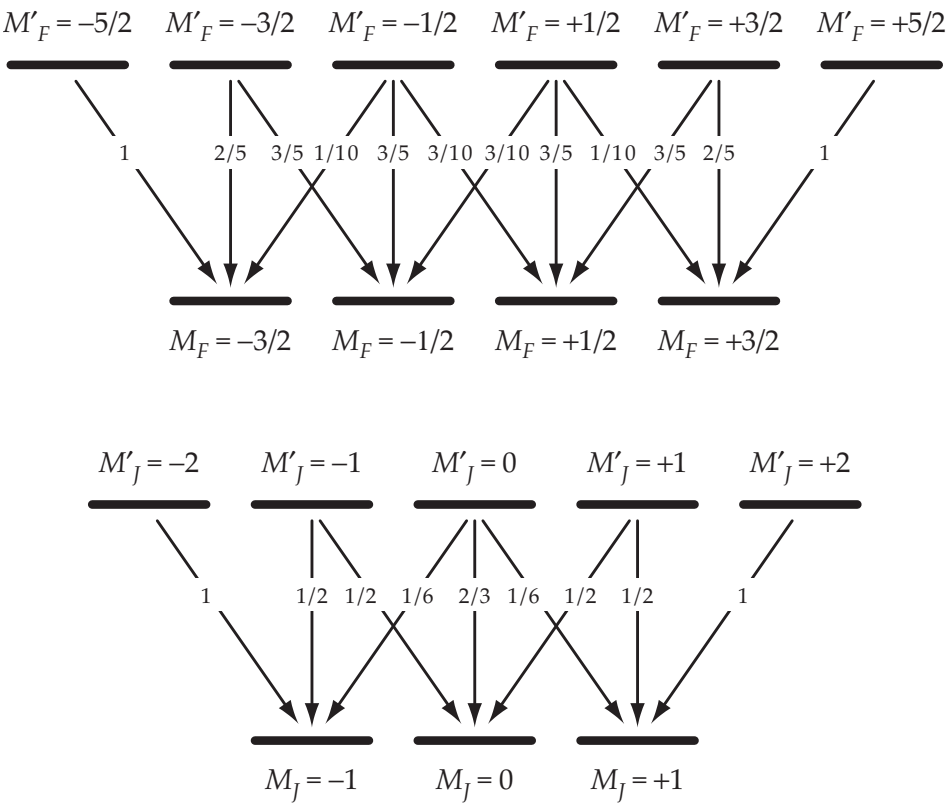

Figure 2.15. Relative strengths of electric dipole transitions between magnetic substates for ^{4}He* ($J = 1 \rightarrow J' = 2$) and ^{3}He* ($F = 3/2 \rightarrow F' = 5/2$).

with N the number of atoms, and σ_x, σ_y and σ_z the rms radii of the sample. The cloud is assumed to be cylindrically symmetric ($\sigma_y = \sigma_x$) around the z-axis. To obtain the three parameters determining the density distribution, the transmittance

$$\frac{I_{\text{out}}(x,z)}{I_{\text{in}}(x,z)} = \frac{I_{\text{abs}}(x,z) - I_{\text{bgr}}(x,z)}{I_{\text{prb}}(x,z) - I_{\text{bgr}}(x,z)} \tag{2.15}$$

is determined from three pictures: a raw absorption image $I_{\text{abs}}(x,z)$ of the cloud, a probe image $I_{\text{prb}}(x,z)$ under the same conditions but without the cloud, and a background image $I_{\text{bgr}}(x,z)$ without probe light. Substituting Eqs. (2.11) and (2.14) into Eq. (2.15) results in an expression for the transmittance,

$$\frac{I_{\text{out}}(x,z)}{I_{\text{in}}(x,z)} = \exp\left\{-\hbar\omega\frac{\Gamma}{2}\frac{\chi(T)}{fI_{\text{sat}}}\frac{N}{2\pi\sigma_x\sigma_z}\exp\left[-\frac{x^2}{2\sigma_x^2} - \frac{z^2}{2\sigma_z^2}\right]\right\}, \tag{2.16}$$

that is used as a fitting function in a least square fitting procedure. The temperature obtained from a preceding TOF measurement is used as input.

The transmittance obtained from a ^{3}He* sample with $T = 2.1$ mK is shown in Fig. 2.16; profiles along the x-axis and z-axis are shown in Fig. 2.17. In the fitting procedure f factors for unpolarized samples are used. This should result in a small rise of absorption. However, there should also be a drop in absorption because the atoms get pushed by the light. As shown in [195], both effects are small in the 100 µs period of probing and since they cancel each other out at

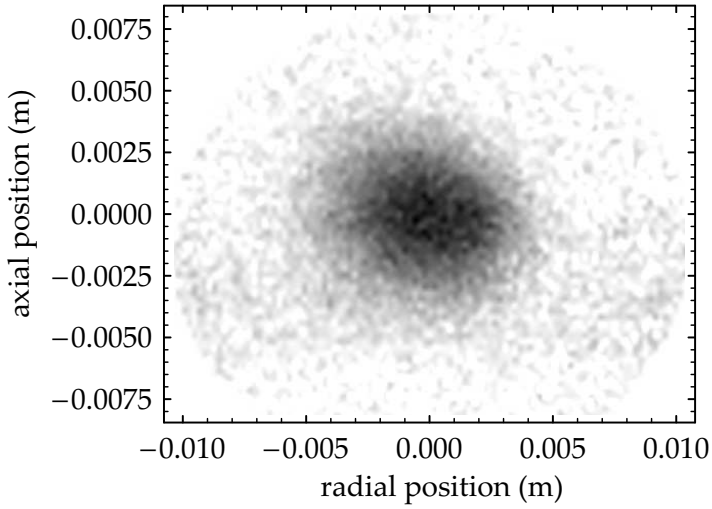

Figure 2.16. Absorption image of a ^{3}He* sample after an expansion of 0.5 ms.

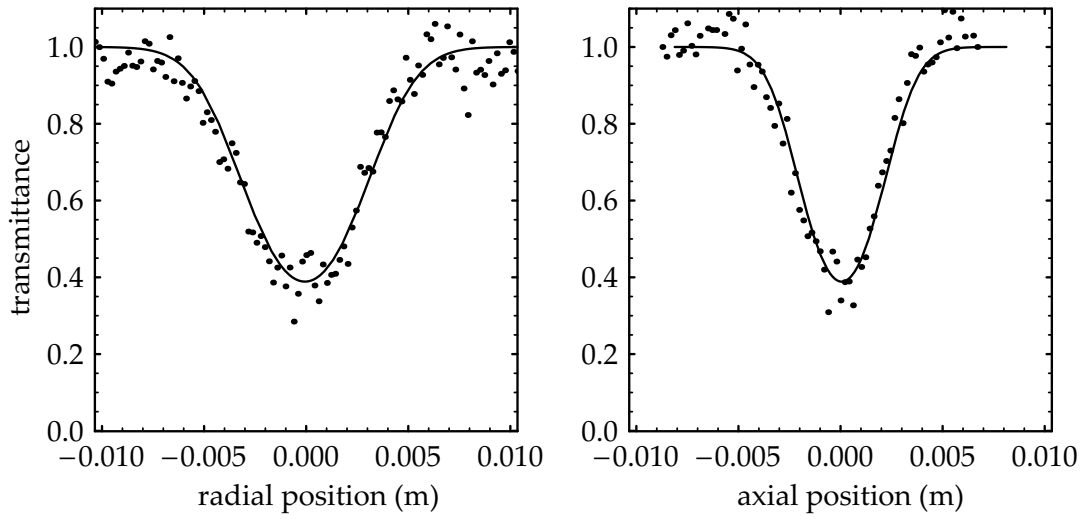

Figure 2.17. Profiles through the center of the sample of the absorption image of Fig. 2.16.

Table 2.2. Experimental details.

trapping light detuning	$\Delta_{\text{laser}}/2\pi = -40$ MHz
total trapping light intensity	$I_{\text{tot}} = 59$ mW/cm^2
magnetic field gradient	$\frac{\partial B}{\partial z} = 2\frac{\partial B}{\partial \rho} = 28$ G/cm

Table 2.3. Characteristic parameters of the magneto-optically trapped He* samples. Experimental errors correspond to one standard deviation.

	^{3}He*	^{4}He*
T (mK)	2.0(3)	1.9(1)
N (−)	$2.6(9) \times 10^8$	$3.7(5) \times 10^8$
σ_ρ (cm)	0.20(3)	0.20(2)
σ_z (cm)	0.14(1)	0.15(2)
V (cm^3)	0.09(3)	0.09(2)
n_0 (cm^{-3})	$3.0(5) \times 10^9$	$4.4(4) \times 10^9$

least partly, both are neglected. The rms radii of the sample in the MOT are obtained by correcting for the expansion of the sample over a time of 500 µs. The values are consistent with fluorescence imaging measurements.

2.10.3 Characteristics of samples

Samples containing a single isotope have been optimized for trapped atom number and analyzed with TOF measurements and absorption imaging. Experimental details concerning the trapping light and magnetic field used for the MOT are summarized in Table 2.2. The results of the measurements are presented in Table 2.3, listing temperature T, trapped atom number N, rms radii σ_ρ and σ_z, volume $V = (2\pi)^{3/2}\sigma_\rho^2\sigma_z$, and central density $n_0 = N/V$.

For ^{4}He* samples, the number of trapped atoms is comparable to other MOTs [24, 148, 196]. As our detuning and intensity of the trapping light as well as our magnetic field gradient are comparable to those in other experiments, also the central density and volume are of the same order of magnitude. For our ^{3}He* sample, the trapped atom number is an improvement by three orders of magnitude compared to results reported previously [102, 103].

The temperature of our samples is higher than predicted by theory [115],

$$T = \frac{\hbar\Gamma}{4k_{\text{B}}}\frac{1 + I_{\text{tot}}/I_{\text{sat}} + (2\Delta_{\text{laser}}/\Gamma)^2}{2|\Delta_{\text{laser}}|/\Gamma} \approx 1.1 \text{ mK} \tag{2.17}$$

The difference is probably caused by the trapping beam alignment that has been optimized for trapped atom number and by an intensity imbalance of about

30% in one of the trapping beam pairs. Pushing of the cloud towards the MCP by remaining magnetic field gradients is unlikely as the strength and direction of the corresponding force depend on the magnetic substate of the atom, and magneto-optically samples are (almost) unpolarized (see Section 5.5).

The single-isotope samples presented here are the starting point for the study of cold ionizing collisions of ^{3}He* atoms or ^{4}He* atoms, as discussed in Chapter 5. The simultaneous trapping of both isotopes is discussed in Chapter 6.

Chapter 3

Magneto-optical trap for metastable helium at 389 nm

A magneto-optical trap (MOT) is a standard tool in the production of cold atomic gases, allowing investigation of cold-collision phenomena [211] as well as the realization of Bose-Einstein condensation (BEC) in alkali-metal species [3] and, more recently, in metastable triplet ^{4}He [147, 162], referred to as ^{4}He*. Metastable triplet helium has a high (19.8 eV) internal energy, which allows for real-time diagnostics and increased sensitivity in BEC probing. Unfortunately, the high internal energy also introduces strong Penning ionization losses in magneto-optically trapped atomic clouds, which imposes limits on the maximum achievable density. The two-body loss rate coefficient associated with this process is about 5×10^{-9} cm^3/s for a MOT on the $2\ ^3S_1 \rightarrow 2\ ^3P_2$ transition at 1083 nm [196], which is about two orders of magnitude larger than the loss rate coefficient in a standard alkali-metal MOT. In BEC experiments, a MOT is used as a bright source of cold atoms to load a magnetic trap with large numbers of atoms. Moreover, as a starting point for evaporative cooling, a dense magnetostatically trapped cloud is desired. So ideally, the magneto-optically trapped cloud must provide this high density. In the present work, we explore the feasibility and the possible advantages of a MOT using the $2\ ^3S_1 \rightarrow 3\ ^3P_2$ transition at 389 nm for metastable helium, in comparison with the conventional $2\ ^3S_1 \rightarrow 2\ ^3P_2$ (1083 nm) magneto-optical trap.

Although the 389 nm transition was recently used in laser cooling experiments [174], it has not found wide application yet. This mainly relates to the fact that 10% of the $3\ ^3P_2$ population decays via the $3\ ^3S_1$ state (Fig. 3.1), making a closed laser cooling transition between magnetic substates impossible. In addition, the shorter 389 nm wavelength leads, in combination with a linewidth $\Gamma/2\pi = 1.51$ MHz, to a relatively high saturation intensity $I_{\mathrm{sat}} = 3.35$ mW/cm^2

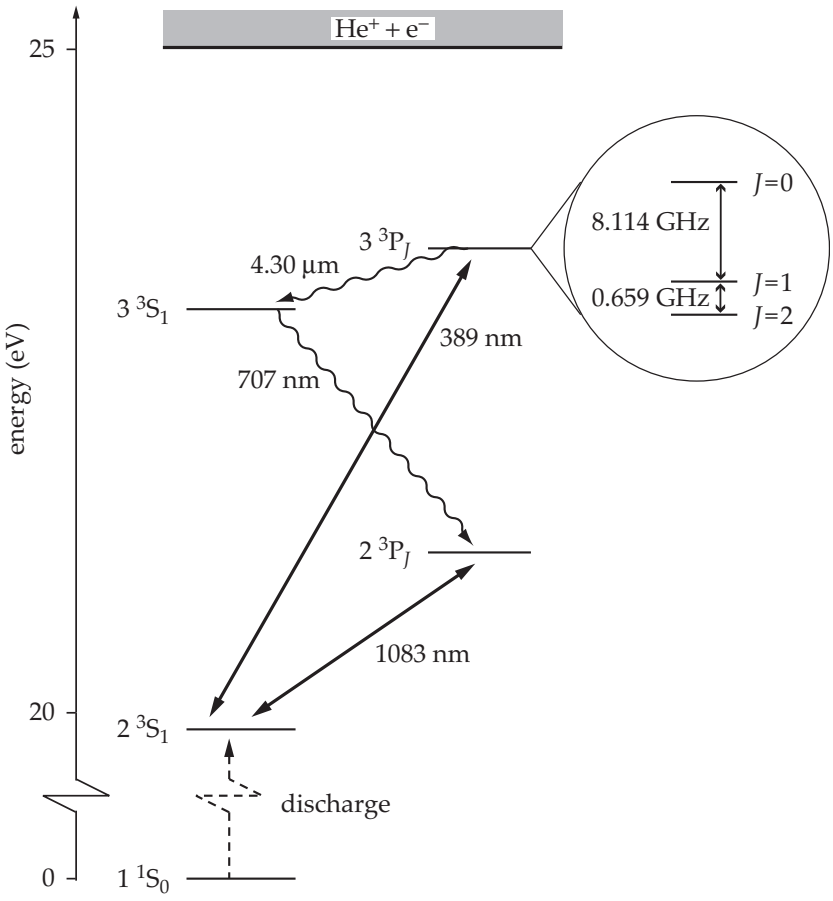

Figure 3.1. Helium level scheme. The long-lived 2 $^3S_1$ metastable state is populated in a DC discharge. The 2 $^3S_1 \rightarrow 3\ ^3P_2$ (389 nm) and 2 $^3S_1 \rightarrow 2\ ^3P_2$ (1083 nm) laser cooling transitions are indicated with bold arrows.

(see Appendix A). In comparison, the $2\,^3S_1 \rightarrow 2\,^3P_2$ transition at 1083 nm has almost the same linewidth, but a saturation intensity of only 0.167 mW/cm^2. To maximize the number of trapped atoms, dedicated metastable helium magneto-optical traps are operated at large detuning and intensity [23, 146, 196]. This implies the need for a high-power laser setup. Nevertheless, the concept of a 389 nm magneto-optical trap is appealing. An interesting feature of the 389 nm transition is the momentum transfer per photon, which is 2.8 times larger than for the 1083 nm photons. Since both transitions have nearly equal linewidths, the spontaneous cooling force increases proportional to the photon momentum. This offers the possibility to compress the cloud substantially in comparison to a 1083 nm MOT at the same detuning and power. Unfortunately, compression may lead to increased losses predominantly due to light-assisted (photoassociative) collisions. However, the two-body loss rate coefficient is expected to be smaller for the 389 nm case (see Section 3.3.1), so that the cloud may be compressed without loss of too many metastables. Furthermore, it should be noted that the 1083 nm and 389 nm transitions are electronically alike, which greatly facilitates the comparison between the two MOT types. Finally, the 389 nm MOT differs from the 1083 nm MOT in yet another respect: two 389 nm photons contain sufficient energy to ionize an atom in the $2\,^3S_1$ state. This may introduce observable additional losses.

In this chapter, we report on the study of a prototype 389 nm MOT for ^{4}He* atoms. In Section 3.1 we present some theoretical considerations regarding laser cooling and trapping at 389 nm. Next, we outline our experimental setup in Section 3.2. Results are given in Section 3.3. Conclusive remarks and an outlook are presented in Section 3.4.

3.1 Theory of the 389 nm MOT

3.1.1 Comparison with 1083 nm MOT

The large photon momentum transfer modifies the equilibrium conditions in a 389 nm MOT with respect to the 1083 nm situation. This follows from regarding the motion of an atom, trapped in a one-dimensional MOT, as an overdamped harmonic oscillation [115, 176]. Within this picture, the oscillation frequency $\omega_{\rm osc}$ and damping coefficient $\epsilon_{\rm d}$, for small velocities and small deviations from trap center, are given by

$$\omega_{\rm osc}^2 = 4\hbar k \frac{4\delta S \zeta}{m(1+2S+4\delta^2)^2}, \tag{3.1}$$

$$\epsilon_{\rm d} = 4\hbar k^2 \frac{4\delta S}{m(1+2S+4\delta^2)^2}, \tag{3.2}$$

with k being the wave number of the MOT laser light, m the atomic mass, $\delta = \Delta/\Gamma$ with Δ the laser detuning from resonance, $S = I/I_{\rm sat}$ the saturation parameter, with I being the intensity per MOT beam, and ζ representing the spatial derivative of the position-dependent Zeeman detuning. The theoretical framework in which Eqs. (3.1) and (3.2) are derived assumes that the Doppler shift

Δ_{rec}, corresponding to the recoil velocity, is small compared to the linewidth Γ. In the 389 nm case, however, $\Delta_{\mathrm{rec}}/\Gamma = 0.44$, which invalidates the assumption of a small recoil Doppler shift. Nevertheless, we proceed with our comparison between a 389 nm MOT and 1083 nm MOT based on Eqs. (3.1) and (3.2), assuming that the conclusions will be approximately correct.

The large photon momentum transfer at 389 nm implies two general differences between the 389 nm and a 1083 nm MOT, which follow immediately from Eqs. (3.1) and (3.2). First, bearing in mind that $k_{389}/k_{1083} = \lambda_{1083}/\lambda_{389} \approx 2.8$, it is obvious that for an equal saturation parameter and detuning the damping coefficient increases by a factor $(k_{389}/k_{1083})^2 \approx 7.8$ as compared to a 1083 nm MOT. Although this does not alter the temperature in the MOT, which does not depend on wavelength and is expected to be almost equal for the two cases, the damping time τ_{389} is shortened to $(k_{1083}/k_{389})^2\,\tau_{1083} \approx 0.13\tau_{1083}$ [115]. Second, for identical MOT parameters, the spring constant $\kappa = m\omega_{\mathrm{osc}}^2$ is increased by a factor 2.8. This has implications for the size of the trapped cloud, which is determined by the equipartition of the potential and kinetic energies. The volume V of the cloud is (following the definition of V as given in Section 3.2.3)

$$V = \left(\frac{2\pi k_{\mathrm{B}} T}{\kappa}\right)^{3/2}, \tag{3.3}$$

where for simplicity we have assumed an isotropic three-dimensional (3D) harmonic oscillator (k_{B} is Boltzmann's constant). It follows that the volume decreases by a factor $(k_{389}/k_{1083})^{3/2} \approx 4.6$, i.e. the cloud is compressed with respect to the 1083 nm situation.

3.1.2 Loading process

All magnetic substates participate in the atom-laser interaction, as the magneto-optically trapped cloud is contained at low magnetic field strengths and irradiated from six directions with circularly polarized light. Therefore, the presence of the second decay channel of the $3\,^3\mathrm{P}_2$ state will not limit the operation of the MOT, as long as there is loading of atoms from the outer regions of the MOT volume. Loading, however, may be frustrated by the nonclosed cycling transition as well as by the relatively large Doppler shift. More specifically, the question arises whether the slowing process of atoms entering the MOT volume can be completed before a spontaneous emission via the $3\,^3\mathrm{S}_1$ cascade takes the atom to a different, nonresonant magnetic substate. If not, the atom needs to be repumped to the cycling transition; otherwise it will escape from the MOT volume. To make a conservative estimate of the capture velocity of a 389 nm MOT, a simple 1D model for an atom traversing the MOT volume is used. In this model, the MOT is replaced by a 389 nm Zeeman slower with a length equal to the MOT beam diameter and a slowing laser with detuning equal to the MOT detuning.

We calculate the position-dependent, instantaneous photon scattering rate for atoms at a given velocity v, interacting with a counterpropagating, red-detuned laser beam at 389 nm inducing σ^+ transitions. This laser beam represents the two MOT laser beams counterpropagating the atomic beam at angles of

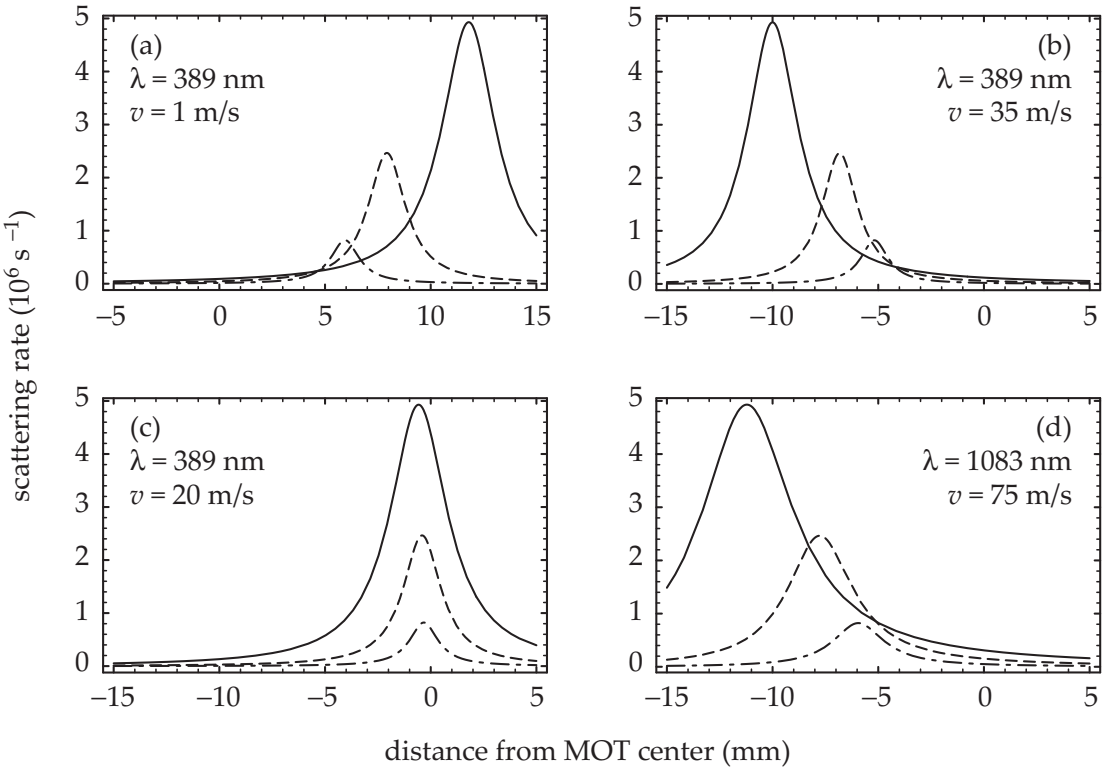

Figure 3.2. (a)–(c) 389 nm and (d) 1083 nm photon scattering rates as a function of distance from the MOT center for $M = 1 \rightarrow M' = 2$ (solid line), $M = 0 \rightarrow M' = 1$ (dashed line), and $M = -1 \rightarrow M' = 0$ (dash-dotted line) transitions.

$\pm 45^\circ$ with respect to the atomic beam (see Section 3.2.1). We assume the atoms to be predecelerated by a Zeeman slower, so that we can choose any initial velocity. We take Zeeman detuning, laser intensity, and Doppler shift into account, the latter of which is taken to be $kv/\sqrt{2}$ to correct for the $\pm 45^\circ$ angle between the atom and (real) laser beams. Furthermore, we consider all three σ^+ transitions, i.e. $M = -1 \rightarrow M' = 0$, $M = 0 \rightarrow M' = 1$ and $M = 1 \rightarrow M' = 2$ (referred to as the laser cooling or cycling transition). In Fig. 3.2, plots are shown of the photon scattering rate for the three σ^+ transitions as a function of the distance from the center of the MOT, measured along the symmetry axis of the Zeeman slower. The MOT light boundaries are at about ± 10 mm from the MOT center (see also Section 3.2.2), and the atoms are moving into the positive direction. Figure 3.2(a) shows the familiar behavior of the scattering force in a MOT. An atom, moving into the positive direction at a typical intra-MOT velocity $v = 1$ m/s, scatters an increasing number of photons from the counterpropagating MOT laser beam as it moves farther away from the MOT center. Consequently, it will be slowed down and eventually pushed back towards the center.

The model can also be used to investigate the capture of atoms emerging from the Zeeman slower. As the slowing light is σ^+-polarized, atoms are optically pumped into the $M = 1$ state and are only captured in the MOT if the scattering rate for transition $M = 1 \rightarrow M' = 2$ is sufficiently large. First, we consider atoms that emerge from the slower with a velocity $v = 75$ m/s

(not shown in Fig. 3.2). Choosing a MOT detuning of -35 MHz, an intensity of $30 I_{\mathrm{sat}}$, and a magnetic-field gradient of 20 G/cm (these conditions are typical for a 1083 nm MOT), the model shows that atoms are not resonant with the slowing light inside the MOT volume and no atoms are captured. Next, we lower v to 35 m/s. We observe that the atoms now interact strongly with the laser light within the MOT volume (see Fig. 3.2(b)). However, the peaks in the scattering rate of the different σ^+ transitions hardly overlap in space, as a result of their different Zeeman detunings. Slowing these atoms down to zero velocity requires about 190 absorption-emission cycles, whereas it takes about 20 cycles (corresponding to a velocity reduction of only 4 m/s) for the atom to end up in one of the nonabsorbing ($M = -1$ or $M = 0$) states. Consequently, the capture process is interrupted. Before this M-state atom becomes sufficiently resonant again, such that it is optically pumped back to the $M = +1$ state, it will have traveled out of resonance with the cycling transition and can no longer be captured by the MOT. Only for velocities $v < 20$ m/s, an atom ending up in the wrong M state is repumped fast enough to continue the deceleration towards zero velocity (Fig. 3.2(c)). From these simulations we conclude that the capture velocity of the 389 nm MOT is about 24 m/s. This velocity is much smaller than the $\sim$ 75 m/s capture velocity of a typical 1083 nm MOT. Figure 3.2(d) illustrates the superior loading capabilities of a 1083 nm MOT of 15 mm radius. The smaller Doppler shift allows for faster atoms to be captured, whereas the closed cycling transition does not impose any constraints on the magnetic-field strength. In fact, the 1083 nm MOT diameter sets the maximum stopping distance, and thus limits the capture velocity. Within the picture provided by the model, increasing the diameter of a 389 nm MOT will not solve the problem described above. To avoid optical pumping to nonresonant magnetic substates in the outer regions of the MOT, only small magnetic-field gradients can be tolerated. Then, to maintain sufficient confinement of the trapped atoms, only small MOT laser detunings are allowed, thereby limiting the capture velocity.

We stress that this model is based on crude simplifications and ignores important features of the MOT. For instance, the orthogonal MOT laser beams, in combination with the spatially varying, three-dimensional magnetic-field vector induce $\sigma^{\pm}$ as well as π transitions. Therefore, the conditions required for repumping to the laser-cooled state may be less stringent than predicted by our simple model, and we conclude that the capture velocity of a 389 nm MOT will be somewhat larger than 24 m/s. As will be discussed in Section 3.2.1, the relatively low capture velocity has negative consequences for the loading rate, which may be partially overcome by the implementation of an auxiliary Zeeman slower in the apparatus. In Section 3.3.3 we present the results of a test of this auxiliary Zeeman slower concept, as well as a derivation of the 389 nm MOT capture velocity from experimental data.

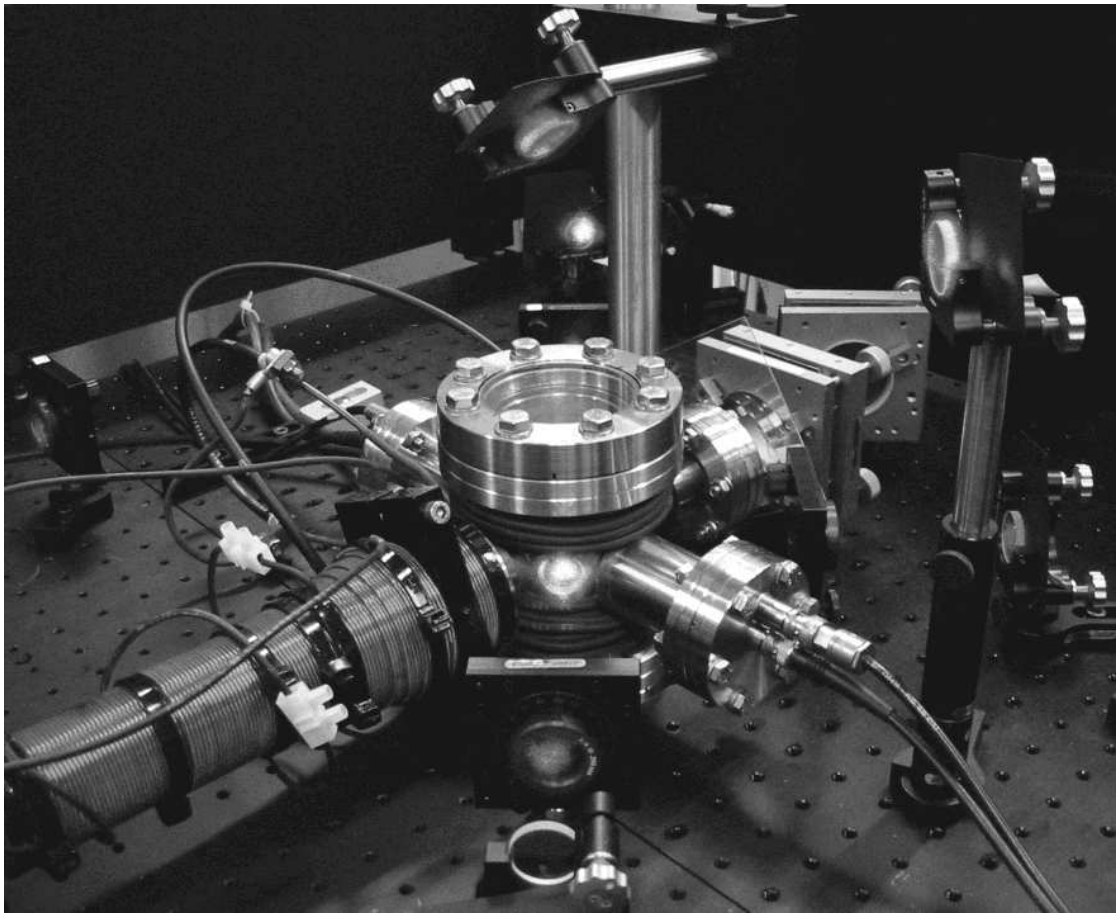

Figure 3.3. Picture of the MOT vacuum chamber with anti-Helmholtz coils and optics. The second part of the Zeeman slower is welded onto the MOT chamber. Scattered laser light (wavelength 389 nm) is visible on mirrors and windows. The channeltron detectors are connected to vacuum feedthroughs.

3.2 Experimental setup

3.2.1 Vacuum apparatus and production of slow metastables

The first stage in our atomic beam apparatus involves a liquid nitrogen-cooled DC-discharge source, producing a beam of ^{4}He* atoms that is laser collimated using the curved-wavefront technique. The beam source is based on the source described by Rooijakkers *et al.* [163]. The collimated beam enters a differentially pumped two-part Zeeman slower that reduces the longitudinal velocity from 1000 m/s to $\sim$ 25 m/s. Laser light with a wavelength of 1083 nm is obtained from a commercial 2 W fiber laser (measured bandwidth 8 MHz) and used for slowing and collimation. The laser is stabilized to the $2\ ^3S_1 \rightarrow 2\ ^3P_2$ transition using saturated absorption spectroscopy in an rf-discharge cell. The slowing light is detuned by -250 MHz using an acousto-optical modulator (AOM). Downstream the Zeeman slower the MOT vacuum chamber is located, with 20 mm diameter laser windows for the MOT beams (see Figs. 3.3 and 3.4). Two channel electron multipliers (channeltrons) are mounted inside to separately

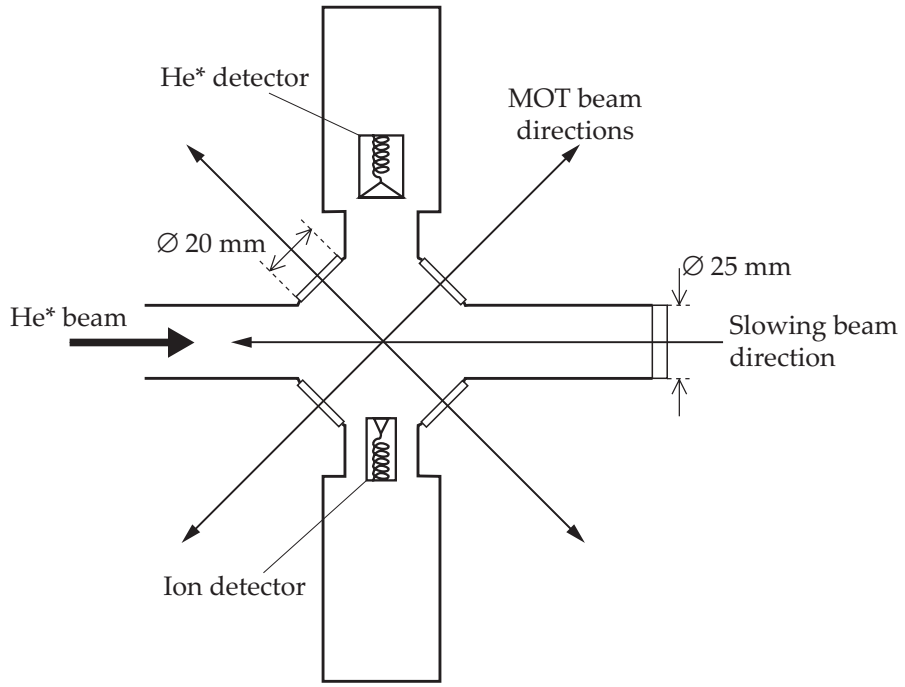

Figure 3.4. Schematic top view of the MOT vacuum chamber. Not shown are the vertical MOT laser beams. Dimensions are given in mm.

detect ions and metastables. Both channeltrons are operated with negative high voltage at the front end; however, one of them is put more closely to the cloud, thereby attracting all positively charged particles and leaving only the neutral metastables to be detected by the other. Also, the detector of metastables is partially hidden behind an aperture in the wall of the vacuum chamber (Fig. 3.4), that shields of its electric field considerably. Two 50 A coils, wound around the vacuum chamber and consisting of 17 turns copper tubing each, produce a quadrupole magnetic-field with a gradient of 43 G/cm along the symmetry axis. The field of the second part of the Zeeman slower inside the MOT region is counteracted with a compensation coil, mounted at the position of the Zeeman-slower exit. The pressure in the MOT chamber is 2×10^{-9} mbar, and increases to 1×10^{-8} mbar when the ^{4}He* beam is switched on.

The reduced capture velocity of a 389 nm MOT is a significant limitation, since a helium atomic beam expands dramatically due to transverse heating during Zeeman deceleration [114]. Calculations of the rms size of the atomic beam along the slowing trajectory show an increase in the rms atomic beam diameter by a factor 1.7 when tuning the end velocity from 75 m/s down to 25 m/s. This may lead to a decrease of a factor 3 in metastable flux. In conjunction with the limited MOT volume, this inevitably will result in a reduced loading rate. To minimize atomic beam expansion at the end of the Zeeman slower, we overlap the slowing laser beam with an additional 1083 nm beam, with identical circular polarization and similar intensity, but different detuning ($\Delta/2\pi = -80$ MHz) obtained using a second AOM. By choosing the same sign of the quadrupole magnetic-field gradient along the slower axis as that of the

Zeeman slower itself, an auxiliary Zeeman slowing stage only centimeters upstream of the MOT volume is established. This should allow trapping of atoms with velocities up to 75 m/s at the end of the Zeeman slower. A calculation of the atomic beam diameter for this case indicates that the loading rate may be increased by a factor 2.4 compared to the case where the Zeeman slower slows atoms down to a velocity of 24 m/s.

3.2.2 Laser setup at 389 nm

The MOT laser light is obtained by frequency doubling the output of a Coherent 899 titanium:sapphire (Ti:S) laser (778 nm with few-hundred kHz bandwidth) in an enhancement cavity containing a 10 mm Brewster-cut LBO crystal. The cavity length is locked to the fundamental wavelength using the Hänsch-Couillaud scheme. The Ti:S laser is pumped by 10 W at 532 nm from a Spectra-Physics Millennia X laser. We routinely produce 700 mW of 389 nm light; peak values of over 1 W of 389 nm at 2.1 W fundamental power have been achieved. We measured 4% short-term ($\sim$ 10 ms) power fluctuations in the 389 nm output.[1] The LBO crystal is flushed with oxygen, which increases the output power by about 10%. A small portion of the UV output is used to stabilize the wavelength to the $2\ ^3S_1 \rightarrow 3\ ^3P_2$ transition with saturated absorption spectroscopy, while Zeeman-tuning the Lamb dip allows continuous adjustment of the detuning between 0 MHz and $\pm$150 MHz. Further details can be found in [97, 98]. A combination of cylindrical and spherical lenses transforms the UV beam into a round, parallel and approximately Gaussian beam with 8 mm waist. The beam profile is truncated by a 20 mm circular aperture, followed by a series of nonpolarizing beamsplitters that split the UV beam into four beams. The individual beam intensities are chosen such that two beams in the horizontal plane can be retrorefelected, while the intensity of the two vertical beams along the symmetry axis of the quadrupole field ensures a more or less spherical ^{4}He* cloud.

3.2.3 MOT diagnostics

Time-of-flight measurement

The internal energy of helium metastables can be exploited in measuring time-of-flight (TOF) spectra of a MOT. A channeltron directly detects part of the expanding cloud after the atoms in the MOT have been released by suddenly switching off the MOT laser, the magnetic coils, and the slowing beams. The integrated TOF signal as obtained in such an experiment is proportional to the total number of trapped atoms, while fitting the recorded signal to a Maxwell-Boltzmann TOF distribution function gives the temperature of the cloud. In our experiment, the channeltron is operated in pulse-counting mode:[2] using an am-

[1] Throughout this chapter, presented uncertainties and noise levels correspond to one standard deviation.

[2] The channeltron cannot be operated in current mode, as it saturates at large count rates.

plifier/discriminator, the count rate is not dependent on the momentary gain of the channeltron. The output of the amplifier/discriminator is subsequently integrated by a calibrated ratemeter. The obtained TOF signals are analyzed with a fitting procedure. The integrated TOF signal gives the number of detected atoms, whereas a Maxwell-Boltzmann fit to the data, which also takes into account the response time of the ratemeter, reveals the temperature. With an accurate measurement of the solid angle covered by the detection area, the accuracy in the absolute number of trapped atoms is determined by the detection efficiency of low-velocity He* atoms, which is estimated to be in the range 10–70% (see also Refs. [163, 196], and references therein). This measuring method therefore cannot provide better than 50% accuracy in the absolute number of trapped atoms.

Fluorescence detection

In addition to the determination of the MOT atom number by time-of-flight measurements, we monitor the fluorescence of the cloud using a calibrated charge coupled device (CCD) camera to independently determine the number of atoms. The cascade via the $3\,^3S_1$ state generates photons with a wavelength of 707 nm, that are far more efficiently detected by a camera than photons from a 1083 nm MOT. Moreover, the 707 nm light does not suffer from reabsorption, because of the insignificant population of the $2\,^3P_2$ level. Therefore, we can safely assume the monitored fluorescence to be proportional to the number of atoms at each point in the cloud image, even at the highest densities obtained in our MOT. To calibrate the camera, we use a small fraction of the Ti:S laser output, with the laser tuned to 707 nm. In the atom number determination, we use dichroic mirrors to block all other wavelengths scattered from the MOT, most importantly the abundant 389 nm light. To extract the number of atoms N from the observed fluorescence power P_{fluor} we use the empirical equation of Townsend *et al.* [197], which relates the emitted power to the number of atoms:

$$P_{\text{fluor}} = N\hbar\omega\frac{\Gamma}{2}\frac{6CS}{1+6CS+4\delta^2}. \tag{3.4}$$

In the above equation, $S = I/I_{\text{sat}}$, where I_{sat} is the saturation intensity in the case of σ^+ transitions in an optically pumped environment, and I is the laser intensity of a single MOT beam. The phenomenological factor C incorporates the effects of reduced saturation; as the six circularly polarized MOT laser beams traverse the cloud in different directions and at varying angles with the quadrupole magnetic field, all transitions between the ground- and excited-state Zeeman levels must be considered, and the saturation intensity I_{sat}, as defined above, no longer applies. It is pointed out in Ref. [197] that C lies somewhere halfway the average of the squared Clebsch-Gordan coefficients of all involved transitions, and 1. For the $2\,^3S_1 \rightarrow 3\,^3P_2$ 389 nm transition, the average of the squares of the Clebsch-Gordan coefficients is 0.56. Therefore, we adopt $C = 0.8 \pm 0.2$, as also chosen by Browaeys *et al.* [23]. This value incorporates

a realistic estimate and an uncertainty that covers the range of all physically possible values of C.

The fluorescence image of the cloud is also used to determine the volume of the cloud. From a fit to a Gaussian distribution, we obtain the rms size in the radial (σ_ρ) and axial (σ_z) directions, and the volume $V = (2\pi)^{3/2}\sigma_\rho^2\sigma_z$ (V contains 68% of the atoms). For a cloud with Gaussian density distribution, this definition of V conveniently connects the number of atoms N to the central density n_0 via $N = n_0 V$. This provides all necessary information to deduce the density distribution as $n(\rho, z) = n_0 \exp(-\rho^2/2\sigma_\rho^2 - z^2/2\sigma_z^2)$.

Ion detection

In the MOT vacuum chamber, positive ions are produced in Penning-ionizing collisions of a ^{4}He* atom with another ^{4}He* atom or with a background-gas molecule. These ions are subsequently attracted to and detected by the obvious channeltron detector, and the resulting output current provides a rough measure of the number of trapped atoms. This signal is particularly useful for optimization purposes. Moreover, the signal is used to monitor the trap decay after the loading of the MOT has suddenly been stopped (see Section 3.3.2). This channeltron is operated at a sufficiently low voltage, such that the output current can safely be assumed to vary linearly with the detection rate.

3.3 Results and discussion

3.3.1 MOT results

Temporal fluctuations in the MOT

While observing the fluorescing cloud in real time with the CCD camera, we noticed nonperiodic intensity fluctuations on a 50 ms time scale. Also, the cloud was irregularly "breathing". To determine the source of these fluctuations, we first took a series of ten pictures of the cloud. The shutter time for each picture was 1/60 s, and the elapsed time between two subsequent exposures was about 5 s. Fitting the cloud size for each individual picture, we obtain an average MOT volume with a standard deviation of 9%, while the temperature remained constant within 2.5%. According to Eqs. (3.1) and (3.3), this may be related to the unstable laser power. In that case the resulting density fluctuations should influence the rate at which ions are produced in two-body Penning collisions. To observe this, we compared the continuous ion signal with the laser intensity as a function of time. It turns out that the 4% laser intensity noise correlates to the ion signal noise, though it does not explain all irregularities in the ion signal. Using Eq. (3.3), we find that the measured intensity fluctuations may give rise to 6% variations in the deduced MOT volume.

Atom number and density distribution

The maximum number of loaded atoms as derived from the fluorescence is $2.5(3) \times 10^7$ at a detuning $\Delta/2\pi = -35$ MHz and gradient $\partial B/\partial z = 39$ G/cm. The total intensity in this case is about $100 I_{\mathrm{sat}}$. It is possible to run the MOT at intensities as low as $40 I_{\mathrm{sat}}$, although the number of trapped atoms increases with intensity. To ensure a reliable estimate of the cloud dimensions and fluorescence intensity, we take the average of five subsequent images. The uncertainty in the number of trapped atoms mainly arises from the inaccuracy of the value of the phenomenological constant C (8%), as well as from the uncertainty associated with the fluorescence measurement, including a 4% inaccuracy in the calibration and by shot-to-shot fluctuations between the individual images used in the average. To ensure consistency between the results of the fluorescence and TOF measurement, we have to assign a value of 15(2)% to the detection efficiency of the channeltron. A Gaussian density function fits well to the cloud image. From the fit we infer the rms radii in the z and ρ dimensions and, thus, the volume V. At an optimized trapped atom number, we find $V = 0.020(5)$ cm^3. By increasing the magnetic-field gradient to $\partial B/\partial z = 45$ G/cm, and decreasing the detuning to $\Delta/2\pi = -35$ MHz, the cloud was compressed to $V = 0.0043(4)$ cm^3. Still, it contained $1.7(2) \times 10^7$ atoms.

Compared to a 1083 nm MOT, typical values for the volume V of the 389 nm MOT are found to be 6 to 25 times smaller [196]. Although the auxiliary laser beam at 1083 nm acts as a seventh MOT beam, its effect on the cloud volume is negligible on account of its large detuning (80 MHz), and the relatively small photon momentum of the 1083 nm light. Using Eq. (3.1) and Eq. (3.3), V can be corrected for the different magnetic-field gradients, saturation parameters, and temperatures for the 389 nm and 1083 nm cases. It follows that the observed compression of the cloud, due to only the increased laser cooling force, is approximately a factor 5, as predicted in Section 3.1.1. The optimum number of atoms is achieved with a relatively large magnetic-field gradient, about twice as large as in a 1083 nm MOT.

With the knowledge of N and V we can determine the central density $n_0 = N/V$, which is $1.4(5) \times 10^9$ cm^{-3} in the case of optimized trapped atom number. The large error bar, indicating the spread about the mean of the central densities obtained from each picture, is probably due to the correlation between the volume and the 389 nm laser power fluctuations. A sudden increase in power leads to a smaller volume, while the fluorescence intensity increases, resulting in an overestimate of the trapped atom number. The aspect ratio σ_z/σ_ρ of the cloud turns out to be 0.96(2). We compared this with the aspect ratio as predicted by Eq. (3.1): since at equilibrium $k_{\mathrm{B}}T = \kappa_\rho \langle \rho^2 \rangle = \kappa_z \langle z^2 \rangle$, with κ_ρ and κ_z the spring constants of the MOT in the radial and axial directions, respectively, it follows that $\sqrt{\kappa_\rho/\kappa_z} = \sigma_z/\sigma_\rho$, resulting in an aspect ratio of 0.79. This may indicate a small temperature difference between the ρ and z directions, also observed in a 1083 nm MOT [196].

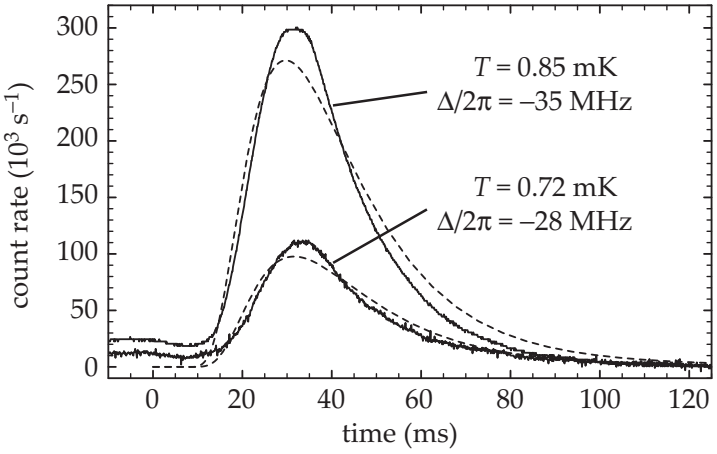

Figure 3.5. Two typical TOF spectra (solid curves) and corresponding fits to the data (dashed curves), at detunings $\Delta/2\pi = -35$ MHz and $\Delta/2\pi = -28$ MHz, respectively. The nonzero offset at $t \leq 0$ ms is ascribed to loss of metastables during loading of the MOT, due to imperfect alignment.

Temperature

Fitting a Maxwell-Boltzmann distribution function to the TOF spectra reveals the temperature T of the atoms in the MOT (Fig. 3.5). A nonzero offset at $t \leq 0$ is observed, which becomes more prominent (at the expense of trapped metastables) when the MOT laser beams are misaligned. The offset may incorporate the loss of metastables due to radiative escape [211], but our setup does not allow us to discriminate between different sources of hot metastables. Measured temperatures range from 0.93(3) mK for $\Delta/2\pi = -41$ MHz and $S = 19$, to 0.47(2) mK at $\Delta/2\pi = -9$ MHz and $S = 15$. In the latter case, however, the number of atoms in the MOT is limited to only 2.2×10^5.

Generally, temperatures in a 1083 nm MOT lie slightly above the prediction by Doppler cooling theory [23, 102, 126, 133, 146, 196], given by [115]

$$k_B T = -\frac{\hbar\Gamma}{4}\frac{1 + 2\mathcal{N}S + (2\delta)^2}{2\delta}, \tag{3.5}$$

with $\mathcal{N}$ is the dimensionality of the molasses. When using Eq. (3.5) to calculate the 389 nm molasses temperature in order to test our results, two features that distinguish the 389 nm transition from the 1083 nm transition are relevant. First, the transition strength, determined by the Einstein coefficient $A_{389}/2\pi \equiv \Gamma_{389}/2\pi = 1.51$ MHz, is slightly less compared to the 1083 nm transition, $\Gamma_{1083}/2\pi = 1.62$ MHz (see Appendix A). Second, the 10% decay via the $3\,^3S_1$ cascade slightly reduces the diffusion, as the recoil of the photons involved is randomly distributed. A recalculation of the momentum diffusion constant for this case yields a 3% reduction. Thus, we expect the 389 nm molasses temperature to be 11% lower with respect to the 1083 nm case. The predicted temperatures now become 1.0 mK for $\Delta/2\pi = -41$ MHz and $S = 19$, and 0.38 mK for $\Delta = -9/2\pi$ MHz and $S = 15$. Comparing these values with the measured temperatures given above, we find that for detunings larger than ~ 25 MHz the

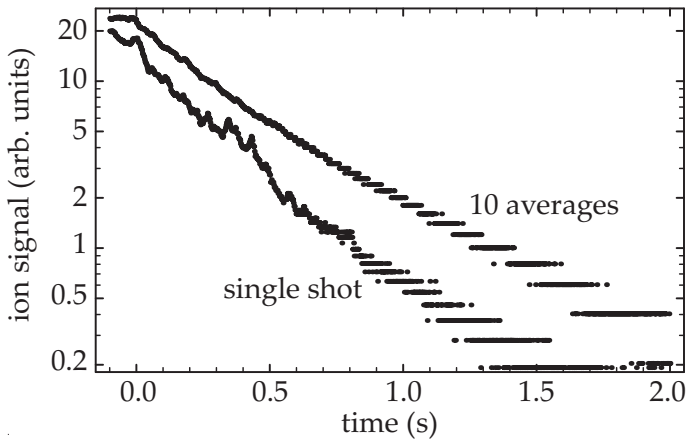

Figure 3.6. Lower curve: typical nonexponential decay of the ion signal after the loading has been stopped at $t = 0$ ms. Upper curve: ion signal obtained after averaging over ten decay curves.

measured values lie slightly below the theoretical values. For smaller detunings, this situation inverts and the measured temperatures tend to exceed the prediction of the properly modified Eq. (3.5). This behavior might indicate that at large detuning sub-Doppler mechanisms are more efficient than at small detuning. In the case of smaller detunings, however, the use of Eq. (3.5) becomes questionable: the large 389 nm photon recoil sets the recoil-temperature limit to 32 μK, just below the Doppler limit of 36 μK.

3.3.2 Trap loss

The number of atoms N in the MOT is governed by the well-known rate equation [13]

$$\frac{\mathrm{d}N(t)}{\mathrm{d}t} = L - \alpha N(t) - \beta \int n^2(\mathbf{r}, t)\, \mathrm{d}^3 r \tag{3.6}$$

where L denotes the loading rate, and α and β are the linear and quadratic loss rate coefficient, associated with processes involving one and two metastables, respectively. Accordingly, when the loading is interrupted, the local density n changes in time following

$$\frac{\mathrm{d}n}{\mathrm{d}t} = -\alpha n - \beta n^2. \tag{3.7}$$

Assuming a Gaussian density profile with a time-independent width, the losses can be expressed in terms of the central density n_0:

$$\frac{\mathrm{d}n_0(t)}{\mathrm{d}t} = -\alpha n_0(t) - \frac{\beta}{2\sqrt{2}} n_0^2(t). \tag{3.8}$$

The losses are largely due to Penning-ionizing collisions, which yield one positively charged ion per loss event. These ions are attracted towards the ion detector, resulting in an ion flux φ.

The loss rate constants are determined from the trap decay which occurs when the loading is stopped by simultaneously blocking all 1083 nm laser beams

entering the apparatus. This disables the Zeeman slower and collimation section, and prevents the auxiliary slowing laser beam from contributing to the two-body collision rate via light-assisted collisions. Switching off the collimation minimizes the Penning ionization contribution of metastables from the atomic beam and, thus, reduces the background signal.

Collisional loss

The decay of the MOT is observed by recording the current $\varphi(t)$ from the ion-detecting channeltron [13, 196]:

$$\varphi(t) = V\left(\epsilon_a \alpha n_0(t) + \frac{\epsilon_b \beta}{4\sqrt{2}} n_0^2(t)\right) + B. \tag{3.9}$$

Here, B is a constant background signal and ϵ_a and ϵ_b are the efficiencies with which ions are produced and detected for losses due to background and two-body collisions, respectively. Collisions that do not lead to Penning ionization but do result in trap loss, e.g. collisions with ground-state helium atoms, reduce ϵ_a. Radiative escape may affect ϵ_b. For the fit procedure, the ratio $\epsilon = \epsilon_b/\epsilon_a$ must be known. From the increase in background pressure when the helium atomic beam is running, we deduce that the background gas consists for 80% of helium when the MOT is on. Unfortunately, our setup is not suited for experimental determination of ϵ, as done by Bardou *et al.* [13]. They experimentally found $\epsilon = 4 \pm 1$. Since in our case the background gas involves mainly ground-state helium atoms, we expect ϵ_a to be smaller than unity. The value of ϵ_b is probably close to unity: following Tol *et al.* [196], one finds that for the 1083 nm case $\epsilon_b \approx 0.98$. We take the obvious underestimate $\epsilon = 1$, which implies that the result of the fit for βn_0 has to be considered an upper limit. The result for α can also be obtained by fitting the tail of the decaying ion signal, where the density is low enough to neglect the contribution of the two-body losses. In this way, the significance of ϵ in the determination of α is strongly (but not completely) reduced.

A typical example of a decaying ion signal is depicted in Fig. 3.6. The decay clearly shows nonexponential behavior, indicating that two-body collisions contribute significantly to the total losses. Since laser power fluctuations cause density fluctuations, much noise is visible in the ion signal. Therefore, an average of ten decay transients is fitted, as also shown in Fig. 3.6. Unfortunately, this may affect the reliability of the fitted parameters as the two-body loss rate depends nonlinearly on intensity. However, apart from intensity noise, the 389 nm output remained constant over a period sufficiently long to perform the measurements.

The fit procedure yields values for the exponential time constant α and the nonexponential time constant βn_0. We typically find $\alpha = 2\ \mathrm{s}^{-1}$ and $\beta n_0 = 3\ \mathrm{s}^{-1}$. This gives the rate coefficient β from the fit parameter βn_0, using n_0 from the fluorescence measurement. We find $\beta = 1.0(4) \times 10^{-9}\ \mathrm{cm}^3/\mathrm{s}$, at a detuning of -35 MHz. Assuming a value $\epsilon = 4$, the result becomes $\beta = 6(2) \times 10^{-10}\ \mathrm{cm}^3/\mathrm{s}$. The value $\beta = 1.0(4) \times 10^{-9}\ \mathrm{cm}^3/\mathrm{s}$, which we interpret as the upper limit,

is significantly below the value for the 1083 nm case of $5.3(9) \times 10^{-9}$ cm^3/s, reported by Tol *et al.* [196] using the same detuning and similar saturation.

The small value for β may be explained by a simple argument from cold-collision theory. During a light-assisted collision, two ^{4}He* atoms are resonantly excited to a molecular complex. For small detunings, this occurs at a relatively large internuclear separation, where the molecular potential $V(R)$ is well-approximated by the dipole-dipole interaction

$$V_{\pm}(R) = \pm\frac{C_3}{R^3}, \tag{3.10}$$

with R the internuclear distance and $C_3 \simeq \hbar\Gamma(\lambda/2\pi)^3$ [211]. The excitation by the red-detuned MOT laser light takes place resonantly when the molecular potential energy compensates the detuning. The resonance condition sets the so-called Condon radius R_C:

$$R_C = \left(\frac{C_3}{\hbar|\Delta|}\right)^{1/3}. \tag{3.11}$$

The red detuning selects an attractive molecular state. Once excited, the two atoms are accelerated towards small internuclear distances, where Penning ionization occurs with high probability. It follows from Eqs. (3.10) and (3.11) that the Condon radius for excitation with 389 nm light is smaller by $\lambda_{1083}/\lambda_{389} \approx 2.8$ compared to excitation with 1083 nm light. Classically, the cross section for the collision is determined by the square of the Condon radius, and is therefore expected to decrease by almost a factor 8.

To identify the role played by light-assisted collisions in the total two-body losses, we assume that β, as defined in Eq. (3.7), can be decomposed in two terms: β_{SS} and β_{SP}. Here β_{SS} is the rate coefficient for losses due to collisions between 2 ^{3}S$_1$ atoms in the absence of light, whereas β_{SP} takes into account the light-assisted collisional losses, depending (for a given detuning and saturation parameter) on the cross section and the Condon radius. We neglect collisions between excited-state atoms, since the excited-state population in our far-red-detuned MOT does not exceed 0.01. We can define β_{SS} and β_{SP} also via Eq. (3.7), with the total density n replaced by the 2 ^{3}S$_1$ density n_S:

$$\frac{\mathrm{d}n_S}{\mathrm{d}t} = -\alpha n_S - (\beta_{SS} + \beta_{SP})n_S^2. \tag{3.12}$$

Since the excited-state population is small, $n_S \approx n$. It now follows immediately from Eqs. (3.7) and (3.12) that, to good approximation, $\beta = \beta_{SS} + \beta_{SP}$.

Loss rate coefficient β_{SS} has been measured in a 1083 nm MOT by Tol *et al.* [196] to be $\beta_{1083}^{SS} = 2.6(4) \times 10^{-10}$ cm^3/s. Subtracting this value from the total rate coefficient $\beta_{1083} = 5.3(9) \times 10^{-9}$ cm^3/s, we infer $\beta_{1083}^{SP} = 5(1) \times 10^{-9}$ cm^3/s, which is much larger than β_{1083}^{SS}. In contrast, the upper limit we find for β_{389} is of the same order of magnitude as β_{389}^{SS} (since the 1083 nm and 389 nm magneto-optical traps, operated under the same conditions, are assumed to lead to similar populations of the 2 ^{3}S$_1$, $M = -1, 0, 1$ levels, we can take $\beta_{389}^{SS} =$

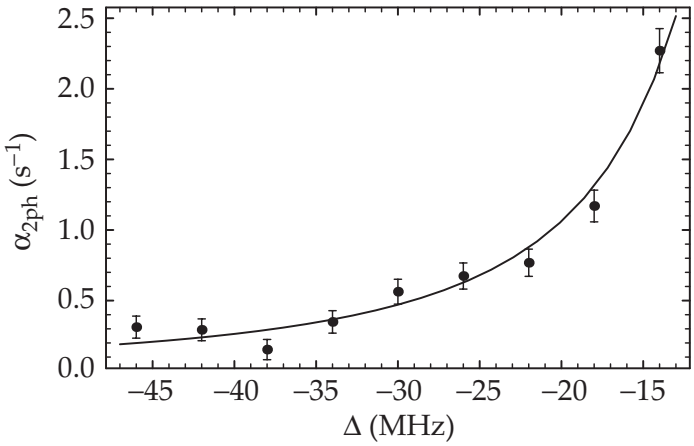

Figure 3.7. Two-photon loss rate constant α_{2ph} versus MOT detuning for total saturation parameter $I_{total}/I_{sat} = 6S = 110$.

β^{SS}_{1083}). To obtain the upper limit for β^{SP}_{389}, we subtract β^{SS}_{389} from β_{389} and find $\beta^{SP}_{389} \leq 7(3) \times 10^{-10}$ cm^3/s. This is in good agreement with the prediction following our simple argument. Finally, with $0 \leq \beta^{SP}_{389} \leq 7(3) \times 10^{-10}$ cm^3/s and $\beta^{SS}_{389} = 2.6(4) \times 10^{-10}$ cm^3/s, we can derive an upper and lower limit for the total quadratic loss rate coefficient, $2 \times 10^{-10} \leq \beta^{SP}_{389} \leq 1 \times 10^{-9}$ cm^3/s.

Two-photon ionization

From the fit to the ion signal decay, we extract the linear loss rate coefficient α. Unlike the situation in 1083 nm magneto-optical traps, α is not solely determined by background-gas collisions, but also by the two-photon ionization rate. We assume that each loss event involves only one ^{4}He* atom and ignore photoionization of the molecular complex formed during a light-assisted collision, as this process enters Eq. (3.8) via β. Hence the loss rate coefficient can be written as

$$\alpha = \alpha_{bgr} + \alpha_{2ph}, \tag{3.13}$$

where α_{bgr} denotes the background-gas collisional rate, and α_{2ph} accounts for the two-photon ionization loss rate. Two processes can be thought to cause the ionization: (instantaneous) two-photon ionization of a 2 ^{3}S$_1$ atom, or photoionization of an atom in either the 3 ^{3}P$_2$ or the 3 ^{3}S$_1$ state. The latter state is populated only during the cascade and has a lifetime of only 35 ns, so its contribution will be negligible. The instantaneous two-photon ionization probability p_{inst} is, for not too large detuning Δ, dependent on intensity S and trapping light detuning Δ, according to

$$p_{inst} \propto \frac{S^2}{\Delta^2}. \tag{3.14}$$

The photoionization probability p_{pi} of a helium atom in the 3 ^{3}P$_2$ state is simply proportional to the incident laser intensity and the cross section for photoionization, which varies only slowly with wavelength [31]. Neglecting this

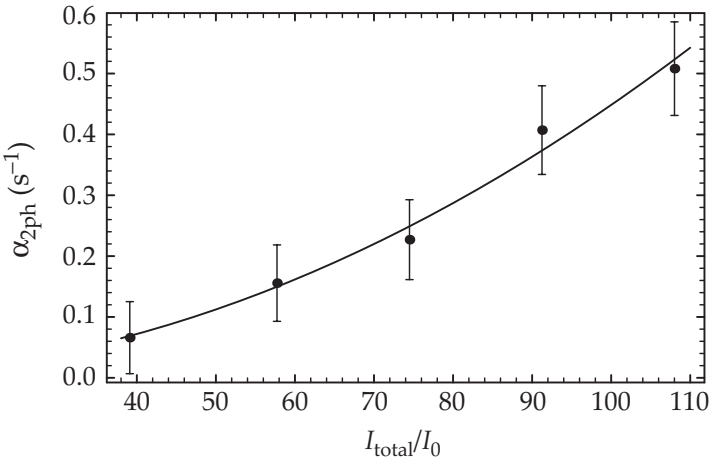

Figure 3.8. Two-photon loss rate constant versus total saturation parameter $I_{\text{total}}/I_{\text{sat}}$ at detuning $\Delta/2\pi = -35$ MHz.

wavelength dependence, the probability of photoionization simply becomes the product of the upper $3\,^3P_2$ state population and the ionization probability itself. For the two-step process, this leads to a dependence on intensity and detuning as

$$p_{\text{pi}} \propto \frac{S^2(\Gamma/2)^2}{\Delta^2 + (S+1)(\Gamma/2)^2}. \tag{3.15}$$

When $\Delta^2 \gg (S+1)(\Gamma/2)^2$, this dependence takes on a form similar to Eq. (3.14). We confirmed this behavior by measuring $\alpha_{2\text{ph}}$ as a function of MOT detuning, as shown in Fig. 3.7. We also checked the intensity dependence, as shown in Fig. 3.8. In both cases, we determined α_{bgr} by measuring α as a function of background pressure, while keeping the detuning and intensity fixed. Assuming a linear variation of α_{bgr} with pressure, against a fixed background $\alpha_{2\text{ph}}$, a fit to the data points yields $\alpha_{\text{bgr}} \approx 1.5(1)\ \text{s}^{-1}$. Under typical experimental conditions, we find $\alpha_{2\text{ph}} \approx 0.5\ \text{s}^{-1}$.

Chang and Fang [31] calculated photoionization cross sections of many singlet and triplet states in helium, including the $3\,^3S$ and $3\,^3P$ states, for various wavelengths. Using their results, we find photoionization rates of about $2\ \text{s}^{-1}$. Since the fraction of $n = 3$ atoms in our MOT is typically below the 1% level, the net loss rate due to the two-step process then would be one order of magnitude smaller than the measured value for $\alpha_{2\text{ph}}$. This suggests that instantaneous two-photon ionization dominates over the two-step ionization losses.

3.3.3 Auxiliary Zeeman slower

To test the performance of the auxiliary Zeeman slower, we first optimized the number of atoms in the MOT in the absence of the extra slowing laser. Then, leaving the MOT parameters unaltered, we unblock the auxiliary laser beam and vary the slowing laser intensities and Zeeman coil current iteratively until a new optimum for the number of atoms is established. Indeed, blocking the

additional laser beam again interrupts the loading, demonstrating that we have tuned the end velocity of the Zeeman slower above the capture velocity of the MOT. With the auxiliary Zeeman slower on, the number of atoms is larger by 40% compared to the case without the auxiliary Zeeman slower. Starting from Eq. (3.6), with α, β, and n_0 known from experiment, we calculate that the auxiliary Zeeman slower enhances the loading rate by a factor 1.6. Despite this improvement, the loading rate remains low. By solving Eq. (3.6), with the measured values for the loss rate constants and the steady-state number of atoms as input, we find a loading rate slightly below 10^8 s^{-1}. Tol *et al.* [196] state a value of 5×10^9 s^{-1} for their 1083 nm MOT. This difference is explained by the smaller MOT diameter, the reduced flux of slow atoms from the Zeeman slower due to atomic beam expansion, and imperfect collimation due to the relatively large bandwidth of the 1083 nm laser.

Starting from the intensity and detuning of the slowing light and an expression for the magnetic field in the Zeeman slower, the end velocity of decelerated atoms can be calculated (see Section 2.5). Confronting the calculations with experimental observations, we derive a capture velocity of 35 m/s for a MOT without an auxiliary slowing beam. Apparently, the prediction of a 24 m/s capture velocity by the model of Section 3.1.2 is an underestimate, and the true capture velocity lies closely to the velocity determined by the resonance condition. Therefore, it is likely that the π and $\sigma^{\pm}$ transitions, caused by MOT laser beams orthogonal to the quantization axis, occur at rates at least comparable to the 10% decay via the $3\,{}^3S_1$ cascade. Apparently, the nonclosed character of the 389 nm transition plays a minor role, even in the case of relatively large (~ 40 G) magnetic fields.

We derive from the settings of the Zeeman slower that atoms with a velocity $\lesssim 75$ m/s are further slowed down to a velocity of 35 m/s by the auxiliary Zeeman slower. This translates to an increase in loading rate by a factor 1.7, in reasonable agreement with the result of the test described above.

3.3.4 Comparison with 1083 nm MOT

Table 3.1 contains MOT results for the 389 nm and 1083 nm case [196]. The MOTs have similar detuning and saturation parameters, which optimize both density and trapped atom number. The smaller number of atoms, N, in the 389 nm MOT is explained by the small loading rate. Despite this small number, the central density n_0 is equal to that of a 1083 nm MOT containing over one order of magnitude more atoms. This is the result of the smaller loss rate constant β, the larger laser cooling force, and the larger magnetic-field gradient. The latter not only contributes to the compression of the cloud, but also reflects the necessity of a large Zeeman detuning to compensate the larger Doppler shift of the atoms to be captured from the Zeeman-decelerated ^{4}He* beam. Furthermore, we observe that the 0.5 s^{-1} contribution of two-photon ionization to the losses in the 389 nm MOT is small compared to the 21 s^{-1} two-body loss rate in a large 1083 nm MOT.

Table 3.1. Comparison of the 389 nm MOT and the 1083 nm MOT described in Ref. [196]. The typical results for both MOTs are obtained under conditions that optimize both density and atom number. For the 389 nm case, $\epsilon = 1$ is assumed.

MOT wavelength	389 nm	1083 nm
Detuning $\Delta/2\pi$ (MHz)	-35	-35
Magnetic field gradient $\partial B/\partial z$ (G/cm)	41	20
Total intensity (I_{sat})	100	90
Number of atoms N	2×10^7	5×10^8
Loading rate L (s^{-1})	$< 10^8$	$> 5 \times 10^9$
Central density n_0 (cm^{-3})	4×10^9	4×10^9
Volume V (cm^3)	0.005	0.12
Temperature T (mK)	0.85	1.1
Two-body loss rate βn_0 (s^{-1})	3	21
Two-body loss rate constant β (cm^3/s)	$1.0(4) \times 10^{-9}$	$5.3(9) \times 10^{-9}$
Two-photon ionization loss rate constant $\alpha_{2\mathrm{ph}}$ (s^{-1})	0.5	0

3.4 Conclusion and outlook

We have shown that it is possible to build a magneto-optical trap for ^{4}He* atoms using transition $2\ ^3\mathrm{S}_1 \rightarrow 3\ ^3\mathrm{P}_2$ at 389 nm. Our prototype MOT demonstrates that a 389 nm MOT offers the advantage of a dense, cold cloud of metastable helium atoms, as compared to a 1083 nm MOT. The relatively large density is allowed by the reduced two-body loss rate coefficient β, whereas the large spontaneous force facilitates substantial compression of the cloud. Intensity noise on the 389 nm output, however, compromises the measurement accuracy. Together with the high background pressure and the small value of β, this has complicated an accurate determination of its value. We conclude that β lies between the experimentally determined upper limit 1.0×10^{-9} cm^3/s, and the two-body loss rate constant in the absence of light, 2×10^{-10} cm^3/s determined in Ref. [196]. Two-photon ionization losses, although present, do not exclude the future possibility of a 389 nm MOT containing large numbers of metastable helium atoms at high phase-space density. To this end, however, the loading rate of the MOT must be improved. A bare 389 nm MOT has limited loading capabilities since the large Doppler shift implies a reduced capture velocity, and the required Zeeman-slower settings then give rise to a smaller flux of slow metastables. The nonclosed character of the 389 nm transition, however, does not play an important role in the process of magneto-optical trapping. In a supplemental study [99, 200], magneto-optical trapping at 389 nm has been investigated starting from a large 1083 nm MOT. Phase-space densities around 4×10^{-6} have been achieved and collisions in the presence of 389 nm light have been studied.

Chapter 4

Theory of homonuclear ionizing collisions of laser-cooled metastable helium isotopes

Soon after the first demonstration of laser cooling and trapping of neutral atoms, it was recognized that collisions between atoms have a profound effect on the physics of laser-cooled atomic gases [70]. It was already known from studies of spin-polarized hydrogen [72, 183] that collisions at low kinetic energies ($\sim 10^{-7}$ eV in gases with a temperature $T = 1$ mK) show many new effects that are absent for collisions at room temperature. Although the unusual features of these so-called cold collisions[1] have attracted much attention by themselves, current interest in cold collisions is due to their importance in various research areas that have emerged since the advent of laser cooling and trapping. The pivotal role of collisions played in experiments on quantum degenerate gases, atomic clocks, quantum computing and cold molecule formation is discussed in [26].

In this chapter, we present a theoretical study of cold ionizing collisions of both ^{3}He and ^{4}He atoms in the metastable 2 $^3S_1$ state, henceforth denoted by ^{3}He* and ^{4}He*, respectively. Starting from the relevant molecular potentials, a model for homonuclear collisions is derived, taking into account quantum threshold behavior, Wigner's spin-conservation rule and quantum statistical symmetry requirements. The model can be applied to collisions of both ^{3}He* and ^{4}He* atoms and shows that, as a result of different quantum statistical symmetry for the two isotopes and the presence of a nuclear spin in the case of ^{3}He, different cross sections are expected for the two isotopes. As the model

[1] Following Suominen [191], we will refer to collisions in laser cooled gases, where temperatures are between ~ 1 mK and ~ 1 μK, as cold collisions. In Suominen's terminology, ultracold collisions correspond to temperatures below ~ 1 μK, the temperature range of evaporative cooling and quantum degeneracy.

provides clear insight into the process of ionizing collisions without requiring heavy numerical calculations, it is complementary to the more complete (and precise) close-coupling theory that has been developed for ^{4}He* collisions by Venturi *et al.* [204, 205] and Leo *et al.* [111]. To verify the validity of our model, the results of both calculations are compared, showing good agreement.

Section 4.1 provides an overview of the basic properties of cold ionizing collisions of He* atoms, emphasizing Wigner's spin-conservation rule and the role played by quantum threshold behavior and quantum statistical symmetry. In Section 4.2, we present the theoretical model and use it to derive values for the ionization cross sections and rate coefficients for homonuclear collisions of laser-cooled ^{3}He* and ^{4}He* atoms. In Section 4.3, we compare the model to the close-coupling theory of [111, 204, 205]. In Chapter 5, the model is used to analyze the results of an experimental study of ionizing collisions in magneto-optically trapped clouds of ^{3}He* or ^{4}He* atoms.

4.1 Cold ionizing collisions of He* atoms

The collisions studied in this chapter are those leading to Penning (PI) or associative ionization (AI),

$$\mathrm{He^* + He^* \rightarrow He + He^+ + e^-} \quad \text{(PI)}, \tag{4.1}$$

$$\mathrm{He^* + He^* \rightarrow He_2^+ + e^-} \quad \text{(AI)}. \tag{4.2}$$

As the He* atom has an internal energy of 19.8 eV and the ionization energy is 24.6 eV, the internal energy of two He* atoms exceeds the He ionization limit by 15 eV, making the (inelastic) collisions of Eqs. (4.1) and (4.2) highly exothermic. An overall understanding of PI and AI processes has been provided by the simple classical-dynamical model of Herman and Čermák [76, 227], where ionization is envisaged as an auto-ionizing transition between two quasi-molecular states,[2]

$$\mathrm{He^* + He^* \rightarrow [He_2^*] \rightarrow \left[He_2^+ + e^-\right] \rightarrow He + He^+ + e^-}. \tag{4.3}$$

In the case of Penning ionization, the transition is to an unbound state of the molecular ion, which then dissociates. In the case of associative ionization, the final state is bound and the molecular ion itself is the reaction product. The aim of this section is to indicate the main features of ionizing collisions at mK temperatures. At this, details about the reaction mechanism of Penning and associative ionization are unimportant and, henceforth, we will not distinguish between Penning and associative ionization and use the term Penning ionization to denote both processes. An extensive treatment of the subject of Penning ionization can be found in [227].

As the interaction driving the auto-ionizing transition of Eq. (4.3) is of an electrostatic nature [227], it only induces transitions between molecular states

[2] With the high ionization probability associated with PI and AI of He* atoms, the energy width associated with quasi-molecular state [He$_2$*] is so large that the concept of a transition between states becomes rather artificial.

of equal total electronic spin. Therefore, ionization rates associated with the reactions of Eqs. (4.1) and (4.2) depend on the total spin states on the reactant and product side of the reaction formulas. For both reactions, the reactants carry an electronic spin of $s = 1$ and can form total spin states with $S = 0, 1$ or 2, while the products, carrying $s = \frac{1}{2}$ (except for ground state helium, which carries no electronic spin), can only form states with $S = 0$ or 1. Clearly, Penning ionization conserving total electronic spin is only possible for collisions with $S = 0, 1$ and an ionization reaction of atoms colliding with $S = 2$ can occur only if spin conservation is violated.

It has been shown [58, 182] that a very weak spin-dipole magnetic interaction can induce spin flips and mediate Penning ionization in collisions of He* atoms with $S = 2$. The corresponding ionization rate is four orders of magnitude smaller compared to those of collisions with $S = 0$ and $S = 1$, for which total electronic spin is conserved [184]. The strong suppression of Penning ionization by spin conservation is known as Wigner's spin-conservation rule [124] and has been observed [82] for collisions of He* atoms.[3]

At the mK temperatures of a laser-cooled sample of He* atoms, collisions occur at relative kinetic energies $E = \mu v_{\mathrm{r}}^2/2 \approx 10^{-7}$ eV, where $\mu = m/2$ is the reduced mass of the colliding atoms, with m the mass of the He atom, and v_{r} the relative velocity between the atoms. The de Broglie wavelength of atomic motion $\Lambda = h/\mu v_{\mathrm{r}} \approx 250\, a_0$, with h Planck's constant, is much larger than the typical scale of the interatomic potential.[4] In this case, the collisions are dominated by quantum threshold behavior [16, 91, 92, 132, 214]. The collision process can be described conveniently using the partial wave method,[5] as the ionization cross section, written as a sum of partial wave contributions,

$$\sigma^{(\mathrm{ion})} = \sum_{\ell} \sigma_{\ell}^{(\mathrm{ion})}, \tag{4.4}$$

is dominated by only a few partial waves ℓ. It is shown in Refs. [91, 92, 210] that for inelastic exothermic collisions, such as Penning ionizing collisions, the quantum threshold behavior of the ℓth partial cross section is given by

$$\sigma_{\ell}^{(\mathrm{ion})} \propto k^{2\ell-1} \quad \text{if } k \to 0. \tag{4.5}$$

Here, $k = (2\mu E/\hbar^2)^{1/2}$ is the wave vector of the asymptotic relative motion of the colliding atoms, with $\hbar = h/2\pi$. In a sample of laser-cooled He* atoms, the

[3] The suppression of Penning ionization in magnetically trapped samples of spin-polarized ^{4}He* atoms has allowed the realization of a Bose-Einstein condensate of metastable helium atoms [147, 162]. Although relatively high densities are obtained in the condensate ($n \approx 10^{13}$ cm^{-3}), the losses due to ionizing collisions give rise to lifetimes of several seconds.

[4] Here, we are interested in collisions in the absence of a light field. Cold collisions in the presence of light are fundamentally different and should be treated by quantum mechanical methods that explicitly treat the dissipation due to excited state spontaneous emission during the collision [91, 92]. In that case, several interatomic potentials must be taken into account. In Chapters 3 and 5, we present a study of these so-called light-assisted (or optical) collisions in magneto-optically trapped clouds of He* atoms.

[5] The method of partial waves is treated in many textbooks, see e.g. [36].

cross section for Penning ionizing collisions is dominated by the s-wave contribution $\sigma_0^{(\mathrm{ion})}$, which diverges as $1/k$ if $k \to 0$. Elastic collisions have very different threshold properties: the cross section $\sigma_0^{(\mathrm{elas})}$ approaches a nonvanishing constant, $\sigma_1^{(\mathrm{elas})} \propto k^4$ and $\sigma_{\ell>1}^{(\mathrm{elas})} \propto k^6$, if $k \to 0$ [43, 210].

Spin conservation and the diverging cross section are specific features of ionizing collisions of He* atoms. For homonuclear collisions, also a fundamental principle plays an important role: dealing with identical particles,[6] the symmetrization postulate of quantum mechanics applies. This postulate requires that the quantum mechanical state of a colliding pair of identical atoms has even or odd symmetry under exchange of the atoms. The symmetrization of the quantum state—even if the identical particles are bosons, and odd if they are fermions—imposes restrictions on the partial waves that contribute to the cross section. This can lead to an increase or a decrease of the cross section compared to collisions of non-identical particles [43]. Since the ^{3}He atom is a fermion and the ^{4}He atom is a boson, the quantum states describing colliding atom pairs have different symmetry and the cross sections are composed of partial wave contributions in a different way.

Wigner's spin-conservation rule, quantum threshold behavior and the symmetrization postulate are the main ingredients for the theoretical model presented in Section 4.2. We will use the model to determine the ionization cross sections of homonuclear collisions of ^{3}He* and ^{4}He* atoms. Using the cross sections, we will derive values for the ionization rate coefficients $K_{SS}^{(\mathrm{th})}$ for unpolarized atomic samples, i.e. samples in which the atoms are equally distributed over the magnetic substates. In Chapter 5 we will determine these rate coefficients experimentally and use the model to analyze the results.

4.2 Theoretical model

Theoretical studies of ionizing collisions of laser-cooled He* atoms have so far focused almost exclusively on collisions of ^{4}He* atoms. To investigate the feasibility of Bose-Einstein condensation, detailed theoretical studies of collisions of spin-polarized ^{4}He* atoms have been performed [58, 182, 205]. Collisions of unpolarized ^{4}He* atoms have also been subject of theoretical studies. Julienne and Mies [91] have provided an estimate for the Penning ionization rate of cold unpolarized ^{4}He* atoms using close-coupling scattering theory adapted to ionizing collisions by multichannel quantum-defect methods. In a report on the experimental study of ionizing collisions of ^{4}He* atoms, Mastwijk *et al.* [126] have also reported a theoretical prediction of the ionization rate for unpolarized atoms. Recently, a detailed study of collisions of ^{4}He* atoms has been reported by Venturi *et al.* [204, 205] and Leo *et al.* [111]. They use complex potentials to

[6] Two particles are identical if their physical properties are exactly the same, this precluding the possibility of an observation that could distinguish between them [128, Chapter 14]. A discussion of the properties of systems of identical particles, correcting some misleading arguments in literature, is presented in [10, Chapter 17].

adapt close-coupling scattering theory to inelastic collisions and calculate elastic and inelastic cross sections for spin-polarized and unpolarized ^{4}He* atoms. In Section 4.3, we will compare our model to these calculations.

For ^{3}He* atoms, only a very basic theoretical study of cold ionizing collisions has been performed so far. In a report on the experimental study of homonuclear ionizing collisions of ^{3}He* and ^{4}He* atoms, Kumakura and Morita [102] present a theoretical model to explain the observed difference in ionization rates between the two isotopes.

The theoretical model presented here is complementary to the more complete close-coupling theory of [111, 204, 205], as it provides clear insight without requiring heavy numerical calculations, and can be applied to ionizing collisions of both ^{3}He* and ^{4}He* atoms. In the spirit of the approach by Orzel *et al.* [141], we will consider ionizing collisions of He* atoms to be the result of two subsequent events. This assumption allows us to use a simple expression for the ionization cross section.

4.2.1 Ionization cross section

From a semi-classical point of view, two stages can be distinguished in the process of a cold ionizing collision of two He* atoms. As collision energies are small, elastic scattering of the atoms occurs at a relatively large internuclear distance $R \gtrsim 100\,a_0$. For partial waves $\ell > 0$, the radial wave function $u_{k\ell}(R)$ (cf. Eq. (4.8)) is scattered by the centrifugal barriers, while scattering for $\ell = 0$ takes places at the internuclear distance where the local de Broglie wavelength $\Lambda(R) = h/\{2\mu[E - V(R)]\}^{1/2}$ becomes comparable to the size of the potential, i.e. $\mathrm{d}\Lambda(R)/\mathrm{d}R \approx 1$ [91, 92]. Here, $V(R)$ is the interaction potential of the colliding atoms (cf. Fig. 4.1). As ionization occurs at a small internuclear distance $R \approx 5\,a_0$, where the electron clouds of both atoms start to overlap [227], the elastic scattering process can be considered to precede the inelastic process of ionization. Here we assume that scattering occurs well before the atoms approach the distance where ionization takes place, so that the two processes can be treated separately.

As Penning ionization is a strong inelastic exothermic process, we can write the ionization cross section for collisions with total electronic spin S as [141]

$$ {}^{(2S+1)}\sigma^{(\mathrm{ion})} = \frac{\pi}{k^2} \sum_{\ell} (2\ell+1)\, {}^{(2S+1)}P_{\ell}^{(\mathrm{tun})}\, {}^{(2S+1)}P^{(\mathrm{ion})}, \tag{4.6} $$

where ${}^{(2S+1)}P_{\ell}^{(\mathrm{tun})}$ is the probability for the atoms to reach a small internuclear distance, and ${}^{(2S+1)}P^{(\mathrm{ion})}$ is the probability for ionization to occur at that place.[7]

[7] In single-channel calculations, inelastic processes can be taken into account using the complex potential approach [88]. In this case, the inelastic cross section, $\sigma^{(\mathrm{abs})} = (\pi/k^2)\sum_{\ell}(2\ell+1)(1 - |\exp(2i\delta_{\ell})|^2)$, is defined as to account for the total loss of probability flux introduced by the imaginary part of the potential and expressed by the complex phase shifts δ_{ℓ}. Analogously, cross section ${}^{(2S+1)}\sigma^{(\mathrm{ion})}$ of Eq. (4.6) can be interpreted as a measure for total flux loss induced by tunneling to small internuclear range and subsequent ionization of the colliding atoms.

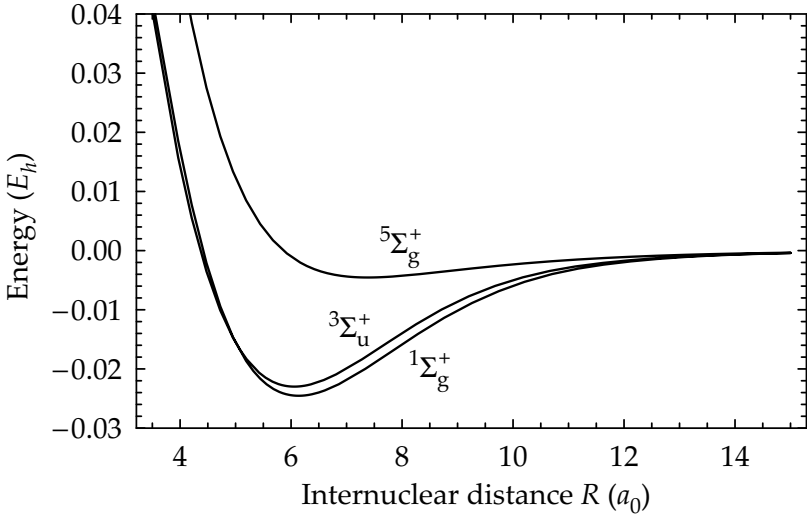

Figure 4.1. Ab initio potential energy curves in atomic units, calculated for ^{4}He* by Müller *et al.* [136]. Bohr radius $a_0 = 0.5291772083 \times 10^{-10}$ m and Hartree energy $E_\mathrm{h} = e^2/4\pi\epsilon_0 a_0 = 4.35974381 \times 10^{-18}$ J.

As total spin S is conserved during ionization, ${}^{(2S+1)}P^{(\mathrm{ion})}$ is very small ($\ll 1$) for collisions that violate Wigner's spin-conservation rule. Here, we neglect ionizing collisions with $S = 2$ and assume that ${}^5P^{(\mathrm{ion})} = 0$. As ionization occurs with essentially unit probability for the other spin states (Müller *et al.* [136] report an ionization probability of 0.975), we set ${}^1P^{(\mathrm{ion})} = {}^3P^{(\mathrm{ion})} = 1$, so that

$$ {}^{(2S+1)}\sigma^{(\mathrm{ion})} = \begin{cases} \dfrac{\pi}{k^2}\displaystyle\sum_\ell (2\ell+1)\, {}^{(2S+1)}P_\ell^{(\mathrm{tun})} & \text{if } S = 0 \text{ or } S = 1, \\ 0 & \text{if } S = 2. \end{cases} \tag{4.7} $$

In the next sections we will calculate the partial wave tunneling probabilities ${}^{(2S+1)}P_\ell^{(\mathrm{tun})}$ and determine the ionization cross section ${}^{(2S+1)}\sigma^{(\mathrm{ion})}$ for $S = 0$ and $S = 1$. The energy dependence of the probabilities ${}^{(2S+1)}P_\ell^{(\mathrm{tun})}$ gives rise to an energy dependent ${}^{(2S+1)}\sigma^{(\mathrm{ion})}$, that displays the quantum threshold behavior of the inelastic collisions of Eq. (4.5). The probabilities are obtained from a one-dimensional scattering calculation of a plane wave incident on an effective potential. The potential is derived in Section 4.2.2 and the scattering calculation is performed in Section 4.2.3. In this calculation, symmetry requirements are not taken into account; we will discussed the consequences of the symmetrization postulate in Section 4.2.5.

4.2.2 Effective potential

As the helium atom, with only two electrons and a nucleus, has a relatively simple structure, interatomic potentials can be calculated with high accuracy. Figure 4.1 shows the short-range part ($3.5\,a_0 < R < 14.0\,a_0$) of the potential curves for two metastable $2\,{}^3\mathrm{S}_1$ helium atoms obtained from Müller *et al.* [136].

The curves are the result of ab initio calculations in the Born-Oppenheimer approximation, where the total electronic spin S is a good quantum number. The possible values $S = 0$, $S = 1$ and $S = 2$ correspond to a singlet, triplet and quintet potential ($^1V(R)$, $^3V(R)$ and $^5V(R)$), respectively. In Fig. 4.1, the curves are labelled in Hund's case (a) notation $^{2S+1}\Lambda^{\pm}_{g/u}$ [105], where $\Lambda = |M_L|$ with M_L the quantum number of the projection of the total electronic orbital angular momentum along the internuclear axis of the molecule, g/u stands for gerade or ungerade, i.e. positive or negative symmetry under inversion of all electronic coordinates of the molecule, and $\pm$ indicates positive or negative symmetry under reflection through a plane including the internuclear axis. As all electrons of the He* atom are in s-states, colliding atom pairs can only have zero total orbital angular momentum, indicated[8] by $\Lambda = \Sigma$.

The potentials can be extended to large internuclear distance using a calculation of the dispersion interaction of two He* atoms reported by Yan and Babb [223]. Using multipole expansion $-C_6/R^6 - C_8/R^8 - C_{10}/R^{10}$, they have calculated dispersion coefficients $C_6 = 3276.680$ a.u., $C_8 = 210566.55$ a.u. and $C_{10} = 21786760$ a.u. Here, we construct potentials valid for $R > 3.5\,a_0$ by fitting the short-range potential curves of Fig. 4.1 smoothly onto the long-range dispersion interaction around $\sim 20\,a_0$ by interpolation using a cubic spline fitted to $R^6 \times {}^{(2S+1)}V(R)$.

The elastic scattering for collisions with $S = 0$ and $S = 1$ is governed by potentials $^1V(R)$ and $^3V(R)$, respectively. Within the framework of the partial wave method, potential scattering by ${}^{(2S+1)}V(R)$ is described by the radial wave equation [88]

$$-\frac{\hbar^2}{2\mu}\frac{\mathrm{d}^2}{\mathrm{d}R^2}u_{k\ell}(R) + \left[\frac{\hbar^2\ell(\ell+1)}{2\mu R^2} + {}^{(2S+1)}V(R) - E\right]u_{k\ell}(R) = 0, \tag{4.8}$$

where $k = (2\mu E/\hbar^2)^{1/2}$ is the wave vector associated with the asymptotic relative motion, ℓ is the quantum number of the relative angular momentum, μ is the reduced mass, and $u_{k\ell}(r)$ is the radial wave function.[9] Eq. (4.8) can be interpreted as a one-dimensional Schrödinger equation ($R \geq 3.5\,a_0$), describing the potential scattering of a particle of mass μ by effective potential

$${}^{(2S+1)}V_\ell(R) = {}^{(2S+1)}V(R) + \frac{\hbar^2\ell(\ell+1)}{2\mu R^2}, \tag{4.9}$$

where the second term is the well-known centrifugal potential.

To calculate the probability ${}^{(2S+1)}P_\ell^{(\mathrm{tun})}$ of atom pairs to reach the distance where ionization occurs, we modify the effective potential curves to simulate

[8] The absolute value of the projected total electronic orbital angular momentum along the internuclear axis of the molecule is denoted by the capital Greek letter that corresponds to the Latin letter, with which an atomic term is indicated if the quantum number associated with its orbital angular momentum would have the same value as Λ, i.e. $\Lambda = 0, 1, 2$ is indicated by Σ, Π, Δ, respectively [105].

[9] Using the method of partial waves, the relative wave function of the colliding atoms is expressed as a sum of partial waves [88], $\psi_k(\boldsymbol{R}) = \sum_\ell \sum_m Y_\ell^m(\theta,\phi)u_{k\ell}(R)/R$, where $Y_\ell^m(\theta,\phi)$ is a spherical harmonic and $u_{k\ell}(R)$ is a radial wave function satisfying the radial wave equation.

the ionization process. In the spirit of [141], we set the curves to a constant value for small internuclear distances, and extend the range of R to negative values,

$$ {}^{(2S+1)}\widetilde{V}_\ell(R) = \begin{cases} {}^{(2S+1)}V_\ell(R_0) & R \leq R_0, \\ {}^{(2S+1)}V_\ell(R) & R > R_0, \end{cases} \tag{4.10} $$

where $R_0 = 6.1\, a_0$ is chosen to be the location of the potential curve minimum. This way, we avoid reflections of the radial wave function from artificial features of the potential energy curve at R_0. Modeling the interatomic interaction by $\widetilde{V}_\ell(R)$, potential scattering is described by the one-dimensional Schrödinger equation ($-\infty < R < \infty$)

$$ -\frac{\hbar^2}{2\mu}\frac{\mathrm{d}^2}{\mathrm{d}R^2}u_{k\ell}(R) + \left[{}^{(2S+1)}\widetilde{V}_\ell(R) - E\right] u_{k\ell}(R) = 0, \tag{4.11} $$

and ionizing collisions correspond to the transmission of the relative particle[10] to $R < 0$: for atoms that reach the region of small R, where ionization takes place, the corresponding relative particle will propagate freely to $R = -\infty$ and never reflect back to $R > R_0$. The disappearance of the particle to $R < 0$ results in a loss of probability flux, typical of an inelastic process, such as Penning ionization.

Figure 4.2 shows plots of $\widetilde{V}_0(R)$, $\widetilde{V}_1(R)$, and $\widetilde{V}_2(R)$ for homonuclear collisions of both ^{3}He* and ^{4}He* atoms, where we have used the reduced mass $\mu = m/2$, with $m = 3.01603$ u for ^{3}He* and $m = 4.0026$ u for ^{4}He*, and 1 u $= 1822.89$ a.u. For an atomic sample with a thermal velocity distribution with temperature T, the mean collision energy is given by $\langle E \rangle = \frac{3}{2}k_\mathrm{B}T$; this relation is used to express the potentials in units of temperature.

The barriers formed by centrifugal potentials with $\ell = 1, 2, \ldots$ are five orders of magnitude smaller than the potential energy associated with the short-range attraction of the colliding atoms. However, even the lowest barrier, with $\ell = 1$, is large compared to the temperature of ~ 1 mK that is typical of samples of laser-cooled He* atoms and the barrier heights increase with increasing ℓ. Therefore, the probability ${}^{(2S+1)}P_\ell^{(\mathrm{tun})}$ is small for $\ell = 1$ and decreases rapidly for larger values of ℓ, and the cross section ${}^{(2S+1)}\sigma^{(\mathrm{ion})}$ of Eq. (4.6) is expected to be dominated by the s-wave contribution. In Section 4.2.3, we use numerical methods to study the scattering by potential ${}^{(2S+1)}\widetilde{V}_\ell(R)$ and calculate ${}^{(2S+1)}\sigma^{(\mathrm{ion})}$ for a range of collision energies. We show that contributions with $\ell > 1$ can be neglected at mK temperatures.

4.2.3 Numerical analysis of one-dimensional scattering

A simple approach to one-dimensional potential scattering starts from the determination of stationary states in the potential. These states are described by wave functions $u_{k\ell}(R)$ that are solutions of the time-independent Schrödinger

[10] The two-body problem of a colliding atom pair is separated into two one-body problems, that of the center of mass of the atom pair and that of the relative particle [36, 88].

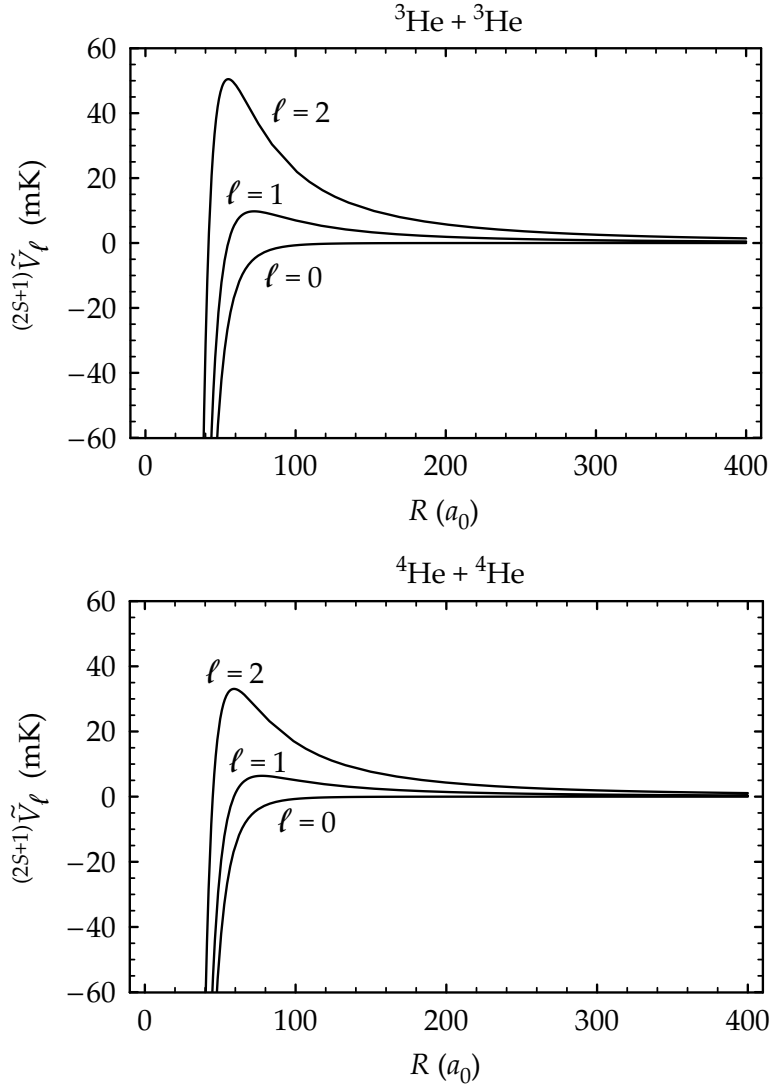

Figure 4.2. Potentials $^{(2S+1)}\widetilde{V}_\ell(R)$ with centrifugal barriers. The centrifugal interaction is smaller than the short-range attraction by five orders of magnitude.

equation of Eq. (4.11). For $R \leq R_0$, the potential $\widetilde{V}_\ell(R)$ is constant and the equation takes the form of a homogeneous, second-order differential equation with constant coefficients. For such an equation the general solution is given by

$$u_{k\ell}(R) = A\exp(ik_1R) + A'\exp(-ik_1R), \tag{4.12}$$

where $k_1 = \{2\mu[E - \widetilde{V}_\ell(R_0)]/\hbar^2\}^{1/2}$ is the local wave vector and A and A' are complex-valued constants. As we are interested in potential scattering of a (relative) particle coming in from $R \gg 1$, we need to determine the stationary state that corresponds to the sum of an incident and a reflected wave for $R \gg 1$, and a single transmitted wave for $R \leq R_0$. We only satisfy this requirement by setting $A = 0$ in Eq. (4.12), obtaining a solution that consists of a single plane wave traveling in the direction of negative R. As there are no boundary conditions determining constant A', we can set it to $A' = 1$, so that we finally obtain

$$u_{k\ell}(R) = \exp(-ik_1R) \quad \text{for } R \leq R_0. \tag{4.13}$$

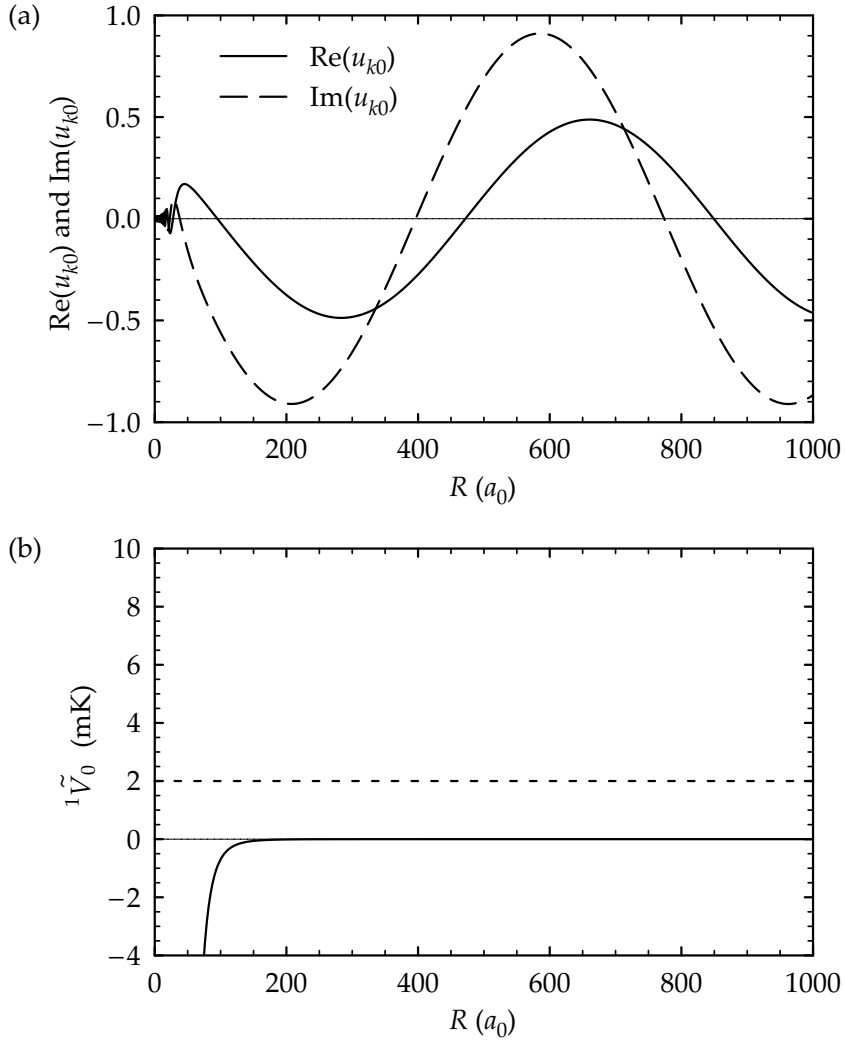

Figure 4.3. s-wave scattering of ^{4}He* atoms with $S = 0$ and $E = 9.5 \times 10^{-9}$ a.u. ($E = 2.0$ mK; $k = 8.3 \times 10^{-3}\, {a_0}^{-1}$). (a) Real and imaginary part of wave function $u_{k0}(R)$. (b) Potential $^1V_0(R)$ (solid line) and the asymptotic kinetic energy E (dotted line). At these low collision energies, the de Broglie wavelength is much larger than the typical scale of the interatomic potential, giving rise to significant quantum reflection. The transmission probability $^1P_0^{(\mathrm{tun})} = 0.66$.

An analytical solution of Eq. (4.11) is not possible for $R > R_0$. However, specifying relative kinetic energy E and quantum number ℓ, a numerical solution can be obtained using the numerical routine `NDSolve` of MATHEMATICA V4.1. From Eq. (4.13), we can obtain the values of $u_{k\ell}(R)$ and $\mathrm{d}u_{k\ell}(R)/\mathrm{d}R$ at a location $R_1 = -10\, a_0$ in the constant potential region,

$$u_{k\ell}(R_1) = \exp(-ik_1 R_1), \tag{4.14}$$

$$\frac{\mathrm{d}}{\mathrm{d}R} u_{k\ell}(R_1) = -ik_1 \exp(-ik_1 R_1). \tag{4.15}$$

Inserting these complex boundary conditions in routine `NDSolve`, we can derive a numerical solution for $R_1 < R < R_2$, with $R_2 \gg 1$. Examples of solutions for

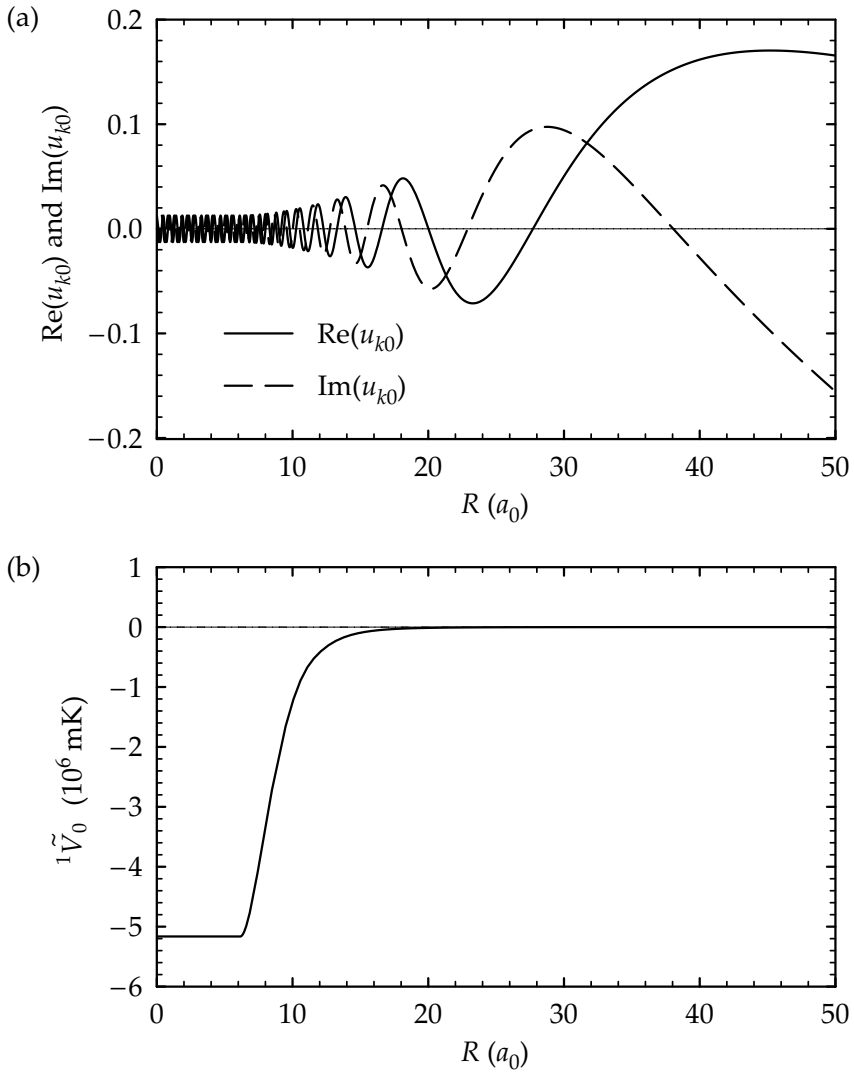

Figure 4.4. Enlargement of the short range behavior of wave function $u_{k0}(R)$. For small internuclear distances, the wave function experiences rapid oscillations and potential $^1V_0(R)$ displays an attractive molecular interaction, which exceeds the collision energy by six orders of magnitude.

homonuclear collisions of ^{4}He* atoms with $S = 0$, $E = 2.0$ mK, and $\ell = 0$ or $\ell = 2$ are shown in Figs. 4.3–4.5.

The scattering process of a particle with wave vector k by potential $\widetilde{V}_\ell(R)$ can be analyzed using the corresponding stationary state $u_{k\ell}(R)$. Calculating the probability fluxes J_{in} and J_{tr} associated with incident and transmitted plane waves, respectively, the transmission probability ${}^{(2S+1)}P_\ell^{(\text{tun})}$ can be written as [36]

$$ {}^{(2S+1)}P_\ell^{(\text{tun})} = \frac{J_{\text{tr}}}{J_{\text{in}}}. \tag{4.16}$$

For the transmitted wave of Eq. (4.13), the probability flux is [36]

$$ J_{\text{tr}} = \frac{\hbar}{2i\mu}\left[u_{k\ell}^*(R)\frac{\mathrm{d}}{\mathrm{d}R}u_{k\ell}(R) - u_{k\ell}(R)\frac{\mathrm{d}}{\mathrm{d}R}u_{k\ell}^*(R)\right] = -\frac{\hbar k_1}{\mu}, \tag{4.17}$$

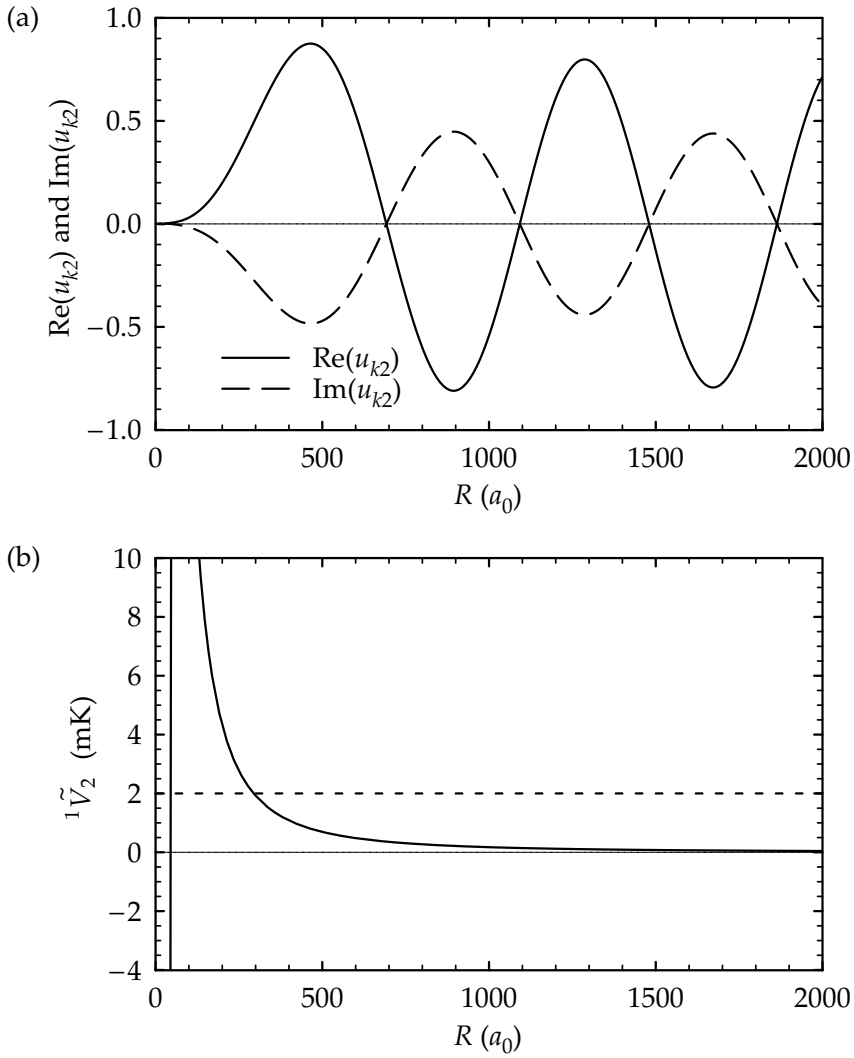

Figure 4.5. d-wave scattering of ^{4}He* atoms with $S = 0$ and $E = 9.5 \times 10^{-9}$ a.u. ($E = 2.0$ mK; $k = 8.3 \times 10^{-3}\, a_0{}^{-1}$). (a) Real and imaginary part of wave function $u_{k2}(R)$. (b) Potential $^1V_2(R)$ (solid line) and the asymptotic kinetic energy E (dotted line). The barrier height of 1.6×10^{-7} a.u. ($T = 33$ mK) is much larger than E, so that the transmission probability is very small, $^1P_2^{(\mathrm{tun})} = 5.8 \times 10^{-4}$.

where the minus sign indicates a probability flux directed to negative R. For $R = R_2 \gg 1$, we can again assume a constant potential and the wave function can be approximated by a sum of two counter-propagating plane waves,

$$u_{k\ell}(R_2) = \tilde{A} \exp(ik_2 R_2) + \tilde{A}' \exp(-ik_2 R_2), \tag{4.18}$$

with $k_2 = \{2\mu[E - \widetilde{V}_\ell(R_2)]/\hbar^2\}^{1/2}$, so that the corresponding probability flux can be written as

$$J = \frac{\hbar k_2 |\tilde{A}|^2}{\mu} - \frac{\hbar k_2 |\tilde{A}'|^2}{\mu}. \tag{4.19}$$

Clearly, the first term corresponds to the reflected wave traveling to positive R and the second term is J_{in}, corresponding to the incident wave traveling to

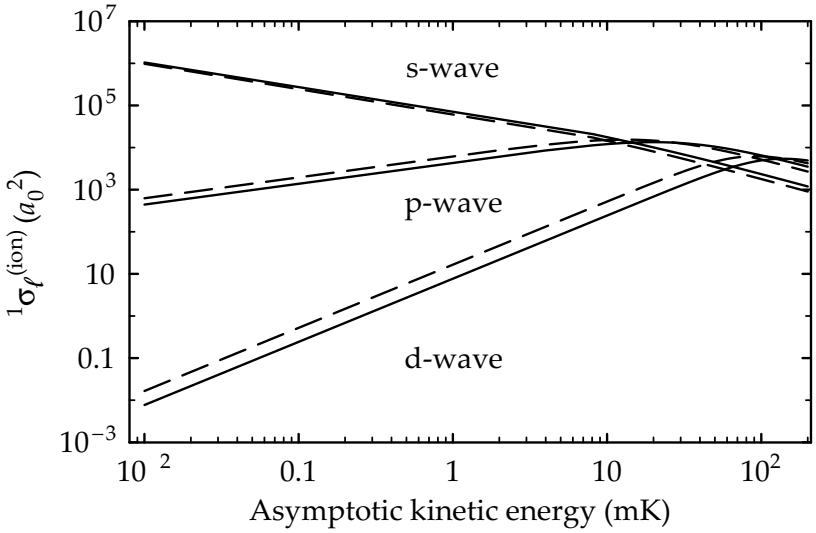

Figure 4.6. The partial wave ionization cross sections ($S = 0$) for ^{3}He* (dashed lines) and ^{4}He* (solid lines) show the familiar quantum threshold behavior $^1\sigma_\ell^{(\mathrm{ion})} \propto k^{2\ell-1}$ if $k \to 0$.

negative R. Consequently, the transmission probability can be written as

$$^{(2S+1)}P_\ell^{(\mathrm{tun})} = \frac{k_1}{k_2}|\tilde{A}'|^{-2}. \tag{4.20}$$

We derive values for $\tilde{A}$ and $\tilde{A}'$ by matching expression Eq. (4.18) at $R = R_2$ to numerical solution $u_{k\ell}(R_2)$,

$$\begin{aligned} u_{k\ell}(R_2) &= \tilde{A}\exp(ik_2R_2) + \tilde{A}'\exp(-ik_2R_2), \\ \frac{\mathrm{d}}{\mathrm{d}R}u_{k\ell}(R_2) &= ik_2\tilde{A}\exp(ik_2R_2) - ik_2\tilde{A}'\exp(-ik_2R_2), \end{aligned} \tag{4.21}$$

Choosing R_2 such that $\widetilde{V}_\ell(R_2) = E/1000$, we make sure that the numerical solution is well approximated by a sum of counter-propagating plane waves: probabilities $^{(2S+1)}P_\ell^{(\mathrm{tun})}$ are accurate within a few tenths of a percent. Furthermore, the difference between probabilities $^1P_\ell^{(\mathrm{tun})}$ and $^3P_\ell^{(\mathrm{tun})}$ at a given collision energy E is only a few percent, as potentials $^1\widetilde{V}(R)$ and $^3\widetilde{V}(R)$ differ very little in the region where elastic scattering takes place: $|^3\widetilde{V}(R) - {}^1\widetilde{V}(R)|/|^1\widetilde{V}(R)| < 10^{-4}$ for $R > 20\,a_0$.

The wave functions of Figs. 4.3 and 4.5 correspond to transmission probabilities $^1P_0^{(\mathrm{tun})} = 0.66$ and $^1P_2^{(\mathrm{tun})} = 5.8 \times 10^{-4}$, respectively. In the case of d-wave scattering, reflection is almost complete, as E is much smaller than the barrier height. However, there is also considerable reflection in the case of s-wave scattering, where a centrifugal barrier is absent. Here, quantum reflection occurs due to the mismatch between the long asymptotic de Broglie wave and the rapidly oscillating wave in the region of small internuclear separation.

Inserting the reduced mass μ for either ^{3}He* or ^{4}He* atoms, we calculate the transmission probabilities $^{(2S+1)}P_0(E)$, $^{(2S+1)}P_1(E)$ and $^{(2S+1)}P_2(E)$ for $S = 0, 1$

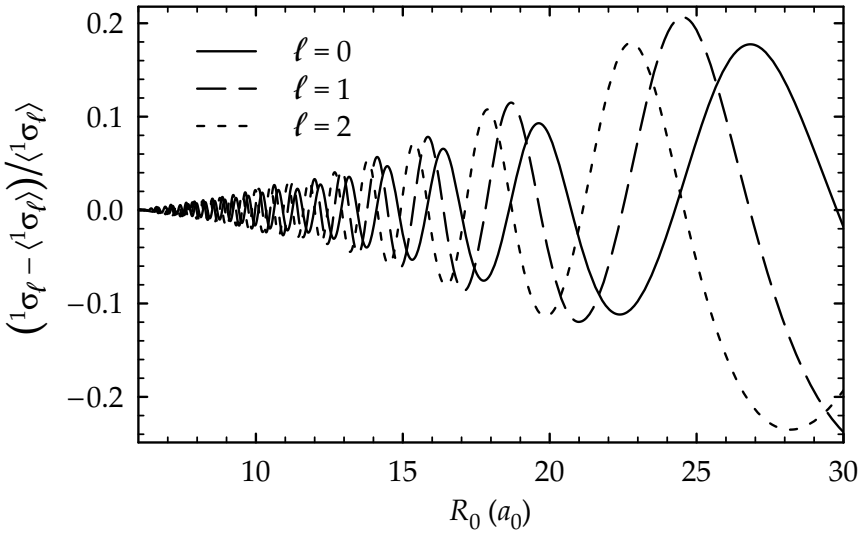

Figure 4.7. Relative variation of the calculated ionization cross section ${}^1\sigma_\ell^{(\mathrm{ion})}$ as a function of R_0. As computational artifacts, the variations indicate the self-consistency of the model and limit the accuracy of the calculated cross sections. Mean values $\langle {}^1\sigma_\ell^{(\mathrm{ion})} \rangle$ are averaged over an integer number of oscillations. Collision energy $E = 1.9 \times 10^{-9}$ a.u. $\left(v = (2E/\mu)^{1/2} = 1 \times 10^{-6}\ \text{a.u.}\right)$ and $S = 0$.

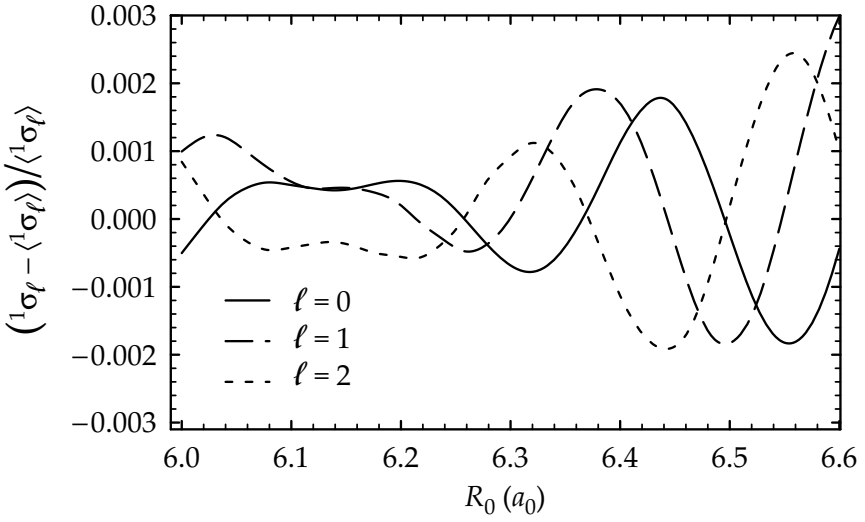

Figure 4.8. Enlargement of Fig. 4.7 around the potential minimum. Choosing $R_0 = 6.1\ a_0$, variations are about 0.2%.

over a wide range of collision energies. Applying

$$ {}^{(2S+1)}\sigma_\ell^{(\mathrm{ion})}(E) = \frac{\pi}{k^2}(2\ell+1)\ {}^{(2S+1)}P_\ell^{(\mathrm{tun})}(E), \tag{4.22}$$

we obtain partial wave ionization cross sections ${}^{(2S+1)}\sigma_0^{(\mathrm{ion})}(E)$, ${}^{(2S+1)}\sigma_1^{(\mathrm{ion})}(E)$ and ${}^{(2S+1)}\sigma_2^{(\mathrm{ion})}(E)$ for both isotopes. It can be seen in Fig. 4.6 that the resulting cross sections satisfy the quantum threshold behavior of Eq. (4.5).

To determine the dependence of the cross sections on the adapted short-

range part of the potential, we have calculated the variation in the cross sections as a function of R_0 for various collision energies; an example of such a calculation is shown in Figs. 4.7 and 4.8. If R_0 is close to the location of the potential curve minimum at 6.1 a_0, the variations are smallest (less than 0.2%). This can be understood from the large increase in kinetic energy that the relative particle experiences in the attractive part of the potential. As the de Broglie wavelength becomes of the order of a_0 at these large energies, quantum reflection in the potential becomes a minor effect and the cross sections are relatively insensitive to variations in the potential. Moreover, with R_0 at the potential minimum, the effective potential curve is smooth and reflection from artificial features (kinks) is avoided.

It has been shown in calculations that the ionization cross sections for ^{4}He* are enhanced if the s-wave scattering length ^5a associated with the quintet potential is near a singularity [111]. The s-wave scattering length describes elastic collisions in the low-temperature limit [43] and shows a singularity (goes through $\pm\infty$) whenever a bound state is removed from the potential [111]. From experiments, it has been determined that $^5a = 214\,a_0 = 11.3$ nm with an error of a few nm [175] and a theoretical prediction gives $152\,a_0 < {}^5a < 230\,a_0$ (or 8.0 nm $< {}^5a <$ 12.2 nm) [49]. In both cases the scattering length is sufficiently far from the singularity to neglect enhancement of the ionization cross sections. For ^{3}He* atoms, the s-wave scattering length for $S = 2$ is predicted to be $94\,a_0 < {}^5a < 113\,a_0$ (or 5.0 nm $< {}^5a <$ 6.0 nm). This is also sufficiently small to neglect effects on the ionization cross sections.

4.2.4 Ionization rate coefficient

In the experiments of Chapter 5, we study ionizing collisions by monitoring the ion production rate $\mathrm{d}N_{\mathrm{ion}}(t)/\mathrm{d}t = K_{\mathrm{SS}} \iiint n^2(\boldsymbol{r},t)\,\mathrm{d}^3r$ in magneto-optically trapped atomic samples of ^{3}He* or ^{4}He* atoms. The ionization rate coefficient K_{SS} (particle^{-1} cm^3/s) depends on the temperature T of the sample and can be written in terms of an ionization cross section $\sigma^{(\mathrm{ion})}(E)$ as [91]

$$K_{\mathrm{SS}}(T) = \int_0^\infty \sigma^{(\mathrm{ion})}(E)\;\; P_T^{(\mathrm{MB})}(v_{\mathrm{r}})\;\; v_{\mathrm{r}}\, dv_{\mathrm{r}}, \tag{4.23}$$

with

$$P_T^{(\mathrm{MB})}(v_{\mathrm{r}}) = \sqrt{\frac{2}{\pi}}\,\frac{v_{\mathrm{r}}^2}{(k_{\mathrm{B}}T/\mu)^{3/2}}\;\exp\!\left(-\frac{v_{\mathrm{r}}^2}{k_{\mathrm{B}}T/\mu}\right), \tag{4.24}$$

the Maxwell-Boltzmann distribution for the relative velocity in the atomic sample under study.[11]

Correspondingly, we can calculate partial wave ionization rate coefficients

$$^{(2S+1)}\mathcal{K}_\ell(T) = \int_0^\infty {}^{(2S+1)}\sigma_\ell^{(\mathrm{ion})}(E)\;\; P_T^{(\mathrm{MB})}(v_{\mathrm{r}})\;\; v_{\mathrm{r}}\, dv_{\mathrm{r}}, \tag{4.25}$$

[11] The collision energy depends on relative velocity via $E = \mu v_{\mathrm{r}}^2/2$ and the root mean square of the relative velocity, $\langle v_{\mathrm{r}}^2\rangle^{1/2} = (k_{\mathrm{B}}T/\mu)^{1/2} = (2k_{\mathrm{B}}T/m)^{1/2}$, is $\sqrt{2}$ times the root mean square of the velocity of each collision partner.

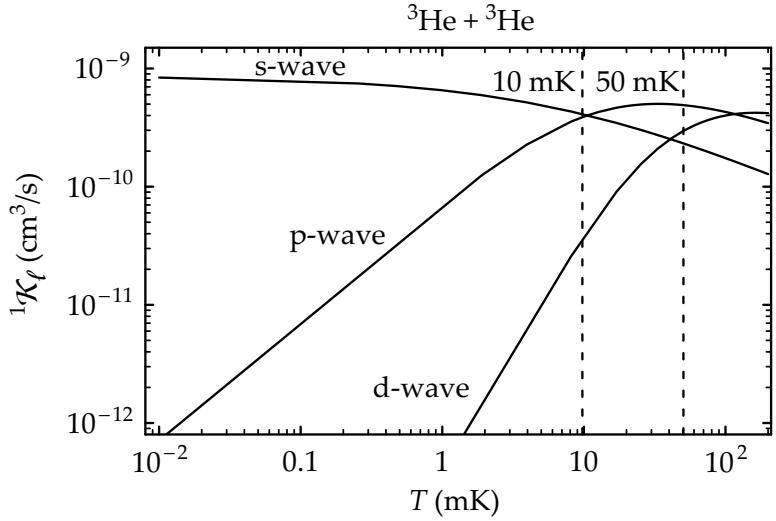

Figure 4.9. Rate coefficients ${}^1\mathcal{K}_\ell(T)$ ($\ell = 0, 1, 2$) for ^{3}He*, calculated from the model including p and d-wave barrier temperatures.

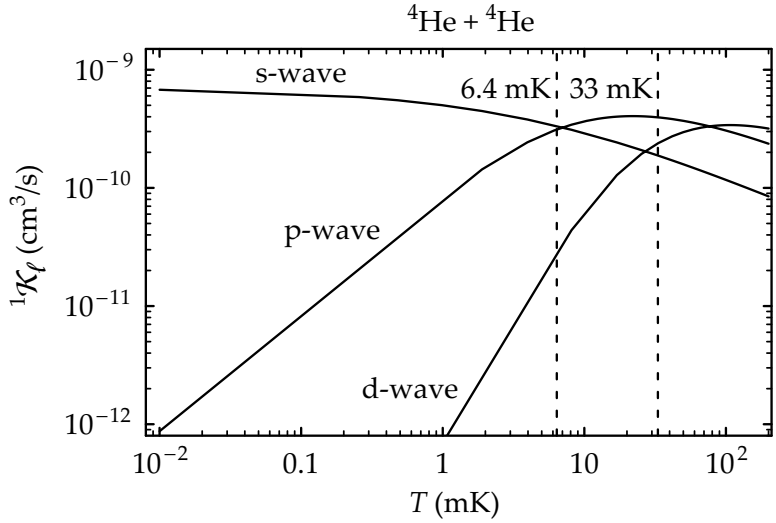

Figure 4.10. Rate coefficients ${}^1\mathcal{K}_\ell(T)$ ($\ell = 0, 1, 2$) for ^{4}He*, calculated from the model including p and d-wave barrier temperatures.

and determine

$$ {}^{(2S+1)}K(T) = \sum_\ell {}^{(2S+1)}\mathcal{K}_\ell(T), \tag{4.26} $$

the ionization rate coefficients associated with a potential ${}^{(2S+1)}V(R)$. Using numerical integration, ${}^{(2S+1)}\mathcal{K}_0(T)$, ${}^{(2S+1)}\mathcal{K}_1(T)$ and ${}^{(2S+1)}\mathcal{K}_2(T)$ are determined for both helium isotopes.[12] The quantum threshold behavior of the rate coefficients is given by

$$ {}^{(2S+1)}\mathcal{K}_\ell \propto k^{2\ell} \quad \text{if } k \to 0. \tag{4.27} $$

[12] As $|{}^3\widetilde{V}(R) - {}^1\widetilde{V}(R)|/|{}^1\widetilde{V}(R)| < 10^{-4}$ for $R > 20\,a_0$, differences between ${}^1\sigma_\ell^{(\mathrm{ion})}$ and ${}^3\sigma_\ell^{(\mathrm{ion})}$, and ${}^1\mathcal{K}_\ell$ and ${}^3\mathcal{K}_\ell$ are only a few percent. For convenience, we have only performed the calculations for $S = 0$ and used the results for both $S = 0$ and $S = 1$.

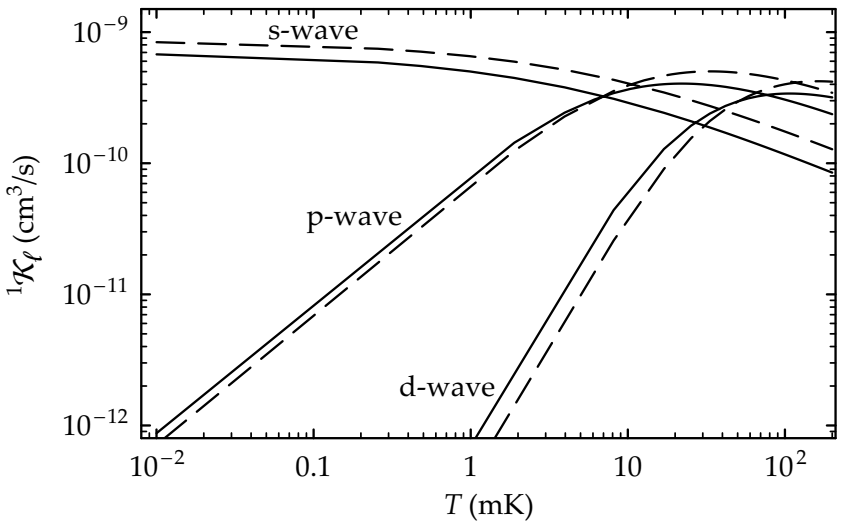

Figure 4.11. Comparison of the rate coefficients $^1\mathcal{K}_\ell(T)$ for ^{3}He* (dotted lines) and ^{4}He* (solid lines).

In particular, we find $^{(2S+1)}\mathcal{K}_0 \to$ constant if $k \to 0$, as the divergence of σ_0 is canceled by $v = \hbar k/\mu$. Figs. 4.9 and 4.10 show plots of the coefficients for a large temperature range, for ^{3}He* and ^{4}He*, respectively. The energy of the centrifugal barriers for $\ell = 1$ and $\ell = 2$ is indicated by dashed vertical lines. For temperatures $T < 5$ mK, the contribution of the d-wave becomes very small and can be ignored if an accuracy of 5% is sufficient. Fig. 4.11 shows plots of the coefficients for both isotopes. Comparing partial wave coefficients for the two isotopes, we see that the dependence on temperature is similar and that curves differ by less than 50%.

We have neglected the atomic hyperfine structure of the interatomic potentials for ^{3}He*. As it is four orders of magnitude smaller than the attractive interaction at short range, its effect on $^{(2S+1)}\sigma_\ell^{(\mathrm{ion})}$ and $^{(2S+1)}\mathcal{K}_\ell$ is negligible. Therefore, the calculations for ^{3}He* and ^{4}He* are identical, apart from the use of a different reduced mass.

4.2.5 Symmetrization of scattering states

Although the interatomic interaction is almost identical in the case of ^{3}He* and ^{4}He*, giving rise to $^{(2S+1)}\sigma_\ell^{(\mathrm{ion})}$ and $^{(2S+1)}\mathcal{K}_\ell$ that are similar, the description of the collision process in terms of partial waves is very different due to the different quantum statistical nature of the two isotopes. As we are dealing with a system of identical particles—bosons in the case of ^{4}He* and fermions in the case of ^{3}He*—the scattering states have a distinct symmetry under exchange of the atoms and partial wave contributions associated with states with improper symmetry must be excluded from summations like Eq. (4.26).

Bosonic ^{4}He*: Symmetric states

During a collision of two ^{4}He* atoms, the total electronic spin $\mathbf{S}$ and relative angular momentum $\boldsymbol{\ell}$ are conserved separately, and both S and ℓ are good quantum numbers.[13] Ignoring the radial part of the quantum states, a basis for the atom pairs is given by

$$\left\{ |(S_1)_A (S_1)_B S M_S\, \ell m\rangle \right\}. \tag{4.28}$$

Here the atoms are assumed to be distinguishable and are labeled with A and B. Both atoms carry a spin $S_1 = 1$ and the total electronic spin S is the result of the addition of these spins. Quantum numbers M_S and m are associated with the projection on the internuclear axis of the total electronic spin and the relative angular momentum ℓ of the two atoms, respectively.

For identical bosons, such as two ^{4}He* atoms, physical states must be symmetric under exchange of the two atoms. Such states are obtained applying symmetrizer $\mathrm{S} = (1 + \mathrm{P}_{12})/\sqrt{2}$ to the basis vectors, (see [36, complement $\mathrm{D}_{\mathrm{XIV}}$] or [25, Section 2.3.1])

$$|S_1 S_2, S M_S, \ell m\rangle = \frac{1}{\sqrt{2}} \left[1 + (-1)^{S+\ell}\right] \, |(S_1)_A (S_1)_B S M_S\, \ell m\rangle. \tag{4.29}$$

As the states differ from zero only if $S + \ell$ is even, we can conclude that it is not possible to construct states with the proper symmetry if $S = 0$ or $S = 2$ and ℓ is odd, or if $S = 1$ and ℓ is even. Consequently, the corresponding partial wave ionization rate coefficients must be excluded from the summation and, for a scattering channel $(S_1 S_2, S M_S)$, we can write

$$^1K = \sum_{\ell \text{ even}} {}^1\mathcal{K}_\ell, \tag{4.30}$$

$$^3K = \sum_{\ell \text{ odd}} {}^3\mathcal{K}_\ell. \tag{4.31}$$

As total electronic spin is conserved, each long-range scattering channel correlates to a single short-range molecular potential of Fig 4.1. Consequently, the strong suppression of ionization in the quintet potential (Section 4.2.1), allows us to set $^5K = 0$ for $S = 2$.

Fermionic ^{3}He*: Antisymmetric states with hyperfine structure

During a collision of two ^{3}He* atoms, the total atomic angular momentum $\mathbf{F} = \mathbf{F}_1 + \mathbf{F}_2$ and the relative angular momentum of the two atoms $\boldsymbol{\ell}$ are conserved separately. Here, $\mathbf{F}_i = \mathbf{S}_i + \mathbf{I}_i$ $(i = 1, 2)$, the total angular momentum $\mathbf{F}_i$ of an atom is the sum of its electronic spin $\mathbf{S}_i$ and its nuclear spin $\mathbf{I}_i$.

Ignoring the radial part of the quantum states and assuming distinguishable atoms, a basis for the atom pair is given by

$$\left\{ |(S_1 I_1 F_1)_A (S_1 I_1 F_2)_B F M_F, \ell m\rangle \right\}, \tag{4.32}$$

[13] Conservation of total parity does not give rise to extra selection rules, as the total parity operation, inverting all electronic and nuclear coordinates, has eigenvalues $(-1)^\ell$ [67].

where atoms A and B have identical electronic and nuclear spins, $S_1 = 1$ respectively $I_1 = \frac{1}{2}$, that add up to F_1 for atom A and F_2 for atom B. The latter two add up to the total atomic angular momentum F with projection onto the internuclear axis M_F. Quantum numbers ℓ and m are the angular momenta associated with the relative motion of the two atoms and its projection onto the internuclear axis, respectively.

If both atoms are in the lower hyperfine level, so that $F_1 = F_2 = \frac{3}{2}$, F can take the values 0, 1, 2 and 3. If both atoms are in the upper hyperfine level, so that $F_1 = F_2 = \frac{1}{2}$, F can take the values 0 and 1. Finally one atom in the lower state, while the other is in the upper gives rise to $F = 1$ and $F = 2$.

As a ^{3}He atom is a fermion, the physical states describing an atom pair must be antisymmetric under exchange of the atoms. Applying antisymmetrizer $\mathrm{A} = (1 - \mathrm{P}_{12})/\sqrt{2}$ to the basis states, we obtain

$$|S_1 I_1 F_1, S_1 I_1 F_2, F M_F, \ell m\rangle = \frac{1}{\sqrt{2}} \Big[|(S_1 I_1 F_1)_A (S_1 I_1 F_2)_B F M_F, \ell m\rangle + (-1)^{F_1+F_2-F+\ell+1} |(S_1 I_1 F_2)_A (S_1 I_1 F_1)_B F M_F, \ell m\rangle \Big] \quad (4.33)$$

If $F_1 = F_2$, the physical states are given by

$$|S_1 I_1 F_1, S_1 I_1 F_1, F M_F, \ell m\rangle = \frac{1}{\sqrt{2}} \left[1 + (-1)^{\ell - F} \right] \, |(S_1 I_1 F_1)_A (S_1 I_1 F_1)_B F M_F, \ell m\rangle, \quad (4.34)$$

only differing from zero if $F - \ell$ is even. Therefore, we must exclude odd (even) partial waves when calculating the ionization rate coefficient for even (odd) F. If $F_1 \neq F_2$, the physical states can be written

$$|S_1 I_1 F_1, S_1 I_1 F_2, F M_F, \ell m\rangle = \frac{1}{\sqrt{2}} \Big[|(S_1 I_1 F_1)_A (S_1 I_1 F_2)_B F M_F, \ell m\rangle + (-1)^{\ell - F + 1} |(S_1 I_1 F_2)_A (S_1 I_1 F_1)_B F M_F, \ell m\rangle \Big] . \quad (4.35)$$

As these states never equal zero, we cannot derive selection rules based on the value of F. For each value, $F = 1$ or $F = 2$, there is exactly one state of positive parity and one of negative parity. For the states with positive (negative) parity, only even (odd) partial waves contribute to the collisions.[14]

Due to the atomic hyperfine interaction, S is not a good quantum number for large internuclear distances, where an atom pair is characterized by $(F_1 F_2, F M_F)$. The ionization rate coefficient associated with the atom pair cannot be written as a sum of the partial wave contributions ${}^{(2S+1)}\mathcal{K}_\ell$, calculated in Section 4.2.3. However, S is a good quantum number for $R \lesssim 30\, a_0$, where the molecular interaction dominates and Wigner's spin-conservation rule applies.

[14] The selection rule for the contribution of partial waves can always be expressed in terms of parity of the corresponding quantum state: positive parity corresponds to even partial waves and negative parity to odd ones [25, Section 2.3.1]. We have expressed the selection rule in terms of S and F in view of convenience.

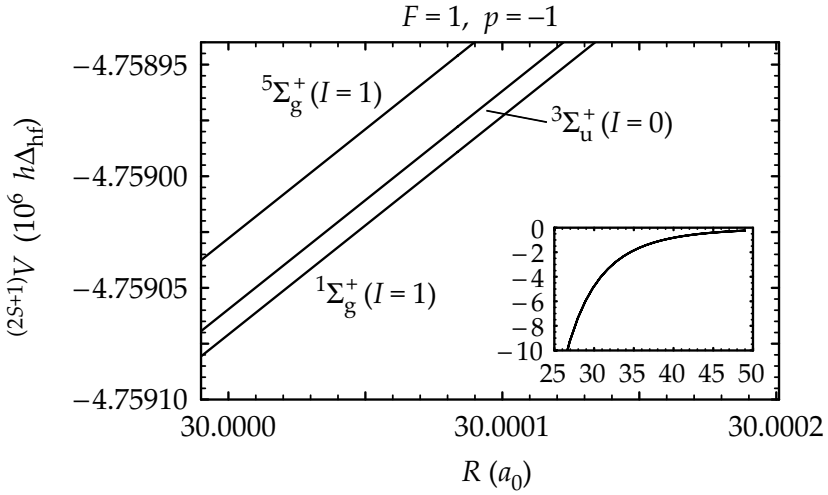

Figure 4.12. Enlargement around $R = 30\,a_0$ of the short-range potentials for ^{3}He* with $F = 1$ and negative parity. The inset shows the potential curves for $25\,a_0 < R < 50\,a_0$; as the hyperfine interaction is small compared to the molecular interaction at small internuclear distance ($R \lesssim 30\,a_0$), the potentials show up as a single curve. The hyperfine splitting of ^{3}He* is $\Delta_{\mathrm{hf}} = 6.739701177$ GHz. The calculation of the curves is presented in Appendix C.

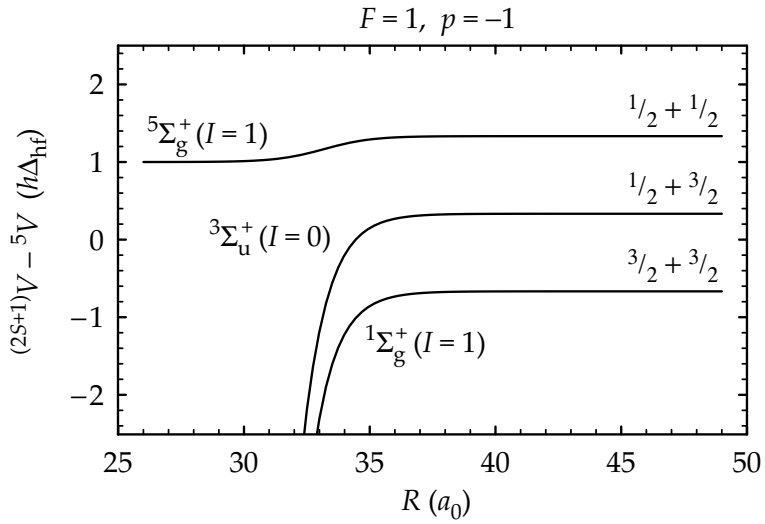

Figure 4.13. Deviation from potential $^5V(R)$ (cf. Fig. 4.1) of the short-range potentials for ^{3}He* with $F = 1$ and negative parity. As potential $^5V(R)$ applies to ^{4}He* [136], it does not show hyperfine structure. The hyperfine splitting of ^{3}He* is $\Delta_{\mathrm{hf}} = 6.739701177$ GHz.

To calculate the rate coefficient, we must analyze the evolution of the states of the colliding atom pair in the region where the atomic hyperfine interaction and molecular interaction are of the same order of magnitude.

In Appendix C, the adiabatic potentials including atomic hyperfine structure are calculated. Figures 4.12 and 4.13 show the adiabatic potentials of negative parity with $F = 1$ around $R = 30\,a_0$, where the molecular exchange interaction

becomes larger than the atomic hyperfine splitting. The exchange interaction increases exponentially for decreasing R (see Eq. (C.4)), so that the potential curves diverge rapidly. To determine the nature of the quantum state evolution through this region of internuclear distance, we compare the absolute energy difference $|E_n - E_m|$ of two scattering states, $|m\rangle$ and $|n\rangle$ (with equal total atomic angular momentum F and equal relative angular momentum ℓ), with the change in the coupling between the scattering states during one period of oscillation in the quasi-molecular system [45, Section 76],

$$\left|\frac{1}{\omega_{nm}}\frac{\mathrm{d}}{\mathrm{d}t}\langle n|\mathrm{H}_{\mathrm{exch}}|m\rangle\right| = \left|\frac{1}{\omega_{nm}}\, v_{\mathrm{r}}\,\frac{\mathrm{d}}{\mathrm{d}R}\langle n|\mathrm{H}_{\mathrm{exch}}|m\rangle\right|, \tag{4.36}$$

where v_{r} is the relative velocity of the colliding atoms, and $1/\omega_{nm} = \hbar/|E_n - E_m|$ is the period of oscillation in the quasi-molecular system. Neglecting the asymptotic kinetic energy, the relative velocity

$$v_{\mathrm{r}} \approx \sqrt{2\left[-^{(2S+1)}V(R)\right]/\mu} \approx 4\times 10^{-5}\ \text{a.u.}$$

at $R = 35\,a_0$. The coupling between the scattering states can be approximated within one order of magnitude by the exchange energy given by Eq. (C.4), so that

$$\frac{\mathrm{d}}{\mathrm{d}R}\langle n|\mathrm{H}_{\mathrm{exch}}|m\rangle \approx -10^{-14}\ \text{a.u.}$$

At $R = 35\,a_0$, the energy difference between the scattering states is on the order of the hyperfine splitting, so that the period of oscillation can be approximated as $(1/\omega_{nm}) \approx 1/2\pi\Delta_{\mathrm{hf}} = 1\times 10^{12}$ a.u. The absolute change in the coupling during one period of oscillation,

$$\left|\frac{1}{\omega_{nm}}\, v_{\mathrm{r}}\,\frac{\mathrm{d}}{\mathrm{d}R}\langle n|\mathrm{H}_{\mathrm{exch}}|m\rangle\right| \approx 4\times 10^{-7}\ \text{a.u.},$$

is much larger than the absolute energy difference between the scattering states

$$|E_n - E_m| \approx h\Delta_{\mathrm{hf}} \approx 1\times 10^{-12}\ \text{a.u.}$$

Therefore, the evolution around $R = 35\,a_0$ is well approximated by a diabatic transition [45, Section 76], where the Hamiltonian of the system is assumed to change infinitely fast and the state of the quasi-molecular system remains unchanged.

To determine the ionization rate coefficient associated with a scattering state, we can expand the state onto the eigenstates of the short-range molecular Hamiltonian, and determine the fraction of ionizing states ($S = 0, 1$) in the expansion. The expansions only involve the angular part of the quantum states involved. For the molecular states, the angular part can be derived applying the antisymmetrizer to the vectors of an appropriate basis. Ignoring the radial part of the quantum states and assuming that the atoms are distinguishable, we write down a basis for the atom pair where the short-range molecular interaction is diagonal,

$$\left\{|(S_1I_1)_A(S_1I_1)_BSI, FM_F, \ell m\rangle\right\}. \tag{4.37}$$

Here, I is the quantum number associated with the sum of the nuclear spins $\mathbf{I} = \mathbf{I}_1 + \mathbf{I}_2$ and S is associated with the sum of the electronic spins $\mathbf{S} = \mathbf{S}_1 + \mathbf{S}_2$. The basis vectors of Eq. (4.32) can be expressed in the short-range basis of Eq. (4.37) using 9-j symbols [229]

$$|(S_1 I_1 F_1)_A (S_1 I_1 F_2)_B F M_F, \ell m\rangle = \sum_S \sum_I |(S_1 I_1)_A (S_1 I_1)_B S I, F M_F, \ell m\rangle \times \langle (S_1\, S_2) S (I_1\, I_2) I\, F | (S_1\, I_1) F_1 (S_2\, I_2) F_2\, F\rangle \quad (4.38)$$

where

$$\langle (S_1\, S_2) S (I_1\, I_2) I\, F | (S_1\, I_1) F_1 (S_2\, I_2) F_2\, F\rangle = [(2S+1)(2I+1)(2F_1+1)(2F_2+1)]^{1/2} \begin{Bmatrix} S_1 & I_1 & F_1 \\ S_2 & I_2 & F_2 \\ S & I & F \end{Bmatrix}. \quad (4.39)$$

Antisymmetrizing the vectors of the basis of Eq. (4.37), we obtain the physical states,

$$|S_1 I_1, S_1 I_1, S I, F M_F, \ell m\rangle = \frac{1}{\sqrt{2}} [1 + (-1)^{\ell - S - I}] \times |(S_1 I_1)_A (S_1 I_1)_B S I, F M_F, \ell m\rangle, \quad (4.40)$$

that are different from zero only if $\ell - S - I$ is even. The states are the angular parts of the eigenstates of the short-range interaction of two ^{3}He* atoms: writing the eigenstates as $|^{2S+1}\Sigma^+_{\mathrm{g/u}}\, I, F M_F, \ell m\rangle$, the corresponding angular part is given by Eq. (4.40).

As F and ℓ are good quantum numbers during a collision, a scattering state $|S_1 I_1 F_1, S_1 I_1 F_2, F M_F, \ell m\rangle$ is expanded onto the molecular states with the same F and ℓ, i.e. the expansion can be confined within the subspace defined by F and ℓ. Table 4.1 lists all possible combinations of F and ℓ for both scattering states and molecular states, and can be used to determine the molecular subspace associated with a scattering state.

A partial wave rate coefficient $\mathcal{K}_\ell(F_1 F_2, F)$ associated with scattering state $|S_1 I_1 F_1, S_1 I_1 F_2, F M_F, \ell m\rangle$ can be expressed as a weighted sum of coefficients ${}^{(2S+1)}K_\ell$ associated with molecular states $|S_1 I_1, S_1 I_1, S I, F M_F, \ell m\rangle$,

$$\mathcal{K}_\ell(F_1 F_2, F) = \sum_{S \neq 2} {}^{(2S+1)}\mathcal{K}_\ell \sum_I |\langle S_1 I_1, S_1 I_1, S I, F M_F, \ell m | S_1 I_1 F_1, S_1 I_1 F_2, F M_F, \ell m\rangle|^2, \quad (4.41)$$

neglecting ionization for $S = 2$. In accordance with a diabatic transition, the weights are projections of the scattering state onto the ionizing molecular states of the subspace defined by F and ℓ. As an example, we calculate coefficients $\mathcal{K}_\ell(\frac{3}{2}\frac{3}{2}, F)$ for scattering states with $F_1 = F_2 = \frac{3}{2}$. Writing

$$|F_1\, F_2\, F\, M_F\rangle_{\mathrm{scat}} = |S_1 I_1 F_1, S_1 I_1 F_2, F M_F, \ell m\rangle \quad (4.42)$$

$$|S\, I\, F\, M_F\rangle_{\mathrm{mol}} = |S_1 I_1, S_1 I_1, S I, F M_F, \ell m\rangle \quad (4.43)$$

Table 4.1. Distinguishing between even and odd ℓ, all occurring values of total atomic angular momentum F for two ^{3}He* atoms, associated with molecular states, $F = |S-I|, \ldots, S+I$, and scattering states, $F = |F_1 - F_2|, \ldots, F_1 + F_2$, are listed. During a collision, parity $(-1)^\ell$ and total atomic angular momentum F are conserved separately. These conservation laws determine the molecular subspace associated with a scattering state in a diabatic transition. Consequently, scattering state $(\frac{3}{2}, \frac{3}{2})$ with odd ℓ and $F = 3$ transforms into molecular state $^5\Sigma_g^+$ $(I = 1)$ (with ℓ and F conserved).

ℓ even	Molecular state $^{2S+1}\Sigma_{g/u}^+(I)$	$F = \lvert S-I\rvert, \ldots, S+I.$	$F = \lvert F_1 - F_2\rvert, \ldots, F_1 + F_2.$	Scattering state (F_1, F_2)
	$^5\Sigma_g^+$ $(I=0)$	2	0	$(\frac{1}{2}, \frac{1}{2})$
	$^3\Sigma_u^+$ $(I=1)$	0 1 2	1 2	$(\frac{3}{2}, \frac{1}{2})$ $(\frac{1}{2}, \frac{3}{2})$
	$^1\Sigma_g^+$ $(I=0)$	0	0 2	$(\frac{3}{2}, \frac{3}{2})$
ℓ odd	Molecular state $^{2S+1}\Sigma_{g/u}^+(I)$	$F = \lvert S-I\rvert, \ldots, S+I.$	$F = \lvert F_1 - F_2\rvert, \ldots, F_1 + F_2.$	Scattering state (F_1, F_2)
	$^5\Sigma_g^+$ $(I=1)$	1 2 3	1	$(\frac{1}{2}, \frac{1}{2})$
	$^3\Sigma_u^+$ $(I=0)$	1	1 2	$(\frac{3}{2}, \frac{1}{2})$ $(\frac{1}{2}, \frac{3}{2})$
	$^1\Sigma_g^+$ $(I=1)$	1	1 3	$(\frac{3}{2}, \frac{3}{2})$

the states are expanded onto the molecular states as

$$|\tfrac{3}{2}\,\tfrac{3}{2}\,0\,M_F\rangle_{\rm scat} = \sqrt{\tfrac{2}{3}}\,|0\,0\,0\,M_F\rangle_{\rm mol} - \sqrt{\tfrac{1}{3}}\,|1\,1\,0\,M_F\rangle_{\rm mol}, \tag{4.44}$$

$$|\tfrac{3}{2}\,\tfrac{3}{2}\,1\,M_F\rangle_{\rm scat} = \sqrt{\tfrac{10}{27}}\,|0\,1\,1\,M_F\rangle_{\rm mol} + \sqrt{\tfrac{5}{9}}\,|1\,0\,1\,M_F\rangle_{\rm mol} - \sqrt{\tfrac{2}{27}}\,|2\,1\,1\,M_F\rangle_{\rm mol}, \tag{4.45}$$

$$|\tfrac{3}{2}\,\tfrac{3}{2}\,2\,M_F\rangle_{\rm scat} = \sqrt{\tfrac{2}{3}}\,|1\,1\,2\,M_F\rangle_{\rm mol} + \sqrt{\tfrac{1}{3}}\,|2\,0\,2\,M_F\rangle_{\rm mol}, \tag{4.46}$$

$$|\tfrac{3}{2}\,\tfrac{3}{2}\,3\,M_F\rangle_{\rm scat} = |2\,1\,3\,M_F\rangle_{\rm mol}. \tag{4.47}$$

The $F = 0$ state is expanded onto singlet and triplet states only and

$$\mathcal{K}_\ell(\tfrac{3}{2}\tfrac{3}{2}, 0) = \tfrac{2}{3}({}^1\mathcal{K}_\ell) + \tfrac{1}{3}({}^3\mathcal{K}_\ell). \tag{4.48}$$

For the $F = 1$ and $F = 2$ states, the expansions show that the diabatic transition transforms the scattering states into a superposition of ionizing an non-ionizing molecular states. Calculating the projections, we obtain

$$\mathcal{K}_\ell(\tfrac{3}{2}\tfrac{3}{2}, 1) = \tfrac{10}{27}({}^1\mathcal{K}_\ell) + \tfrac{5}{9}({}^3\mathcal{K}_\ell), \tag{4.49}$$

$$\mathcal{K}_\ell(\tfrac{3}{2}\tfrac{3}{2}, 2) = \tfrac{2}{3}({}^1\mathcal{K}_\ell). \tag{4.50}$$

Considering the $F = 3$ state, we see that $\mathcal{K}_\ell(\frac{3}{2}\frac{3}{2}, 3) = 0$, as it is expanded onto quintet states only. This result can also be obtained from Table 4.1 requiring conservation of angular momenta F and ℓ.

Taking into account conservation of total parity, we can write the ionization rate coefficient for a homonuclear collision of two ^{3}He* atoms, characterized by (F_1F_2, F), as

$$K(F_1F_2, F) = \begin{cases} \displaystyle\sum_{\ell\,\text{even}} \mathcal{K}_\ell(F_1F_2, F) & \text{for positive parity,} \\ \displaystyle\sum_{\ell\,\text{odd}} \mathcal{K}_\ell(F_1F_2, F) & \text{for negative parity.} \end{cases} \tag{4.51}$$

For $F_1 = F_2$, the summation is over even ℓ if $F = 0$ or $F = 2$, and over odd ℓ if $F = 1$ or $F = 3$.

4.3 Unpolarized rate coefficients

Using the ionization rate coefficients obtained in the previous section, we can derive the unpolarized ionization rate coefficients $K_{\rm SS}^{\rm (th)}$, i.e. the rate coefficient for a laser-cooled sample of He* atoms where the magnetic substates of the atoms are evenly populated.

For an unpolarized sample of ^{4}He* atoms we obtain

$$K_{\rm SS,4He}^{\rm (th)} = \frac{1}{(2S_1+1)^2}\sum_S\sum_{M_S} {}^{(2S+1)}K = \tfrac{1}{9}\left[({}^1K) + 3({}^3K)\right] \tag{4.52}$$

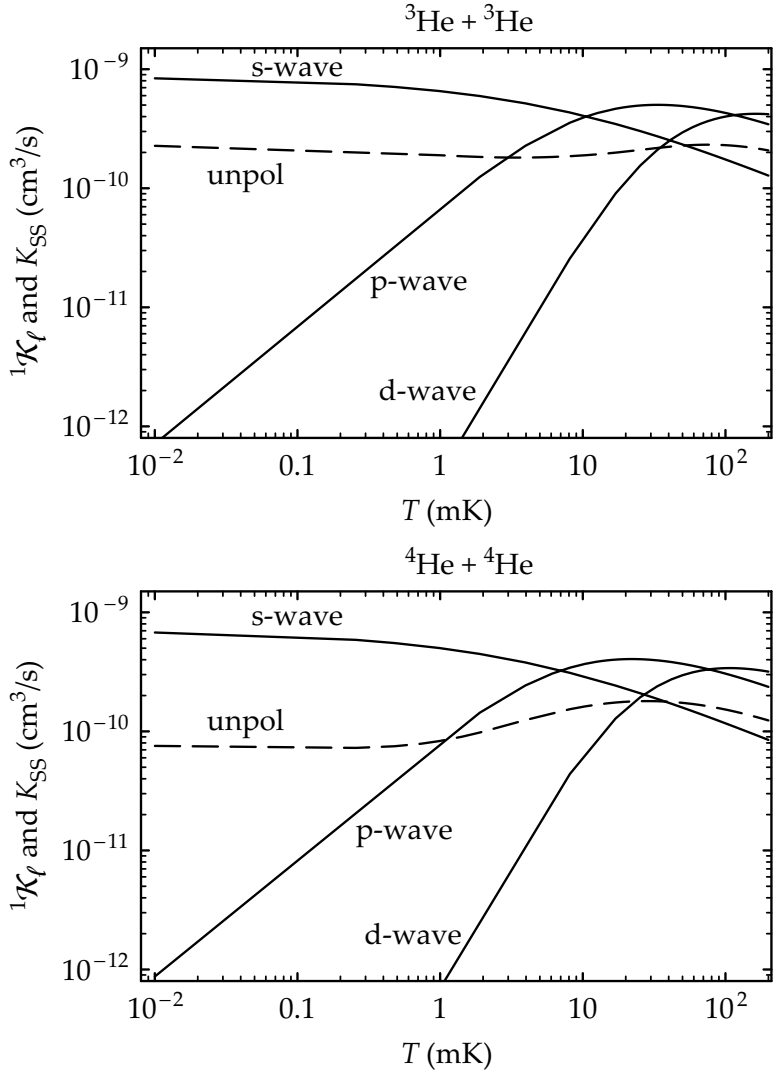

Figure 4.14. Partial wave ionization rate coefficients $^1\mathcal{K}_\ell$ and unpolarized rate coefficient $K_{SS}^{(th)}$ for ^{3}He* and ^{4}He*.

where ^1K and ^3K are given by Eqs. (4.30) and (4.31), respectively. For mK temperatures, only partial waves up to $\ell = 1$ have to be taken into account[15] and we obtain

$$K_{SS,^4He}^{(th)} \approx \tfrac{1}{9}\left[(^1\mathcal{K}_0) + 3(^3\mathcal{K}_1)\right], \tag{4.53}$$

where $^1\mathcal{K}_0$ and $^3\mathcal{K}_1$ are the partial wave ionization rate coefficients for ^{4}He*, calculated in Section 4.2.3 and displayed in Fig. 4.9.

In the case of ^{3}He*, we are interested in an unpolarized gas of atoms in the $F_1 = F_2 = \frac{3}{2}$ hyperfine level. The unpolarized rate coefficient is given by

$$K_{SS,^3He}^{(th)} = \frac{1}{(2F_1+1)^2}\sum_F \sum_{M_F} K(F_1F_2, F). \tag{4.54}$$

[15]For $T = 2$ mK, $K_1/K_0 = 0.34$ and $K_2/K_0 = 0.007$ for ^{4}He* and $K_1/K_0 = 0.22$ and $K_2/K_0 = 0.003$ for ^{3}He*.

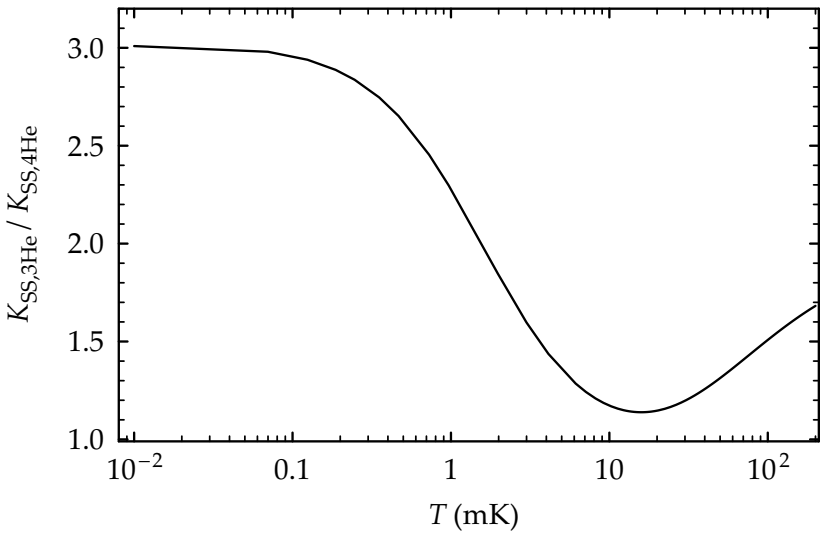

Figure 4.15. Ratio of unpolarized ionization rate coefficients $K^{(th)}_{SS,3He}/K^{(th)}_{SS,4He}$, including partial wave contributions up to $\ell = 2$.

Table 4.2. Comparison between various theoretical results.

	Ref.	T (μK)	$K^{(th)}_{SS}$	This work
^{4}He*	[126]	500	7.3×10^{-11}	7.5×10^{-11}
	[111]	1	1.0×10^{-10}	7.7×10^{-11}
	[111]	500	1.1×10^{-10}	7.5×10^{-11}
	[111]	1000	1.1×10^{-10}	8.3×10^{-11}
	[102]	500	2.2×10^{-10}	7.5×10^{-11}
^{3}He*	[102]	500	1.0×10^{-9}	2.0×10^{-10}

Taking into account only s-wave and p-wave contributions, we use Eqs. (4.48)–(4.51) to obtain

$$K^{(th)}_{SS,3He} \approx \tfrac{1}{16}\left[4(^1\mathcal{K}_0) + \tfrac{1}{3}(^3\mathcal{K}_0) + \tfrac{10}{9}(^1\mathcal{K}_1) + \tfrac{5}{3}(^3\mathcal{K}_1)\right], \tag{4.55}$$

where $^1\mathcal{K}_0$, $^3\mathcal{K}_0$, $^1\mathcal{K}_1$ and $^3\mathcal{K}_1$ are the partial wave ionization rate coefficients for ^{3}He*, calculated in Section 4.2.3 and displayed in Fig. 4.10. The ionization rate coefficients for an unpolarized sample of ^{3}He* atoms and ^{4}He* atoms are displayed in Fig. 4.14. It can be seen in Fig. 4.15, where the ratio of the unpolarized rate coefficients for the two isotopes is displayed, that unpolarized ^{3}He* atoms have a larger rate coefficient than unpolarized ^{4}He* atoms for temperatures between 10 μK and 100 mK.

In Table 4.2, we compare our model to the theoretical work reported in Refs. [102, 111, 126]. We see that our model agrees well with the results the detailed close-coupling theory of [111] and the simpler calculation of [126], but that there is a large discrepancy with the results of Kumakura and Morita [102]. However, this is not surprising, since their model does not account for quantum

reflection for s-wave scattering. As we have shown in Section 4.2.3, quantum reflection is significant and we estimate that the omission of this effect leads to rate coefficients that are too large by factor of about 2. Moreover, Kumakura and Morita assume that the evolution of the scattering states during the collision of two ^{3}He* atoms can be approximated by an adiabatic transition. Consequently, they apply the noncrossing rule [139] to derive the number of ionization channels for each partial wave ionization rate coefficient. As shown in 4.2.5, the system is well approximated by a diabatic transition and we estimate that the assumptions of an adiabatic transition leads to an unpolarized rate coefficient that is 50% too large. This would explain the difference in ratio $K^{(\mathrm{th})}_{\mathrm{SS,3He}}/K^{(\mathrm{th})}_{\mathrm{SS,4He}}$ between our model and the value reported by Kumakura and Morita.

At $T = 2$ mK, our model predicts

$$K^{(\mathrm{th})}_{\mathrm{SS,4He}} = 9.9 \times 10^{-11}\ \mathrm{cm}^3/\mathrm{s}, \tag{4.56}$$

$$K^{(\mathrm{th})}_{\mathrm{SS,3He}} = 1.8 \times 10^{-10}\ \mathrm{cm}^3/\mathrm{s}, \tag{4.57}$$

$$K^{(\mathrm{th})}_{\mathrm{SS,3He}}/K^{(\mathrm{th})}_{\mathrm{SS,4He}} = 1.8. \tag{4.58}$$

In Chapter 5, we report the experimental study of homonuclear ionizing collisions in laser-cooled samples of ^{3}He* atoms and ^{4}He* atoms at this temperature. There, we will use our model to analyze the measurements.

Chapter 5

Experimental ionization rates of laser-cooled metastable helium isotopes

Magneto-optical traps (MOTs) have been deployed with great success in the experimental study of inelastic collisions at mK temperatures [210, 211]. As magneto-optical trapping forces have a limited capture velocity and only act on particles that are resonantly excited by the trapping light, reaction products from inelastic collisions are generally not confined in the trap. Measurement of the consequent trap loss is an excellent tool to study the collision processes at mK temperatures, as loss rates can be accurately determined, either by monitoring the decreasing atom number in the MOT (if the loading of atoms is stopped), or by detection of the flux of reaction products escaping from the trap in steady state.

Experiments have shown [13, 23, 102, 103, 126, 127, 149, 196] that trap loss from magneto-optically trapped He* samples is dominated (in a good vacuum) by light-assisted ionizing collisions, where colliding atom pairs are excited at large internuclear distance to an attractive resonant dipole-dipole potential [191, 210, 211] that asymptotically connects to the atom-pair state $2\,^3\mathrm{S} + 2\,^3\mathrm{P}_2$.[1] Light-assisted collisions are not suited to investigate effects of quantum threshold behavior and quantum statistical symmetry requirements, as the dynamics of these collisions is very complex [191, 210, 211] and the number of partial waves contributing in a collision is relatively large.[2] The number of contributing partial waves is larger compared to collisions in the absence of trapping light (partial waves up to $\ell = 6$ contribute in light-assisted collisions in He* samples with

[1] For ^{3}He* samples, the corresponding atom-pair state is given by $2\,^3\mathrm{S}\,(F = \frac{3}{2}) + 2\,^3\mathrm{P}\,(F' = \frac{5}{2})$.

[2] On the other hand, light-assisted collisions provide a wealth of information about (for instance) molecular structure in studies concerning photoassociation spectroscopy [80, 113].

a temperature $T = 0.5$ mK [102]), because the resonant dipole-dipole interaction with its long range lowers the centrifugal barriers.

In Chapter 4, it is predicted that quantum threshold and quantum statistical effects are clearly observable for collisions where ionization is not preceded by optical excitation. As these collisions contribute very little to the total loss rate in a MOT, the corresponding ionization rate coefficients cannot be obtained from trap loss measurements. However, an accurate determination of these rate coefficients is possible from comparative measurements (with an electron-multiplier detector) of ion production rates in the absence and presence of the trapping light, a method applied for the first time by Bardou *et al.* [13].

In this chapter, we present an experimental investigation of the isotopic difference in the ionization rates associated with cold collisions of He* atoms in the absence of light fields. We present measurements of trap loss due to light-assisted collisions and comparative ion production rate measurements in the absence and presence of trapping light. From these measurements we determine the ionization rate coefficients in the absence of light fields. We have performed the measurements on the magneto-optically trapped samples of either ^{3}He* or ^{4}He* atoms that are described in Chapter 2. The isotopic difference in the rate coefficients is interpreted with the theoretical model of Chapter 4.

In Section 5.1, we distinguish between linear and quadratic trap loss mechanisms and show that ionization rates can be deduced from trap loss measurements if the contribution of ionizing mechanisms to trap loss is determined. In Section 5.2, we present an overview of trap loss mechanisms occurring in our He* samples. The loss mechanisms are subdivided into ionizing and non-ionizing contributions, and estimates of the respective ionization and trap loss rates are given. Section 5.3 presents trap loss measurements on magneto-optically trapped samples of ^{3}He* and ^{4}He* atoms, and the subsequent determination of the ionization rate coefficients associated with light-assisted collisions. In Section 5.4, we present the experimental determination of the ionization rate coefficients $K_{\mathrm{SS,3He}}$ and $K_{\mathrm{SS,4He}}$ in the absence of the trapping light. The rate coefficients are corrected for polarization of the magnetic substate distribution in Section 5.5. The analysis of the results and comparison with the theoretical model is presented in Section 5.6.

5.1 Trap loss and ionization

For magneto-optically trapped He* samples, the time-evolution of the number of trapped atoms N can be described by the phenomenological equation [13, 23]

$$\frac{\mathrm{d}N(t)}{\mathrm{d}t} = L - \alpha N(t) - \beta \iiint n^2(\boldsymbol{r}, t)\, \mathrm{d}^3 r, \tag{5.1}$$

where t denotes time. Writing down this differential equation, we assume that $N(t)$ is controlled by three simultaneously occurring processes, corresponding to the three terms on the right-hand side of the equation. The first term is a

constant loading rate L, representing the capture of atoms from the decelerated atomic beam into the MOT. The second and third term are the linear trap loss rate and quadratic trap loss rate, respectively, defined in terms of the local atomic density of the sample $n(\boldsymbol{r}, t)$, if $L = 0$, by

$$\frac{\mathrm{d}n(\boldsymbol{r}, t)}{\mathrm{d}t} = -\alpha\, n(\boldsymbol{r}, t) - \beta\, n^2(\boldsymbol{r}, t). \tag{5.2}$$

The nomenclature of the loss rate terms refers to their proportionality to density $n(\boldsymbol{r}, t)$ and density squared $n^2(\boldsymbol{r}, t)$. Analogously, the proportionality constants, α and β, are referred to as the linear and quadratic loss rate coefficient, respectively.

Both linear and quadratic trap loss are caused by a number of different loss mechanisms, that can be subdivided into ionization mechanisms and mechanisms where atoms are lost without the formation of ions. The ion production (not necessarily He^+ or He_2^+) associated with ionization mechanisms can be expressed as an ionization rate,

$$\frac{\mathrm{d}N_{\mathrm{ion}}(t)}{\mathrm{d}t} = \epsilon_a \alpha N(t) + \frac{\epsilon_b \beta}{2} \iiint n^2(\boldsymbol{r}, t)\, \mathrm{d}^3 r, \tag{5.3}$$

where ϵ_a and ϵ_b are the weights of ionization mechanisms in linear and quadratic trap loss, respectively. The quadratic ionization rate is half of the ionizing quadratic trap loss rate, as a single ion is formed for every pair of colliding He* atoms that is lost from the trap.

Ionization rates in He* samples can be measured accurately with an MCP detector. If the ionization weights associated with a He* sample (ϵ_a and ϵ_b) have been determined, ionization rate measurements can be used to study trap loss and to determine the ionization rate coefficient K_{SS} in the absence of trapping light. Section 5.2 presents an overview of the linear and quadratic trap loss mechanisms occurring in the He* samples, subdivided into ionizing and non-ionizing processes. The ionization weights ϵ_a and ϵ_b are determined from estimates of ionization and trap loss rates associated with linear and quadratic trap loss mechanisms, respectively.

5.2 Overview of trap loss mechanisms

For the He* samples studied in this chapter, only *collisional* loss mechanisms give rise to significant ionization and trap loss rates.[3] Quadratic trap loss is determined by collisions between trapped He* atoms, while linear trap loss results from collision with particles traversing the trapping volume, such as background gas particles and He atoms from the atomic beam. If cross section data are available for the appropriate collision energy, ionization and trap loss rates can be calculated from the atomic density in the trapped sample, the

[3] As we are using trapping light with a wavelength $\lambda = 1083$ nm, photoionization of trapped He* atoms can be neglected. In Chapter 3, we have shown that photoionization leads to significant linear trap loss if trapping light with $\lambda = 389$ nm is used.

Table 5.1. Total cross section σ and trap loss rate for collisions of trapped ^{4}He* atoms with ^{4}He(1 ^{1}S) atoms from the atomic beam ($E_r = 4.9$ meV) and background gas ($E_r = 16.5$ meV). For a beam with flux F, the loss rate is given by σF, whereas background gas with density $\tilde{n}$ give rise to a loss rate $\sigma \bar{v}_r \tilde{n}$. Here, $\bar{v}_r = (2E_r/\mu)^{1/2}$ is the mean relative velocity of the colliding atoms and $\mu = m/2$ their reduced mass, with m the mass of the ^{4}He atom.

Reagent	E_r (meV)	σ (10^{-16} cm^2)	F (cm^{-2} s^{-1})	$\tilde{n}$ (cm^{-3})	σF or $\sigma \bar{v}_r \tilde{n}$ (s^{-1})
^{4}He	4.9	200[a]	10^{14}	—	~ 2
^{4}He	16.5	140[b]	—	1×10^7	0.02

[a] Vrinceanu *et al.* [207].

[b] Mastwijk [125, Chapter 5] and Rothe *et al.* [168].

background gas density and the atomic beam flux. For all relevant collision processes involving ^{4}He* atoms, cross section data can be found in literature[4] and ionization and trap loss rates can be calculated. This is not possible for ^{3}He* samples, as the number of reported collision studies on the fermionic isotope is very limited. However, relevant cross sections are not expected to show a large isotopic dependence and, after having estimated loss rates from ^{4}He* samples, we will map out trap loss from ^{3}He* samples assuming similar cross sections for both isotopes.

5.2.1 Collisions in ^{4}He* samples

For ^{4}He* samples, linear trap loss is dominated by collisions with ^{4}He atoms in the 1 ^{1}S ground state from the atomic beam. At the collision energy $E_r \approx 4.9$ meV, Penning or associative ionization is forbidden by energy conservation[5] and the cross section associated with these non-ionizing collisions has a value of $\sigma = 200 \times 10^{-16}$ cm^2 [207]. The beam of ground state He atoms has an estimated intensity on the order of 10^{19} s^{-1} sr^{-1}, corresponding to a flux on the order of $F = 10^{14}$ cm^{-2} s^{-1} at the position of the trapped sample, i.e. a distance of 3.7 m in front of the source. The consequent trap loss rate (per trapped ^{4}He* atom) can be calculated easily as $\sigma F \approx 2$ s^{-1}. For convenience, the calculation is also presented in Table 5.1.[6]

At the low pressure in the trapping chamber of 7.0×10^{-10} mbar, trap loss due to collisions with background gas particles is relatively small. The background gas consists mainly of ^{4}He atoms, with a corresponding partial pressure

[4] An overview of collision studies with ^{4}He* atoms can be found in [185, 227].

[5] At thermal collision energies, associative ionization (or the Hornbeck-Molnar process [85]), $\mathrm{He}(n\,^{2S+1}L) + \mathrm{He}(1\,^1\mathrm{S}) \rightarrow \mathrm{He}_2^+ + e$, only occurs if the excited atom $\mathrm{He}(n\,^{2S+1}L)$ is in a state that is higher-lying than 3 ^{1}S [212].

[6] In contrast to other work [23, 79, 149, 196], the beam of He* atoms is not separated from the beam of ground state He atoms.

Table 5.2. Ionization cross section σ and ionization rate $\sigma\bar{v}_r\tilde{n}$ for collisions between trapped ^{4}He* atoms and thermal background gas molecules. The ionization rates are upper limits, as they are obtained assuming a background gas density $\tilde{n} = 1.2 \times 10^6$ cm^{-3}, corresponding to a partial pressure $\tilde{p} = \tilde{n}k_B T = 5 \times 10^{-11}$ mbar, the total partial pressure for all background gas constituents other than ground state helium. Here, $\bar{v}_r = (2E_r/\mu)^{1/2}$ is the mean relative velocity of the colliding atoms and μ their reduced mass.

Reagent	E_r (meV)	σ (10^{-16} cm^2)	$\sigma\bar{v}_r\tilde{n}$ (s^{-1})
H_2	22	0.1[a]	2×10^{-4}
H_2O	6.0	131[b]	9×10^{-4}
O_2	4.7	8[c]	4×10^{-5}
N_2	4.1	2[d]	1×10^{-5}

[a] Martin *et al.* [123].

[b] Mastwijk [125, Chapter 5]; calculated from the relation $\sigma = k/\bar{v}_r$, where $\bar{v}_r = (8k_B T/\pi\mu)^{1/2}$ is the mean relative velocity of a gas at temperature T.

[c] Parr *et al.* [142].

[d] Yamazaki *et al.* [222].

$\tilde{p} = 6.5 \times 10^{-10}$ mbar. Other constituents, presumably H_2O and H_2 (and less likely N_2 and O_2), contribute a partial pressure of 5×10^{-11} mbar. In Table 5.1 the trap loss rate associated with collisions with background ^{4}He atoms is calculated from the background gas density $\tilde{n} = \tilde{p}/k_B T$ and the mean collision velocity $\bar{v}_r = (2E_r/\mu)^{1/2}$, with $E_r \approx 16.5$ meV. The resulting rate of 0.02 s^{-1} is considerably larger than the trap loss rate from collisions with background gas molecules. The cross sections for collisions of trapped ^{4}He* with H_2O, H_2, N_2 and O_2 are all smaller than 300×10^{-16} cm^2 [125, Chapter 5] and the corresponding contribution is at most 3×10^{-3} s^{-1}. As Penning ionization is an important reaction mechanism in these collisions, their contribution to the ionization rate is of more concern.

As shown in Table 5.2, ionization cross sections for collisions of ^{4}He* with background gas molecules are all relatively small, except for collisions with H_2O molecules.[7] As the background gas composition is unknown, we cannot make an accurate estimate of the linear ionization rate. However, we obtain an upper limit of 9×10^{-4} s^{-1} assuming that, next to ^{4}He atoms, only H_2O molecules are present. Ionization rates for various background gas compositions are presented in Table 5.2.

Another source of linear ionization is formed by collisions of trapped ^{4}He* atoms with ^{4}He* atoms from the atomic beam. As discussed in Chapter 2, the capture velocity of the Zeeman slower is 1350 m/s and ^{4}He* atoms with a larger

[7] The large cross section results from a large attractive force between ^{4}He* and H_2O, a consequence of the permanent dipole moment of the H_2O molecule [125, Chapter 2].

Table 5.3. Ionization cross section σ and trap loss rate $\sigma\bar{v}_r\tilde{n}$ for collisions between trapped ^{4}He* atoms and ^{4}He* atoms from the atomic beam. About half of the atoms emerging from the source have a longitudinal velocity $v < 1350$ m/s and are decelerated in the Zeeman slower to a velocity around 50 m/s. Collisions with the nonslowed beam are dominant.

Reagent	v_{beam} (m/s)	E_r (meV)	σ (10^{-16} cm^2)	F (cm^{-2} s^{-1})	σF (s^{-1})
^{4}He*	1586	6.5	181[a]	4×10^{11}[b]	7×10^{-3}
^{4}He*	50	0.0064	1160[c]	8×10^{9}[d]	9×10^{-4}

[a] Obtained from $\sigma = \sigma_1(E_1/E_r)^\alpha$, where $E_1 = 1$ meV, $\sigma_1 = 318 \times 10^{-16}$ cm^2 and $\alpha = 0.3$. Müller *et al.* [136] have shown that the cross section for ^{4}He*–^{4}He* collisions satisfies this (semi-classical) energy dependence for collision energies 0.1 meV $< E_r <$ 100 meV.

[b] Rooijakkers [163] reports a maximum flux after collimation of 10^{12} s^{-1} cm^{-2}. Correcting for the source current used here and the capture of 50% of the flux in the Zeeman slower, we obtain a maximum flux of nonslowed atoms travelling through the trapped sample of 4×10^{11} cm^{-2} s^{-1}.

[c] Venturi *et al.* [204]; calculated from the relation $\sigma = k/\bar{v}_r$, where $\bar{v}_r = (8k_BT/\pi\mu)^{1/2}$ is the mean relative velocity of a gas a temperature T.

[d] Simulations of the Zeeman deceleration process have shown that, due to transverse heating, the flux of slowed atoms is smaller by a factor of 50, compared to the flux of nonslowed atoms.

velocity are not decelerated. At the position of the trapped cloud, this results in a metastable beam with a slowed and a non-slowed part. At the source current used, the velocity distribution of the metastable beam is such that about half of the atoms are captured in the Zeeman slower. These atoms are slowed to a velocity of 50 m/s. The remaining atoms form the non-slowed beam, that traverses the trapped sample with a mean velocity of 1586 m/s. Based on the source current used in our setup, the central flux of ^{4}He* atoms in the non-slowed beam is estimated to be 4×10^{11} cm^{-2} s^{-1}. Calculations show that the flux in the slowed beam is smaller by a factor of 50 due to transverse heating of the atomic beam in the deceleration process. To estimate the ionization occurring in the capture process of decelerated He* atoms from the beam into the MOT, we assume that the decelerated atomic beam travels through the trapped sample prior to the capture process. Using ionization cross sections from literature, we calculate the ionization rates for collisions with non-slowed ($v_{\text{beam}} = 1587$ m/s) and slowed ($v_{\text{beam}} = 50$ m/s) atoms in Table 5.3.

Linear ionization is determined by collisions with slowed and non-slowed atoms in the metastable beam and by collisions with background gas molecules. The rates add up to an upper limit of 8.8×10^{-3} s^{-1}. The corresponding trap loss rate is small compared to the total linear trap loss rate of ~ 2 s^{-1}, that is dominated by collisions with ground state ^{4}He atoms from the atomic beam. Calculating the ratio of the loss rates, we determine an ionization weight $\epsilon_a \lesssim 10^{-3}$.

Table 5.4. Ionization cross section σ and ionization rate for collisions between magneto-optically-trapped ^{4}He* atoms in the presence and absence of near-resonant light with a wavelength $\lambda = 1083$ nm. The density in the trapped samples $n(\boldsymbol{r})$ and the trapped atom number N are obtained from Table 5.5.

Reagent	E_r (μeV)	σ (10^{-12} cm^2)	$(\sigma\bar{v}_\mathrm{r}/N)\int n^2(\boldsymbol{r})\,\mathrm{d}^3r^a$ (s^{-1})
^{4}He* + light	0.01	16[b]	4
^{4}He*	0.01	0.4[b]	0.1

[a] For samples with a Gaussian density distribution, as given by Eq. (5.5), the ionization rate can be written $\beta n_0/4\sqrt{2}$ in the presence of trapping light and $Kn_0/2\sqrt{2}$ in the absence of trapping light.

[b] Tol *et al.* [196]; calculated from the relation $\sigma = k/\bar{v}_\mathrm{r}$, where $\bar{v}_\mathrm{r} = (8k_\mathrm{B}T/\pi\mu)^{1/2}$ is the mean relative velocity of a gas a temperature T.

For magneto-optically trapped samples of ^{4}He* atoms similar to those studied here, it has been shown [77, 196] that quadratic loss is dominated by ionizing light-assisted collisions. Ionizing quadratic trap loss makes up for 97.5% of the total quadratic loss, while escape of fast ^{4}He* atoms is responsible for the remaining 2.5% of the loss events, either through fine-structure-changing collisions (1.9%) or (presumably) radiative escape (0.6%) [77, Chapter 5] [99]. This means that in the presence of trapping light $\epsilon_b \approx 1$. The ionization cross section for light-assisted collisions is exceptionally large due to the optical excitation of the colliding atom pair to long-range dipole-dipole potentials [210, 211]. For the trapping light intensity and detuning used in the experiments, the ionization cross section is 16×10^{-12} cm^2. Using the number of the trapped atoms and the density profile of our samples (see Table 5.5), we obtain an ionization rate of 4 s^{-1}, as shown in Table 5.4. As two atoms are lost from the MOT for every produced ion, a typical quadratic trap loss rate is twice as large, 8 s^{-1}.

Also in the absence of trapping light, ionizing collisions dominate quadratic trap loss. As shown in Table 5.4, the cross section is smaller by a factor of 40, yielding an ionization rate of 0.1 s^{-1}. The corresponding loss rate is 0.2 s^{-1}. As fine-structure-changing collisions and radiative escape do not play a role in the absence of trapping light, virtually all trap loss is due to Penning ionization and ionization weight ϵ_b is again very close to one.

5.2.2 Collisions in ^{3}He* samples

For ^{3}He* samples, trap loss is governed by the same trap loss mechanisms as for ^{4}He* samples, but a similar calculation of trap loss and ionization rates is not possible, as collision studies on ^{3}He* are rare [185, 227] and cross section data available in literature are very limited. However, relevant cross sections are not expected to show a large isotopic dependence and we will assume the same order of magnitude for both isotopes. In the following, we only discuss

trap loss mechanisms yielding different loss rates for both isotopes and show that differences in ionization weights ϵ_a and ϵ_b are negligible.

As the velocity of ^{3}He* atoms from the source is larger and therefore, the nonslowed portion is larger (90%, see Chapter 2), the ionization rate associated with linear trap loss is expected to be almost twice as large. However, it is still negligible compared to ionization rates from light-assisted collisions and, as the ionization cross section for collisions in the absence of light fields is expected to be about twice as large compared to ^{4}He (Chapter 4), the ionizing linear trap loss is small compared to that in the absence of a light field as well.

For ^{3}He* samples, we assume an analogous domination of the quadratic trap loss by ionizing light-assisted collisions. Due to its smaller masses, ^{3}He atoms are accelerated towards each other at a larger rate, so that the probability for spontaneous decay at internuclear distances $R \gtrsim 10\, a_0$ decreases compared to light-assisted collisions of two ^{4}He* atoms. The smaller decay probability results in an increase of fine-structure-changing collisions at the expense of radiative escape.[8] However, the total contribution of the two non-ionizing processes to trap loss is expected to be approximately the same, so that ionizing light-assisted collisions dominate quadratic trap loss for ^{3}He* samples. Furthermore, hyperfine changing collisions do not contribute to quadratic trap loss as these inelastic collisions are forbidden by energy conservation. Trapped ^{3}He* atoms are in the lower $F = \frac{3}{2}$ hyperfine level and the endothermal hyperfine changing collision requires an energy larger than the hyperfine splitting $E_{\mathrm{hf}} = 28$ μeV, corresponding to a temperature $E_{\mathrm{hf}}/\frac{3}{2}k_{\mathrm{B}} = 0.2$ K.

5.2.3 Ionization rate

Reviewing the obtained loss rates, we can draw the same conclusions for both isotopes. Linear trap loss is dominated by collisions of trapped atoms with ground state atoms from the atomic beam, giving rise to a trap loss rate on the order of 2 s^{-1}. Linear ionization is the result of collisions with slowed and nonslowed atoms from the atomic beam, and collisions with background molecules, yielding a rate of about 1×10^{-2} s^{-1}. This ionization rate is small compared to the quadratic ionization rates associated with ionizing collisions of trapped atoms in the presence and absence of trapping light. Therefore, we can set, to a good approximation, $\epsilon_a = 0$ and $\epsilon_b = 1$, both in the presence and absence of trapping light, for both isotopes. Consequently, the ionization rate of Eq. (5.3) can be approximated by

$$\frac{\mathrm{d}N_{\mathrm{ion}}(t)}{\mathrm{d}t} \approx \frac{\beta}{2} \iiint n^2(\boldsymbol{r}, t)\, \mathrm{d}^3 r. \tag{5.4}$$

Finally, quadratic trap loss is dominated by quadratic ionization. For ^{4}He* samples, the corresponding rate is 8 s^{-1} in the presence of trapping light, and 0.2 s^{-1} in the absence of trapping light. For ^{3}He* samples, the rates are expected to be larger as a result of the different quantum statistical symmetry.

[8] The reasoning is based on the model for light-assisted collisions developed by Gallagher and Pritchard [65].

5.3 Ionization rates for light-assisted collisions

We have determined the ionization rate coefficient $\beta/2$ for light-assisted collisions of ^{3}He* or ^{4}He* atoms from trap loss experiments, where the decay of the trapped atom number in the MOT is monitored when the loading of atoms to the MOT is abruptly stopped [210, 211]. The loss rate coefficients α and β determine the exact shape of the decay and are obtained via curve fitting. For magneto-optically trapped samples of alkali atoms, trap loss experiments are usually performed by monitoring the fluorescence of trapped atoms, as the fluorescence light intensity is proportional to the trapped atom number [197]. However, we can make use of Eq. (5.4), that gives the relation between ionization rate $\mathrm{d}N_{\mathrm{ion}}(t)/\mathrm{d}t$ and the density distribution of the trapped sample $n(\boldsymbol{r},t)$, and determine the loss rate coefficients using the unshielded MCP detector (see Chapter 2). As the negative high voltage on the front plate of the detector is exposed to the sample, positive ions are attracted to the detector, producing a current signal that is proportional to the ionization rate. The current signal is converted to voltage signal $\varphi(t)$ and monitored with a Tektronix TDS 210 digital oscilloscope.

As shown in Chapter 2, the magneto-optically trapped He* samples have a Gaussian density distribution, that can be written as

$$n(x,y,z,t) = n_0(t)\,\exp\left(-\frac{x^2}{2\sigma_x^2}-\frac{y^2}{2\sigma_y^2}-\frac{z^2}{2\sigma_z^2}\right), \tag{5.5}$$

with $n_0(t)$ the time-dependent density in the center ($x=y=z=0$) of the sample, and σ_x, σ_y and σ_z the radii of the three-dimensional Gaussian distribution. Introducing the effective volume $V=(2\pi)^{3/2}\sigma_x\sigma_y\sigma_z$, such that $n_0(t)=N(t)/V$, the evolution of central density $n_0(t)$ can be obtained from Eq. (5.1) as

$$\frac{\mathrm{d}n_0(t)}{\mathrm{d}t} = \frac{L}{V} - \alpha n_0(t) - \frac{\beta}{2\sqrt{2}} n_0^2(t). \tag{5.6}$$

If the loading of atoms into the MOT is abruptly stopped, the central density shows a decay that is proportional to the decay of the trapped atom number. Solving Eq. (5.6) with $L=0$, an expression for the decay is obtained,

$$n_0(t) = \frac{n_0(0)}{\left(1+\dfrac{\beta n_0(0)}{2\sqrt{2}\alpha}\right)\exp(\alpha t) - \dfrac{\beta n_0(0)}{2\sqrt{2}\alpha}}. \tag{5.7}$$

The current signal measured with the MCP is proportional to the ionization rate of Eq. (5.4). For a Gaussian density distribution, the rate can be written as $\mathrm{d}N_{\mathrm{ion}}/\mathrm{d}t = V\beta n_0^2/4\sqrt{2}$, so that the current signal, converted into a voltage, can be written as

$$\varphi(t) = eR_{\mathrm{eff}}\frac{\beta}{4\sqrt{2}}\,n_0^2(t) + \varphi_{\mathrm{bgr}}, \tag{5.8}$$

where e is the electron charge and R_{eff} is an effective resistance. Substitution of Eq. (5.7) into Eq. (5.8) gives an expression for the decaying ionization signal, from which α and $\beta n_0(0)$ can be obtained by fitting to the measured decay trace.

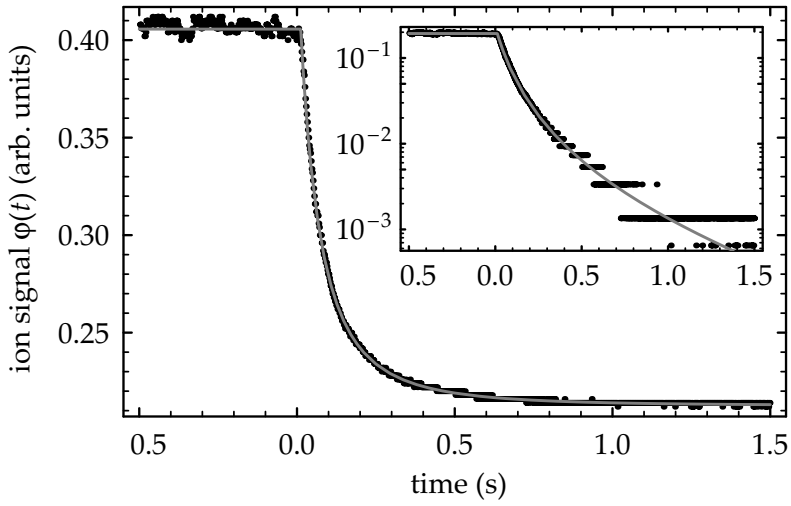

Figure 5.1. Ionization signal for a trap loss measurement on a ^{3}He* sample. At $t = 0$, the input of atoms to the MOT is stopped abruptly. The rapid decay of the ionization signal (black dots) is non-exponential, as shown in the inset. Fitting the signal to our model (grey line) yields trap loss rates $\beta n_0(0) = 20\ \mathrm{s}^{-1}$ and $\alpha = 0.7\ \mathrm{s}^{-1}$.

The loading of atoms into the MOT is stopped by blocking the Zeeman slowing light with the acousto-optic modulator used for frequency detuning the slowing light from the atomic transition. Ionization rate decays are averaged four times using the digital oscilloscope. It has been verified that the variations in the central density are small enough that an averaged decay curve allows an accurate determination of loss rates α and $\beta n_0(0)$. An example of an averaged ionization trace and a fit is displayed in Figure 5.1.

We have performed trap loss measurements on the ^{3}He* and ^{4}He* samples discussed in Chapter 2. Loss rates α and $\beta n_0(0)$ are determined in the fitting procedure. The central density in the samples $n_0(0)$ is derived from absorption imaging, so that the loss rate coefficient β can be determined. The resulting rate coefficients, α and β, are presented[9] in Table 5.5, along with other experimental results, including numbers discussed in Chapter 2.

The linear loss rate coefficients are on the order of 2 s^{-1}, as estimated for linear trap loss due to collisions with ground state atoms from the atomic beam. Reversing the reasoning of Section 5.2.1, we can determine the intensity of the beam of ground state atoms. Using the total cross section $\sigma = 200 \times 10^{-16}\ \mathrm{cm}^2$ for collisions between trapped ^{4}He* atoms and ground state ^{4}He atoms from the atomic beam, and the distance between source and trapped sample, we calculate that the loss rate coefficient $\alpha = 0.6(3)\ \mathrm{s}^{-1}$ corresponds to an intensity of $4 \times 10^{18}\ \mathrm{s}^{-1}\ \mathrm{sr}^{-1}$. Rooijakkers et al. [163] report a maximum intensity of ^{4}He* atoms of $5 \times 10^{14}\ \mathrm{s}^{-1}\ \mathrm{sr}^{-1}$. Correcting for the source current here, we obtain an intensity of $4 \times 10^{14}\ \mathrm{s}^{-1}\ \mathrm{sr}^{-1}$ and a fraction of ^{4}He* atoms in the atomic beam of 10^{-4}.

The quadratic loss rate coefficient for ^{3}He*, $\beta_{^3\mathrm{He}} = 5.5(8) \times 10^{-9}\ \mathrm{cm}^3/\mathrm{s}$,

[9] Throughout this chapter, presented uncertainties correspond to one standard deviation.

Table 5.5. Characteristic parameters of the magneto-optically trapped He* samples. Experimental errors correspond to one standard deviation.

	^{3}He*	^{4}He*
T (mK)	2.0(3)	1.9(1)
N (−)	$2.6(9) \times 10^8$	$3.7(5) \times 10^8$
n_0 (cm^{-3})	$3.0(5) \times 10^9$	$4.4(4) \times 10^9$
α (s^{-1})	0.8(2)	0.6(3)
β (cm^3/s)	$5.5(8) \times 10^{-9}$	$3.3(7) \times 10^{-9}$
K_{SS} (cm^3/s)	$1.8(3) \times 10^{-10}$	$8(2) \times 10^{-11}$
$K_{SS}^{(eq)}$ (cm^3/s)	$1.9(3) \times 10^{-10}$	$1.0(2) \times 10^{-10}$

is almost twice as large as the loss rate coefficient for ^{4}He* samples, $\beta_{4He} = 3.3(7) \times 10^{-9}$ cm^3/s, which is in good agreement with the loss rate coefficient determined for a similar ^{4}He* sample in [196]. Kumakura and Morita [102] have pointed out that the isotopic difference stems from a difference in the relative number of ionization channels, opened up by the lowering of centrifugal barriers by the long-range, resonant dipole-dipole interaction. Quantum statistical symmetry requirements play a role for these collisions, but the effects are washed out, as the number of participating partial waves is much larger than one. However, with an additional measurement, we can determine ionization rate coefficients in the absence of trapping light, where these quantum statistical effects are not obscured, as predicted in Chapter 4.

5.4 Ionization in the absence of trapping light

Collisions where ionization is not preceded by absorption of trapping light contribute little to the ionization rate in magneto-optically trapped He* samples. However, the corresponding ionization rate coefficients can be determined from a comparative measurement of the ionization rate in the presence and absence of trapping light, a method applied for the first time by Bardou *et al.* [13]. During a short time interval of 100 µs, the trapping and slowing light is blocked using the acousto-optical modulators used for detuning of the frequencies from the atomic transition. With the trapping light present, the observed ionization signal

$$\varphi_{on}(t) = eR_{eff}\frac{\beta}{4\sqrt{2}}n_0^2(0) + \varphi_{bgr} \tag{5.9}$$

is relatively large. During the time interval where the trapping light is absent, the ionization rate is much smaller, as it is determined by collisions between either ^{4}He*(2 ^{3}S) or ^{3}He*(2 ^{3}S, $F = \frac{3}{2}$) atoms. Introducing the ionization rate coefficient in the absence of trapping light, K_{SS}, the ionization signal can be

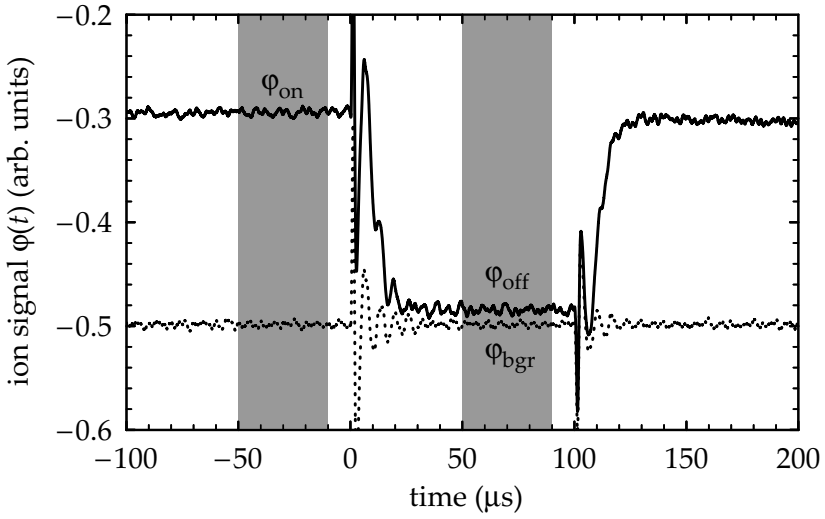

Figure 5.2. Ionization rates in the presence and absence of trapping (and slowing) light. The signals are averaged over 40 μs time intervals indicated by the shaded areas to obtain $(\bar{\varphi}_{\mathrm{on}} - \bar{\varphi}_{\mathrm{bgr}})$ and $(\bar{\varphi}_{\mathrm{off}} - \bar{\varphi}_{\mathrm{bgr}})$.

written as

$$\varphi_{\mathrm{off}}(t) = eR_{\mathrm{eff}}\frac{K_{\mathrm{SS}}}{2\sqrt{2}}n_0^2(0) + \varphi_{\mathrm{bgr}}. \tag{5.10}$$

Blocking the trapping and slowing light every 200 ms for 100 μs, the ionization signal is averaged 256 times using a Tektronix TDS 3032B digital oscilloscope. The measurement is repeated with the atomic beam blocked to obtain the (constant) background ionization signal $\varphi_{\mathrm{bgr}}(t)$, including an offset originating from the MCP signal amplifier.

Examples of average ionization signals are displayed in Figure 5.2. To obtain $(\bar{\varphi}_{\mathrm{on}} - \bar{\varphi}_{\mathrm{bgr}})$ and $(\bar{\varphi}_{\mathrm{off}} - \bar{\varphi}_{\mathrm{bgr}})$, the average of signals $\varphi_{\mathrm{on}}(t)$, $\varphi_{\mathrm{off}}(t)$ and $\varphi_{\mathrm{bgr}}(t)$ over 40 μs time intervals is determined, as indicated in Figure 5.2 . The mean values are used to derive the ionization rate coefficient K_{SS} as

$$\frac{\bar{\varphi}_{\mathrm{on}} - \bar{\varphi}_{\mathrm{bgr}}}{\bar{\varphi}_{\mathrm{off}} - \bar{\varphi}_{\mathrm{bgr}}} = \frac{\beta}{2K_{\mathrm{SS}}}. \tag{5.11}$$

The ratio of the ionization signals in the presence and absence of trapping light equals the ratio the ionization rate coefficients $\beta/2$ and K_{SS}

Although the atoms are not confined with the trapping light absent, the expansion of the trapped He* sample during 100 μs is insignificant and can be neglected if the duty cycle of the experiment is chosen sufficiently long. As the ionization signal in the presence of the trapping light is assumed to correspond to the ionization rate coefficient $\beta/2$ as derived from the trap loss measurement described in Section 5.3, it is checked that switching the light with a period of 200 ms does not influence the trapped sample.

Performing extensive comparative ionization rate measurements on our He* samples, we have determined ionization rate coefficients $K_{\mathrm{SS,3He}} = 1.8\,(3) \times 10^{-10}$ cm^3/s and $K_{\mathrm{SS,4He}} = 8\,(2) \times 10^{-11}$ cm^3/s (see also Table 5.5). Clearly, the

ionizing rate coefficient for ^{3}He* samples is larger than the coefficient for ^{4}He* samples. As shown by Herschbach *et al.* [79], the rate coefficients measured depend on parameters of the MOT and must be corrected for the polarization in the distribution over magnetic substates that is impressed on the He* samples by optical pumping. The corrected rate coefficients can be compared with the theoretical model of Chapter 4, that assumes an equal distribution over magnetic substates.

5.5 Polarization effects

In a MOT, optical pumping processes cause the magnetic substate distribution to deviate from a uniform distribution, with the stretched substates slightly overpopulated. In these partially polarized samples, quadratic ionization rates are smaller as compared with unpolarized samples. Calculating the substate distribution, a correction is derived for the rate coefficients $K_{\rm SS}$ obtained in Section 5.4.

Following the approach of [79], the process of optical pumping in a trapped sample is described using a rate equation model. Starting from the intensity and detuning of the trapping light, and an expression for the quadrupole magnetic field, rate equations are formulated and subsequently solved to obtain the steady state substate population in the sample. In these calculations we take into account that the intensities of the trapping beams are not balanced and that (consequently) the trapped sample is not exactly centered on the zero point of the magnetic field. The steady-state population P_M satisfies $\sum_M P_M = 1$, where M is the azimuthal quantum number.

For partially polarized ^{4}He* samples, the ionization rate coefficient $K_{\rm SS}$ can be corrected to obtain the rate coefficient for an unpolarized sample,

$$K^{\rm (eq)}_{\rm SS,4He} = K_{\rm SS,4He} \left\langle 3P_0^2 + 6P_{-1}P_1 \right\rangle , \tag{5.12}$$

where the expression between brackets is averaged over the trapped sample, weighted by the local density. The expression is obtained by projecting a statistical mixture of substates, given by (P_{-1}, P_0, P_1), onto the quasi-molecular state

$$|^1\Sigma_{\rm g}^+\rangle = \sqrt{\tfrac{1}{3}}\,\left(|-1;+1\rangle + |+1;-1\rangle - |0;0\rangle\right), \tag{5.13}$$

thereby neglecting partial waves $\ell = 1$ and higher, and performing the average. State $|(M_S)_A;(M_S)_B\rangle$ represents a pair of distinguishable atoms with quantum numbers $(M_S)_A$ and $(M_S)_B$, associated with the projection of respective spins $(S)_A = 1$ and $(S)_B = 1$ onto the internuclear axis.

For ^{3}He* samples, the subspace of ionizing quasi-molecular states associated with $\ell = 0$ is given by $|0\,0\,0\,M_F\rangle_{\rm mol}$, $|1\,1\,0\,M_F\rangle_{\rm mol}$ and $|1\,1\,2\,M_F\rangle_{\rm mol}$ (notation defined in Eq. (4.43)) and projection of the statistical mixture onto the subspace,

Table 5.6. Distribution of trapped atoms over magnetic substates for experimental MOT parameters. The populations are averaged over the trapped samples, where the local density is used as a weight. The rather large intensity imbalance of two counterpropagating laser beams (see Chapter 2) results in an asymmetric population of substates. As $\langle P_M P_{M'} \rangle \neq \langle P_M \rangle \langle P_{M'} \rangle$, it is not possible to substitute values for $\langle P_M \rangle$ into Eqs. (5.12) and (5.14).

^{4}He*	$\langle P_{-1} \rangle = 0.21$	$\langle P_0 \rangle = 0.30$	$\langle P_1 \rangle = 0.49$
^{3}He*	$\langle P_{-3/2} \rangle = 0.16$	$\langle P_{1/2} \rangle = 0.27$	
	$\langle P_{-1/2} \rangle = 0.21$	$\langle P_{3/2} \rangle = 0.36$	

followed by weighted averaging over the trapped sample, yields

$$K^{(\mathrm{eq})}_{\mathrm{SS,3He}} = K_{\mathrm{SS,3He}} \left\langle \tfrac{32}{13}(P_{-3/2}P_{-1/2} + P_{-3/2}P_{1/2} + P_{-1/2}P_{3/2} + P_{1/2}P_{3/2}) + \tfrac{40}{13}(P_{-3/2}P_{3/2} + P_{-1/2}P_{1/2}) \right\rangle , \quad (5.14)$$

Here, we have assumed that partial wave rate coefficients $^1\mathcal{K}_0$ and $^3\mathcal{K}_0$ are identical.[10] The averaged substate populations $\langle P_M \rangle$, obtained from the rate equation model, are shown in Table 5.6. Please note that it is not possible to substitute values for $\langle P_M \rangle$ into Eqs. (5.12) and (5.14), as $\langle P_M P_{M'} \rangle \neq \langle P_M \rangle \langle P_{M'} \rangle$.

The corrected rate coefficients are given in Table 5.5. Because of the different substate structure ($J = 1$ compared to $F = 3/2$) and different quantum statistical symmetry, the corrections differ for the two isotopes, rather large in case of ^{4}He*, with $K^{(\mathrm{eq})}_{\mathrm{SS,4He}} = 1.33\, K_{\mathrm{SS,4He}}$, and smaller in case of ^{3}He*, with $K^{(\mathrm{eq})}_{\mathrm{SS,3He}} = 1.10\, K_{\mathrm{SS,3He}}$.

5.6 Discussion and conclusions

Clearly, the ionization rate coefficient for ^{3}He* is larger than that for ^{4}He*. As shown in Chapter 4, this is a consequence of the different quantum statistical symmetry of the two isotopes and the presence of a nuclear spin in the case of ^{3}He*, properties that clearly manifests itself in ionizing collisions in the quantum threshold regime.[11] The ratio $K^{(\mathrm{eq})}_{\mathrm{SS,3He}}/K^{(\mathrm{eq})}_{\mathrm{SS,4He}} = 1.8(5)$ agrees very well to the theoretical prediction of 1.8 (at a temperature of 2 mK), which is an indication that our model provides a good description of homonuclear ionizing collisions of He* isotopes. For ^{4}He*, this was already confirmed by comparison of our results with other theoretical work reported in literature.

[10] It was shown in Section 4.2.4, that differences between $^1\mathcal{K}_\ell$ and $^3\mathcal{K}_\ell$ are only a few percent.

[11] In heavier metastable rare-gas systems, complementary studies of quantum statistical effects in ionizing collisions have been performed [95, 141]. As Wigner's spin-conservation rule does not apply for these heavy systems [52], quantum statistical effects can be observed as a suppression or enhancement of ionization rates if trapped samples are polarized.

The rate coefficients, $K^{(eq)}_{SS,3He} = 1.9(3) \times 10^{-10}$ cm^3/s and $K^{(eq)}_{SS,4He} = 1.0(2) \times 10^{-10}$ cm^3/s, show a surprisingly good agreement with our theoretical predictions at 2 mK of $K^{(th)}_{SS,3He} = 1.8 \times 10^{-10}$ cm^3/s and $K^{(th)}_{SS,4He} = 9.9 \times 10^{-11}$ cm^3/s. There is also a good agreement with the calculated values of Leo *et al.* [111]. However, our values do not agree with other experimental values, that suffer from mutual inconsistency themselves, as was pointed out by Leo *et al.* [111].

In particular, there are rather large discrepancies between the values reported here and those reported by Kumakura and Morita [102] for ^{3}He*. The discrepancy between the theoretical predictions can be explained from too simple assumptions in the theoretical model of Kumakura and Morita (which shows good agreement with their experimental results). As their model does not take into account quantum reflection for s-wave scattering, it yields too large theoretical predictions. Furthermore, the model assumes adiabatic transitions in ^{3}He collisions, thereby overestimating the ratio of ionization rate coefficients. The discrepancy between the experimental values is more difficult to interpret. The ionization rate coefficients are the result of an extensive analysis, including the determination of the density distribution and temperature of the trapped samples, as well as the distribution over the magnetic substates. The ionization rate coefficient is particularly sensitive to the density in the sample. It must be checked carefully if frequency drifts of the probe laser light or stray magnetic fields are small enough to avoid incomplete absorption, which would result in underestimation of the density and overestimation of the ionization rate coefficients. If the number of trapped atoms is obtained from fluorescence imaging [102], an accurate calibration of the CCD chip is crucial. Furthermore, collisions of trapped atoms with background atoms or atoms from the atomic beam must be considered. If the trapped atom number is small ($< 10^7$), quadratic ionization becomes small and other (linear) ionization mechanism possibly play a part, hampering accurate measurements.

It would be interesting to extend the work presented in Chapters 4 and 5 to trapped samples containing both isotopes and study *heteronuclear* ionizing collisions. In the case of collisions between distinguishable particles, quantum statistical symmetry requirements should be absent, which could be confirmed from an investigation of ionizing collisions. Another interesting extension of the work presented here, is the study of the ionization rates for samples with a prepared substate population. It might be possible to study depolarization due to collisions [111]. Finally, ionizing collisions can also be investigated in the quantum degenerate regime [175]. Ionization rates could be used to study quantum statistical properties of a quantum degenerate mixture with high spatial and temporal resolution. It is conceivable that phase separation in a quantum degenerate mixture (see Chapter 6) can be observed through the ionization rate in the sample.

Chapter 6

Simultaneous magneto-optical trapping of a boson-fermion mixture of He* atoms

Metastable triplet helium (He*) provides unique possibilities for the study of dilute quantum gases. Its metastability offers new detection strategies unavailable with alkali species. In particular, the Penning ionization process,

$$\mathrm{He^*} + \mathrm{He^*} \rightarrow \mathrm{He^+} + \mathrm{He}(1\,{}^1\mathrm{S}) + e^- \tag{6.1}$$

(or $\mathrm{He^*} + \mathrm{He^*} \rightarrow \mathrm{He_2}^+ + e^-$), provides a small but detectable flux of ions. This real-time probe can be used to study density-dependent phenomena occurring in trapped samples. The achievement of Bose-Einstein condensation in a dilute gas of ^{4}He* atoms [147, 162] has already demonstrated the feasibility of quantum degeneracy experiments with metastable helium. Considering the availability of the fermionic isotope ^{3}He*, research might be extended to Fermi degeneracy and boson-fermion quantum degenerate mixtures. Recently, impressive results were obtained in this field, including the observation of Pauli blocking of collisions [48], the study of boson-fermion quantum degenerate mixtures of ^{6}Li/^{7}Li [173, 198], ^{6}Li/^{23}Na [73] and ^{40}K/^{87}Rb [134], and the formation of molecular condensates in the BEC-BCS crossover regime [71, 89, 231]. With the extra detection strategies, the ^{3}He*/^{4}He* mixture provides a unique new system for quantum degeneracy experiments.

6.1 Prospects for a quantum degenerate mixture

In their liquid and solid phases, ^{3}He, ^{4}He and mixtures thereof have been studied extensively [215]. Although the underlying physics is closely related and similar phenomena can be observed, the dilute gas regime is strongly deviant:

the atomic densities are smaller by many orders of magnitude and the interparticle interactions are weak [108, 109]. Furthermore, at sufficiently low temperatures, elastic scattering behavior is solely determined by the s-wave scattering length, which is specific to the internal state of the atoms.

For pursuing quantum degeneracy in a magnetically trapped, dilute mixture of ^{3}He* and ^{4}He* atoms, it is necessary that all atoms occupy the fully stretched magnetic substate of the metastable 2 $^3S_1$ level. Only in these substates, the $F = 3/2$, $M_F = 3/2$ state for ^{3}He* and the $M_J = 1$ state for ^{4}He*, Penning ionizing collisions are strongly suppressed. For spin-polarized ^{4}He* atoms, the two-body loss rate constant is $\beta \approx 10^{-14}$ cm^3/s [147, 162, 182], four orders of magnitude smaller than in an unpolarized sample in a magneto-optical trap (MOT). As this loss rate is induced by the spin-dipole interaction in pair collisions [182], the loss rate for a spin-polarized mixture of ^{3}He* and ^{4}He* atoms is expected to be of the same order of magnitude, i.e. $\sim 10^{-14}$ cm^3/s. For spin-polarized ^{3}He* atoms, further suppression of the two-body loss rate is expected due to the vanishing cross-section for cold collisions of identical fermions, whilst hyperfine-changing collisions between ^{3}He* atoms cannot occur because of the inverted hyperfine structure of the 2 $^3S_1$ level.

The low Penning ionization rates allow sympathetic cooling in a magnetic trap of ^{3}He* atoms by collisions with ^{4}He* atoms that are cooled by rf-induced evaporation. Evaporative cooling of fermions in different spin states [47] is not applicable to ^{3}He* atoms because Penning ionization rates will be too high. These high ionization rates and the absence of magnetic field dependent Feshbach resonances hamper the investigation of BCS-like phenomena.

The relevant parameters governing the sympathetic cooling process are the boson-boson scattering length ^{4-4}a and the boson-fermion scattering length ^{3-4}a. Both experimental and theoretical values of ^{4-4}a are available. The most accurate experimental value is 11.3 nm with an error of a few nm [175]. A similar accuracy is achieved in a theoretical prediction: starting from a calculation of the $^5\Sigma_g^+$ molecular potential of two spin-polarized atoms, Dickinson et al. [49] investigate the wavefunction of the $v = 14$ least bound state in this potential and arrive at upper and lower bounds of 12.2 nm and 8 nm, respectively. Mass scaling of the molecular potential shows that the interspecies scattering length will be exceptionally large. If $^{4-4}a < 9.4$ nm, then ^{3-4}a is large and positive. Most likely, $^{4-4}a > 9.4$ nm and then ^{3-4}a is large and negative. For a conservative estimate, $9 < {}^{4-4}a\,(\text{nm}) < 13$, we find that $^{3-4}a < -25$ nm or $^{3-4}a > 133$ nm. In either case, evaporative cooling of ^{3}He* atoms via collisions with ^{4}He* atoms should be very efficient.

In the quantum degenerate regime the large value of ^{3-4}a corresponds to a large mean-field interaction. This allows a study of quantum phenomena such as component phase separation [135] (if $^{3-4}a > 0$) or stability properties of the mixture [134] (if $^{3-4}a < 0$) at atomic densities as low as $n = 10^{13}$ cm^{-3}. The monitoring of ion production rates provides a unique detection tool for these phenomena, especially in the case of phase separation, where different phases and mixtures are expected as a function of the density of the bosons and/or

fermions, which may be varied experimentally.

In this chapter, we present the first step towards the study of these mixtures by discussing the realization and characterization of a MOT containing both He* isotopes. Previously, several groups have studied samples of two atomic species in a MOT, either two isotopes of a single element [42, 117, 131, 192, 221] or two different elements [69, 119, 170–172, 177, 190, 193, 194, 218, 228]. In our MOT up to 1.5×10^8 metastable atoms of each isotope are simultaneously confined at a temperature of 2 mK and a total atomic density of $\sim 10^9$ cm^{-3}. These numbers are comparable to single-isotope He* traps and present good prospects for evaporative cooling experiments.

6.2 Experimental setup

In the experiment, a MOT is loaded from a collimated and Zeeman slowed He* beam, produced by a liquid nitrogen cooled, DC-discharge source. The apparatus is similar to the ^{4}He* apparatus described previously [196], modified to manipulate both helium isotopes, either separately or simultaneously. The beam source is operated with an isotopically enriched mixture of the two helium isotopes containing approximately equal concentrations of each and is recycled and purified using liquid nitrogen cooled molecular sieves. The two-isotope beam is collimated by transversal laser cooling in two dimensions before entering the Zeeman slower.

Due to its smaller mass, ^{3}He* atoms emerge from the source with a larger mean velocity than ^{4}He* atoms. To achieve a large flux of slow ^{3}He* atoms, the capture velocity of the Zeeman slower is increased to ~ 1370 m/s. The MOT is operated in a stainless steel vacuum chamber, where two anti-Helmholtz coils produce a magnetic quadrupole field with an axial magnetic gradient $dB/dz = 0.35$ T/m.

Both helium isotopes are slowed and confined in the MOT with 1083 nm light that is near resonant with the $2\ ^3S_1 \rightarrow 2\ ^3P_2$ optical transition (natural linewidth $\Gamma/2\pi = 1.62$ MHz; saturation intensity $I_{\mathrm{sat}} = 0.167$ mW/cm^2 for the cycling transition). The isotope shift for this transition is 34 GHz and, therefore, two separate ytterbium-doped fiber lasers are used, one for each isotope. The lasers are frequency locked to the laser cooling lines using saturated absorption spectroscopy in rf-discharge cells. The two laser beams are overlapped on a non-polarizing beam splitter, producing two beams of about equal power containing both frequencies. One beam is used for the transversal laser cooling of the He* atomic beam, the other is coupled into a single mode polarization maintaining fiber to achieve perfect beam overlap, and is used for the Zeeman slower and the MOT. Acousto-optic modulators are used to generate the slowing frequencies ν_{ZS3} and ν_{ZS4}, and the trapping frequencies ν_{MOT3} and ν_{MOT4}. Figure 6.1 gives an overview of the optical transitions at 1083 nm for each isotope, together with the four laser cooling frequencies. The trapping beam is split up into six independent Gaussian beams with $1/e^2$ intensity widths of 1.8 cm. The total peak intensity is $I_{\mathrm{peak}} = 57$ mW/cm^2 ($I_{\mathrm{peak}}/I_{\mathrm{sat}} \approx 335$) for each frequency.

The slowing beam is focused onto the atomic beam source. At the position of the trapped cloud the $1/e^2$ intensity width is 2.2 cm and the two frequency components have peak intensities of $I_{\text{peak}} = 9\ \text{mW/cm}^2$ ($I_{\text{peak}}/I_{\text{sat}} \approx 54$).

The trapped clouds are studied using two microchannel plate (MCP) detectors. Operated at a voltage of -1.5 kV and positioned at a distance of 11 cm from the trap center, the MCP detectors allow for independent monitoring of the ions and He* atoms that escape the trap. With an exposed negative high voltage on its front plate, one MCP detector attracts all ions produced in Penning-ionizing collisions. The other MCP is mounted behind a grounded grid and detects only He* atoms that exit the trap in its direction.

The decaying ion flux, measured on the unshielded MCP detector after interrupting the loading of one or two isotopes, is used to study trap loss. The signal is used to determine the loss rate coefficients α and β defined via $dn/dt = -\alpha n - \beta n^2$ [13]. In this way, the ion production rate acts as a real-time probe to monitor Penning-ionizing collisions in the trapped cloud [13, 78–80, 102, 103, 153].

The shielded MCP detector is used to perform time-of-flight measurements. For this purpose, the trapping and slowing light for one or two isotopes, and the magnetic field are switched off abruptly. During the free ballistic expansion, a small fraction of the released atom cloud hits the MCP detector and the resulting signal is used to determine the temperature of the trapped cloud and the number of trapped atoms. An absolute calibration is performed using absorption imaging of the trapped cloud with a narrow-band diode laser and an IR-sensitive CCD camera. Absorption imaging allows the determination of the density distribution and atom number of the sample.

6.3 Trapping of single isotopes

First, we studied single-isotope MOTs of both isotopes separately. In these traps, typically $N = 3 \times 10^8$ ^{3}He* or ^{4}He* atoms are confined at a central density $n_0 = 3 \times 10^9\ \text{cm}^{-3}$ and a temperature $T = 2$ mK. The uncertainty in the atom number determination is $\sim 30\%$. The density is limited to a few $10^9\ \text{cm}^{-3}$ by light-assisted Penning ionizing collisions. Previous studies of ^{4}He* MOTs [23, 149, 196] report similar numbers.

The results of the ^{3}He* MOT are similar to those of the ^{4}He* MOT yielding a number of trapped ^{3}He* atoms that is three orders of magnitude larger than reported previously [102, 103]. At first sight this may be surprising, as the level structure of ^{3}He is complicated by hyperfine splittings, as seen in Figure 6.1. However, operated on transition C_3, the ^{3}He* MOT confines large atom numbers without the application of repumping light to excite the $F = 1/2$ ground state.

Despite the inverted hyperfine structure of the excited state and the relatively large splitting of 1125Γ between the $F' = 3/2$ and $F' = 5/2$ levels, the high intensity of the trapping beams leads to significant off-resonant excitation of transition C_5 and decay into the $F = 1/2$ ground state. A repumping beam, however, is not required, since the trapping and slowing frequencies ν_{MOT3} and

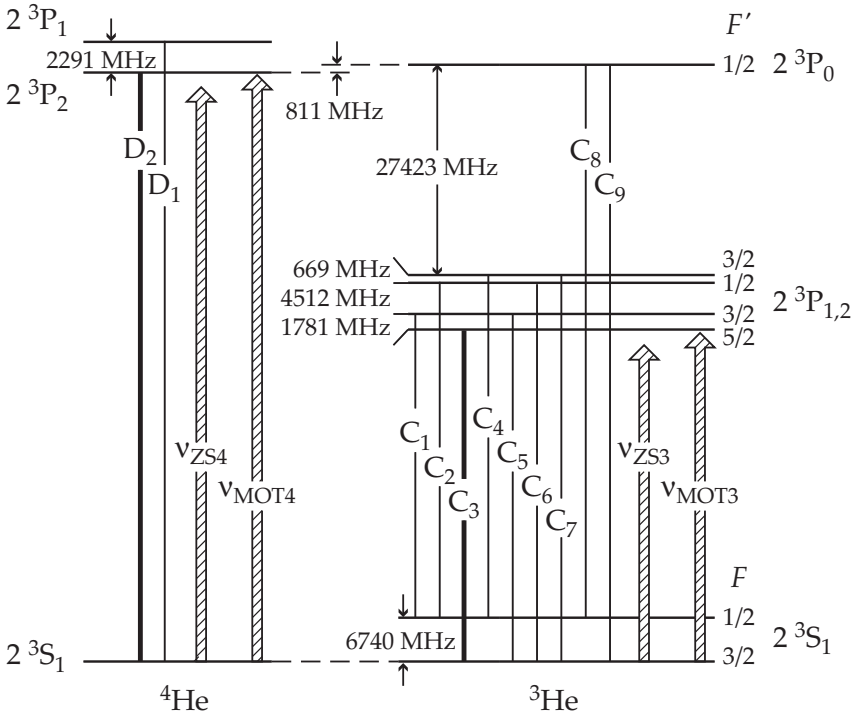

Figure 6.1. Overview of the optical transitions at 1083 nm of the ^{3}He and ^{4}He atom. The trapping frequencies ν_{MOT3} and ν_{MOT4}, and slowing frequencies ν_{ZS3} and ν_{ZS4} are also included. The trapping and slowing frequencies are detuned from the laser cooling transitions (C_3 for ^{3}He, D_2 for ^{4}He) by -40 MHz and -500 MHz, respectively. The isotope shift puts laser frequencies ν_{MOT4} and ν_{ZS4} near transition C_9 of ^{3}He.

ν_{ZS3} excite transitions C_2 and C_4 at a sufficiently high rate to repopulate the $F = 3/2$ ground state. The frequency detuning of ν_{ZS3} from transition C_2 is relatively small, -32Γ, making this combination the dominant repumping route. In absence of ν_{ZS3}, sufficient repumping is provided by the excitation of transitions C_2 and C_4 by frequency component ν_{MOT3}. The detunings from the transitions are larger at 251Γ and -161Γ, respectively.

Figure 6.2a (solid curve) shows the ^{3}He* signal and ion signal from a pure ^{3}He* MOT, when the slowing light is switched off abruptly. Measurements with the shielded MCP detector show zero loss of metastables from the trap irrespective of the presence of ν_{ZS3}. The decay is dominated by Penning ionizing pair collisions in the cloud, characterized by $\beta_{33} n_{0,3} = 5.2\ \mathrm{s}^{-1}$ and $\alpha = 0.7\ \mathrm{s}^{-1}$. With $n_{0,3}$ from absorption imaging, $\beta_{33} \approx 8 \times 10^{-9}\ \mathrm{cm}^3/\mathrm{s}$ is deduced. At equal detuning and intensity of the trapping laser, we find for a pure ^{4}He* MOT that $\beta_{44} \approx 4 \times 10^{-9}\ \mathrm{cm}^3/\mathrm{s}$. The isotopic difference between β_{33} and β_{44} is a result of the different number of ionization channels for light-assisted collisions of pairs of ^{3}He* or ^{4}He* atoms [102, 103].

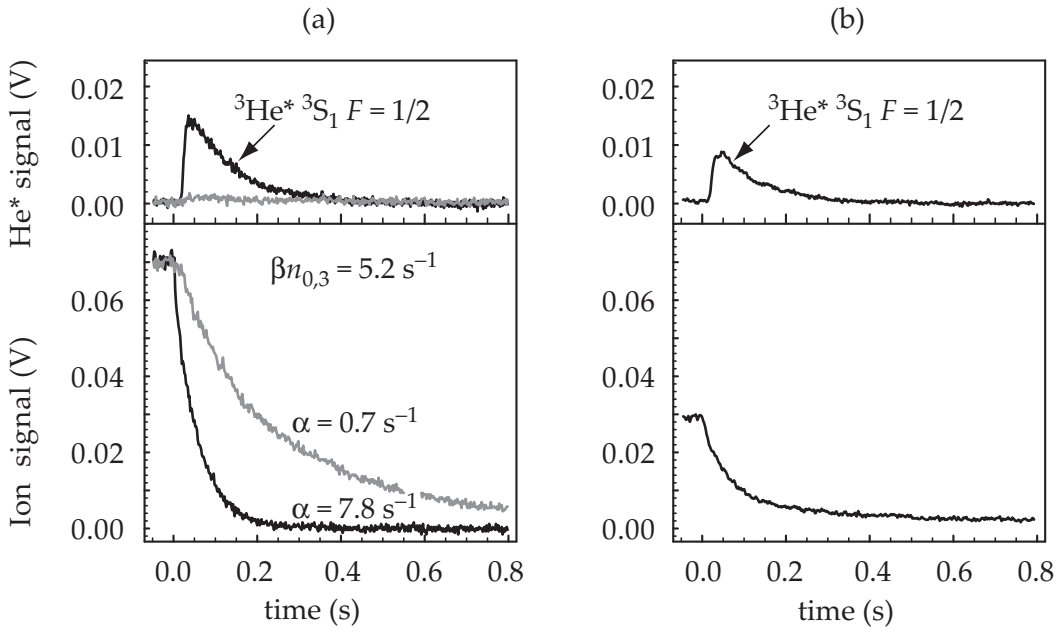

Figure 6.2. He* signals and ion signals observed when the slowing light is abruptly blocked at $t = 0$. (a) Single-isotope ^{3}He* MOT with (black) and without (gray) the ν_{MOT4} frequency component added at $t = 0$. (b) Two-isotope MOT.

6.4 Simultaneous trapping of both isotopes

In the two-isotope MOT, four frequencies are present and a second optical pumping loss channel for ^{3}He* atoms to the non-trapped $F = 1/2$ state is opened up. Due to a relatively small frequency difference of -524Γ, the ^{4}He trapping light frequently excites transition C_9. Now, the repumping provided by ν_{MOT3} via off-resonant excitation of C_2 and C_4 is insufficient. This can be seen in Fig. 6.2a (dotted curve), where the effect is shown of frequency component ν_{MOT4} on the decay dynamics of the ^{3}He* MOT. At $t = 0$, when the slowing light is blocked, ν_{MOT4} is added to the trapping light and a flux of ^{3}He* atoms escaping the trap is observed. The decaying ion signal indicates that the ^{3}He* atoms are transferred to the $F = 1/2$ state at a rate $\alpha = 7.8\ \mathrm{s}^{-1}$. However, this extra loss channel does not limit the realization of a two-isotope MOT with a large number of ^{3}He* atoms. As shown in Fig. 6.2b, the two-isotope MOT loses ^{3}He* atoms only if the slowing light is blocked. During loading there is still sufficient repumping by ν_{ZS3} and optical pumping loss is negligible.

In the Zeeman slower two frequencies, ν_{ZS3} and ν_{ZS4}, are present to simultaneously slow the two isotopes. Here, optical pumping of ^{3}He* atoms to non-slowed substates by the ^{4}He slowing light can occur if the slowing light is not perfectly σ^+ polarized. Calculations show that the $M_F = 3/2 \rightarrow M_F' = 1/2$ Zeeman component of transition C_9 becomes resonant with σ^- polarized ^{4}He slowing light around $B = 199$ G.

After optimization of the slowing efficiency, the numbers of trapped atoms in the two-isotope MOT are comparable to the corresponding numbers in single-isotope traps; trapped atom numbers $N_i \approx 1.5 \times 10^8$ for each isotope ($i = 3, 4$)

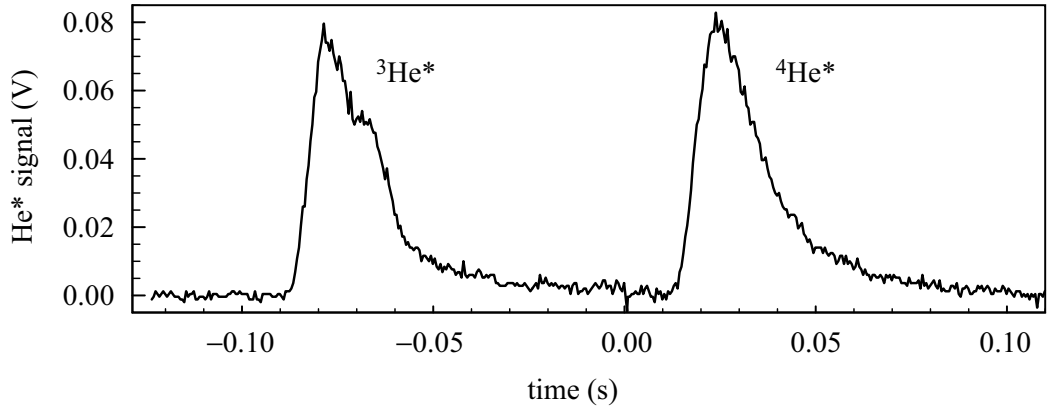

Figure 6.3. Flux of He* atoms after the subsequent release of ^{3}He* atoms (at $t = -100$ ms) and ^{4}He* atoms (at $t = 0$ ms) from the two-isotope MOT. Two peaks corresponding to the two isotopes are observed. Only the second peak can be used to determine an accurate temperature and atom number.

are obtained. These large atom numbers are obtained by applying only the four frequencies ν_{MOT3}, ν_{ZS3}, ν_{MOT4} and ν_{ZS4}.[1] Fluorescence measurements with the CCD camera show that the clouds of both isotopes have nearly equal size and are spatially overlapped. Figure 6.3 shows the flux of He* atoms on the shielded MCP after subsequent release of the two isotopes. First ^{3}He* atoms are released by switching off the ν_{MOT3} and ν_{ZS3} components of the trapping and slowing light. The quadrupole magnetic field perturbs the free ballistic expansion of these atoms, giving rise to a shoulder on the first peak in the signal. The ^{4}He* atoms are released with a delay of 100 ms by simultaneously switching off the remaining frequency components ν_{MOT4} and ν_{ZS4} together with the magnetic field.

In steady state, the loading rate of the MOT, $R_{3,4} \approx 3 \times 10^8$ s^{-1}, is balanced by the trap loss:

$$R_i = \alpha_i N_i + \beta_{ii} \iiint n_i^2 \, \mathrm{d}^3 r + \beta_{34} \iiint n_3 n_4 \, \mathrm{d}^3 r, \tag{6.2}$$

with $i = 3, 4$. For each isotope, the atom number confined in the two-isotope trap is comparable to the atom number confined in the single-isotope trap. This shows that loss due to interspecies collisions, characterized by β_{34}, is small compared to the loss processes characterized by α_3 and β_{33}, or α_4 and β_{44}. Different collision mechanisms for homonuclear and heteronuclear collisions in the presence of resonant light are responsible for the differing loss coefficients. During homonuclear collisions, resonant light can excite the atom pair to a resonant dipole-dipole potential $V(R) \sim R^{-3}$. As heteronuclear collisions are governed by a Van der Waals potential $V(R) \sim R^{-6}$, resonant excitation occurs at much smaller internuclear distances, yielding loss rates that are smaller by about one order of magnitude [210].

[1] In the related case of the simultaneous magneto-optical trapping of ^{6}Li atoms and ^{7}Li atoms, eight different frequencies are needed to achieve significant atom numbers [131].

6.5 Conclusion

We have demonstrated that it is possible to trap up to 1.5×10^8 ^{3}He* atoms together with an equal number of ^{4}He* atoms in a two-isotope magneto-optical trap. For ^{4}He*, this result is comparable to results achieved with single-isotope MOTs and for ^{3}He* it is an improvement by three orders of magnitude when compared with previous results. This opens up the road to sympathetic cooling of ^{3}He* and realization of quantum degeneracy in a dilute gas of ^{3}He* atoms or a mixture of ^{3}He* and ^{4}He* atoms.

Chapter 7

Atomic fountain clock based on ^{3}He*

In this chapter, the possibilities of an atomic fountain clock based on ^{3}He* are investigated. The intended clock transition $2\,^3\mathrm{S}(F = 3/2) \rightarrow 2\,^3\mathrm{S}(F = 1/2)$ has a transition frequency of 6.7 GHz and is very suitable for the stabilization of a microwave signal using the method of separated oscillatory fields. As discussed in Section 1.3, the ^{3}He* fountain clock provides possibilities for innovative research on atomic clocks. In particular, the cold collision frequency shift in a clock based on a fermionic atomic species might be studied, and measurements of a possible time variation of the fine-structure constant might be considered.

In the following, calculations are presented of the expected stability, accuracy and Ramsey fringe contrast of a ^{3}He* fountain clock. Furthermore it is investigated if an experimental study of the innovative aspects of the clock is feasible. To provide a framework for the calculations, a brief discussion of atomic fountain clocks is provided, where a ^{3}He* fountain clock is used as a starting point. Extensive treatments on atomic fountain clocks can be found in [9, 15, 110].

In an atomic fountain clock a microwave frequency generator (local oscillator) is stabilized to an atomic hyperfine transition (clock transition) by means of interrogation with separated oscillatory fields [159]. A schematic of a possible ^{3}He* fountain clock is depicted in Fig. 7.1. The clock is operated in a cyclic fashion with clock cycles of about 1 s. A cycle begins with the capture of about 4×10^8 atoms in a MOT. The trapped sample with a temperature of 0.2 mK (obtained in optical molasses [79]) is launched upward with a velocity of about 3.3 m/s in a moving molasses [35]. The atoms fly up and down through a cylindrical TE_{011} microwave cavity, where a (near) resonant microwave signal drives the clock transition with a $\pi/2$ pulse; the interaction time of the atoms with the microwave field is about 0.03 s and the time between the two passages is about 0.4 s. The transition probability associated with the interrogation with

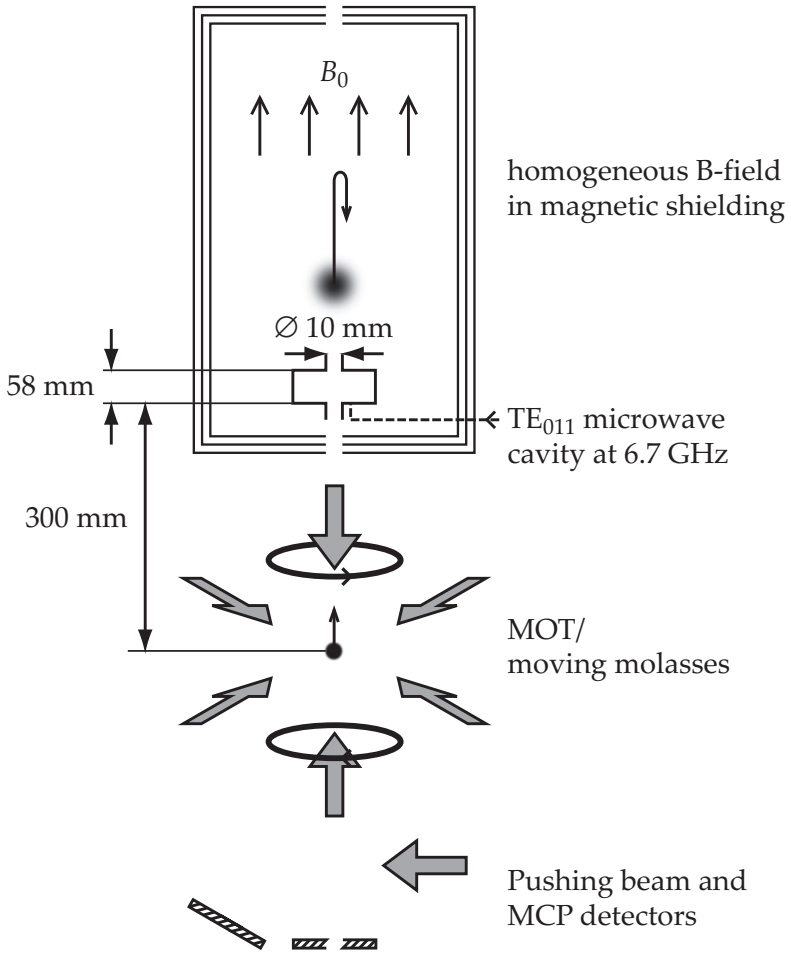

Figure 7.1. Schematic of a possible atomic fountain clock based on ^{3}He*. The resonance frequency of the cylindrical TE_{011} microwave cavity depends on the radius and height of the cavity [87] and is very near the frequency of the clock transition. A state-selective detection scheme is achieved using two MCP detectors and a laser beam. The laser beam is resonant with the ground (or excited) state of the clock transition and pushes atoms in this state to the detector that is displaced from the symmetry axis of the fountain. Atoms in the other state fall onto the detector that is mounted directly under the cavity. The latter has a hole in the center to transmit the vertical trapping beams.

separated oscillatory fields depends strongly on the detuning of the microwave frequency from the frequency of the clock transition and is measured with a state-selective detection scheme. The probability signal is used to update the error signal that is applied to the local oscillator.

In the interrogation region (microwave cavity and free flight region) a magnetic field of high spatial homogeneity and temporal stability is applied to raise the degeneracy of the various hyperfine transitions. In the microwave cavity, a single ($\Delta m = 0$) hyperfine transition is excited, so that the interrogation is limited to atoms in a specific magnetic substate. In a laser-cooled sample, the ^{3}He* atoms are about evenly distributed over the $2F + 1 = 4$ magnetic substates, $M_F = -\frac{3}{2}, -\frac{1}{2}, +\frac{1}{2}, +\frac{3}{2}$, so that the fraction of interrogated atoms is $\lesssim 0.25$.[1]

7.1 Fountain of laser-cooled ^{3}He* atoms

To determine the number of detected atoms in a clock cycle, the ballistic expansion of a laser-cooled sample of ^{3}He* atoms, launched upward, is modeled with the expressions of Appendix B. As the initial size of the sample is small compared to the (expanded) size at the microwave cavity, it can be neglected and all atoms are assumed to originate from the MOT center. The atomic velocity components are given by the Maxwell-Boltzmann distributions $f(v_x, \sigma_{vx})$, $f(v_y, \sigma_{vy})$ and $f(v_z, \sigma_{vz})$ of Eqs. (B.1), (B.2) and (B.33), respectively, where the rms velocities are assumed to be equal, $\sigma_{v,x} = \sigma_{v,y} = \sigma_{v,z} = \sigma_v = (k_\mathrm{B}T/m)^{1/2}$, with T the temperature of the sample and m the mass of the ^{3}He atom. The number of atoms with velocities between v_x and $v_x + \mathrm{d}v_x$, v_y and $v_y + \mathrm{d}v_y$, and v_z and $v_z + \mathrm{d}v_z$ is

$$Nf(v_x, \sigma_{vx}) f(v_y, \sigma_{vy}) f(v_z, \sigma_{vz})\, \mathrm{d}v_x \mathrm{d}v_y \mathrm{d}v_z = \frac{N}{(2\pi)^{3/2}\sigma_v^3} \exp\left[-\frac{v_x^2 + v_y^2 + (v_z - v_{z,0})^2}{2\sigma_v^2}\right] \mathrm{d}v_x \mathrm{d}v_y \mathrm{d}v_z, \quad (7.1)$$

with N the total number of atoms in the sample and $v_{z,0}$ the mean launch velocity. As the fountain geometry is cylindrically symmetric, it is convenient to apply the coordinate transformation $(v_x, v_y, v_z) \rightarrow (v_r, \varphi, v_z)$ with

$$v_x = v_r \cos\varphi, \quad (7.2)$$

$$v_y = v_r \sin\varphi, \quad (7.3)$$

$$v_z = v_z. \quad (7.4)$$

The transformed distribution function is

$$Nf_{\mathrm{cyl}}(v_r, \varphi) f(v_z, \sigma_{vz})\, \mathrm{d}v_r \mathrm{d}\varphi\, \mathrm{d}v_z = \frac{N}{(2\pi)^{3/2}\sigma_v^3} v_r \exp\left[-\frac{v_r^2 + (v_z - v_{z,0})^2}{2\sigma_v^2}\right] \mathrm{d}v_r \mathrm{d}\varphi\, \mathrm{d}v_z \quad (7.5)$$

[1] To minimize collision frequency shifts, the atoms in the unprobed states are usually removed using a microwave pulse and a laser beam [110]. The population of the probed state, $F = 1$ and $M_F = 0$, in a ^{87}Rb fountain has been increased to 50% using a configuration of two microwave cavities and laser beams [59].

and the number of atoms with velocities between v_r and $v_r + \mathrm{d}v_r$, and v_z and $v_z + \mathrm{d}v_z$ is given by

$$Nf(v_r,\sigma_{vr})f(v_z,\sigma_{vz})\,\mathrm{d}v_r\mathrm{d}v_z = N\int_0^{2\pi}\left[f_{\mathrm{cyl}}(v_r,\varphi)f(v_z,\sigma_{vz})\,\mathrm{d}v_r\mathrm{d}v_z\right]\mathrm{d}\varphi$$
$$= \frac{N}{\sqrt{2\pi}\,\sigma_v^3}\,v_r\,\exp\left[-\frac{v_r^2+(v_z-v_{z,0})^2}{2\sigma_v^2}\right]\,\mathrm{d}v_r\mathrm{d}v_z \quad (7.6)$$

Atoms that experience the interrogation with separated oscillatory fields and reach the detection region afterwards, must fly up through the cavity holes, reach an apex above the cavity, and fall back through the holes. This places a restriction on both the radial and longitudinal velocity components v_r and v_z of the detected atoms. To reach an apex above the cavity,

$$v_z > v_{\mathrm{min}} = \sqrt{2(d+h)g} \quad (7.7)$$

with $g = 9.81$ m/s the acceleration of free fall, $d = 300$ mm the distance from MOT center to the bottom of the cavity, and $h = 58$ mm the height of the cavity. Atoms fall downward through the lower cavity hole if

$$v_r t_1 < \rho \quad (7.8)$$

with $\rho = 5$ mm the radius of the cavity holes, and

$$t_1 = \frac{v_z}{g}\left(1+\sqrt{1-2dg/v_z^2}\right) \quad (7.9)$$

the time at which an atom with initial velocity v_z ($> \sqrt{2dg}$) reaches $z = d$ after the apex. The number of detected atoms with initial velocity between v_z ($> v_{\mathrm{min}}$) and $v_z + \mathrm{d}v_z$ can be determined from

$$N\tilde{f}(v_z)\,\mathrm{d}v_z = N\int_0^{\rho/t_1}\left[f(v_r,\sigma_{vr})f(v_z,\sigma_{vz})\mathrm{d}v_z\right]\mathrm{d}v_r$$
$$= \frac{N}{\sqrt{2\pi}\,\sigma_v}\left\{1-\exp\left[-\frac{(\rho/t_1)^2}{2\sigma_v^2}\right]\right\}\exp\left[-\frac{(v_z-v_{z,0})^2}{2\sigma_v^2}\right]\,\mathrm{d}v_z. \quad (7.10)$$

The number of detected atoms can now be calculated as

$$N_{\mathrm{detect}} = N\int_{v_{\mathrm{min}}}^{v_{\mathrm{max}}}\tilde{f}(v_z)\,\mathrm{d}v_z, \quad (7.11)$$

where $v_{\mathrm{max}} = \sqrt{2Hg}$, with $H = 1$ m, the assumed height of the clock setup.

Clock cycles are assumed to begin with the launch of a sample containing 4×10^8 ^{3}He* atoms with a temperature $T = 0.2$ mK. As the fraction of atoms in the probed magnetic substate is 0.25, it follows that $N = 1\times10^8$. The number of detected atoms N_{detect} can be calculated by numerical integration and is plotted against the mean launch velocity $v_{z,0}$ in Fig. 7.2. The number reaches a maximum of 5.4×10^3 for a velocity $v_{z,0} = 3.3$ m/s. The fraction $N_{\mathrm{detect}}/N \ll 1$, as the small atomic mass results in a relatively large rms velocity $\sigma_v = 0.74$ m/s and a significant expansion and consequent cutting, both in the longitudinal and radial direction, of the launched sample. Velocity distribution $\tilde{f}(v_z)$ is plotted in Fig. 7.3 for $v_{z,0} = 3.3$ m/s.

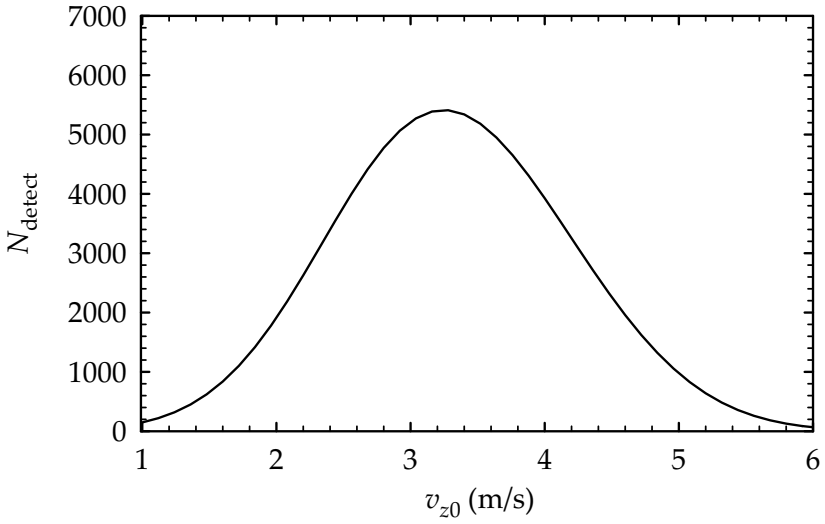

Figure 7.2. Number of detected atoms as a function of launch velocity. The sample contains $N = 1 \times 10^8$ atoms and has a temperature of 0.2 mK. The microwave cavity has a hole with a diameter of 10 mm, a height of 58 mm and is positioned 300 mm above the MOT center (see Fig. 7.1).

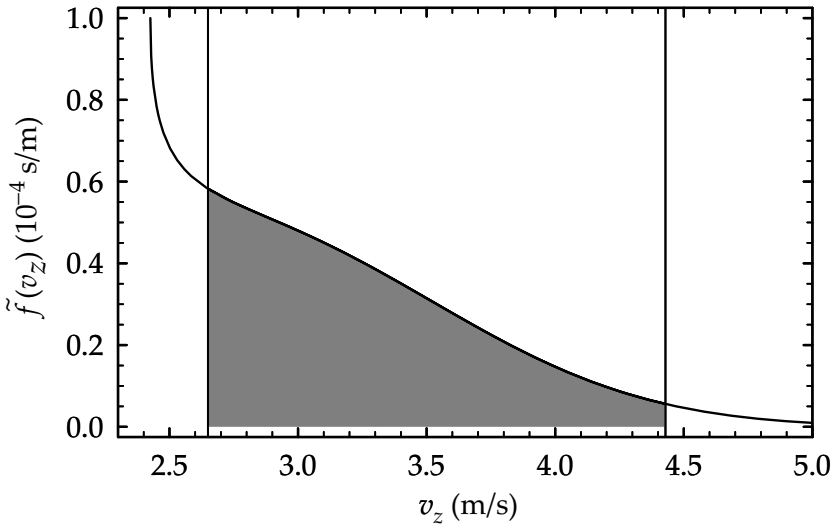

Figure 7.3. Velocity distribution $\tilde{f}(v_z)$ for $v_{z,0} = 3.3$ m/s. The shaded area under the curve, between v_{min} and v_{max}, represents the number of detected atoms.

7.2 Clock transition in magnetic field

For the fountain geometry of Fig. 7.1, possible clock transitions are characterized by $\Delta M = 0$. For ^{3}He*, two hyperfine transitions, $|\frac{3}{2}, \pm\frac{1}{2}\rangle \rightarrow |\frac{1}{2}, \pm\frac{1}{2}\rangle$ (notation $|F, M_F\rangle$ valid for small magnetic fields), are suitable, displaying a different magnetic field dependence. Considering the hyperfine interaction $\mathrm{H_{hf}} = -\frac{2}{3}h\nu_0\,\mathbf{I}\cdot\mathbf{S}$ and Zeeman interaction $\mathrm{H_{Zeeman}} = \mu_\mathrm{B}(g_S\mathbf{S} + g_I\mathbf{I})\cdot\boldsymbol{B}$ in the (six dimensional) state space corresponding to state ($2\,^3$S, F) [41], the magnetic field dependence of the transition frequencies is calculated as

$$\nu_\pm = \nu_0\left[1 \pm \tfrac{2}{3}(g_S - g_I)\frac{\mu_\mathrm{B}B}{\nu_0} + (g_S - g_I)\Big(\frac{\mu_\mathrm{B}B}{\nu_0}\Big)^2\right]^{1/2} \tag{7.12}$$

where $\nu_0 = 6739701177$ Hz [166, 167] and the Landé g-factors are given in Table A.2. At a magnetic field typical for atomic fountain clocks of ^{133}Cs or ^{87}Rb, $B_\mathrm{low} \approx 1$ G, both transitions depend linearly on magnetic field, with

$$\frac{\partial\nu_\pm}{\partial B} = \pm\tfrac{1}{3}(g_S - g_I)\mu_\mathrm{B} \approx \pm 9.33\times 10^5\ \mathrm{Hz/G}. \tag{7.13}$$

At large magnetic fields the transition frequencies show a different behavior. While transition frequency ν_+ increases monotonously, transition ν_- has a minimum $\frac{2}{3}\sqrt{2}\,\nu_0 \approx 6.35$ GHz at a magnetic field $B_\mathrm{high} = \nu_0/3\mu_\mathrm{B}(g_S + g_I) \approx 803$ G.[2] At the minimum, the frequency depends only quadratically on magnetic field, with

$$\tfrac{1}{2}\frac{\partial^2\nu_-}{\partial B^2} = \tfrac{3}{8}\sqrt{2}\,\frac{\mu_\mathrm{B}(g_S - g_I)^2}{\nu_0} \approx 617\ \mathrm{Hz/G^2}. \tag{7.14}$$

The Zeeman shift of the clock transition is an important effect in the accuracy budget of atomic fountains and is of critical importance for an atomic fountain clock based on ^{3}He*. Here, two basic configurations for a ^{3}He* fountain clock are considered, both based on transition ν_-. In the low-field configuration, the magnetic field in the interrogation region is B_low, so that the clock transition depends linearly on magnetic field. In the high-field configuration, the magnetic field is B_high and the clock transition depends quadratically on the magnetic field.

For both configurations, the excited and ground states are denoted by $|\mathrm{e}\rangle$ and $|\mathrm{g}\rangle$, respectively. In the low-field configuration, the states can be written $|\mathrm{e}\rangle = |F, M_F\rangle = |\frac{1}{2}, -\frac{1}{2}\rangle$ and $|\mathrm{g}\rangle = |F, M_F\rangle = |\frac{3}{2}, -\frac{1}{2}\rangle$, and can be expanded onto the $\{|M_S, M_I\rangle\}$ basis, using $|F, M_F\rangle = \sum_{M_S}\sum_{M_I}|M_S, M_I\rangle\langle M_S, M_I|F, M_F\rangle$, as

$$|\mathrm{e}\rangle = \sqrt{\tfrac{1}{3}}\,|0, -\tfrac{1}{2}\rangle - \sqrt{\tfrac{2}{3}}\,|-1, +\tfrac{1}{2}\rangle, \tag{7.15}$$

$$|\mathrm{g}\rangle = \sqrt{\tfrac{2}{3}}\,|0, -\tfrac{1}{2}\rangle + \sqrt{\tfrac{1}{3}}\,|-1, +\tfrac{1}{2}\rangle. \tag{7.16}$$

[2] Including singlet-triplet mixing [121], the clock transition has a minimum at $B = 795$ G.

In the high-field configuration, the states can be expanded onto the $\{|M_S, M_I\rangle\}$ basis as

$$|\mathrm{e}\rangle = -\sqrt{\tfrac{1}{2}}\,|0,-\tfrac{1}{2}\rangle + \sqrt{\tfrac{1}{2}}\,|-1,+\tfrac{1}{2}\rangle, \tag{7.17}$$

$$|\mathrm{g}\rangle = \sqrt{\tfrac{1}{2}}\,|0,-\tfrac{1}{2}\rangle + \sqrt{\tfrac{1}{2}}\,|-1,+\tfrac{1}{2}\rangle. \tag{7.18}$$

7.3 Method of separated oscillatory fields

To determine the transition probability for an interrogation with separated oscillatory fields, the atom can be approximated by a two-level system given by Hamiltonian

$$\mathrm{H}_{\mathrm{atom}} = \frac{\hbar\omega_0}{2}\big(|\mathrm{e}\rangle\langle\mathrm{e}| - |\mathrm{g}\rangle\langle\mathrm{g}|\big), \tag{7.19}$$

where, in the low-field configuration $\omega_0/2\pi \approx 6.74$ GHz, and in the high-field configuration, $\omega_0/2\pi \approx 6.35$ GHz. The coupling between a ^{3}He* atom and the microwave field

$$\boldsymbol{B} = B\hat{\boldsymbol{z}}\cos(\omega_{\mathrm{rf}}\,t) \tag{7.20}$$

in the cavity is given by [202]

$$\mathrm{H}_{\mathrm{md}} = (g_S\mu_{\mathrm{B}}\mathbf{S} + g_I\mu_{\mathrm{B}}\mathbf{I})\cdot\boldsymbol{B} \approx g_S\mathrm{S}_z\mu_{\mathrm{B}}B\cos(\omega_{\mathrm{rf}}\,t). \tag{7.21}$$

In basis $\{|\mathrm{e}\rangle, |\mathrm{g}\rangle\}$, the Hamiltonian $\mathrm{H} = \mathrm{H}_{\mathrm{atom}} + \mathrm{H}_{\mathrm{md}}$ is represented by

$$H = -\frac{\hbar}{2}\begin{pmatrix} -\omega_0 + 2\Omega_1\cos(\omega t) & 2\Omega_0\cos(\omega t) \\ 2\Omega_0\cos(\omega t) & \omega_0 + 2\Omega_2\cos(\omega t)\end{pmatrix}, \tag{7.22}$$

where, in the low-field configuration, $\hbar\Omega_0 = -\frac{1}{3}\sqrt{2}\,g_S\mu_{\mathrm{B}}B$ and $\hbar\Omega_1 = 2\hbar\Omega_2 = \frac{2}{3}g_S\mu_{\mathrm{B}}B$, and in the high-field configuration, $\hbar\Omega_0 = \frac{1}{4}g_S\mu_{\mathrm{B}}B$ and $\hbar\Omega_1 = \hbar\Omega_2 = \frac{1}{2}g_S\mu_{\mathrm{B}}B$.

The Hamiltonian has a more simple form in a frame that rotates around the z-axis with angular frequency $\omega/2$ [36, complement $\mathrm{F_{IV}}$]. The transformation to the rotating frame can be expressed in terms of rotation operator $\mathrm{R} = \exp(i\omega\mathrm{S}_z t/\hbar)$ [36, complement $\mathrm{F_{IV}}$], with spin operator S_z, as

$$|\widetilde{\psi}\rangle = \mathrm{R}|\psi\rangle, \tag{7.23}$$

$$\widetilde{\mathrm{H}} = \mathrm{R}\mathrm{H}\mathrm{R}^\dagger - i\hbar\mathrm{R}\frac{\mathrm{d}\mathrm{R}^\dagger}{\mathrm{d}t}. \tag{7.24}$$

In basis $\{|\mathrm{e}\rangle, |\mathrm{g}\rangle\}$, the rotation operator is represented by matrix

$$R = \begin{pmatrix}\exp(i\omega t/2) & 0 \\ 0 & \exp(-i\omega t/2)\end{pmatrix}. \tag{7.25}$$

The matrix describing the Hamiltonian in the rotating frame becomes after matrix multiplication

$$\widetilde{H} = -\frac{\hbar}{2}\begin{pmatrix}(\omega-\omega_0) + 2\Omega_1\cos(\omega t) & \Omega_0(1+\exp(2i\omega t)) \\ \Omega_0(1+\exp(-2i\omega t)) & -(\omega-\omega_0) + 2\Omega_2\cos(\omega t)\end{pmatrix}. \tag{7.26}$$

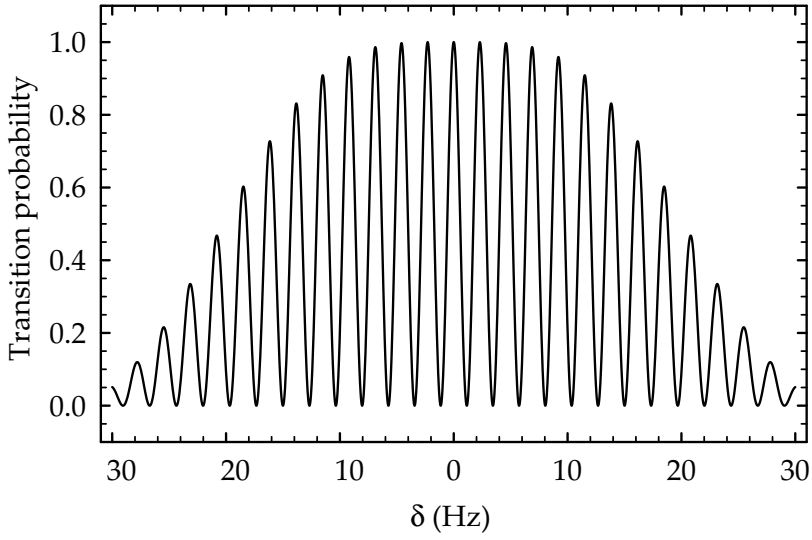

Figure 7.4. Transition probability of an atom launched with a velocity of 3.3 m/s through a microwave cavity with a uniform field. The lower side of the cavity is at 30 cm above the MOT center and the cavity height is 58 mm, so that the interaction time $\tau = 28$ ms and the free drift time $T = 0.4$ s. The central fringe has a fringe contrast of 1 and a FWHM width of 1.2 Hz.

As the interaction time between the atoms and the microwave field is much longer than the oscillation period of the field, the oscillating terms can be neglected (secular approximation [36, complement C_{XIII}]),

$$\widetilde{H} \approx -\frac{\hbar}{2}\begin{pmatrix} \delta & \Omega_0 \\ \Omega_0 & -\delta \end{pmatrix} = -\frac{\hbar}{2}(\boldsymbol{\Omega}\cdot\boldsymbol{\sigma}), \tag{7.27}$$

where detuning $\delta = \omega - \omega_0$, rotation vector $\boldsymbol{\Omega} = \Omega_0\hat{\boldsymbol{x}} + \delta\hat{\boldsymbol{z}}$, and $\boldsymbol{\sigma} = \sigma_x\hat{\boldsymbol{x}} + \sigma_y\hat{\boldsymbol{y}} + \sigma_z\hat{\boldsymbol{z}}$, with Pauli matrices $\sigma_x = \left(\begin{smallmatrix} 0 & 1 \\ 1 & 0 \end{smallmatrix}\right)$, $\sigma_y = \left(\begin{smallmatrix} 0 & -i \\ i & 0 \end{smallmatrix}\right)$ and $\sigma_z = \left(\begin{smallmatrix} 1 & 0 \\ 0 & -1 \end{smallmatrix}\right)$.

The Schrödinger equation in the rotating frame,

$$i\hbar\frac{\mathrm{d}}{\mathrm{d}t}|\widetilde{\psi}\rangle = \widetilde{H}|\widetilde{\psi}\rangle, \tag{7.28}$$

can be solved by direct integration

$$|\widetilde{\psi}(t)\rangle = U(t,t_0)|\widetilde{\psi}(t_0)\rangle = \exp\Big[\frac{i}{2}(\boldsymbol{\sigma}\cdot\boldsymbol{\Omega})(t-t_0)\Big]|\widetilde{\psi}(t_0)\rangle. \tag{7.29}$$

The evolution operator is more conveniently written as [36, complement A_{IX}]

$$U(t,t_0) = \Big\{I\cos\Big[\frac{\Omega}{2}(t-t_0)\Big] + i\,\frac{(\boldsymbol{\sigma}\cdot\boldsymbol{\Omega})}{\Omega}\,\sin\Big[\frac{\Omega}{2}(t-t_0)\Big]\Big\}, \tag{7.30}$$

where $I = \left(\begin{smallmatrix} 1 & 0 \\ 0 & 1 \end{smallmatrix}\right)$ is the unit matrix and $\Omega = |\boldsymbol{\Omega}| = (\delta^2 + \Omega_0^2)^{1/2}$ is the Rabi flopping frequency.

For an interrogation with separated oscillatory fields, the interaction of the atoms with the microwave field in the cavity can be represented by rotation

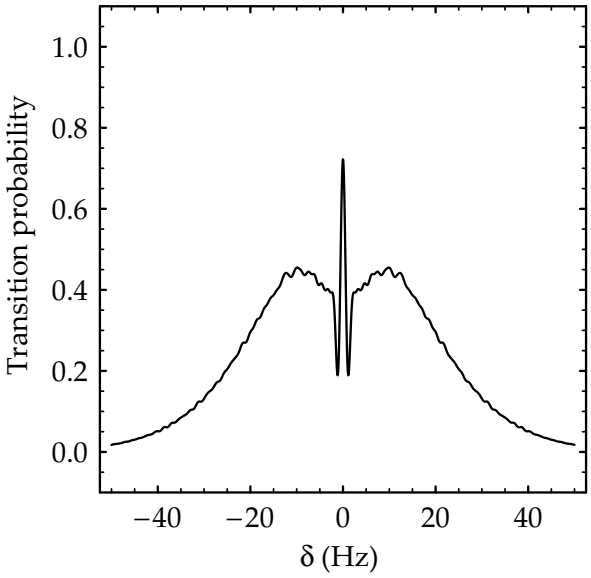

Figure 7.5. Transition probability of a sample of $N = 5.4 \times 10^3$ ^{3}He* atoms with a temperature of 0.2 mK, launched with a mean velocity of 3.3 m/s. Due to the large spread in the vertical velocity, all secondary fringes are washed out and only the central fringe survives. The fringe contrast is 0.6 and the FWHM width is 1.4 Hz.

vector,

$$\mathbf{\Omega} = \begin{cases} \Omega_0(t)\hat{\boldsymbol{x}} + \delta\hat{\boldsymbol{z}} & \text{if } 0 < t < \tau, \\ \delta\hat{\boldsymbol{z}} & \text{if } \tau < t < \tau + T, \\ \Omega_0(t)\hat{\boldsymbol{x}} + \delta\hat{\boldsymbol{z}} & \text{if } \tau + T < t < 2\tau + T, \end{cases} \tag{7.31}$$

where τ is the interaction time, the period of time the atom spends in the cavity, and T is the free drift time, the period of time the atom spends above the cavity. The magnetic field amplitude of the microwave field is chosen such that $\int_0^\tau \Omega_0(t)\,\mathrm{d}t = \pi/2$. For an atom starting off in the ground state and a uniform microwave field, i.e. $\Omega_0(t) = \Omega_0$, the transition probability can be written [159]

$$\left|\langle\widetilde{\mathrm{e}}|U(2\tau+T,0)|\widetilde{\mathrm{g}}\rangle\right|^2 = 4\,\frac{\Omega_0^2}{\Omega^2}\,\sin^2(\Omega\tau/2)\left[\cos(\delta T/2)\,\cos(\Omega\tau/2) - \frac{\delta}{\Omega}\,\sin(\delta T/2)\,\sin(\Omega\tau/2)\right]^2 \tag{7.32}$$

where $U(2\tau+T,0) = U(2\tau+T,\tau+T)\,U(\tau+T,\tau)\,U(\tau,0)$. The probability is shown as a function of detuning in Fig. 7.4. The transition probability for microwave excitation in a TE_{011} cavity, where magnetic field amplitude $B = B_0\sin(\pi z/d)$ with the cavity between $z = 0$ and $z = d$, cannot be given in an analytical form, but is easily calculated numerically.

Figure 7.5 shows the averaged Ramsey fringe pattern (using a sine-shaped magnetic-field amplitude) of a sample of $N = 5.4 \times 10^3$ ^{3}He* atoms with a temperature of 0.2 mK and a mean launch velocity of 3.3 m/s (the vertical velocities are distributed according to $\tilde{f}(v_z)$, shown in Fig. 7.3). The FWHM width of the central fringe is 1.4 Hz. Such a narrow fringe can in principle be used to stabilize the microwave frequency to the clock transition.

7.4 Expected stability

To characterize the performance of an atomic clock, the stability is a crucial factor. The stability (or more precisely frequency instability) is a measure of the stochastic and/or environmentally induced fluctuations of the output frequency of an atomic frequency standard and is expressed as the Allan variance of the fractional frequency difference

$$y(t) = \frac{\nu(t) - \nu_0}{\nu_0}. \tag{7.33}$$

The Allan variance is obtained from a measurement procedure, where the fractional frequency difference is integrated over a time τ (not to be confused with the interaction time τ of the method of separated oscillatory fields), typically between 10 s and 10^4 s, to obtain averages

$$\langle y_k \rangle = \frac{1}{\tau} \int_{t_k}^{t_k+\tau} y(t)\, \mathrm{d}t. \tag{7.34}$$

From a set of N values for $\langle y_k \rangle$, the Allan variance is obtained as [2]

$$\sigma_y(\tau) = \frac{1}{\sqrt{2(N-1)}} \left[\sum_{k=1}^{N-1} \left(\langle y_k \rangle - \langle y_{k-1} \rangle \right)^2 \right]^{1/2}. \tag{7.35}$$

In fountain clocks, the stability contains noise contributions from the detection system (electron noise in the case of a MCP detector) and the interrogation oscillator, as well as quantum projection noise [86]. For an atomic fountain clock based on ^{133}Cs with $N = 6 \times 10^5$ it has been shown that detector noise and interrogation oscillator noise can be made small compared to quantum projection noise [169], that is given by [62, 217]

$$\sigma_y(\tau) = \frac{1}{\pi Q_{\mathrm{atom}}} \sqrt{\frac{T_\mathrm{c}}{\tau}} \frac{1}{\sqrt{N}}, \qquad \tau \gg T_\mathrm{c}. \tag{7.36}$$

For a ^{3}He* fountain clock, the number of detected atoms is considerably smaller, so that the quantum projection noise contribution is larger and it is natural to assume that the stability will be ultimately limited by quantum projection noise.

With a FWHM width of the central Ramsey fringes of $\Delta_{\mathrm{fringe}} = 1.4$ Hz, the quality factor of the transition $Q_{\mathrm{atom}} = \nu_0/\Delta_{\mathrm{fringe}} = 4.8 \times 10^9$. Assuming a 100% detection efficiency, $N = 5.4 \times 10^3$ and, for a typical cycle time $T_\mathrm{c} = 1$ s, the Allan variance is

$$\sigma_y(\tau) = 9.0 \times 10^{-13} \tau^{-1/2}. \tag{7.37}$$

This number is comparable to state of the art Cs beam atomic frequency standards [181], but inferior to atomic fountain clocks based on ^{133}Cs, $\sigma_y(\tau) = 4 \times 10^{-14} \tau^{-1/2}$ [110], or ^{87}Rb, $\sigma_y(\tau) = 1.5 \times 10^{-13} \tau^{-1/2}$ [110], or the optical frequency standard based on a single ^{199}Hg$^+$ ion, $\sigma_y(\tau) \leq 7 \times 10^{-15} \tau^{-1/2}$ [18]. To obtain a stability of 10^{-15}, an averaging time of $\tau = 8.08 \times 10^5$ s $= 224$ h is required in the case of ^{3}He*.

7.5 Expected accuracy

A good stability is a prerequisite for an accurate atomic clock, but not all stable clocks are accurate. Where the stability characterizes fluctuations of the output frequency, the accuracy (or sometimes systematic inaccuracy) indicates the level of precision at which the output frequency is known. Various effects of fundamental and technical nature result in shifts of the output frequency from the atomic frequency. Various measurements and calculations are performed to determine these shifts, making up the so-called accuracy budget in an accuracy evaluation [110, 181]. For fountain clocks, the accuracy budget includes (amongst others) the Stark shift due to blackbody radiation, the cold collision frequency shift and the Zeeman shift. The corresponding uncertainties are a few 10^{-16}, resulting in a total (in)accuracy of 4×10^{-16} (or slightly larger) for state of the art Cs fountain clocks [50]. For the ^{3}He* fountain clock, the cold collision frequency is expected to be negligible, as ^{3}He is a fermion. As a result of the magnetic field dependence of the clock transition (see Eq. (7.12)), the Zeeman shift is expected to be relatively large. Here, the uncertainty of the Zeeman shift correction is estimated, which can be considered a limiting value for the accuracy of a ^{3}He* fountain clock.

During the free flight stage in the Ramsey interrogation procedure, the evolution of the quantum state of the (two-level) atomic system, undergoing a Zeeman shift $\omega_{\text{atom}}(t) = \omega_0 + \delta_{\text{Zeeman}}(t)$ is given by

$$U(\tau + T, \tau) = I \cos\big(\langle\delta\rangle T/2\big) + i\sigma_z \sin\big(\langle\delta\rangle T/2\big) \tag{7.38}$$

where

$$\langle\delta\rangle = \frac{1}{T}\int_{\tau}^{\tau+T} \big[\omega - \omega_{\text{atom}}(t)\big]\,\mathrm{d}t = (\omega - \omega_0) - \langle\delta_{\text{Zeeman}}\rangle \tag{7.39}$$

with $\langle\delta_{\text{Zeeman}}\rangle = (1/T)\int_{\tau}^{\tau+T} \delta_{\text{Zeeman}}(t)\,\mathrm{d}t$. In the low-field configuration, the clock transition depends linearly on magnetic field and the Ramsey fringe pattern of a single atom is shifted by (Eq. (7.13))

$$\langle\delta_{\text{Zeeman}}\rangle/2\pi \approx (-9.33 \times 10^5) \times \langle B\rangle \tag{7.40}$$

where $\langle B\rangle = (1/T)\int_{\tau}^{\tau+T} B(t)\,\mathrm{d}t$, with B in Gauss and $\langle\delta_{\text{Zeeman}}\rangle$ in rad/s. Assuming that the magnetic field is known with an uncertainty $\delta B < 0.1$ mG (order of magnitude of the best commercial NMR probes), the uncertainty in the Zeeman shift correction is $\langle\delta_{\text{Zeeman}}\rangle/2\pi \approx 93$ Hz. The corresponding relative uncertainty is 1×10^{-8}, which is far inferior to the uncertainty of Cs fountain clocks (by almost eight orders of magnitude). It can be concluded that, as a result of the linear magnetic field dependence, the low-field configuration is not suitable for frequency metrology.

In the high-field configuration, the clock transition depends only quadratically on the magnetic field and the Zeeman shift of the Ramsey fringe pattern of a single atom is given by (Eq. (7.14))

$$\langle\delta_{\text{Zeeman}}\rangle/2\pi \approx 617 \times \langle B^2\rangle. \tag{7.41}$$

If the magnetic field is known with an uncertainty $\delta B < 0.1$ mG, the uncertainty in the Zeeman shift correction is $\langle \delta_{\text{Zeeman}} \rangle / 2\pi \approx 6 \times 10^{-6}$ Hz and the relative uncertainty is 1×10^{-15}, which is comparable to the uncertainty of the total accuracy budget of Cs fountain clocks. For Cs (and Rb) fountain clocks, the Zeeman shift correction is deduced from a leveraged measurement of the magnetic field by recording Ramsey fringes on a magnetically dependent transition. Choosing a transition with $\Delta M = 0$ and a frequency close to the clock frequency, the excitation is driven in the microwave cavity and the uncertainty of the resulting correction is only $\lesssim 10^{-16}$ [110]. In the case of ^{3}He*, a single $\Delta M = 0$ field-dependent transition is available, ν_+ (see Eq. (7.12)). As its transition frequency is 7.8 GHz, excitation in the microwave cavity is not straightforward.

7.6 Monte Carlo simulations

The Zeeman shift correction of Eq. (7.41) applies to the Ramsey fringe pattern of a single atom, as shown in Fig. 7.4. To determine the effect of the magnetic field on the Ramsey fringe pattern of a sample of atoms (see Fig. 7.5), a Monte Carlo simulation is performed. Only the high-field configuration is considered.

The simulation is performed with a code written in ANSI C. For a number of 5400 atoms, the evolution of the quantum state is calculated with Eq. (7.30). For each atom, a random velocity v_z is generated, distributed according to the probability function $\tilde{f}(v_z)$ of Eq. (7.10). For a given magnetic field $B(z)$ in the interrogation region (microwave cavity and free flight region), the rotation vector $\boldsymbol{\Omega} = \Omega_0(t)\hat{\boldsymbol{x}} + \delta(t)\hat{\boldsymbol{z}}$ is determined and the corresponding transition probability is calculated. The Ramsey fringe pattern is obtained by calculating the average transition probability for atoms in the sample, over a range of detunings $\delta/2\pi = (\omega - \omega_0)/2\pi$, from -50 Hz to $+50$ Hz. Temporal instabilities of the magnetic field profile are neglected, as they can be controlled at high level with a stable current supply and mu-metal shields [87].

Ramsey fringe patterns are calculated for several magnetic field profiles of limited homogeneity, expressed in terms of the rms deviation

$$\sigma_B = \frac{1}{T} \int_{\tau}^{\tau+T} \big(B_{\text{high}} - B(t) \big) \, \mathrm{d}t, \tag{7.42}$$

as experienced by an atom that is launched with a velocity $v_z = 3.3$ m/s. For a constant magnetic field $B(t) = B_{\text{high}}$, the relative homogeneity $\sigma_B/B = 0$ and the fringe pattern is shown in Fig. 7.5. The central fringe has a contrast of 0.6 and a FWHM width of 1.1 Hz. Figure 7.6 shows the Ramsey fringe pattern for three magnetic field profiles (also shown). For a magnetic field profile with a relative homogeneity of $\sigma_B/B = 5 \times 10^{-7}$, the fringe profile hardly deviates from the ideal case. However, if a relative homogeneity of $\sigma_B/B = 3 \times 10^{-5}$ or $\sigma_B/B = 8 \times 10^{-5}$ is chosen [39], the fringe pattern becomes distorted. In the first case, an asymmetric central fringe is still visible (contrast of 0.6), but in the second case, the central fringe is washed out and, although narrow features (1 Hz) are visible, the contrast is only 0.15.

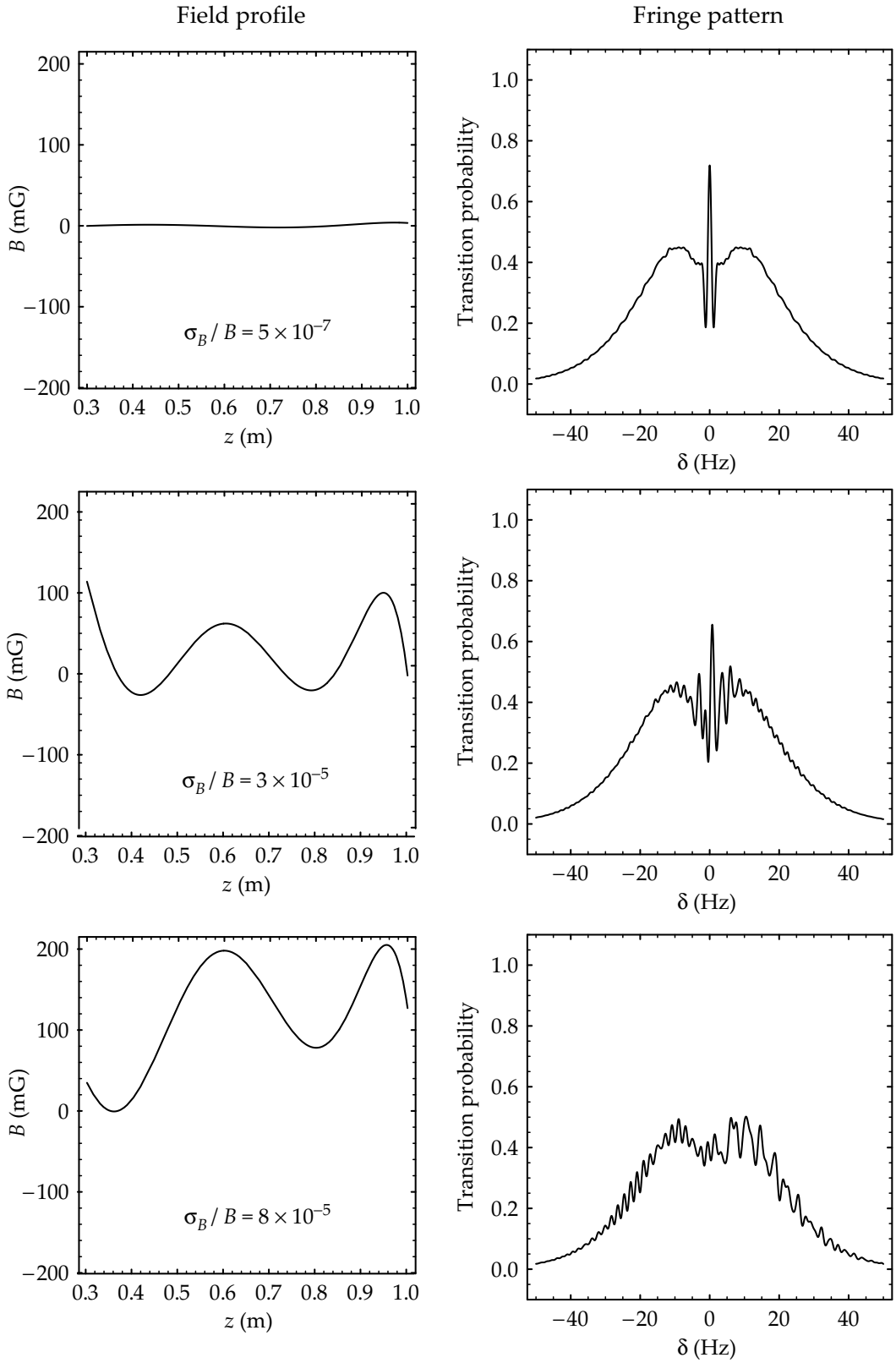

Figure 7.6. Magnetic field profile in the interrogation region (0.30 m $< z <$ 1.00 m) and the resulting Ramsey fringe pattern for a sample of $N = 1 \times 10^8$ ^{3}He* atoms with a temperature of 0.2 mK, launched upward with a mean velocity of 3.3 m/s. The number of detected atoms is 5400. The relative homogeneity σ_B / B is indicated with the magnetic field profile.

7.7 Discussion and conclusions

The expected performance of the ^{3}He* fountain clock is inferior to the performance of ^{133}Cs and ^{87}Rb fountain clocks. Both the stability, $\sigma_y(\tau) = 7 \times 10^{-13}\tau^{-1/2}$, and the uncertainty of the Zeeman shift correction $\sigma_\nu/\nu = 1 \times 10^{-15}$, are larger by one order magnitude. Moreover, the contrast of the Ramsey fringe pattern depends strongly on the homogeneity of the magnetic field in the interrogation region, as the vertical velocity distribution of the detected atoms is fairly broad. Using conventional techniques, a relative magnetic field homogeneity of the order of $\sigma_B/B \approx 6 \times 10^{-5}$ can be obtained [39]. For homogeneities of this magnitude, the visibility of the corresponding Ramsey fringe pattern could be as poor as 0.15. It should also be noted that the achievement of a relative homogeneity better than 10^{-4} requires time-consuming shimming techniques [87].

The expected performance hampers an investigation of the innovative aspects of the ^{3}He* fountain clock, mentioned in Section 1.3. The relatively poor stability makes an investigation of frequency shifts with a precision $\lesssim 10^{-15}$ virtually impossible, as averaging times $\tau > 100$ h would be required.

The suppressed cold collision frequency shift in the ^{3}He* fountain clock and the negligible contribution to the accuracy budget are neutralized by the large contribution of the Zeeman frequency shift. In Cs fountain clocks, the uncertainty of the collision frequency shift is $\leq 5 \times 10^{-16}$ [110], while the the uncertainty of the Zeeman shift in the ^{3}He* fountain clock is expected to be 1×10^{-15}. For Rb fountain clocks, the collisional frequency shift is smaller by at least a factor of 50 [60, 186] and the corresponding uncertainty is only $\leq 1 \times 10^{-16}$ [17]. Apart from its relative contribution to the accuracy budget, the cold collision frequency shift in the ^{3}He* fountain clock could never be investigated[3] as the atomic density in the interrogation region is very small, $n = 4 \times 10^2$ cm^{-3} at the apex for a mean launch velocity of 3.3 m/s.

The output frequency of two atomic clocks based on different atomic species can be compared to detect possible variations of the fine-structure constant $\alpha = e^2/4\pi\epsilon_0\hbar c$. Variations in the ratio of the output frequencies are related to variations in the fine-structure constant through [155]

$$\frac{\mathrm{d}}{\mathrm{d}t}\ln\left(\frac{\nu_1}{\nu_2}\right) = \left[L_d F_{\mathrm{rel}}(Z_1) - L_d F_{\mathrm{rel}}(Z_2)\right]\frac{1}{\alpha}\frac{\mathrm{d}\alpha}{\mathrm{d}t}. \tag{7.43}$$

The function $L_d F_{\mathrm{rel}}(Z)$ that expresses the sensitivity of the hyperfine transition frequency of an atomic species to the fine-structure constant is plotted in Fig. 7.7, with Z the atomic number. A measurement of the output frequency of the ^{3}He* fountain clock against a Cs fountain clock is characterized by a sensitivity $L_d F_{\mathrm{rel}}(Z_{\mathrm{He}}) - L_d F_{\mathrm{rel}}(Z_{\mathrm{Cs}}) = -0.74$, that is larger than the sensitivity associated with a measurement of a Rb clock against a Cs fountain clock,

[3] The suppression of the collision frequency shift could be investigated by comparing the frequency shift for a sample of identical fermions ($M_F = -1/2$) to the frequency shift for a sample of non-identical fermions (all M_F equally populated).

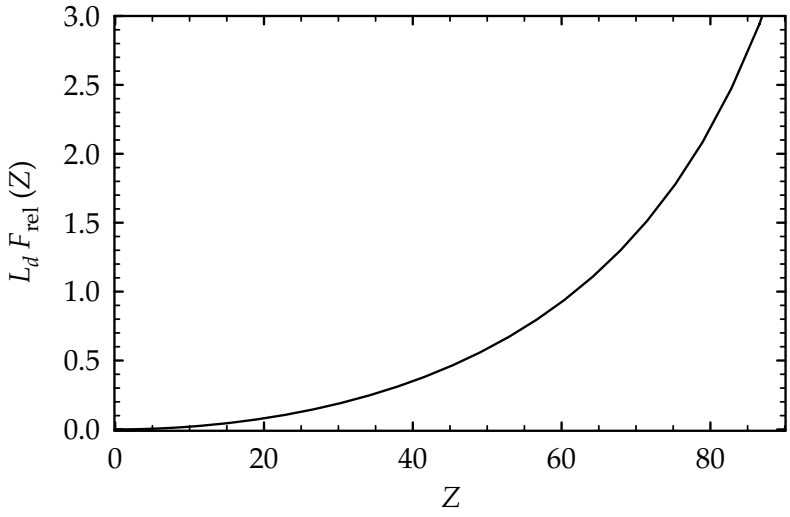

Figure 7.7. Function $L_d F_{\mathrm{rel}}$ plotted against atomic number Z.

$L_d F_{\mathrm{rel}}(Z_{\mathrm{Rb}}) - L_d F_{\mathrm{rel}}(Z_{\mathrm{Cs}}) = -0.45$. However, due to the relatively poor stability and accuracy of the ^{3}He* clock, measurements of the variation of α are not expected to be as accurate as measurements that are obtained when comparing a Rb and Cs clock, where $\frac{\mathrm{d}}{\mathrm{d}t}\ln(\nu_{\mathrm{Rb}}/\nu_{\mathrm{Cs}}) = (0.2 \pm 7.0) \times 10^{-16}\ \mathrm{yr}^{-1}$ was determined [122]. Recently, the combined comparisons of microwave transitions in ^{133}Cs and ^{87}Rb and optical transitions in atomic hydrogen and ^{199}Hg$^+$ have led to a limit on $\frac{1}{\alpha}\frac{\mathrm{d}\alpha}{\mathrm{d}t}$ of $(-0.9 \pm 2.9) \times 10^{-15}\ \mathrm{yr}^{-1}$ [61].

Naturally, methods to improve the performance of the ^{3}He* fountain clock are conceivable. Detection of atoms in a limited velocity range (velocity selection) would yield an improvement of the fringe contrast. However, it would also result in a decrease of the stability, which is undesirable. Further cooling of the launched sample, which might be realized with sympathetic cooling (which has not yet been demonstrated for ^{3}He* atoms), would yield an improvement of both the fringe contrast and stability. Still, the accuracy of the fountain clock would be relatively poor due to the Zeeman shift of the clock frequency, while a better knowledge or control of the magnetic field in the interrogation region seems unrealistic for the time being. Therefore, it must be concluded that it would not be sensible to perform an experimental study of a ^{3}He* fountain clock.

Finally, it should be noted that with the introduction of frequency combs [84], much effort is devoted to the development of all-optical atomic clocks [51]. It is very likely that in the near future optical clocks can be made more accurate than microwave fountain clocks, while a superior stability has already been demonstrated (mainly due to the high quality factor Q_{atom} of optical transitions). The accuracy of microwave fountain clocks is predicted to approach 1×10^{-16} [110], where for single-ion optical clocks accuracies approaching 1×10^{-18} have been predicted [46].

Appendix A

Laser cooling transitions

In the various experiments discussed in this thesis, laser cooling of He* atoms is performed using laser light with a wavelength of 389 nm or 1083 nm. In this appendix, a discussion of relevant aspects of the associated atomic transitions (referred to as laser cooling transitions) is presented. First, the (hyper)fine structure of the spectral terms connected by the transitions is discussed. The transition with wavelength $\lambda = 1083$ nm connects spectral terms $2\,^3S_1$ and $2\,^3P$, and the transition with $\lambda = 389$ nm connects $2\,^3S_1$ and $3\,^3P$. Also, the Zeeman effect on the relevant (hyper)fine-structure states is described, i.e. $2\,^3S_1(F = \frac{1}{2}, \frac{3}{2})$ and $2\,^3P(F' = \frac{1}{2}, \frac{3}{2}, \frac{1}{2}, \frac{3}{2}, \frac{5}{2})$ for ^{3}He ($\lambda = 1083$ nm), and $2\,^3S_1$, $2\,^3P_{0,1,2}$ and $3\,^3P_{0,1,2}$ for ^{4}He ($\lambda = 1083$ nm and 389 nm). To determine the saturation intensity of the laser cooling transitions, the optical excitation of the transitions is described from a semi-classical point of view, where the interaction of laser light with the atomic transition is represented by the electric dipole operator.

(Hyper)fine structure

For ^{4}He, spectral terms $n\,^3P$ are split up into fine-structure states. The ^{3}He atom has a nuclear spin $I = \frac{1}{2}$, so that spectral term $2\,^3S_1$ shows hyperfine structure and term $2\,^3P$ both fine and hyperfine structure. For the latter term, fine-structure and hyperfine interaction are of the same order of magnitude and are well described with a phenomenological theory that incorporates singlet-triplet mixing [41, 83]. Figure A.1 shows the states and the intervals in-between for the transitions with $\lambda = 1083$ nm of both ^{3}He and ^{4}He. Spectral term $3\,^3P$ has a similar structure as $2\,^3P$ with energy intervals as given in the caption of Fig. A.1. As a result of a large spin-spin and spin-other-orbit interaction, the fine-structure intervals in the $n\,^3P$ spectral term do not comply with the Landé interval rule

Table A.1. Atomic properties of isotopes ^{3}He and ^{4}He.

	^{3}He	^{4}He
Atomic mass m (amu[a])	3.0160[b]	4.0026[b]
Nuclear spin I	$\frac{1}{2}$	0
Natural abundance (%)	0.00014[c]	99.99986[c]
Ionization limit (cm^{-1})	198300[d]	198311[d]
Internal energy 2 ^{3}S$_1$ state (cm^{-1})	159847[d]	159856[d]

[a] The atomic mass unit (1 amu or 1 u) corresponds to 1.6605×10^{-27} kg.

[b] Reference [8, 38, 40].

[c] Representative values obtained from atmospheric helium gas by mass spectrometry [40, 165]. The isotopic ratio ^{3}He/^{4}He in natural materials varies from 1×10^{-8} (continental rocks) to 5×10^{-4} (primitive solar system material and lunar soil) [208].

[d] Values calculated by Drake [54]. The internal energies for ^{3}He are calculated from the corresponding energies for ^{4}He, taking into account the normal mass shift and first and second order mass polarization corrections. The isotopic differences in the energies are $< 10^{-4}$ and irrelevant for the work presented in this thesis. Expressed in convenient units, the internal energies are 24.59 eV for the ionization limit and 19.82 eV for the 2 ^{3}S$_1$ state.

Table A.2. Values of the g-factors [41, 224, 225].

	g_S	g_L	g_I
^{3}He, 2 ^{3}S$_1$	2.002	0	2.317×10^{-3}
^{4}He, 2 ^{3}S$_1$	2.002	0	0
^{3}He, 2 ^{1}P	2.002	0.9999	2.317×10^{-3}
^{3}He, 2 ^{3}P	2.002	0.9999	2.317×10^{-3}
^{4}He, 2 ^{3}P	2.002	0.9999	0
^{4}He, 3 ^{3}P	2.002	0.9999	0

[36, complement B$_{XIV}$]. The transitions are denoted by D$_0$–D$_2$ for ^{4}He, and C$_1$–C$_9$ for ^{3}He. Transitions D$_2$ and C$_3$ are the laser cooling transitions. Table A.1 provides an overview of some atomic properties of both isotopes.

Zeeman effect

The Zeeman effect on the various states is well described by Hamiltonian [41]

$$H_Z = \mu_B(g_L \mathbf{L} \cdot \mathbf{B} + g_S \mathbf{S} \cdot \mathbf{B} + g_I \mathbf{I} \cdot \mathbf{B}), \tag{A.1}$$

with g-factor as given in Table A.2. To calculate the Zeeman energy diagrams for the states, the fine-structure interaction, hyperfine interaction and Zeeman interaction are taken into account simultaneously. For the states of ^{4}He and the 2 ^{3}S$_1(F)$ of ^{3}He, (hyper)fine interaction Hamiltonians are constructed from the

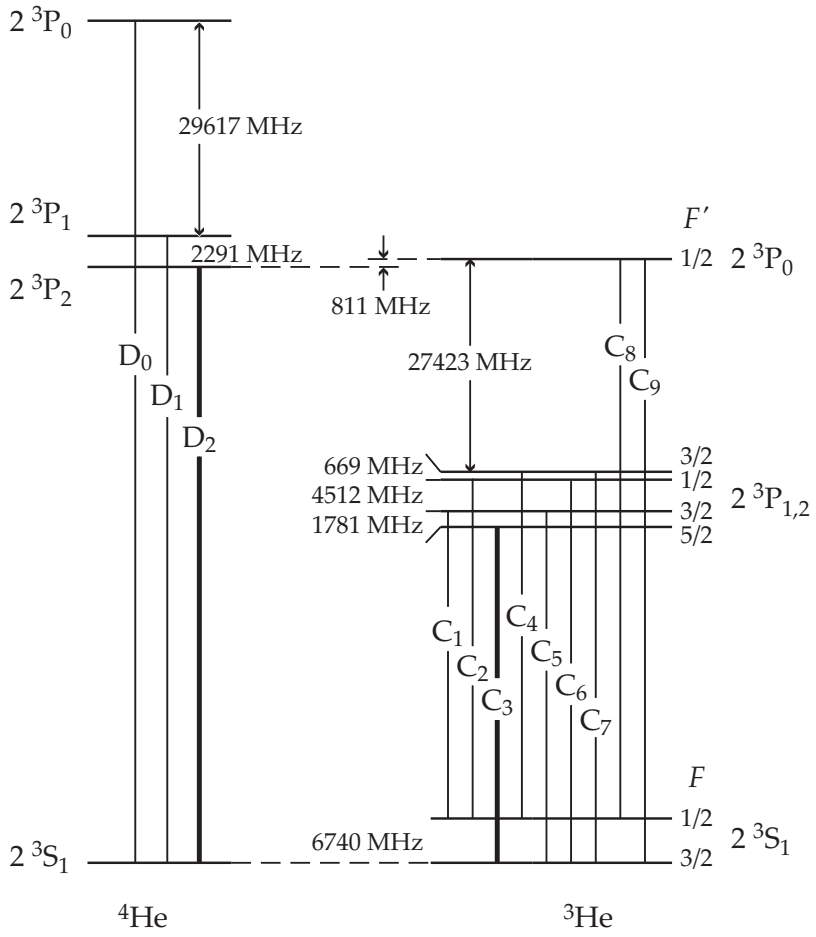

Figure A.1. Relevant levels and transitions in ^{3}He and ^{4}He around a wavelength of 1083 nm. The energy interval $2\,^3P_0 - 2\,^3P_1$ is taken from [189], and interval $2\,^3P_0 - 2\,^3P_1$ is taken from [68]. Spectral term $3\,^3P$ has a similar structure as $2\,^3P$, with intervals of 659 MHz ($3\,^3P_1 - 3\,^3P_2$) and 8114 MHz ($3\,^3P_0 - 3\,^3P_1$) [225]. The hyper(fine) intervals in spectral term $2\,^3P$ of ^{3}He are taken from [154] and the hyperfine interval in $2\,^3S_1$ is taken from [166, 167]. The isotope shift of transition $2\,^3S_1 \rightarrow 2\,^3P$ is taken from [230]. The values provided in the figure are less accurate than the values reported in the various references, as higher accuracies are irrelevant in the laser cooling experiments presented in this thesis. Please note that the energy scale shows several discontinuities.

values of the energy intervals. The calculations are confined to the subspaces spanned by the corresponding states, i.e. mixing with other states is neglected. For states $2\,^3\mathrm{P}(F')$ of ^{3}He, the phenomenological theory of [83] is applied, where coupling by the (hyper)fine interaction of states $2\,^3\mathrm{P}(F')$ to $2\,^1\mathrm{P}$ is taken into account.[1] A thorough study of the Zeeman effect on the 1083 nm transitions in ^{3}He and ^{4}He (including an overview of pre-existing work) is given in [41]. The Zeeman diagrams for the ground states, $2\,^3\mathrm{S}_1(F)$ and $2\,^3\mathrm{S}_1$, are shown in Figs. A.2 and A.3, respectively. The Zeeman diagrams for the excited states, $2\,^3\mathrm{P}(F')$, $2\,^3\mathrm{P}$ and $3\,^3\mathrm{P}$, are shown in Figs. A.4, A.5 and A.6, respectively. If the Zeeman energy shift is small compared to the (hyper)fine splitting, the Zeeman Hamiltonian can be approximated as

$$\mathrm{H_Z} = \mu_\mathrm{B} g_J \, \mathbf{J} \cdot \mathbf{B}, \tag{A.2}$$

in the case of ^{4}He*, and

$$\mathrm{H_Z} = \mu_\mathrm{B} g_F \, \mathbf{F} \cdot \mathbf{B}, \tag{A.3}$$

in the case of ^{3}He*. As $g_J > 0$ and $g_F > 0$ for the (hyper)fine states discussed here, the energy curves of Figs. A.2–A.6 can be labeled (in the low-field limit) in order of increasing energy with $M_J = -J, -J+1 \ldots, J$ in the case of ^{4}He*, and $M_F = -F, -F+1 \ldots, F$ in the case of ^{3}He*.

[1] A theoretical calculation of the ^{3}He $2\,^3$P structure with an accuracy of about 1 MHz has confirmed the validity of the phenomenological approach [81].

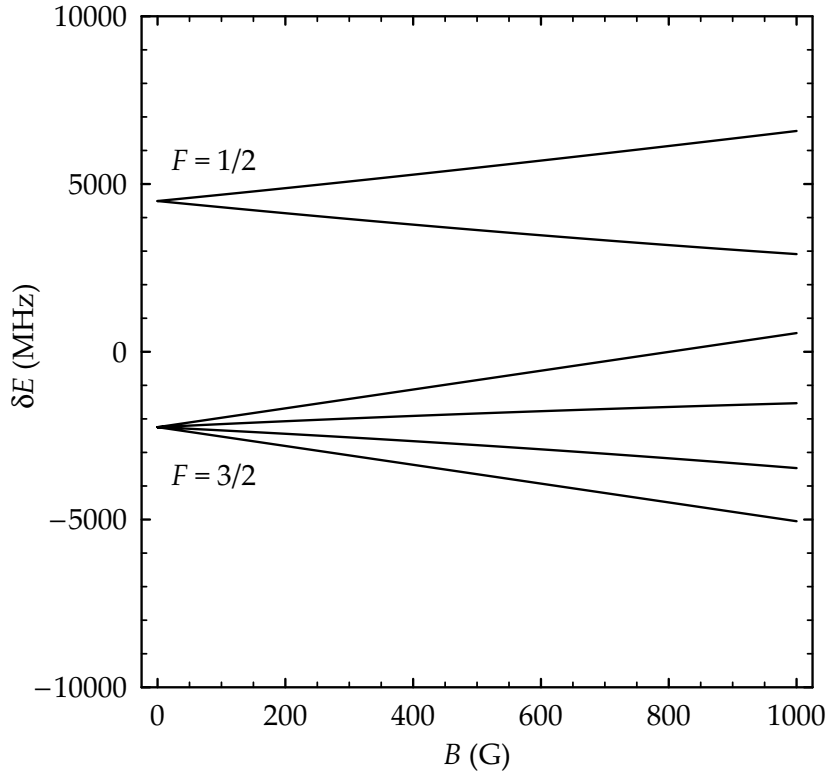

Figure A.2. Zeeman diagrams for the 2 ^{3}S states of ^{3}He. For $F = \frac{1}{2}$, Landé factor $g_F = \frac{4}{3}g_S - \frac{1}{3}g_I \approx 2.669$; for $F = \frac{3}{2}$, $g_F = \frac{2}{3}g_S + \frac{1}{3}g_I \approx 1.335$.

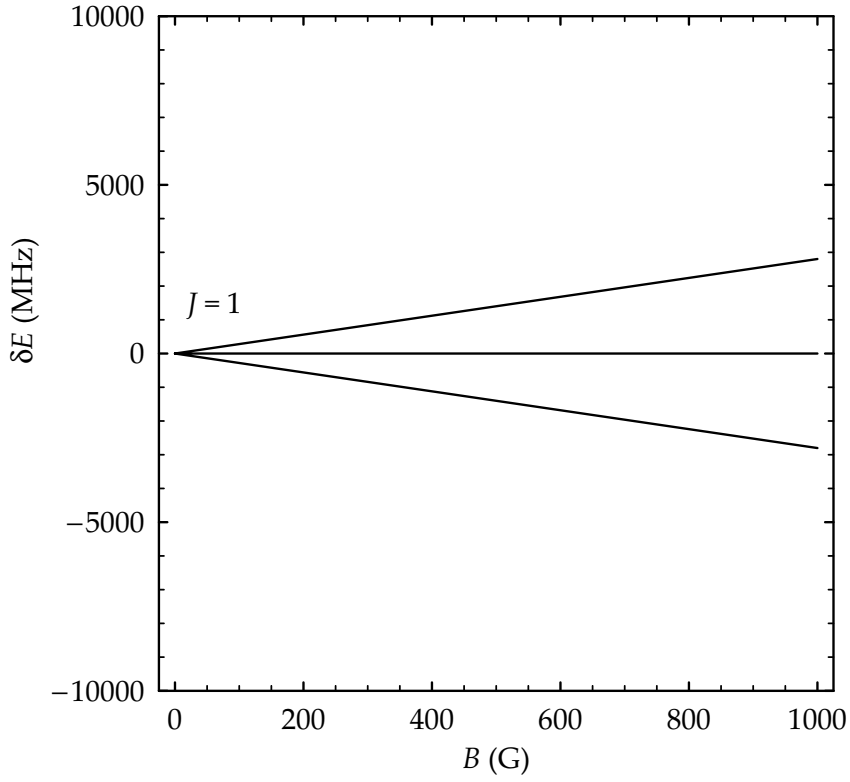

Figure A.3. Zeeman diagrams for the 2 ^{3}S states of ^{4}He. Landé factor $g_J = g_S \approx 2.002$.

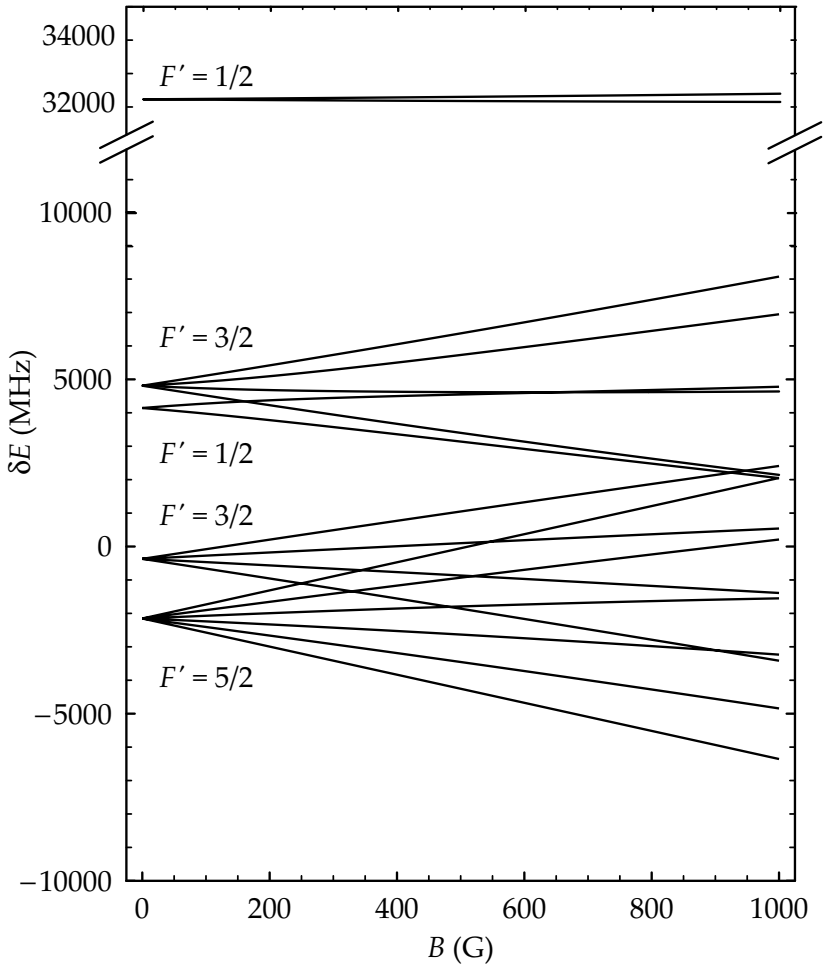

Figure A.4. Zeeman diagrams for the 2 ^{3}P states of ^{3}He.

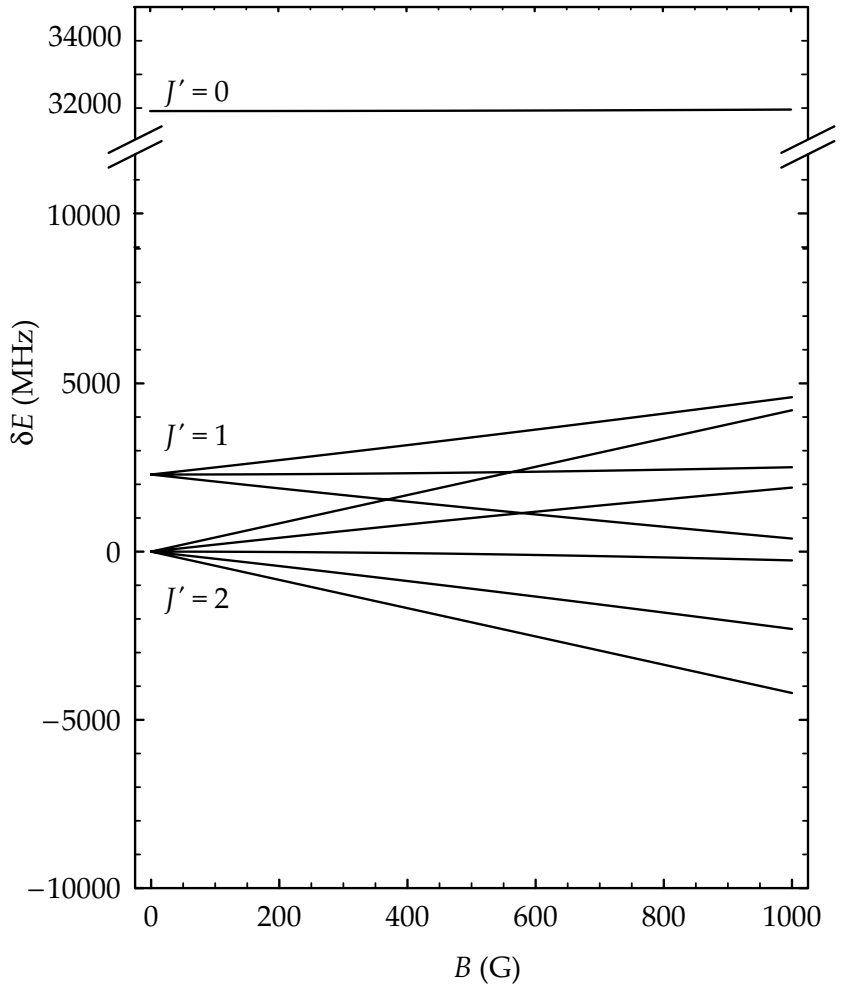

Figure A.5. Zeeman diagrams for the 2 ^{3}P states of ^{4}He.

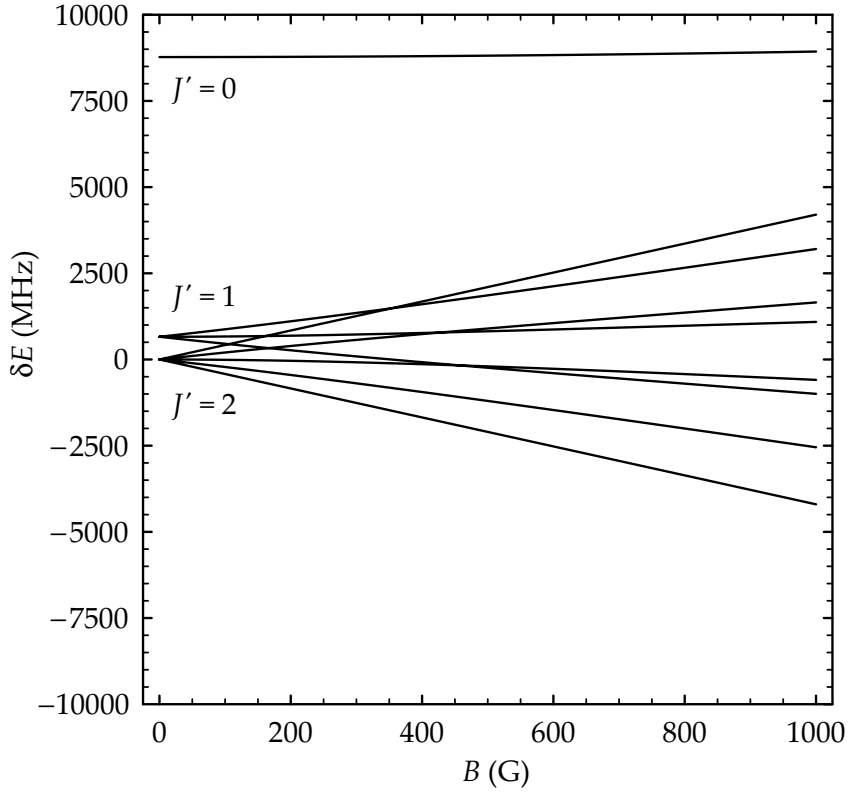

Figure A.6. Zeeman diagram for the 3 ^{3}P states of ^{4}He.

Optical excitation

The interaction of laser light with an atomic transition $|\mathrm{g}\rangle \rightarrow |\mathrm{e}\rangle$ can be treated with the electric dipole operator $e\mathbf{r}$ [130]: the coupling of ground state $|\mathrm{g}\rangle$ to excited state $|\mathrm{e}\rangle$ by a light wave

$$\boldsymbol{E}(\boldsymbol{r},t) = E\boldsymbol{\epsilon}_q \cos(\boldsymbol{k}\cdot\boldsymbol{r} - \omega t) \tag{A.4}$$

is given by the square of the Rabi frequency,

$$\Omega_{\mathrm{ge}}^2 = \left|\langle \mathrm{g}|e(\boldsymbol{\epsilon}_q\cdot\mathbf{r})\,|\mathrm{e}\rangle\right|^2 \frac{E^2}{\hbar^2} = \left|\langle \mathrm{g}|e\mathrm{r}_q|\mathrm{e}\rangle\right|^2 \frac{E^2}{\hbar^2}, \tag{A.5}$$

where E is the amplitude of the electric field of the laser light and $\langle \mathrm{g}|e\mathrm{r}_q|\mathrm{e}\rangle$ is the matrix element between ground and excited state of the component of the electric dipole operator associated with the polarization of the light (given by polarization vector $\boldsymbol{\epsilon}$). To simplify matters, three distinct polarization states are considered:[2] π-polarization ($q=0$, $\boldsymbol{\epsilon}_0 = \hat{\boldsymbol{z}}$), σ^--polarization ($q=-1$, $\boldsymbol{\epsilon}_{-1} = (\hat{\boldsymbol{x}} - i\hat{\boldsymbol{y}})/\sqrt{2}$), and σ^+-polarization ($q=1$, $\boldsymbol{\epsilon}_1 = -(\hat{\boldsymbol{x}} + i\hat{\boldsymbol{y}})/\sqrt{2}$) [55, 130]. The strength of the coupling (square of the Rabi frequency) depends on the electric field amplitude (or light intensity $I = \epsilon_0 E^2 c/2$) and on the electron wave functions of the atom through the dipole matrix element.

Electric dipole matrix elements can be calculated by reduction to the (L,S) basis [130]. For the laser cooling transitions of ^{4}He ($2\,^3\mathrm{S}_1 \rightarrow n\,^3\mathrm{P}_2$), the matrix element is reduced to

$$\begin{aligned}\left\langle 2\,^3\mathrm{S}_1 M_J\middle|e\mathrm{r}_q\middle|n\,^3\mathrm{P}_2 M_J'\right\rangle &= (-1)^{L'-S-M_J'}\sqrt{(2J+1)(2J'+1)} \\ &\times \begin{Bmatrix} L' & J' & S \\ J & L & 1\end{Bmatrix}\begin{pmatrix} J & 1 & J' \\ M_J & q & -M_J'\end{pmatrix}\left\langle 2\,^3\mathrm{S}\middle\|e\mathrm{r}_q\middle\|n\,^3\mathrm{P}\right\rangle \\ &= (-1)^{M_J'}\sqrt{\tfrac{15}{9}}\begin{pmatrix} 1 & 1 & 2 \\ M_J & q & -M_J'\end{pmatrix}\left\langle 2\,^3\mathrm{S}\middle\|e\mathrm{r}_q\middle\|n\,^3\mathrm{P}\right\rangle, \end{aligned} \tag{A.6}$$

with $q = M_J' - M_J$, $L=0$, $S=1$, $J=1$, $L'=1$ and $J'=2$. For transition $M_J = 1 \rightarrow M_J' = 2$,

$$\left\langle 2\,^3\mathrm{S}_1, M_J = 1\middle|e\mathrm{r}_q\middle|n\,^3\mathrm{P}_2, M_J' = 2\right\rangle = \sqrt{\tfrac{1}{3}}\left\langle 2\,^3\mathrm{S}\middle\|e\mathrm{r}_q\middle\|n\,^3\mathrm{P}\right\rangle. \tag{A.7}$$

Matrix elements for $J' = 0, 1$ can be calculated in a similar manner.

For the laser cooling transition of ^{3}He $\left(2\,^3\mathrm{S}_1(F'=\frac{3}{2}) \rightarrow 2\,^3\mathrm{P}_2(F'=\frac{5}{2})\right)$, the hyperfine interaction must be taken into account and the matrix element is

[2] Other polarization states can be expanded onto these states.

reduced to

$$\begin{aligned}\left\langle 2\,^3\mathrm{S}_1(F=\tfrac{3}{2})M_F\middle|er_q\middle|2\,^3\mathrm{P}_2(F'=\tfrac{5}{2})M'_F\right\rangle \\ = (-1)^{1+L'+S+J+J'+I-M'_F}\sqrt{(2J+1)(2J'+1)(2F+1)(2F'+1)} \\ \times \begin{Bmatrix} L' & J' & S \\ J & L & 1 \end{Bmatrix}\begin{Bmatrix} J' & F' & I \\ F & J & 1 \end{Bmatrix}\begin{pmatrix} F & 1 & F' \\ M_F & q & -M'_F \end{pmatrix}\left\langle 2\,^3\mathrm{S}\middle\|er_q\middle\|2\,^3\mathrm{P}\right\rangle \\ = (-1)^{1/2-M'_F}\sqrt{2}\begin{pmatrix} 3/2 & 1 & 5/2 \\ M_F & q & -M'_F \end{pmatrix}\left\langle 2\,^3\mathrm{S}\middle\|er_q\middle\|2\,^3\mathrm{P}\right\rangle, \quad \text{(A.8)}\end{aligned}$$

with $q = M'_F - M_F$. Quantum numbers L, S, J, L' and J' have the same values as in the case of ^{4}He, while $F = \frac{3}{2}$ and $F' = \frac{5}{2}$. For transition $M_F = \frac{3}{2} \rightarrow M'_F = \frac{5}{2}$,

$$\left\langle 2\,^3\mathrm{S}_1(F=\tfrac{3}{2})M_F=\tfrac{3}{2}\middle|er_q\middle|2\,^3\mathrm{P}_2(F'=\tfrac{5}{2})M'_F=\tfrac{5}{2}\right\rangle = \sqrt{\tfrac{1}{3}}\left\langle 2\,^3\mathrm{S}\middle\|er_q\middle\|n\,^3\mathrm{P}\right\rangle. \quad \text{(A.9)}$$

Other matrix elements with $F' = \frac{5}{2}$ can be calculated in a similar manner. However, Eq. (A.8) cannot be applied to matrix elements with $F' = \frac{1}{2}, \frac{3}{2}$, as the corresponding excited states are admixtures of states with $J' = F' - \frac{1}{2}$ and $J' = F' + \frac{1}{2}$ [137]. To a good approximation, the matrix elements can be reduced to a sum of two reduced matrix elements with $J' = F' - \frac{1}{2}$ and $J' = F' + \frac{1}{2}$. Resulting matrix elements for all electric dipole transitions, $2\,^3\mathrm{S}_1(F)M_F \rightarrow 2\,^3\mathrm{P}(F')M'_F$ are given in [137]. Although singlet-triplet mixing is neglected in these calculations, the matrix elements are accurate to a few 10^{-3} [41].

For a given transition, the saturation intensity is defined as the intensity of the light wave, $I = \epsilon_0 E^2 c/2$, for which [130]

$$2\Omega_{\mathrm{ge}}^2 = \Gamma^2. \quad \text{(A.10)}$$

In this thesis, the saturation intensities associated with transitions $M_J = 1 \rightarrow M'_J = 2$ and $M_F = \frac{3}{2} \rightarrow M'_F = \frac{5}{2}$ are denoted by I_{sat}. As the reduction of the matrix elements leads to identical expressions for both ^{3}He and ^{4}He, Eqs. (A.7) and (A.9), the corresponding intensities I_{sat} are given by the same expression in both cases. Substituting Eqs. (A.7) and (A.9) into Eq. (A.5), and using Eq. (A.10) and [118]

$$\frac{\omega^3}{3\pi\epsilon_0\hbar c^3}\,\frac{2L'+1}{2L+1}\left|\left\langle 2\,^3\mathrm{S}\middle\|er_q\middle\|n\,^3\mathrm{P}\right\rangle\right|^2 = \Gamma, \quad \text{(A.11)}$$

with $\omega = 2\pi c/\lambda$ (and $L = 0$ and $L' = 1$), it follows that

$$I_{\mathrm{sat}} = \frac{\pi hc\Gamma}{3\lambda^3}. \quad \text{(A.12)}$$

The values for I_{sat} of the various laser cooling transition are given in Table A.3. The values for the 1083 nm transitions of ^{3}He and ^{4}He are virtually the same.

Table A.3. Spectroscopic data, saturation intensity and laser cooling parameters for the various laser cooling transitions.

	^{3}He $2\,^3S_1(F=\frac{3}{2}) \rightarrow 2\,^3P_2(F'=\frac{5}{2})$	^{4}He $2\,^3S_1 \rightarrow 2\,^3P_2$	^{4}He $2\,^3S_1 \rightarrow 3\,^3P_2$
Vacuum wavelength λ (nm)	1083.4622[a]	1083.3306[b]	388.9751[b]
Lifetime excited state (ns)	98.0[c]	98.0[c]	94.8[c]
Lifetime ground ($2\,^3S_1$) state (ks)	7.9[d]	7.9[d]	7.9[d]
Linewidth transition $\Gamma/2\pi$ (MHz)	1.62[c]	1.62[c]	1.51[c]
Saturation intensity I_{sat} (mW/cm^2)	0.167[e]	0.167[e]	3.35[e]
Doppler temperature T_{Dop} (μK)	39.0[f]	39.0[f]	36.2[f]
Recoil velocity v_{rec} (m/s)	0.122[g]	0.0920[g]	0.256[g]

[a] Calculated from the wavelength associated with $2\,^3S_1 \rightarrow 2\,^3P_2$ in ^{4}He and the transition isotope shift [83, 180].

[b] Reference [54].

[c] Derived from theoretical oscillator strengths reported in [53]. The mass difference between the ^{3}He and ^{4}He atom results in lifetimes and linewidths that differ by 10^{-4} for the transitions at 1083 nm. For state $3\,^3P_2$ of ^{4}He, the decay to state $3\,^3S_1$ is taken into account.

[d] The main decay process of the metastable $2\,^3S_1$ state is a single-photon magnetic-dipole transition [104, 220].

[e] Calculated with $I_{\mathrm{sat}} = \pi hc\Gamma/3\lambda^3$, see Eq. (A.12).

[f] Calculated with $T_{\mathrm{Dop}} = \hbar\Gamma/2k_{\mathrm{B}}$.

[g] Calculated with $v_{\mathrm{rec}} = \hbar k/m = h/\lambda m$.

Appendix B

Atom flux from a ballistic expansion

Considering a magneto-optically trapped sample of metastable atoms and a microchannel plate (MCP) detector at a given distance from the sample, the count rate of atoms hitting the detector surface in a TOF measurement is determined. For a detector set up in current mode configuration, the current signal is proportional to the count rate, if the detector is operating in the linear output regime. As an intermediate step, the atom flux vector field associated with a sample undergoing a ballistic expansion is calculated. The coordinate system of Figure B.1 is used, so that gravity points in the $-\hat{z}$-direction.[1]

The atomic velocity components in the trapped sample, v_x, v_y and v_z, are assumed to be given by Maxwell-Boltzmann distributions,

$$f(v_x, \sigma_{vx}) = \frac{1}{\sqrt{2\pi}\sigma_{vx}} \exp\left[-\frac{v_x^2}{2\sigma_{vx}^2}\right], \tag{B.1}$$

$$f(v_y, \sigma_{vy}) = \frac{1}{\sqrt{2\pi}\sigma_{vy}} \exp\left[-\frac{v_y^2}{2\sigma_{vy}^2}\right], \tag{B.2}$$

$$f(v_z, \sigma_{vz}) = \frac{1}{\sqrt{2\pi}\sigma_{vz}} \exp\left[-\frac{v_z^2}{2\sigma_{vz}^2}\right], \tag{B.3}$$

with σ_{vx}^2, σ_{vy}^2 and σ_{vz}^2 variances of the one-dimensional distributions. Usually, a trapped sample is in thermal equilibrium, $\sigma_{vx} = \sigma_{vy} = \sigma_{vz} = (k_B T/m)^{1/2}$, with T the temperature of the sample and m the mass of the atom. However, for the purpose of generality, different variances are assumed here. In accordance with observations it is assumed that, at $t = 0$, the sample has a Gaussian density distribution $n(x_0, y_0, z_0) = N f(x_0, \sigma_{x_0}) f(y_0, \sigma_{y_0}) f(z_0, \sigma_{z_0})$, where N is the number

[1] In Chapters 2 and 5, the z-axis is chosen as the symmetry axis of the anti-Helmholtz coils, which lies in the horizontal plane.

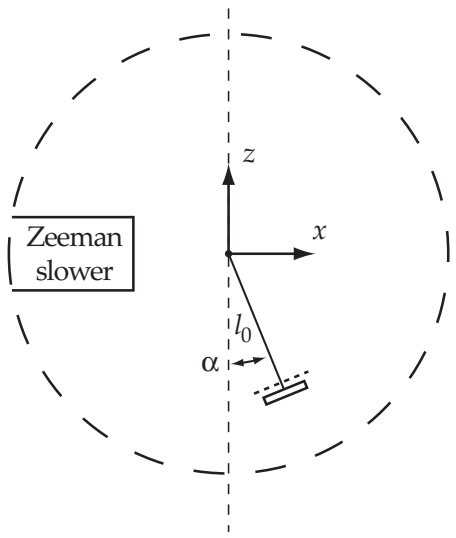

Figure B.1. Coordinate system in MOT vacuum chamber, and MCP detector for TOF measurements. Gravity points in the $-\hat{z}$-direction.

of trapped atoms and

$$f(x_0, \sigma_{x_0}) = \frac{1}{\sqrt{2\pi}\sigma_{x_0}} \exp\left[-\frac{x_0^2}{2\sigma_{x_0}^2}\right], \tag{B.4}$$

$$f(y_0, \sigma_{y_0}) = \frac{1}{\sqrt{2\pi}\sigma_{y_0}} \exp\left[-\frac{y_0^2}{2\sigma_{y_0}^2}\right], \tag{B.5}$$

$$f(z_0, \sigma_{z_0}) = \frac{1}{\sqrt{2\pi}\sigma_{z_0}} \exp\left[-\frac{z_0^2}{2\sigma_{z_0}^2}\right], \tag{B.6}$$

with σ_{x_0}, σ_{y_0} and σ_{z_0} the radii of the one-dimensional Gaussian distributions. Consequently, the trapped sample is characterized at $t = 0$ by probability distribution

$$\mathcal{F}_{\boldsymbol{v},\boldsymbol{r_0}}(\boldsymbol{v}, \boldsymbol{r_0}) = f(v_x, \sigma_{vx}) f(v_y, \sigma_{vy}) f(v_z, \sigma_{vz})\, f(x_0, \sigma_{x_0}) f(y_0, \sigma_{y_0}) f(z_0, \sigma_{z_0}), \tag{B.7}$$

with $\boldsymbol{v} = (v_x, v_y, v_z)$ and $\boldsymbol{r_0} = (x_0, y_0, z_0)$. The number of particles in infinitesimal volume $\mathrm{d}x_0\mathrm{d}y_0\mathrm{d}z_0$ at position $\boldsymbol{r_0}$ with velocity components between v_x and $v_x + \mathrm{d}v_x$, v_y and $v_y + \mathrm{d}v_y$, and v_z and $v_z + \mathrm{d}v_z$ can now be written as

$$N\mathcal{F}_{\boldsymbol{v},\boldsymbol{r_0}}(\boldsymbol{v}, \boldsymbol{r_0})\, \mathrm{d}v_x\mathrm{d}v_y\mathrm{d}v_z\, \mathrm{d}x_0\mathrm{d}y_0\mathrm{d}z_0, \tag{B.8}$$

as $\iiint \iiint \mathcal{F}_{\boldsymbol{v},\boldsymbol{r_0}}(\boldsymbol{v}, \boldsymbol{r_0})\, \mathrm{d}v_x\mathrm{d}v_y\mathrm{d}v_z\, \mathrm{d}x_0\mathrm{d}y_0\mathrm{d}z_0 = 1$.

Using Newton's equations for the ballistic motion of a particle in the earth's gravitational field (acceleration of free fall g),

$$\left.\begin{aligned} x &= x_0 + v_x t, \\ y &= y_0 + v_y t, \\ z &= z_0 + v_z t - \tfrac{1}{2} g t^2, \end{aligned}\right\} \longleftrightarrow \left\{\begin{aligned} v_x &= (x - x_0)/t, \\ v_y &= (y - y_0)/t, \\ v_z &= (z - z_0)/t + \tfrac{1}{2} g t, \end{aligned}\right. \tag{B.9}$$

the number of particles is derived that are in infinitesimal volume $\mathrm{d}x_0\mathrm{d}y_0\mathrm{d}z_0$ at $\boldsymbol{r_0}$ if $t = 0$, but are situated in infinitesimal volume $\mathrm{d}x\mathrm{d}y\mathrm{d}z$ at $\boldsymbol{r} = (x, y, z)$ if $t \geq 0$. Applying the coordinate transformation $\boldsymbol{v} \to \boldsymbol{r}$ gives

$$\begin{aligned} &N\mathcal{F}_{\boldsymbol{r},\boldsymbol{r_0}}(\boldsymbol{r}, \boldsymbol{r_0}, t)\,\mathrm{d}x\mathrm{d}y\mathrm{d}z\,\mathrm{d}x_0\mathrm{d}y_0\mathrm{d}z_0 \\ &\qquad = N\mathcal{F}_{\boldsymbol{v},\boldsymbol{r_0}}\big(\boldsymbol{v}(\boldsymbol{r}), \boldsymbol{r_0}\big)\,\Big|J(\boldsymbol{v}, \boldsymbol{r})\Big|\,\mathrm{d}x\mathrm{d}y\mathrm{d}z\,\mathrm{d}x_0\mathrm{d}y_0\mathrm{d}z_0 \\ &= \frac{1}{(2\pi)^{3/2}\sigma_{vx}\sigma_{vy}\sigma_{vz}}\,\exp\left[-\frac{(x-x_0)^2}{2\sigma_{vx}^2t^2} - \frac{(y-y_0)^2}{2\sigma_{vy}^2t^2} - \frac{(z-z_0+\frac{1}{2}gt^2)^2}{2\sigma_{vz}^2t^2}\right] \\ &\times \frac{N}{(2\pi)^{3/2}\sigma_{x_0}\sigma_{y_0}\sigma_{z_0}}\,\exp\left[-\frac{x_0^2}{2\sigma_{x_0}^2} - \frac{y_0^2}{2\sigma_{y_0}^2} - \frac{z_0^2}{2\sigma_{z_0}^2}\right]\,\frac{1}{t^3}\,\mathrm{d}x\mathrm{d}y\mathrm{d}z\,\mathrm{d}x_0\mathrm{d}y_0\mathrm{d}z_0, \end{aligned} \tag{B.10}$$

with the Jacobian given by

$$J(\boldsymbol{v}, \boldsymbol{r}) = \begin{vmatrix} \dfrac{\partial v_x}{\partial x} & \dfrac{\partial v_x}{\partial y} & \dfrac{\partial v_x}{\partial z} \\ \dfrac{\partial v_y}{\partial x} & \dfrac{\partial v_y}{\partial y} & \dfrac{\partial v_y}{\partial z} \\ \dfrac{\partial v_z}{\partial x} & \dfrac{\partial v_z}{\partial y} & \dfrac{\partial v_z}{\partial z} \end{vmatrix} = \frac{1}{t^3}. \tag{B.11}$$

Integration over all space $\boldsymbol{r_0}$ gives the number of particles in infinitesimal volume $\mathrm{d}x\mathrm{d}y\mathrm{d}z$ at $\boldsymbol{r}$ for a time $t \geq 0$ during the ballistic expansion,

$$\begin{aligned} N\mathcal{F}_{\boldsymbol{r}}(\boldsymbol{r}, t)\,\mathrm{d}x\mathrm{d}y\mathrm{d}z &= N\iiint\big[\mathcal{F}_{\boldsymbol{r},\boldsymbol{r_0}}(\boldsymbol{r}, \boldsymbol{r_0}, t)\,\mathrm{d}x\mathrm{d}y\mathrm{d}z\big]\,\mathrm{d}x_0\mathrm{d}y_0\mathrm{d}z_0 \\ &= Nf_x(x, t)f_y(y, t)f_z(z, t)\,\mathrm{d}x\mathrm{d}y\mathrm{d}z, \end{aligned} \tag{B.12}$$

where

$$f_x(x, t) = \frac{1}{\sqrt{2\pi}\sigma_x(t)}\,\exp\left[-\frac{x^2}{2\sigma_x^2(t)}\right], \tag{B.13}$$

$$f_y(y, t) = \frac{1}{\sqrt{2\pi}\sigma_y(t)}\,\exp\left[-\frac{y^2}{2\sigma_y^2(t)}\right], \tag{B.14}$$

$$f_z(z, t) = \frac{1}{\sqrt{2\pi}\sigma_z(t)}\,\exp\left[-\frac{(z+\frac{1}{2}gt^2)^2}{2\sigma_z^2(t)}\right], \tag{B.15}$$

with $\sigma_i(t) = \sqrt{\sigma_{i_0}^2 + \sigma_{vi}^2t^2}$ $(i = x, y, z)$ the time-dependent rms radii of the expanding sample.

According to Eq. (B.12), the time-dependent density distribution of the expanding sample can be given in the form of a scalar field,

$$n(\boldsymbol{r}, t) = N\,\mathcal{F}_{\boldsymbol{r}}(\boldsymbol{r}, t) = N\,f_x(x, t)f_y(y, t)f_z(z, t). \tag{B.16}$$

The description of a sample of atoms by a continuous density distribution implies the continuum hypothesis known from fluid dynamics [14]. The hypothesis allows the introduction of the *local* velocity vector field $\boldsymbol{u}(\boldsymbol{r}, t)$, not to be

confused with the *material* velocity $\boldsymbol{v} = (v_x, v_y, v_z)$ of an individual atom, and the analogy can be further extended with the introduction of the atom flux vector field,

$$\boldsymbol{\Phi}(\boldsymbol{r}, t) = n(\boldsymbol{r}, t)\, \boldsymbol{u}(\boldsymbol{r}, t), \tag{B.17}$$

where $\int\int_{\mathcal{S}} (\boldsymbol{\Phi} \cdot \boldsymbol{n})\, \mathrm{d}\sigma$ represents the rate at which atoms are flowing across surface $\mathcal{S}$, with $\boldsymbol{n}$ the unit normal on $\mathcal{S}$ [14]. Velocity field $\boldsymbol{u}(\boldsymbol{r}, t)$ can be obtained from density field $n(\boldsymbol{r}, t)$ using the continuity equation [14],

$$\nabla \cdot \boldsymbol{\Phi} = -\frac{\partial n}{\partial t}. \tag{B.18}$$

As the distribution functions of Eqs. (B.1)–(B.6) can be factorized (i.e. there is no coupling between the three spatial dimensions indicated by x, y and z), the local velocity components can be written $\boldsymbol{u}(\boldsymbol{r}, t) = \big(u_x(x,t), u_y(y,t), u_z(z,t)\big)$. Applying the chain rule, the continuity equation is written

$$\left(\frac{1}{f_x}\frac{\partial f_x u_x}{\partial x} + \frac{1}{f_x}\frac{\partial f_x}{\partial t}\right) + \left(\frac{1}{f_y}\frac{\partial f_y u_y}{\partial y} + \frac{1}{f_y}\frac{\partial f_y}{\partial t}\right) + \left(\frac{1}{f_z}\frac{\partial f_z u_z}{\partial z} + \frac{1}{f_z}\frac{\partial f_z}{\partial t}\right) = 0, \tag{B.19}$$

and, using the method of separation of variables, separate partial differential equations are obtained for the velocity components,

$$\frac{1}{f_x}\frac{\partial f_x u_x}{\partial x} + \frac{1}{f_x}\frac{\partial f_x}{\partial t} = C_1, \tag{B.20}$$

$$\frac{1}{f_y}\frac{\partial f_y u_y}{\partial y} + \frac{1}{f_y}\frac{\partial f_y}{\partial t} = C_2, \tag{B.21}$$

$$\frac{1}{f_z}\frac{\partial f_z u_z}{\partial z} + \frac{1}{f_z}\frac{\partial f_z}{\partial t} = -C_1 - C_2, \tag{B.22}$$

where C_1 and C_2 are constants. The (unique) physical solution is found by setting $C_1 = C_2 = 0$. Applying the chain rule, the differential equations can be written

$$\frac{\partial u_x}{\partial x} + \left[\frac{1}{f_x}\frac{\partial f_x}{\partial x}\right] u_x = -\frac{1}{f_x}\frac{\partial f_x}{\partial t} \tag{B.23}$$

$$\frac{\partial u_y}{\partial y} + \left[\frac{1}{f_y}\frac{\partial f_y}{\partial y}\right] u_y = -\frac{1}{f_y}\frac{\partial f_y}{\partial t} \tag{B.24}$$

$$\frac{\partial u_z}{\partial z} + \left[\frac{1}{f_z}\frac{\partial f_z}{\partial z}\right] u_z = -\frac{1}{f_z}\frac{\partial f_z}{\partial t}. \tag{B.25}$$

Solutions are easily found using routine `DSolve` of MATHEMATICA V4.1,

$$u_x(x,t) = \frac{\sigma_{vx}^2 t^2}{\sigma_x^2(t)}\,\frac{x}{t}, \tag{B.26}$$

$$u_y(y,t) = \frac{\sigma_{vy}^2 t^2}{\sigma_y^2(t)}\,\frac{y}{t}, \tag{B.27}$$

$$u_z(z,t) = \frac{\sigma_{vz}^2 t^2}{\sigma_z^2(t)}\left(\frac{z}{t} + \frac{gt}{2}\right) - gt. \tag{B.28}$$

The expression for the atom flux vector field $\boldsymbol{\Phi}(x,y,z;t)$ is obtained by substitution of Eq. (B.16) and Eqs. (B.26)–(B.28) into Eq. (B.17).

The count rate measured with a MCP detector equals the atom flux integrated over the detector surface $\mathcal{S}$ and can be written as surface integral[2]

$$R_{\mathrm{MCP}} = \iint_{\mathcal{S}} (\boldsymbol{\Phi}\cdot\boldsymbol{n})\,\mathrm{d}\sigma, \tag{B.29}$$

where $\boldsymbol{n}$ is the unit normal on $\mathcal{S}$ pointing into the detector. As an example, the surface integral for an infinitely large detector surface, perpendicular to gravity, at a distance l_0' under a trapped sample is calculated:

$$\begin{aligned} R_{\mathrm{MCP}} = \iint_{\mathcal{S}} (\boldsymbol{\Phi}\cdot\boldsymbol{n})\,\mathrm{d}\sigma &= \int_{-\infty}^{\infty}\int_{-\infty}^{\infty} (\boldsymbol{\Phi}(x,y,-l_0';t)\cdot(0,0,-1))\,\mathrm{d}x\mathrm{d}y \\ &= -\int_{-\infty}^{\infty}\int_{-\infty}^{\infty} \Phi_z(x,y,-l_0';t)\,\mathrm{d}x\mathrm{d}y \\ = \frac{1}{2\sqrt{2\pi}\,\sigma_z^3(t)}\,\frac{1}{t}\,&\left[gt^2(\sigma_{z_0}^2+\sigma_{vz}^2t^2)+2l_0'\,\sigma_{vz}^2t^2\right]\,\exp\left[\frac{(-l_0'+\frac{1}{2}gt^2)^2}{2\sigma_z^2(t)}\right]. \end{aligned} \tag{B.30}$$

This expression is also given in [226, Eq. (14)], where a derivation is given (based on a single coordinate transformation) that is limited to detector surfaces perpendicular to the direction gravity. Using Eq. (B.29), count rates for (parametrizable) detector surface of arbitrary position and orientation can be calculated.

The MCP detector depicted in Fig. B.1 is at an angle α with respect to the direction of gravity. The detector is pointing towards the MOT center, i.e. the detector surface is perpendicular to the line connecting MOT center and center of the detector surface. To obtain an analytical expression for the corresponding count rate, the detector surface is modeled with a square $\mathcal{S}$ with sides $2r$, centered at $(x,y,z) = (x_{\mathrm{MCP}},0,-z_{\mathrm{MCP}}) = (l_0\sin\alpha,0,-l_0\cos\alpha)$. The square is given by explicit representation

$$\mathcal{S}: z(x,y) = ax+b, \text{ with } \begin{cases} x_1 < x < x_2, \\ -r < y < r, \end{cases} \tag{B.31}$$

with $a = x_{\mathrm{MCP}}/z_{\mathrm{MCP}}$, $b = -{l_0}^2/z_{\mathrm{MCP}}$, $x_1 = x_{\mathrm{MCP}} - r/\sqrt{1+a^2}$, and $x_2 = x_{\mathrm{MCP}} + r/\sqrt{1+a^2}$. Note that the MOT center is at $(x,y,z) = (0,0,0)$. Count rate R_{MCP} is given by

$$\begin{aligned} R_{\mathrm{MCP}} = \iint_{\mathcal{S}} (\boldsymbol{\Phi}\cdot\boldsymbol{n})\,\mathrm{d}\sigma &= \frac{1}{\sqrt{1+a^2}}\int_{-r}^{r}\int_{x_1}^{x_2} (\boldsymbol{\Phi}(x,y,ax+b;t)\cdot(a,0,-1))\,\mathrm{d}x\mathrm{d}y \\ &= \frac{1}{\sqrt{1+a^2}}\int_{-r}^{r}\int_{x_1}^{x_2} (a\Phi_x(x,y,ax+b;t)-\Phi_z(x,y,ax+b;t))\,\mathrm{d}x\mathrm{d}y \end{aligned} \tag{B.32}$$

The integral is not evaluated here, as it results in an inconvenient expression. Eq. (B.32) is used in the fitting procedure of Chapter 2.

[2] Please note that $(\boldsymbol{\Phi}\cdot\boldsymbol{n}) \geq 0$ is required over the entire detector surface in order to obtain a sensible result.

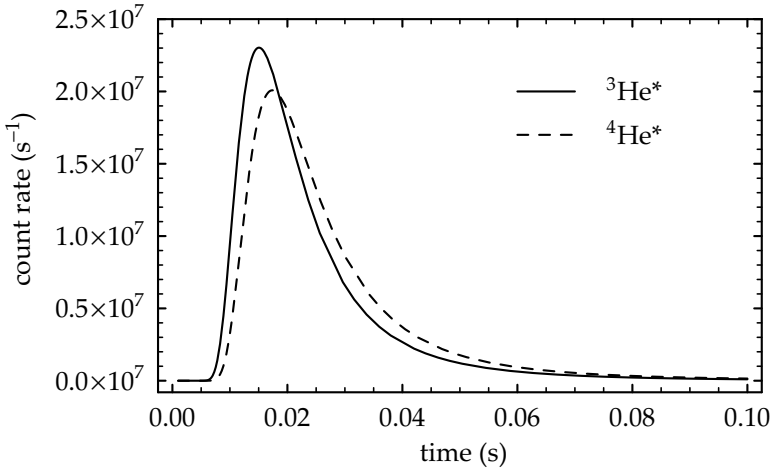

Figure B.2. Calculated count rate on the MCP detector from a ^{3}He* sample and a ^{4}He* sample. The samples contain 3×10^8 atoms and have a temperature of 2 mK. The total number of counts is 4.05×10^5 for ^{3}He* and 4.09×10^5 for ^{4}He*.

The MCP detector used in the TOF measurements of Chapters 2 and 6 (Hamamatsu, model F4655) has an effective diameter of 14.5 mm, and its position is given by $l_0 = 106(2)$ mm and $\alpha = 22.2°$, so that $(x_{\mathrm{MCP}}, 0, -z_{\mathrm{MCP}})$ =(40.1 mm, 0, −98.1 mm). The disc-shaped surface is modeled with a square of equal surface area, i.e. $r = 6.43$ mm.[3] Furthermore, $a = 0.408$, $b = -114.5$ mm, $x_1 = 34.1$ mm, and $x_2 = 46.0$ mm. As $\sigma_{x_0}, \sigma_{y_0}, \sigma_{z_0} \ll l_0$, the initial size of the cloud is set to zero, $\sigma_{x_0} = \sigma_{y_0} = \sigma_{z_0} = 0$. Furthermore, the velocity distribution is assumed to be isotropic, $\sigma_{vx} = \sigma_{vy} = \sigma_{vz} = \sigma_v$. Assuming a temperature of 2 mK and a trapped atom number of 3×10^8, the count rate curves from the detector for a sample of either ^{3}He* or ^{4}He* atoms are shown in Figure B.2.

Initial vertical velocity

If the trapped sample has a nonzero velocity component $v_z = v_{z_0}$ (as in the case for atomic fountain clocks utilizing moving molasses [35]), the corresponding Maxwell-Boltzmann distribution is given by

$$f(v_z, \sigma_{vz}) = \frac{1}{\sqrt{2\pi}\sigma_{vz}} \exp\left[-\frac{(v_z - v_{z_0})^2}{2\sigma_{vz}^2}\right], \tag{B.33}$$

yielding

$$f_z(z,t) = \frac{1}{\sqrt{2\pi}\sigma_z(t)} \exp\left[-\frac{(z + \frac{1}{2}gt^2 - 2v_{z_0}t)^2}{2\sigma_z^2(t)}\right]. \tag{B.34}$$

The corresponding velocity vector field component is given by

$$u_z(z,t) = \frac{\sigma_{vz}^2 t^2}{\sigma_z^2(t)}\left(\frac{z}{t} + \frac{gt}{2}\right) - gt + \frac{\sigma_{z_0}^2}{\sigma_z^2(t)} v_{z_0}. \tag{B.35}$$

Count rate R_{MCP} can again be calculated using Eqs. (B.17) and (B.29).

[3] Using numerical integration, it is determined that differences in the count rates for a disc-shaped and square detector surface are negligible at mK temperatures.

Appendix C

Interaction potentials for ^{3}He* + ^{3}He*

To calculate the ionization rate coefficient for a laser-cooled sample of ^{3}He* atoms, we must gain insight in the evolution of the electronic spins of the two colliding atoms during collisions. At large internuclear distance, the atomic hyperfine interaction couples the electronic spin S_i to the nuclear spin I_i to form the total angular momentum of an individual atom $F_i = 3/2$ or $1/2$. At short internuclear distance, the molecular interaction couples the electronic spins to form total electronic spin S. To determine the dynamics of the transition from one coupling scheme to the other, we need to calculate the interaction potential for two ^{3}He* atoms for total atomic angular momenta $F = 0, 1, 2, 3$. To calculate the potentials, we take into account only the electronic interaction and the atomic hyperfine structure [25, Chapter 2] and need to solve the time-independent Schrödinger equation

$$(\mathrm{H_{el}} + \mathrm{H_{hfs}})|\psi\rangle = E|\psi\rangle. \tag{C.1}$$

In the $|\boldsymbol{r}\rangle$ representation, the electronic Hamiltonian (in the Born-Oppenheimer approximation) is given by [116, Chapter 13]

$$\mathrm{H_{el}} = -\frac{\hbar^2}{2m}\sum_i^n \nabla_i^2 - \sum_\alpha^N \sum_i^n \frac{Ze^2}{|\boldsymbol{R}_\alpha - \boldsymbol{r}_i|} + \sum_j^n \sum_{i<j}^n \frac{e^2}{|\boldsymbol{r}_i - \boldsymbol{r}_j|} + \frac{Z^2e^2}{R}, \tag{C.2}$$

where α refers to the $N = 2$ nuclei with atomic number $Z = 2$, and i and j refer to the $n = 4$ electrons with mass m. The first term represents the kinetic energy of the electrons; the second term represents the attractions between the electrons and the nuclei, with $\boldsymbol{r}_i$ the position of electron i and $\boldsymbol{R}_\alpha$ the position of nucleus α; the third term represents the repulsions between the electrons; the last term represents the repulsions between the nuclei, with $R = |\boldsymbol{R}_1 - \boldsymbol{R}_2|$ the

internuclear distance. The electronic interaction gives rise to three electronic configurations, indicated by $^1\Sigma_g^+$, $^3\Sigma_u^+$ and $^5\Sigma_g^+$.

For the $^5\Sigma_g^+$ state of ^{4}He* + ^{4}He* (where hyperfine interaction is absent), the interaction potential $^5V(R)$ has been calculated[1] with ab initio methods by Müller *et al.* [136]. The calculation applies to $3.5\,a_0 \leq R \leq 14.0\,a_0$, but the potential can be extended to large internuclear distance using a calculation of the dispersion interaction, $-C_6/R^6 - C_8/R^8 - C_{10}/R^{10}$, by Yan and Babb [223], as discussed in Chapter 4.

The interaction potentials for states $^1\Sigma_g^+$ and $^3\Sigma_u^+$ can be determined from $^5V(R)$ using the exchange energy [111],

$$^{(2S+1)}V(R) = {}^5V(R) - {}^{(2S+1)}V_{\rm exch}(R), \tag{C.3}$$

where the exchange energy is given by

$$^{(2S+1)}V_{\rm exch}(R) = {}^{(2S+1)}A\, R^\gamma \exp(-\beta R), \tag{C.4}$$

where $\gamma = 4.91249$, $\beta = 1.183933$ a.u., $^1A = 6.3245 \times 10^{-3}$ a.u. and $^3A = 4.6317 \times 10^{-3}$ a.u. ($^5A = 0$).

The atomic hyperfine interaction is given by [166, 167]

$$\mathrm{H}_{\rm hfs} = -\tfrac{2}{3}h\Delta_{\rm hf}(\mathbf{I}_1\cdot\mathbf{J}_1 + \mathbf{I}_2\cdot\mathbf{J}_2) = -\tfrac{1}{3}h\Delta_{\rm hf}(\mathbf{F}_1^2 - \mathbf{S}_1^2 - \mathbf{I}_1^2 + \mathbf{F}_2^2 - \mathbf{S}_2^2 - \mathbf{I}_2^2), \tag{C.5}$$

where $\Delta_{\rm hf} = 6.73970177$ GHz. The hyperfine structure in inverted.

The electronic Hamiltonian is diagonal in basis $\left\{|S_1I_1, S_2I_2, SM_S, IM_I\rangle\right\}$ (Hund's case a coupling) with

$$\mathrm{H}_{\rm el}|S_1I_1, S_2I_2, SM_S, IM_I\rangle = {}^{(2S+1)}V(R)\,|S_1I_1, S_2I_2, SM_S, IM_I\rangle. \tag{C.6}$$

The atomic hyperfine interaction is diagonal in basis $\left\{|S_1I_1, S_2I_2, F_1M_{F1}, F_2M_{F2}\rangle\right\}$ (Hund's case e coupling) with

$$\begin{aligned}&\mathrm{H}_{\rm hfs}|S_1I_1, S_2I_2, F_1M_{F1}, F_2M_{F2}\rangle\\ &\quad= -\tfrac{1}{3}h\Delta_{\rm hf}\Big[F_1(F_1+1) + F_2(F_2+1) - \tfrac{11}{2}\Big]\,|S_1I_1, S_2I_2, F_1M_{F1}, F_2M_{F2}\rangle.\end{aligned} \tag{C.7}$$

We construct the corresponding diagonal matrices and apply (unitary) transformations to a representation in basis $\left\{|S_1I_1, S_2I_2, SI, FM_F\rangle\right\}$. In this basis, we construct a matrix for the combined electromagnetic and hyperfine interaction by adding the two. The corresponding potential curves are constructed by calculating the eigenvalues of the matrix for a range of internuclear distances R.

As total angular momentum F and parity p are conserved, matrix elements between states with different values of F and/or a different parity are zero. Therefore, we can restrict calculations to submatrices of given total angular momentum and parity. We distinguish between submatrices for

$$F = 0\,,\ p = + \tag{C.8}$$

$$F = 1\,,\ p = \pm \tag{C.9}$$

$$F = 2\,,\ p = \pm \tag{C.10}$$

$$F = 3\,,\ p = - \tag{C.11}$$

[1] The ab initio calculations performed by Stärck and Meyer [188] and Gadéa *et al.* [64] are more accurate than the calculations of Müller *et al.*, but additional accuracy is irrelevant here.

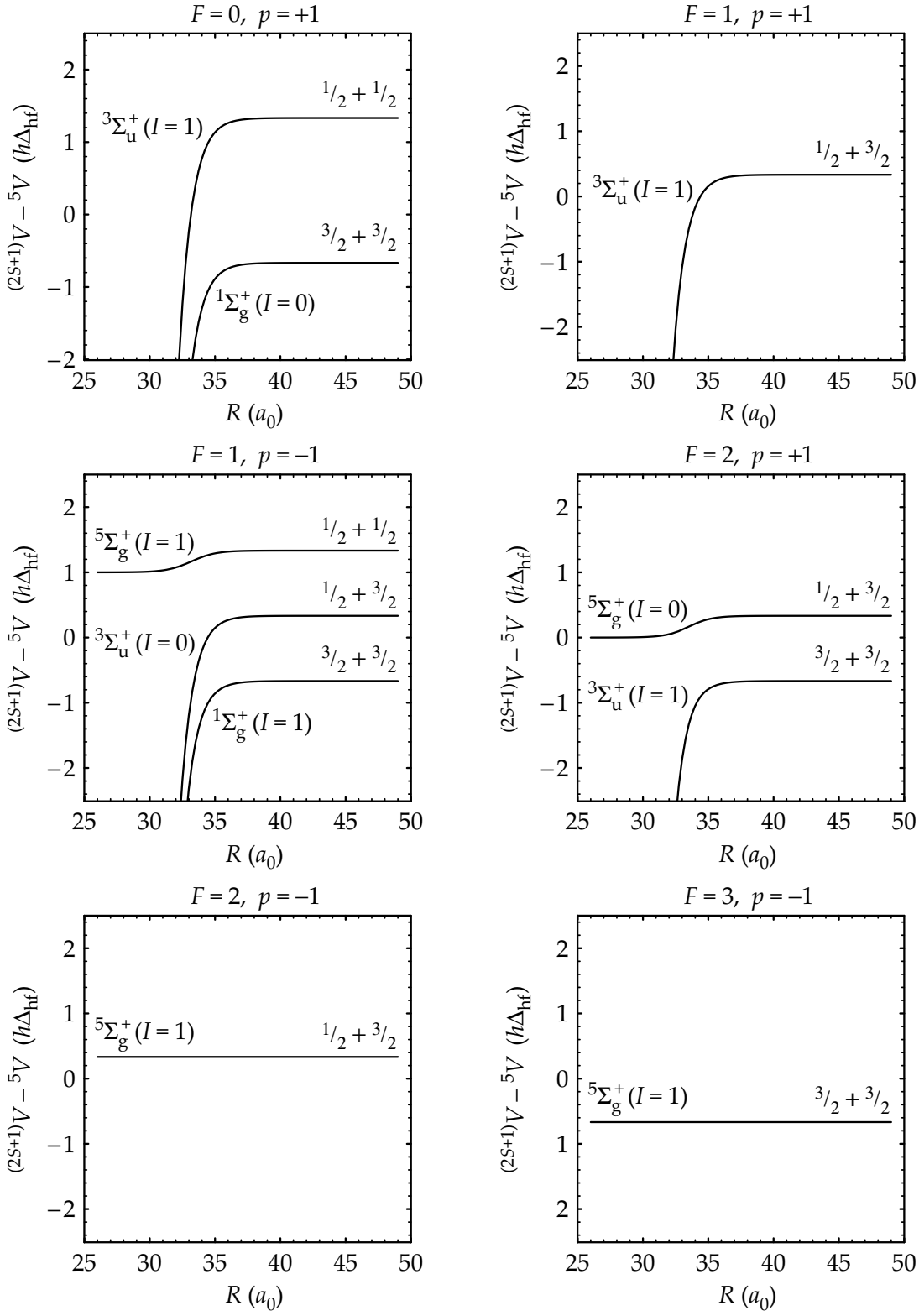

Figure C.1. Interaction potentials for ^{3}He* + ^{3}He*, relative to the interaction potentials for state $^5\Sigma_g^+$ of ^{4}He* + ^{4}He*.

Results are shown in Fig. C.1. Potential curves are depicted relative to ${}^5V(R)$ to show the important features. Around $R = 35\,a_0$, the electrostatic and atomic hyperfine interaction are of the same order of magnitude. The electrostatic in-

teraction increases exponentially and, as discussed in Chapter 4, a cold collision along these potentials can be modeled as a diabatic transition, expanding the eigenstate of the atomic hyperfine interaction $|S_1 I_1, S_2 I_2, F_1 M_{F1}, F_2 M_{F2}\rangle$ onto the eigenstates of the electronic interaction $\{|S_1 I_1, S_2 I_2, S M_S, I M_I\rangle\}$.

Bibliography

[1] C. S. Adams and E. Riis, Laser cooling and trapping of neutral atoms, *Prog. Quant. Electr.* **21**, 1–79 (1997).

[2] D. W. Allan, Time and frequency (time-domain) characterization, estimation, and prediction of precision clocks and oscillators, *IEEE Trans. Ultrason. Ferroelectr. Freq. Control* **34**, 647–654 (1987).

[3] M. H. Anderson, J. R. Ensher, M. R. Matthews, C. E. Wieman, and E. A. Cornell, Observation of Bose-Einstein condensation in a dilute atomic vapour, *Science* **269**, 198–201 (1995).

[4] S. V. Andreev, V. I. Balykin, V. S. Letokhov, and V. G. Minogin, Radiative slowing and reduction of the energy spread of a beam of sodium atoms to 1.5 K in an oppositely directed laser beam, *Pis. Zh. Eksp. Teor. Fiz.* **34**, 463–467 (1981), Eng. transl. 1981 JETP Lett. **34** 442.

[5] S. V. Andreev, V. I. Balykin, V. S. Letokhov, and V. G. Minogin, Radiative slowing down and monochromatization of a beam of sodium atoms in a counterpropagating laser beam, *Zh. Eksp. Teor. Fiz.* **82**, 1429–1441 (1982), Eng. transl. 1982 Sov. Phys.–JETP **55** 828.

[6] A. Aspect, E. Arimondo, R. Kaiser, N. Vansteenkiste, and C. Cohen-Tannoudji, Laser cooling below the one-photon recoil energy by velocity-selective coherent population trapping, *Phys. Rev. Lett.* **61**, 826–829 (1988).

[7] A. Aspect, N. Vansteenkiste, R. Kaiser, H. Haberland, and M. Karrais, Preparation of a pure intense beam of metastable helium by laser cooling, *Chem. Phys.* **145**, 307–315 (1990).

[8] G. Audi and A. H. Wapstra, The 1995 update to the atomic mass evaluation, *Nucl. Phys.* **A595**, 409–480 (1995).

[9] C. Audoin and B. Guinot, *The measurement of time: time, frequency and the atomic clock* (Cambridge University Press, 2001).

[10] L. E. Ballentine, *Quantum Mechanics—A modern development* (World Scientific, Singapore, 1998).

[11] V. I. Balykin, V. S. Letokhov, and V. I. Mishin, Cooling of sodium atoms by resonant laser emission, *Zh. Eksp. Teor. Fiz.* **78**, 1376–1385 (1980), Eng. transl. 1980 Sov. Phys.–JETP **51** 692.

[12] V. I. Balykin, V. S. Letokhov, and V. I. Mushin, Observation of the cooling of free sodium atoms in a resonance laser field with a scanning frequency, *Pis. Zh. Eksp. Teor. Fiz.* **29**, 614–618 (1979), Eng. transl. 1979 JETP Lett. **29** 560.

[13] F. Bardou, O. Emile, J.-M. Courty, C. I. Westbrook, and A. Aspect, Magneto-optical trapping of metastable helium: Collisions in the presence of resonant light, *Europhys. Lett.* **20**, 681–686 (1992).

[14] G. K. Batchelor, *An introduction to fluid dynamics* (Cambridge University Press, 1967).

[15] A. Bauch and H. R. Telle, Frequency standards and frequency measurement, *Rep. Prog. Phys.* **65**, 789–843 (2002).

[16] H. A. Bethe, Theory of disintegration of nuclei by neutrons, *Phys. Rev.* **47**, 747–759 (1935).

[17] S. Bize, *Tests fondamentaux à l'aide d'horloges à atomes froids de rubidium et de césium*, Ph.D. thesis, Université de Paris VI (2001), unpublished.

[18] S. Bize, S. A. Diddams, U. Tanaka, C. E. Tanner, W. H. Oskay, R. E. Drullinger, T. E. Parker, T. P. Heavner, S. R. Jefferts, L. Hollberg, W. M. Itano, and J. C. Bergquist, Testing the stability of fundamental constants with the $^{199}Hg^{+}$ single-ion optical clock, *Phys. Rev. Lett.* **90**, 150802 (2003).

[19] E. D. Black, An introduction to Pound-Drever-Hall laser frequency stabilization, *Am. J. Phys.* **69**, 79–87 (2001).

[20] C. C. Bradley, C. A. Sackett, and R. G. Hulet, Bose-Einstein condensation of lithium: Observation of limited condensate number, *Phys. Rev. Lett.* **78**, 985–989 (1997).

[21] C. C. Bradley, C. A. Sackett, J. J. Tollett, and R. G. Hulet, Evidence of Bose-Einstein condensation in an atomic gas with attractive interactions, *Phys. Rev. Lett.* **75**, 1687–1690 (1995).

[22] J. Brossel, A. Kastler, and J. Winter, Generation optique d'une inégalité de population entre les sous-niveaux Zeeman de l'état fondamental des atomes, *J. Phys. Radium* **13**, 668 (1952).

[23] A. Browaeys, J. Poupard, A. Robert, S. Nowak, W. Rooijakkers, E. Arimondo, L. Marcassa, D. Boiron, C. I. Westbrook, and A. Aspect, Two body loss rate in a magneto-optical trap of metastable He, *Eur. Phys. J. D* **8**, 199–203 (2000).

[24] A. Browaeys, A. Robert, O. Sirjean, J. Poupard, S. Nowak, D. Boiron, C. I. Westbrook, and A. Aspect, Thermalization of magnetically trapped metastable helium, *Phys. Rev. A* **64**, 034703 (2001).

[25] J. P. Burke, Jr., *Theoretical investigation of cold alkali atom collisions*, Ph.D.

thesis, University of Colorado (1999), unpublished.

[26] K. Burnett, P. S. Julienne, P. D. Lett, E. Tiesinga, and C. J. Williams, Quantum encounters of the cold kind, *Nature* **416**, 225–232 (2002).

[27] M. Cashen and H. Metcalf, Optical forces on atoms in nonmonochromatic light, *J. Opt. Soc. Am. B* **20**, 915–924 (2003).

[28] M. Cashen, O. Rivoire, V. Romanenko, L. Yatsenko, and H. Metcalf, Strong optical forces in frequency-modulated light, *Phys. Rev. A* **64**, 063411 (2001).

[29] M. Cashen, O. Rivoire, L. Yatsenko, and H. Metcalf, Coherent exchange of momentum between atoms and light, *J. Opt. B: Quantum Semiclass. Opt.* **4**, 75–79 (2002).

[30] M. T. Cashen and H. Metcalf, Bichromatic force on helium, *Phys. Rev. A* **63**, 025406 (2001).

[31] T. N. Chang and T. K. Fang, Effect of positive-energy orbitals on the photoionization cross sections and oscillator strengths of He and divalent atoms, *Phys. Rev. A* **52**, 2638–2644 (1995).

[32] S. Chu, The manipulation of neutral particles, *Rev. Mod. Phys.* **70**, 685–706 (1998).

[33] S. Chu, Cold atoms and quantum control, *Nature* **416**, 206–210 (2002).

[34] S. Chu, L. Hollberg, J. E. Bjorkholm, A. Cable, and A. Ashkin, Three-dimensional viscous confinement and cooling of atoms by resonance radiation pressure, *Phys. Rev. Lett.* **55**, 48–51 (1985).

[35] A. Clairon, C. Salomon, S. Guelatti, and W. D. Phillips, Ramsey resonance in a Zacharias fountain, *Europhys. Lett.* **16**, 165–170 (1991).

[36] C. Cohen-Tannoudji, B. Diu, and F. Laloë, *Quantum mechanics* (John Wiley & Sons, 1977).

[37] C. N. Cohen-Tannoudji, Manipulating atoms with photons, *Rev. Mod. Phys.* **70**, 707–719 (1998).

[38] T. B. Coplen, Atomic weights of the elements 1999, *Pure Appl. Chem.* **73**, 667–683 (2001).

[39] G. A. Costanzo, M. Siccardi, V. Barychev, and A. De Marchi, Virtues and problems of the high C-field Cs beam frequency standard, *IEEE Trans. Ultrason. Ferroelectr. Freq. Control* **47**, 249–255 (2000).

[40] J. S. Coursey, D. J. Schwab, and R. A. Dragoset, *Atomic Weights and Isotopic Compositions* (version 2.4) (2003), [Online] Available: `http://physics.nist.gov/Comp` [cited 14 July 2004], National Institute of Standards and Technology, Gaithersburg, MD.

[41] E. Courtade, F. Marion, P.-J. Nacher, G. Tastevin, K. Kiersnowski, and T. Dohnalik, Magnetic field effects on the 1083 nm atomic line of helium, *Eur. Phys. J. D* **21**, 25–55 (2002).

[42] S. G. Crane, X. Zhao, W. Taylor, and D. J. Vieira, Trapping an isotopic mix-

ture of fermionic ^{84}Rb and bosonic ^{87}Rb atoms, *Phys. Rev. A* **62**, 011402(R) (2000).

[43] J. Dalibard, Collisional dynamics of ultra-cold gases, in *Proceedings of the international school of physics 'Enrico Fermi', course CXL: Bose-Einstein condensation in atomic gases*, edited by M. Inguscio, S. Stringari, and C. E. Wieman, pp. 321–349 (IOS Press, 1999).

[44] K. B. Davis, M.-O. Mewes, M. R. Andrews, N. J. van Druten, D. S. Durfee, D. M. Kurn, and W. Ketterle, Bose-Einstein condensation in a gas of sodium atoms, *Phys. Rev. Lett.* **75**, 3969–3973 (1995).

[45] A. S. Davydov, *Quantum mechanics* (Pergamon Press, 1965).

[46] H. G. Dehmelt, Mono-ion oscillator as potential ultimate laser frequency standard, *IEEE Trans. Instrum. Meas.* **31**, 83–87 (1982).

[47] B. DeMarco and D. S. Jin, Onset of Fermi degeneracy in a trapped atomic gas, *Science* **285**, 1703–1706 (1999).

[48] B. DeMarco, S. B. Papp, and D. S. Jin, Pauli blocking of collisions in a quantum degenerate atomic Fermi gas, *Phys. Rev. Lett.* **86**, 5409–5412 (2001).

[49] A. S. Dickinson, F. X. Gadéa, and T. Leininger, Scattering lengths for spin-polarized metastable helium-3 and helium-4, *J. Phys. B* **37**, 587–593 (2004).

[50] S. A. Diddams, J. C. Bergquist, S. R. Jefferts, and C. W. Oates, Standards of time and frequency at the outset of the 21st century, *Science* **306**, 1318–1324 (2004).

[51] S. A. Diddams, T. Udem, J. C. Bergquist, E. A. Curtis, R. E. Drullinger, L. Hollberg, W. M. Itano, W. D. Lee, C. W. Oates, K. R. Vogel, and D. J. Wineland, An optical clock based on a single trapped $^{199}Hg^{+}$ ion, *Science* **293**, 825–828 (2001).

[52] M. R. Doery, E. J. D. Vredenbregt, S. S. Op de Beek, H. C. W. Beijerinck, and B. J. Verhaar, Limit on suppression of ionization in metastable neon traps due to long-range anisotropy, *Phys. Rev. A* **58**, 3673–3682 (1998).

[53] G. W. F. Drake, High precision calculations for helium, in *Atomic, Molecular and Optical Physics Handbook*, edited by G. W. F. Drake, chapter 11, pp. 154–171 (AIP Press, Woodbury, NY, 1996).

[54] G. W. F. Drake, High precision theory of atomic helium, *Phys. Scr.* **T83**, 83–92 (1999).

[55] A. R. Edmonds, *Angular momentum in quantum mechanics* (Princeton University Press, 1957).

[56] K. S. E. Eikema, J. Walz, and T. W. Hänsch, Continuous coherent Lyman-α excitation of atomic hydrogen, *Phys. Rev. Lett.* **86**, 5679–5682 (2001).

[57] D. W. Fahey, W. F. Parks, and L. D. Schearer, High flux beam source of thermal rare-gas metastable atoms, *J. Phys. E* **13**, 381–383 (1980).

[58] P. O. Fedichev, M. W. Reynolds, U. M. Rahmanov, and G. V. Shlyapnikov, Inelastic decay processes in a gas of spin-polarized triplet helium, *Phys. Rev. A* **53**, 1447–1453 (1996).

[59] C. Fertig and K. Gibble, Laser-cooled ^{87}Rb clock, *IEEE Trans. Instrum. Meas.* **48**, 520–523 (1999).

[60] C. Fertig and K. Gibble, Measurement and cancellation of the cold collision frequency shift in an ^{87}Rb fountain clock, *Phys. Rev. Lett.* **85**, 1622–1625 (2000).

[61] M. Fisher, N. Kolachevsky, M. Zimmermann, R. Holzwarth, T. Udem, T. W. Hänsch, M. Abgrall, J. Grünert, I. Maksimovic, S. Bize, H. Marion, F. Pereira Dos Santos, P. Lemonde, G. Santarelli, Ph. Laurent, A. Clairon, C. Salomon, M. Haas, U. D. Jentschura, and C. H. Keitel, New limits on the drift of fundamental constants from laboratory measurements, *Phys. Rev. Lett.* **92**, 230802 (2004).

[62] P. T. Fisk, Trapped-ion and trapped-atom microwave frequency standards, *Rep. Prog. Phys.* **60**, 761–817 (1997).

[63] M. W. Fleming and A. Mooradian, Spectral characteristics of external-cavity controlled semiconductor lasers, *IEEE J. Quant. Electr.* **17**, 44–59 (1981).

[64] F. X. Gadéa, T. Leininger, and A. S. Dickinson, Calculated scattering length for spin-polarized metastable helium, *J. Chem. Phys.* **117**, 7122–7127 (2002).

[65] A. Gallagher and D. E. Pritchard, Exoergic collisions of cold Na*–Na, *Phys. Rev. Lett.* **63**, 957–960 (1989).

[66] B. Gao, Effects of Zeeman degeneracy on the steady-state properties of an atom interacting with a near-resonant laser field: Analytic results, *Phys. Rev. A* **48**, 2443–2448 (1993).

[67] B. Gao, Theory of slow-atom collisions, *Phys. Rev. A* **54**, 2022–2039 (1996).

[68] M. C. George, L. D. Lombardi, and E. A. Hessels, Precision microwave measurement of the $2\,^3P_1 - 2\,^3P_0$ interval in atomic helium: A determination of the fine-structure constant, *Phys. Rev. Lett.* **87**, 173002 (2001).

[69] J. Goldwin, S. B. Papp, B. DeMarco, and D. S. Jin, Two-species magneto-optical trap with ^{40}K and ^{87}Rb, *Phys. Rev. A* **65**, 021402(R) (2002).

[70] P. L. Gould, P. D. Lett, P. S. Julienne, W. D. Phillips, H. R. Thorsheim, and J. Weiner, Observation of associative ionization of ultracold laser-trapped sodium atoms, *Phys. Rev. Lett.* **60**, 788–791 (1988).

[71] M. Greiner, C. A. Regal, and D. S. Jin, Emergence of a molecular Bose-Einstein condensate from a Fermi gas, *Nature* **426**, 537–540 (2003).

[72] T. J. Greytak, Prospects for Bose-Einstein condensation in magnetically trapped atomic hydrogen, in *Bose-Einstein condensation*, edited by A. Griffin, D. W. Snoke, and S. Stringari, chapter 7, pp. 131–159 (Cambridge Uni-

versity Press, 1995).

[73] Z. Hadzibabic, C. A. Stan, K. Dieckmann, S. Gupta, M. W. Zwierlein, A. Görlitz, and W. Ketterle, Two-species mixture of quantum degenerate Bose and Fermi gases, *Phys. Rev. Lett.* **88**, 160401 (2002).

[74] T. W. Hänsch and A. L. Schwalow, Cooling of gases by laser radiation, *Opt. Comm.* **13**, 68–69 (1975).

[75] W. Happer, Optical pumping, *Rev. Mod. Phys.* **44**, 169–249 (1972).

[76] Z. Herman and V. Čermák, Associative ionization in mixtures of carbon monoxide with sodium and potassium and the mechanism of associative ionization reactions, *Coll. Czech. Chem. Commun.* **31**, 649–658 (1966).

[77] N. Herschbach, *Trapped triplet helium atoms: Inelastic collisions and evaporative cooling*, Ph.D. thesis, Vrije Universiteit Amsterdam (2003), unpublished.

[78] N. Herschbach, P. Tol, A. Tychkov, W. Hogervorst, and W. Vassen, Magnetic trapping and evaporative cooling of metastable triplet helium, *J. Opt. B: Quantum Semiclass. Opt.* **5**, S65–S74 (2003).

[79] N. Herschbach, P. J. J. Tol, W. Hogervorst, and W. Vassen, Suppression of Penning ionization by spin polarization of cold He($2\,^3$S) atoms, *Phys. Rev. A* **61**, 050702 (2000).

[80] N. Herschbach, P. J. J. Tol, W. Vassen, W. Hogervorst, G. Woestenenk, J. W. Thomsen, P. van der Straten, and A. Niehaus, Photoassociation spectroscopy of cold He($2\,^3$S) atoms, *Phys. Rev. Lett.* **84**, 1874–1877 (2000).

[81] K. Hijikata and K. Ohtsuki, The calculation of the fine and hyperfine intervals of $2\,^1$P and $2\,^3$P states of ^{3}He, *J. Phys. Soc. Japan* **57**, 4141–4149 (1988).

[82] J. C. Hill, L. L. Hatfield, N. D. Stockwell, and G. K. Walters, Direct demonstration of spin-angular-momentum conservation in the reaction $\mathrm{He}(2\,^3\mathrm{S}_1) + \mathrm{He}(2\,^3\mathrm{S}_1) \rightarrow \mathrm{He}(1\,^1\mathrm{S}_0) + \mathrm{He}^+ + e^-$, *Phys. Rev. A* **5**, 189–195 (1972).

[83] E. A. Hinds, J. D. Prestage, and F. M. J. Pichanick, Phenomenological theory of the $2\,^3$P state of ^{3}He, *Phys. Rev. A* **32**, 2615–2621 (1985).

[84] R. Holzwarth, T. Udem, T. W. Hänsch, J. C. Knight, W. J. Wadsworth, and P. St. J. Russell, Optical frequency synthesizer for precision spectroscopy, *Phys. Rev. Lett.* **85**, 2264–2267 (2000).

[85] J. A. Hornbeck and J. P. Molnar, Mass spectrometric studies of molecular ions in the noble gases, *Phys. Rev.* **84**, 621–625 (1951).

[86] W. M. Itano, J. C. Bergquist, J. J. Bollinger, J. M. Gilligan, D. J. Heinzen, F. L. Moore, M. G. Raizen, and D. J. Wineland, Quantum projection noise: population fluctuations in two-level systems, *Phys. Rev. A* **47**, 3554–3570 (1993).

[87] T. Jeltes, *An atomic fountain clock based on metastable* ^{3}He, Master's thesis,

Vrije Universiteit Amsterdam (2002), unpublished.

[88] C. J. Joachain, *Quantum collision theory* (North-Holland Publishing, 1975).

[89] S. Jochim, M. Bartenstein, A. Altmeyer, G. Hendl, S. Riedl, C. Chin, J. Hecker Denschlag, and R. Grimm, Bose-Einstein condensation of molecules, *Science* **302**, 2101–2103 (2003).

[90] M. A. Joffe, W. Ketterle, A. Martin, and D. E. Pritchard, Transverse cooling and deflection of an atomic beam inside a Zeeman slower, *J. Opt. Soc. Am. B* **10**, 2257–2262 (1993).

[91] P. S. Julienne and F. H. Mies, Collisions of ultracold trapped atoms, *J. Opt. Soc. Am. B* **6**, 2257–2269 (1989).

[92] P. S. Julienne, A. M. Smith, and K. Burnett, Theory of collisions between laser cooled atoms, in *Advances in Atomic, Molecular and Optical Physics*, edited by D. Bates and B. Bederson, volume 30, pp. 141–198 (Academic Press, 1993).

[93] M. A. Kasevich, E. Riis, S. Chu, and R. G. DeVoe, rf spectroscopy in an atomic fountain, *Phys. Rev. Lett.* **63**, 612–615 (1989).

[94] A. Kastler, Quelques suggestions concernant la production optique et la détection optique d'une inégalité de population des niveaux de quantification spatiale des atomes: Application à l'expérience de Stern et Gerlach et à la résonance magnétique, *J. Phys. Radium* **11**, 255–265 (1950).

[95] H. Katori, H. Kunugita, and T. Ido, Quantum statistical effect on ionizing collisions of ultracold metastable Kr isotopes, *Phys. Rev. A* **52**, R4324–R4327 (1995).

[96] D. Kleppner, A short history of atomic physics in the twentieth century, *Rev. Mod. Phys.* **71**, S78–S84 (1999).

[97] J. C. J. Koelemeij, *Interaction of UV light with cold metastable helium atoms*, Ph.D. thesis, Vrije Universiteit Amsterdam (2004), unpublished.

[98] J. C. J. Koelemeij, W. Hogervorst, and W. Vassen, High-power frequency-stabilized laser for laser cooling of metastable helium at 389 nm, *Rev. Sci. Instrum.* **76**, 033104 (2005).

[99] J. C. J. Koelemeij, A. S. Tychkov, T. Jeltes, W. Hogervorst, and W. Vassen, High densities and optical collisions in a two-colour magneto-optical trap for metastable helium, *J. Phys. B* **37**, 3501–3520 (2004).

[100] A. E. A. Koolen, G. T. Jansen, K. F. E. M. Domen, H. C. W. Beijerinck, and K. A. H. van Leeuwen, Large-angle adjustable coherent atomic beam splitter by Bragg scattering, *Phys. Rev. A* **65**, 041601(R) (2002).

[101] M. Kumakura and N. Morita, Visible observation of metastable helium atoms confined in an infrared/visible double resonance trap, *Jpn. J. Appl. Phys., Part 2* **31**, L276–L279 (1992).

[102] M. Kumakura and N. Morita, Laser trapping of metastable ^{3}He atoms:

Isotopic difference in cold Penning ionization, *Phys. Rev. Lett.* **82**, 2848–2851 (1999).

[103] M. Kumakura and N. Morita, Magneto-optical trapping of metastable helium-3 atoms, *Appl. Phys. B* **70**, 555–559 (2000).

[104] G. Łach and K. Pachucki, Forbidden transitions in the helium atom, *Phys. Rev. A* **64**, 042510 (2001).

[105] L. D. Landau and E. M. Lifshitz, *Quantum mechanics—Non-relativistic theory*, second edition (Pergamon Press, 1965).

[106] J. Lawall, F. Bardou, B. Saubamea, K. Shimizu, M. Leduc, A. Aspect, and C. Cohen-Tannoudji, Two-dimensional subrecoil laser cooling, *Phys. Rev. Lett.* **73**, 1915–1918 (1994).

[107] R. Legere and K. Gibble, Quantum scattering in a juggling atomic fountain, *Phys. Rev. Lett.* **81**, 5780–5783 (1998).

[108] A. J. Leggett, Bose-Einstein condensation in the alkali gases: Some fundamental concepts, *Rev. Mod. Phys.* **73**, 307–356 (2001).

[109] A. J. Leggett, Erratum: Bose-Einstein condensation in the alkali gases: Some fundamental concepts [Rev. Mod. Phys. 73, 307 (2001)], *Rev. Mod. Phys.* **75**, 1083 (2003).

[110] P. Lemonde, Ph. Laurent, G. Santarelli, M. Abgrall, Y. Sortais, S. Bize, C. Nicolas, S. Zhang, A. Clairon, N. Dimarcq, P. Petit, A. G. Mann, A. N. Luiten, S. Chang, and C. Salomon, Cold-atom clocks on earth and in space, in *Frequency measurement and control: Advanced techniques and future trends*, edited by A. N. Luiten, *Topics in applied physics*, volume 79, pp. 131–153 (Springer, 2001).

[111] P. J. Leo, V. Venturi, I. B. Whittingham, and J. F. Babb, Ultracold collisions of metastable helium atoms, *Phys. Rev. A* **64**, 042710 (2001).

[112] J. Léonard, A. P. Mosk, M. Walhout, P. van der Straten, M. Leduc, and C. Cohen-Tannoudji, Analysis of photoassociation spectra for giant helium dimers, *Phys. Rev. A* **69**, 032702 (2004).

[113] J. Léonard, M. Walhout, A. P. Mosk, T. Müller, M. Leduc, and C. Cohen-Tannoudji, Giant helium dimers produced by photoassociation of ultracold metastable atoms, *Phys. Rev. Lett.* **91**, 073203 (2003).

[114] V. S. Letokhov and V. G. Minogin, Laser radiation pressure on free atoms, *Phys. Rep.* **73**, 1–65 (1981).

[115] P. D. Lett, W. D. Phillips, S. L. Rolston, C. E. Tanner, R. N. Watts, and C. I. Westbrook, Optical molasses, *J. Opt. Soc. Am. B* **6**, 2084–2107 (1989).

[116] I. N. Levine, *Quantum Chemistry*, third edition (Allyn and Bacon, Newton, Massachusetts, 1983).

[117] T. Loftus, J. R. Bochinski, and T. W. Mossberg, Simultaneous multi-isotope trapping of ytterbium, *Phys. Rev. A* **63**, 053401 (2001).

[118] R. Loudon, *The Quantum Theory of Light* (Oxford University Press, 1973).

[119] L. G. Marcassa, G. D. Telles, S. R. Muniz, and V. S. Bagnato, Collisional losses in a K-Rb cold mixture, *Phys. Rev. A* **63**, 013413 (2000).

[120] H. S. Margolis, G. P. Barwood, G. Huang, H. A. Klein, S. N. Lea, K. Szymaniec, and P. Gill, Hertz-level measurement of the optical clock frequency in a single $^{88}Sr^{+}$ ion, *Science* **306**, 1355–1358 (2004).

[121] F. Marin, F. Minardi, F. S. Pavone, M. Inguscio, and G. W. F. Drake, Hyperfine structure of the $3\ ^3P$ state of ^3He and isotope shift for the $2\ ^3S - 3\ ^3P_0$ transition, *Z. Phys. D* **32**, 285–293 (1995).

[122] H. Marion, F. Pereira Dos Santos, M. Abgrall, S. Zhang, Y. Sortais, S. Bize, I. Maksimovic, D. Calonico, J. Grünert, C. Mandache, P. Lemonde, G. Santarelli, Ph. Laurent, A. Clairon, and C. Salomon, Search for variations of fundamental constants using atomic fountain clocks, *Phys. Rev. Lett.* **90**, 150801 (2003).

[123] D. W. Martin, C. Weiser, R. F. Sperlein, D. L. Bernfeld, and P. E. Siska, Collision energy dependence of product branching in Penning ionization: $He^*(2\ ^1S, 2\ ^3S) + H_2$, D_2 and HD, *J. Chem. Phys.* **90**, 1564–1576 (1989).

[124] H. S. W. Massey, E. H. S. Burhop, and H. B. Gilbody, *Electronic and ionic impact phenomena*, volume 3 (Oxford University Press, 1971).

[125] H. C. Mastwijk, *Cold collisions of metastable helium atoms*, Ph.D. thesis, Universiteit Utrecht (1997), unpublished.

[126] H. C. Mastwijk, J. W. Thomsen, P. van der Straten, and A. Niehaus, Optical collisions of cold, metastable helium atoms, *Phys. Rev. Lett.* **80**, 5516–5519 (1998).

[127] H. C. Mastwijk, M. van Rijnbach, J. W. Thomsen, P. van der Straten, and A. Niehaus, Photo induced collisions with laser cooled He^* atoms, *Eur. Phys. J. D* **4**, 131–137 (1998).

[128] A. Messiah, *Quantum Mechanics—Two volumes bound as one* (Dover Publications, Mineola, New York, 1999, unabridged reprint in one volume of the English translation of *Méchanique Quantique*, published in two volumes in the United States as *Quantum Mechanics* by John Wiley & Sons c.1958).

[129] H. Metcalf, Magneto-optical trapping and its application to helium metastables, *J. Opt. Soc. Am. B* **6**, 2206–2210 (1989).

[130] H. J. Metcalf and P. van der Straten, *Laser cooling and trapping*, Graduate texts in contemporary physics (Springer, New York, 1999).

[131] M.-O. Mewes, G. Ferrari, F. Schreck, A. Sinatra, and C. Salomon, Simultaneous magneto-optical trapping of two lithium isotopes, *Phys. Rev. A* **61**, 011403(R) (1999).

[132] F. H. Mies and M. Raoult, Analysis of threshold effects in ultracold atomic collisions, *Phys. Rev. A* **62**, 012708 (2000).

[133] D. V. J. Milic, *Laser cooling and trapping of metastable helium atoms*, Ph.D. thesis, Australian National University (1999), unpublished.

[134] G. Modugno, G. Roati, F. Riboli, F. Ferlaino, R. J. Brecha, and M. Inguscio, Collapse of a degenerate Fermi gas, *Science* **297**, 2240–2242 (2002).

[135] K. Mølmer, Bose condensates and Fermi gases at zero temperature, *Phys. Rev. Lett.* **80**, 1804–1807 (1998).

[136] M. W. Müller, A. Merz, M.-W. Ruf, H. Hotop, W. Meyer, and M. Movre, Experimental and theoretical studies of the Bi-excited collision systems $He^*(2\,^3S) + He^*(2\,^3S, 2\,^1S)$ at thermal and subthermal kinetic energies, *Z. Phys. D* **21**, 89–112 (1991).

[137] P. J. Nacher and M. Leduc, Optical pumping in ^{3}He with a laser, *J. Phys. Paris* **46**, 2057–2073 (1985).

[138] R. J. Napolitano, S. C. Zilio, and V. S. Bagnato, Adiabatic following conditions for the deceleration of atoms with the Zeeman detuning technique, *Opt. Comm.* **80**, 110–114 (1990).

[139] E. E. Nikitin and S. Ya. Umanskii, *Theory of slow atomic collisions* (Springer-Verlag, 1984).

[140] C. W. Oates, K. R. Vogel, and J. L. Hall, High precision linewidth measurement of laser-cooled atoms: resolution of the Na $3p\,^2P_{3/2}$ lifetime discrepancy, *Phys. Rev. Lett.* **76**, 2866–2869 (1996).

[141] C. Orzel, M. Walhout, U. Sterr, P. S. Julienne, and S. L. Rolston, Spin polarization and quantum-statistical effects in ultracold ionizing collisions, *Phys. Rev. A* **59**, 1926–1935 (1999).

[142] T. P. Parr, D. M. Parr, and R. M. Martin, Velocity dependence for the chemi-ionization of Ar, Kr, N_2, CO, and O_2 by He(2 ^{1}S) and He(2 ^{3}S) metastable atoms, *J. Chem. Phys.* **76**, 316–324 (1982).

[143] H. M. Pask, R. J. Carman, D. C. Hanna, A. C. Tropper, C. J. Mackechnie, P. R. Barber, and J. M. Dawes, Ytterbium-doped silica fiber lasers: Versatile sources for the 1–1.2 µm region, *IEEE J. Sel. Top. Quantum Electron.* **1**, 2–13 (1995).

[144] W. Paul, Electromagnetic traps for charged and neutral particles, *Rev. Mod. Phys.* **62**, 531–540 (1990).

[145] F. M. Penning, Über Ionisation durch metastabile Atome, *Die Naturwissenschaften* **15**, 818 (1927).

[146] F. Pereira Dos Santos, J. Léonard, J. Wang, C. J. Barrelet, F. Perales, E. Rasel, C. S. Unnikrishnan, M. Leduc, and C. Cohen-Tannoudji, Production of a Bose-Einstein condensate of metastable helium atoms, *Eur. Phys. J. D* **19**, 103–109 (2002).

[147] F. Pereira Dos Santos, J. Léonard, J. Wang, C. J. Barrelet, F. Perales, E. Rasel, C. S. Unnikrishnan, M. Leduc, and C. Cohen-Tanoudji, Bose-Einstein condensation of metastable helium, *Phys. Rev. Lett.* **86**, 3459–3462

(2001).

[148] F. Pereira Dos Santos, F. Perales, J. Léonard, A. Sinatra, J. Wang, F. S. Pavone, E. Rasel, C. S. Unnikrishnan, and M. Leduc, Efficient magneto-optical trapping of a metastable helium gas, *Eur. Phys. J. AP* **14**, 69–76 (2001).

[149] F. Pereira Dos Santos, F. Perales, J. Léonard, A. Sinatra, J. Wang, F. S. Pavone, E. Rasel, C. S. Unnikrishnan, and M. Leduc, Penning collisions of laser-cooled metastable helium atoms, *Eur. Phys. J. D* **14**, 15–22 (2001).

[150] S. J. H. Petra, *Nanolithography with metastable helium atoms*, Ph.D. thesis, Vrije Universiteit Amsterdam (2004), unpublished.

[151] W. D. Phillips, Laser cooling and trapping of neutral atoms, *Rev. Mod. Phys.* **70**, 721–741 (1998).

[152] W. D. Phillips and H. Metcalf, Laser deceleration of an atomic beam, *Phys. Rev. Lett.* **48**, 596–599 (1982).

[153] M. Pieksma, M. Čížek, J. W. Thomsen, P. van der Straten, and A. Niehaus, Energy distributions of He^+ and $He_2{}^+$ ions formed in ultracold $He(2\,{}^3S_1)$+$He(2\,{}^3P_2)$ collisions, *Phys. Rev. A* **66**, 022703 (2002).

[154] J. D. Prestage, C. E. Johnson, E. A. Hinds, and F. M. J. Pichanick, Precise study of hyperfine structure in the $2\,{}^3P$ state of ^3He, *Phys. Rev. A* **32**, 2712–2724 (1985), note: Eq. (3) is incorrect: the Zeeman energies of the hyperfine levels of state $2\,{}^3S_1$ with $M_F = \pm\frac{1}{2}$ should be $W(F, \pm\frac{1}{2}) = E/2 \pm (g_j/2)\mu_B B + \frac{1}{2}\,(-1)^{F-1/2}\left[E^2 \pm \frac{2}{3}E(g_J - g_I)\mu_B B + (g_J - g_I)^2(\mu_B B)^2\right]^{1/2}$.

[155] J. D. Prestage, R. L. Tjoelker, and L. Maleki, Atomic clocks and variations of the fine structure constant, *Phys. Rev. Lett.* **74**, 3511–3514 (1995).

[156] J. V. Prodan, W. D. Phillips, and H. Metcalf, Laser production of a very slow monoenergetic atomic beam, *Phys. Rev. Lett.* **49**, 1149–1153 (1982).

[157] E. L. Raab, M. Prentiss, A. Cable, S. Chu, and D. E. Pritchard, Trapping of neutral sodium atoms with radiation pressure, *Phys. Rev. Lett.* **59**, 2631–2634 (1987).

[158] I. I. Rabi, J. R. Zacharias, S. Millman, and P. Kusch, A new method of measuring nuclear magnetic moment, *Phys. Rev.* **53**, 318 (1938).

[159] N. F. Ramsey, *Molecular beams* (Clarendon Press, 1969).

[160] N. F. Ramsey, Experiments with separated oscillatory fields and hydrogen masers, *Rev. Mod. Phys.* **62**, 541–552 (1990).

[161] L. Ricci, M. Weidemüller, T. Esslinger, A. Hemmerich, C. Zimmermann, V. Vuletic, W. König, and T. W. Hänsch, A compact grating-stabilized diode laser system for atomic physics, *Opt. Comm.* **117**, 541–549 (1995).

[162] A. Robert, O. Sirjean, A. Browaeys, J. Poupard, S. Nowak, D. Boiron, C. I. Westbrook, and A. Aspect, A Bose-Einstein condensate of metastable atoms, *Science* **292**, 461–464 (2001).

[163] W. Rooijakkers, W. Hogervorst, and W. Vassen, An intense collimated beam of metastable helium atoms by two-dimensional laser cooling, *Opt. Comm.* **123**, 321–330 (1996).

[164] W. Rooijakkers, W. Hogervorst, and W. Vassen, Laser deceleration and trapping of metastable helium atoms, *Opt. Comm.* **135**, 149–156 (1997).

[165] K. J. R. Rosman and P. D. P. Taylor, Isotopic composition of the elements 1997, *Pure Appl. Chem.* **70**, 217–235 (1998).

[166] S. D. Rosner and F. M. Pipkin, Hyperfine structure of the 2 $^3S_1$ state of He^3, *Phys. Rev. A* **1**, 571–586 (1970).

[167] S. D. Rosner and F. M. Pipkin, Errata: Hyperfine structure of the 2 $^3S_1$ state of He^3 [Phys. Rev. A **1**, 571 (1970)], *Phys. Rev. A* **3**, 521–522 (1971).

[168] E. W. Rothe, R. H. Neynaber, and S. M. Trujillo, Velocity dependence of the total cross section for the scattering of metastable He($^3S_1$) by helium, argon, and krypton, *J. Chem. Phys.* **42**, 3310–3314 (1965).

[169] G. Santarelli, Ph. Laurent, P. Lemonde, A. Clairon, A. G. Mann, S. Chang, A. N. Luiten, and C. Salomon, Quantum projection noise in an atomic fountain: A high stability cesium frequency standard, *Phys. Rev. Lett.* **82**, 4619–4622 (1999).

[170] M. S. Santos, P. Nussenzveig, L. G. Marcassa, K. Helmerson, J. Flemming, S. C. Zilio, and V. S. Bagnato, Simultaneous trapping of two different atomic species in a vapor-cell magneto-optical trap, *Phys. Rev. A* **52**, R4340–4343 (1995).

[171] M. S. Santos, P. Nussenzveig, L. G. Marcassa, K. Helmerson, J. Flemming, S. C. Zilio, and V. S. Bagnato, Erratum: Simultaneous trapping of two different atomic species in a vapor-cell magneto-optical trap [Phys. Rev. A 52, R4340 (1995)], *Phys. Rev. A* **54**, 1739 (1996).

[172] U. Schlöder, H. Engler, U. Schünemann, R. Grimm, and M. Weidemüller, Cold inelastic collisions between lithium and cesium in a two-species magneto-optical trap, *Eur. Phys. J. D* **7**, 331–340 (1999).

[173] F. Schreck, L. Khaykovich, K. L. Corwin, G. Ferrari, T. Bourdel, J. Cubizolles, and C. Salomon, Quasipure Bose-Einstein condensate immersed in a fermi sea, *Phys. Rev. Lett.* **87**, 080403 (2001).

[174] R. Schumann, C. Schubert, U. Eichmann, R. Jung, and G. von Oppen, Laser cooling of metastable He atoms in an inhomogeneous electric field, *Phys. Rev. A* **59**, 2120–2125 (1999).

[175] S. Seidelin, J. Viana Gomes, R. Hoppeler, O. Sirjean, D. Boiron, A. Aspect, and C. I. Westbrook, Getting the elastic scattering length by observing inelastic collisions in ultracold metastable helium atoms, *Phys. Rev. Lett.* **93**, 090409 (2004).

[176] K. Sengstock and W. Ertmer, Laser manipulation of atoms, in *Advances in atomic, molecular and optical physics*, pp. 1–44 (Academic Press, 1995).

[177] J. P. Shaffer, W. Chalupczak, and N. P. Bigelow, Photoassociative ionization of heteronuclear molecules in a novel two-species magneto-optical trap, *Phys. Rev. Lett.* **82**, 1124–1127 (1999).

[178] F. Shimizu, K. Shimizu, and H. Takuma, Laser cooling of a neon atomic beam in metastable states, *Jpn. J. Appl. Phys.* **26**, L1847–L1849 (1987).

[179] F. Shimizu, K. Shimizu, and H. Takuma, Four-beam laser trap of neutral atoms, *Opt. Lett.* **16**, 339–341 (1991).

[180] D. Shiner, R. Dixson, and V. Vedantham, Three-nucleon charge radius: A precise laser determination using ^{3}He, *Phys. Rev. Lett.* **74**, 3553–3556 (1995).

[181] J. H. Shirley, W. D. Lee, and R. E. Drullinger, Accuracy evaluation of the primary frequency standard NIST-7, *Metrologia* **38**, 427–458 (2001).

[182] G. V. Shlyapnikov, J. T. M. Walraven, U. M. Rahmanov, and M. W. Reynolds, Decay kinetics and Bose condensation in a gas of spin-polarized triplet helium, *Phys. Rev. Lett.* **73**, 3247–3250 (1994).

[183] I. F. Silvera, Spin-polarized hydrogen: Prospects for Bose-Einstein condensation and two-dimensional superfluidity, in *Bose-Einstein condensation*, edited by A. Griffin, D. W. Snoke, and S. Stringari, chapter 8, pp. 160–172 (Cambridge University Press, 1995).

[184] O. Sirjean, S. Seidelin, J. Viana Gomes, D. Boiron, C. I. Westbrook, A. Aspect, and G. V. Shlyapnikov, Ionization rates in a Bose-Einstein condensate of metastable helium, *Phys. Rev. Lett.* **89**, 220406 (2002).

[185] P. E. Siska, Molecular-beam studies of Penning ionization, *Rev. Mod. Phys.* **65**, 337–412 (1993).

[186] Y. Sortais, S. Bize, C. Nicolas, A. Clairon, C. Salomon, and C. Williams, Cold collision frequency shifts in a ^{87}Rb atomic fountain, *Phys. Rev. Lett.* **85**, 3117–3120 (2000).

[187] R. Srianand, H. Chand, P. Petitjean, and B. Aracil, Limits on the time variation of the electromagnetic fine-structure constant in the low energy limit from absorption lines in the spectra of distant quasars, *Phys. Rev. Lett.* **92**, 121302 (2004).

[188] J. Stärck and W. Meyer, Long-range interaction potential of the $^5\Sigma_g^+$ state of He_2, *Chem. Phys. Lett.* **225**, 229–232 (1994).

[189] C. H. Storry, M. C. George, and E. A. Hessels, Precision microwave measurement of the $2\,^3P_1 - 2\,^3P_2$ interval in atomic helium, *Phys. Rev. Lett.* **84**, 3274–3277 (2000).

[190] C. I. Sukenik and H. C. Busch, Simultaneous trapping of rubidium and metastable argon in a magneto-optical trap, *Phys. Rev. A* **66**, 051402(R) (2002).

[191] K.-A. Suominen, Theories for cold atomic collisions in light fields, *J. Phys. B* **29**, 5981–6007 (1996).

[192] W. Süptitz, G. Wokurka, F. Strauch, P. Kohns, and W. Ertmer, Simultaneous cooling and trapping of ^{85}Rb and ^{87}Rb in a magneto-optical trap, *Opt. Lett.* **19**, 1571–1573 (1994).

[193] G. D. Telles, W. Garcia, L. G. Marcassa, V. S. Bagnato, D. Ciampini, M. Fazzi, J. H. Müller, D. Wilkowski, and E. Arimondo, Trap loss in a two-species Rb-Cs magneto-optical trap, *Phys. Rev. A* **63**, 033406 (2001).

[194] G. D. Telles, L. G. Marcassa, S. R. Muniz, S. G. Miranda, A. Antunes, C. Westbrook, and V. S. Bagnato, Inelastic collisions of a Na/Rb mixture in a magneto-optical trap, *Phys. Rev. A* **59**, R23–R26 (1999).

[195] P. J. J. Tol, *Trapping and evaporative cooling of metastable helium*, Ph.D. thesis, Vrije Universiteit Amsterdam (2005), unpublished.

[196] P. J. J. Tol, N. Herschbach, E. A. Hessels, W. Hogervorst, and W. Vassen, Large numbers of cold metastable helium atoms in a magneto-optical trap, *Phys. Rev. A* **60**, R761–R764 (1999).

[197] C. G. Townsend, N. H. Edwards, C. J. Cooper, K. P. Zetie, C. J. Foot, A. M. Steane, P. Szriftgiser, H. Perrin, and J. Dalibard, Phase-space density in the magneto-optical trap, *Phys. Rev. A* **52**, 1423–1440 (1995).

[198] A. G. Truscott, K. E. Strecker, W. I. McAlexander, G. B. Partridge, and R. G. Hulet, Observation of Fermi pressure in a gas of trapped atoms, *Science* **291**, 2570–2572 (2001).

[199] Bose-Einstein condensation of metastable helium has been achieved in the Laser Centre of the Vrije Universiteit Amsterdam on 27 January 2005 (A. S. Tychkov, T. Jeltes, P. J. J. Tol, N. Herschbach, W. Hogervorst, and W. Vassen, to be published).

[200] A. S. Tychkov, J. C. J. Koelemeij, T. Jeltes, W. Hogervorst, and W. Vassen, Two-color magneto-optical trap for metastable helium, *Phys. Rev. A* **69**, 055401 (2004).

[201] J.-P. Uzan, The fundamental constants and their variation: observational and theoretical status, *Rev. Mod. Phys.* **75**, 403–455 (2003).

[202] J. Vanier and C. Audoin, *The Quantum Physics of Atomic Frequency Standards* (IOP Publishing Ltd, 1989).

[203] N. Vansteenkiste, C. Gerz, R. Kaiser, L. Hollberg, C. Salomon, and A. Aspect, A frequency-stabilized LNA laser at 1.083 µm: Application to the manipulation of helium 4 atoms, *J. Phys. II* **1**, 1407–1428 (1991).

[204] V. Venturi and I. B. Whittingham, Close-coupled calculation of field-free collisions of cold metastable helium atoms, *Phys. Rev. A* **61**, 060703 (2000).

[205] V. Venturi, I. B. Whittingham, P. J. Leo, and G. Peach, Close-coupled calculation of collisions of magnetostatically trapped metastable helium atoms, *Phys. Rev. A* **60**, 4635–4646 (1999).

[206] E. J. D. Vredenbregt and K. A. H. van Leeuwen, Laser cooling and trapping visualized, *Am. J. Phys.* **71**, 760–765 (2003).

[207] D. Vrinceanu and H. R. Sadeghpour, He(1 ^{1}S)–He(2 ^{3}S) collision and radiative transition at low temperatures, *Phys. Rev. A* **65**, 062712 (2002).

[208] L.-B. Wang, P. Mueller, R. J. Holt, Z.-T. Lu, T. P. O'Connor, Y. Sano, and N. C. Sturchio, Laser spectroscopic measurement of helium isotope ratios, *Geophys. Res. Lett.* **30**, 1592–1595 (2003).

[209] J. K. Webb, M. T. Murphy, V. V. Flambaum, V. A. Dzuba, J. D. Barrow, C. W. Churchill, J. X. Prochaska, and A. M. Wolfe, Further evidence for cosmological evolution of the fine structure constant, *Phys. Rev. Lett.* **87**, 091301 (2001).

[210] J. Weiner, *Cold and ultracold collisions in quantum microscopic and mesoscopic systems* (Cambridge University Press, 2003).

[211] J. Weiner, V. S. Bagnato, S. Zilio, and P. S. Julienne, Experiments and theory in cold and ultracold collisions, *Rev. Mod. Phys.* **71**, 1–85 (1999).

[212] H. F. Wellenstein and W. W. Robertson, Collisional relaxation processes for the $n = 3$ states of helium. II. Associative ionization, *J. Chem. Phys.* **56**, 1077–1082 (1972).

[213] C. E. Wieman, D. E. Pritchard, and D. J. Wineland, Atom cooling, trapping, and quantum manipulation, *Rev. Mod. Phys.* **71**, S253–S262 (1999).

[214] E. P. Wigner, On the behavior of cross sections near thresholds, *Phys. Rev.* **73**, 1002–1009 (1948).

[215] J. Wilks and D. S. Betts, *An introduction to liquid helium*, second edition (Clarendon Press, Oxford, 1987).

[216] D. Wineland and H. Dehmelt, Proposed $10^{14}\Delta\nu < \nu$ laser fluorescence spectroscopy on Tl^+ mono-ion oscillator III, *Bull. Am. Phys. Soc.* **20**, 637 (1975).

[217] D. J. Wineland, W. M. Itano, J. C. Bergquist, and F. L. Walls, Proposed stored $^{201}Hg^+$ ion frequency standard, in *Proceedings of the 35th Annual Frequency Control Symposium*, pp. 602–611 (1981).

[218] V. Wippel, C. Binder, W. Huber, L. Windholz, M. Allegrini, F. Fuso, and E. Arimondo, Photoionization cross-sections of the first excited states of sodium and lithium in a magneto-optical trap, *Eur. Phys. J. D* **17**, 285–291 (2001).

[219] J. L. Wiza, Microchannel plate detectors, *Nucl. Instrum. Methods* **162**, 587–601 (1979).

[220] J. R. Woodworth and H. W. Moos, Experimental determination of the single-photon transition rate between 2 $^3S_1$ and 1 $^1S_0$ states of He I, *Phys. Rev. A* **12**, 2455–2463 (1975).

[221] X. Xu, T. H. Loftus, J. L. Hall, A. Gallagher, and J. Ye, Cooling and trapping of atomic strontium, *J. Opt. Soc. Am. B* **20**, 968–976 (2003).

[222] M. Yamazaki, S. Maeda, N. Kishimoto, and K. Ohno, Classical trajectory

calculations of collision energy dependence of Penning ionization cross-sections for N_2 and CO by He* 2 ^{3}S; optimization of anisotropic model potentials, *Chem. Phys. Lett.* **355**, 311–318 (2002).

[223] Z.-C. Yan and J. F. Babb, Long-range interactions of metastable helium atoms, *Phys. Rev. A* **58**, 1247–1252 (1998).

[224] Z.-C. Yan and G. W. F. Drake, High-precision calculations of the Zeeman effect in the 2 ^3P_J, 2 $^1P_1$, 2 $^3S_1$, and 3 ^3P_J states of helium, *Phys. Rev. A* **50**, R1980–R1983 (1994).

[225] D.-H. Yang, P. McNicholl, and H. Metcalf, Precision measurement of the crossing between the $(J, M) = (0, 0)$ and $(1, 1)$ sublevels and fine-structure splittings in 3 ^{3}P helium, *Phys. Rev. A* **33**, 1725–1729 (1986).

[226] I. Yavin, M. Weel, A. Andreyuk, and A. Kumarakrishnan, A calculation of the time-of-flight distribution of trapped atoms, *Am. J. Phys.* **70**, 149–152 (2001).

[227] A. J. Yencha, Penning ionization and related processes, in *Electron spectroscopy: Theory, techniques and applications*, edited by C. R. Brundle and A. D. Baker, volume 5, pp. 197–373 (Academic Press, 1984).

[228] Y. E. Young, R. Ejnisman, J. P. Shaffer, and N. P. Bigelow, Heteronuclear hyperfine-state-changing cold collisions, *Phys. Rev. A* **62**, 055403 (2000).

[229] R. N. Zare, *Angular Momentum: Understanding Spatial Aspects in Chemistry and Physics* (John Wiley & Sons, 1988).

[230] P. Zhao, J. R. Lawall, and F. M. Pipkin, High-precision isotope-shift measurement of the 2 ^{3}S $-$ 2 ^{3}P transition in helium, *Phys. Rev. Lett.* **66**, 592–505 (1991).

[231] M. W. Zwierlein, C. A. Stan, C. H. Schunck, S. M. F. Raupach, S. Gupta, Z. Hadzibabic, and W. Ketterle, Observation of Bose-Einstein condensation of molecules, *Phys. Rev. Lett.* **91**, 250401 (2003).

List of publications

HOMONUCLEAR IONIZING COLLISIONS OF LASER-COOLED METASTABLE HELIUM ATOMS,
R. J. W. Stas, J. M. McNamara, W. Hogervorst, and W. Vassen,
to be submitted.
Based on Chapters 4 and 5.

SIMULTANEOUS MAGNETO-OPTICAL TRAPPING OF A BOSON-FERMION MIXTURE OF METASTABLE HELIUM ATOMS,
R. J. W. Stas, J. M. McNamara, W. Hogervorst, and W. Vassen,
Physical Review Letters **93**, 053001 (2004).
Chapter 6 is based on this publication.

MAGNETO-OPTICAL TRAP FOR METASTABLE HELIUM AT 389 NM,
J. C. J. Koelemeij, R. J. W. Stas, W. Hogervorst, and W. Vassen,
Physical Review A **67**, 053406 (2003).
Chapter 3 is based on this publication.

Not related to this thesis
AN INTENSE, SLOW AND COLD BEAM OF METASTABLE NE(3S) $^3P_2$ ATOMS,
J. G. C. Tempelaars, R. J. W. Stas, P. G. M. Sebel, H. C. W. Beijerinck,
and E. J. D. Vredenbregt, *European Physical Journal D* **18**, 113–121 (2002).

PROSPECTS FOR BOSE-EINSTEIN CONDENSATION OF METASTABLE NEON ATOMS,
H. C. W. Beijerinck, E. J. D. Vredenbregt, R. J. W. Stas, M. R. Doery,
and J. G. C. Tempelaars, *Physical Review A* **61**, 023607 (2000).

ORBIT DYNAMICS IN A LOW ENERGY ELECTRON LINEAR ACCELERATOR,
H. L. Hagedoorn, J. I. M. Botman, R. W. de Leeuw, and R. J. W. Stas,
in *EPAC 96: Fifth European Particle Accelerator Conference*, edited by S. Myers,
A. Pacheco, R. Pascual, Ch. Petit-Jean-Genaz, and J. Poole, pp. 944–946
(Institute of Physics Publishing, 1997).

Summary

This thesis presents experimental and theoretical work performed at the Laser Centre of the Vrije Universiteit in Amsterdam to study laser-cooled metastable triplet helium (He*) atoms. Samples containing about 3×10^8 He* atoms—either fermionic ^{3}He* atoms, bosonic ^{4}He* atoms or mixtures thereof—are cooled to a temperature around 1 mK and form the starting point of the presented studies. The studies include an investigation of cold ionizing collisions in the absence of resonant light, an investigation of magneto-optical trapping with ultraviolet light, a feasibility study of an atomic fountain clock based on ^{3}He* atoms and the first demonstration of magneto-optical trapping of an isotopic mixture of He* atoms. The metastable $2\,^3S_1$ state carries a large internal energy of 19.8 eV, but can be regarded as an effective ground state in all studies presented, as its lifetime is 7.9 ks.

Chapter 1 serves as an introduction and may be regarded as a motivation for the research. The chapter places the work into a broader perspective and presents phenomena of direct relevance to the work. It is shown that Penning ionization gives rise to a strong reactivity of the He* atom and that it allows the use of charged-particle detectors (microchannel plate detectors or channel electron multipliers) as detection tools.

Samples of He* atoms are obtained in a magneto-optical trap (MOT) using trapping light with a wavelength of 1083 nm. The light is resonant with atomic transition $2\,^3S_1(F = \frac{3}{2}) \rightarrow 2\,^3P(F' = \frac{5}{2})$ in case of ^{3}He*, and $2\,^3S_1 \rightarrow 2\,^3P_2$ in case of ^{4}He*. The experimental setup used for the experiments is discussed in Chapter 2. To characterize the trapped samples, absorption images are taken with a CCD camera and time-of-flight measurements are performed using a microchannel plate detector. The number of atoms of about 3×10^8 is comparable to other numbers reported for ^{4}He* MOTs. However, it represents an improvement by three orders of magnitude compared to results reported for ^{3}He*.

Chapter 3 deals with the investigation of a new MOT for ^{4}He* atoms using trapping light with a wavelength of 389 nm. The trapping light drives the non-closed atomic transition $2\,^3S_1 \rightarrow 3\,^3P_2$ and trapped samples are characterized with fluorescence images and time-of-flight measurements using a channel electron multiplier. Trap loss is studied by monitoring the ionization rate

in the trapped sample with a second channel electron multiplier; the ions are formed in a Penning ionization process and are not confined in the trap. It is observed that two-photon ionization has a small contribution to trap loss and that trap loss due to light-assisted collisions is significantly smaller compared to a 1083 nm MOT. As a result of the reduced trap loss and a stronger trapping force, higher phase-space density can be obtained. However, the limited capture velocity hampers the trapping of a large number of atoms: up to 2×10^7 atoms have been confined.

Cold ionizing collisions in the absence of resonant light are studied in samples of ^{3}He* or ^{4}He* atoms. To analyze experimental results, a theoretical model for homonuclear ionizing collisions of He* isotopes is presented in Chapter 4. The model incorporates quantum threshold behavior, Wigner's spin-conservation rule and quantum statistical symmetry requirements. Starting from molecular potentials, the model is used to calculate the inelastic cross section for Penning ionization, as well as the ionization rate coefficient for an unpolarized sample. The model complements a more complete close-coupling theory reported in literature and is applied to collisions of both ^{3}He* atoms and ^{4}He* atoms.

The experimental determination of the rate coefficients is presented in Chapter 5. Measurements of trap loss due to light-assisted collisions and comparative measurements of ionization rates in the absence and presence of trapping light are performed successively. The derived ionization rate coefficient is $1.9(3) \times 10^{-10}$ cm^3/s in case of ^{3}He*, and $1.0(2) \times 10^{-10}$ cm^3/s in case of ^{4}He*. The coefficients are corrected for polarization effects in the samples and show very good agreement with the calculated values. The model shows that the isotopic difference in the ionization rate coefficients results from the different quantum statistical symmetry of the two isotopes and the presence of a nuclear spin in the case of ^{3}He.

The simultaneous magneto-optical trapping of both ^{3}He* and ^{4}He* atoms is demonstrated for the first time in Chapter 6. As the number of trapped atoms is about 1.5×10^8 of each isotope, the samples form a perfect starting point for experiments aimed at quantum degeneracy in a mixture of spin-polarized ^{3}He* and ^{4}He* atoms. Optical pumping of ^{3}He* atoms to a non-trapped hyperfine state is investigated and it is shown that large atom numbers can be confined without additional repumping lasers.

Finally, the feasibility of an atomic fountain clock based on laser-cooled ^{3}He* atoms is investigated in Chapter 7. It is argued that an atomic fountain clock based on ^{3}He* atoms would allow the investigation of the suppression of the cold collision frequency shift for identical fermions and that a clock based on an atom with small mass is interesting for measurements of possible variations of the fine-structure constant α. A calculation of the expected stability, accuracy and Ramsey fringe contrast shows that the expected performance of the ^{3}He* fountain clock is significantly inferior compared to existing fountain clocks. As this hampers the investigation of cold collision frequency shifts or precise measurements of possible variations of α, it is concluded that it would not be sensible to perform an experimental study of a ^{3}He* fountain clock at the time being.

Samenvatting

Fermionische en bosonische heliumatomen in een magneto-optische val

In dit proefschrift wordt experimenteel en theoretisch werk besproken dat is uitgevoerd in het Laser Centrum van de Vrije Universiteit in Amsterdam. Het betreft onderzoek aan wolken van lasergekoelde metastabiele heliumatomen (He*), waarbij zowel fermionische ^{3}He* atomen, bosonische ^{4}He* atomen en mengsels van beide isotopen zijn onderzocht. De wolken hebben een afmeting van enkele millimeters en bevatten ongeveer 3×10^8 He* atomen bij een temperatuur van ongeveer 1 mK. Het onderzoek is hoofdzakelijk gericht op kwantumstatistische verschijnselen en bestaat uit een aantal deelstudies, waaronder een onderzoek naar koude ioniserende botsingen in de afwezigheid van resonant licht, een onderzoek naar het magneto-optisch opsluiten met behulp van ultraviolet licht, een haalbaarheidsonderzoek ten aanzien van een atoomklok gebaseerd op ^{3}He* atomen en de eerste demonstratie ooit van de magneto-optische opsluiting van een mengsel van ^{3}He* en ^{4}He* atomen. De metastabiele toestand $2\,^3S_1$ heeft een interne energie van 19.8 eV en kan dankzij de levensduur van 7.9 ks worden beschouwd als de effectieve grondtoestand in alle hier besproken experimenten.

Hoofdstuk 1 dient ter introductie en motivatie. Aan de ene kant wordt het onderzoek in een breder perspectief geplaatst en aan de andere kant komen aspecten aan de orde die van groot belang zijn voor het onderzoek, zoals het proces van Penning-ionisatie. Er wordt duidelijk gemaakt dat Penning-ionisatie bijzondere detectiemogelijkheden biedt, namelijk het gebruik van *charged-particle* detectoren (*microchannel plate* detectoren of *channel electron multipliers*) mogelijk maakt.

In hoofdstuk 2 wordt de experimentele opstelling beschreven en komen de eerste metingen aan koude He* wolken aan de orde. De wolken worden gevormd in een magneto-optische val (MOT) waarbij gebruik wordt gemaakt van laserlicht met een golflengte van 1083 nm. Dit licht is resonant met de atomaire overgang $2\,^3S_1(F = \frac{3}{2}) \rightarrow 2\,^3P(F' = \frac{5}{2})$ in het geval van ^{3}He*, en $2\,^3S_1 \rightarrow 2\,^3P_2$ in het geval van ^{4}He*. De wolken worden geanalyseerd met behulp van

time-of-flight metingen met een microchannel plate detector en absorptiemetingen met een CCD camera. Het behaalde aantal atomen van ongeveer 3×10^8 is vergelijkbaar met getallen uit de literatuur als het gaat om ^{4}He*. In het geval van ^{3}He* zijn de behaalde aantallen drie ordes groter dan eerder gepubliceerde waarden.

Hoofdstuk 3 beschrijft de studie van een nieuw type magneto-optische val voor ^{4}He* atomen. Er wordt gebruik gemaakt van laserlicht met een golflengte van 389 nm dat resonant is met de niet-gesloten overgang $2\,^3S_1 \rightarrow 3\,^3P_2$. De ^{4}He* wolken worden geanalyseerd met behulp van *time-of-flight* metingen met een *channel electron multiplier* en fluorescentie metingen met een CCD camera. De verschillende verliesprocessen in de val worden geanalyseerd door te kijken naar de ionenproductie in de wolk met een tweede *channel electron multiplier*; de ionen ontstaan als gevolg van Penning-ionisatie en worden door een elektrisch veld naar de detector getrokken. Het blijkt dat verlies ten gevolge van lichtgeïnduceerde botsingen (*light-assisted collisions*) aanzienlijk kleiner is dan in het geval een magneto-optische val op basis van 1083 nm licht. Het verminderde deeltjesverlies en de grotere lichtkracht leiden ertoe dat in een val op basis van 389 nm licht een grotere faseruimtedichtheid bereikt wordt dan in een val op basis van 1083 nm licht. Aan de andere kant wordt het aantal deeltjes in de val begrensd tot 2×10^7 door de beperkte invangsnelheid van de MOT. De bijdrage aan deeltjesverlies door twee-foton-ionisatie blijkt klein.

Een aanzienlijk deel van dit proefschrift beschrijft een onderzoek aan koude ioniserende botsingen in ^{3}He* wolken en ^{4}He* wolken, waarbij de nadruk ligt op botsingen in afwezigheid van resonant licht. Ten behoeve van de analyse van experimentele resultaten wordt in hoofdstuk 4 een theoretisch model gepresenteerd. Het model beschrijft homonucleaire ioniserende botsingen van He* atomen en gaat uit van een aantal belangrijke eigenschappen van deze botsingen, te weten het effect van kwantummechanische energiedrempels, Wigner's wet van behoud van spin en de symmetrie-eigenschappen van een systeem van twee niet-onderscheidbare deeltjes. Uitgaande van de (relevante) moleculaire potentialen wordt het model gebruikt om inelastische botsingsdoorsnedes voor Penning-ionisatie te berekenen en vervolgens ionisatiesnelheden in ongepolariseerde He* wolken af te leiden. Het model wordt toegepast op beide isotopen en vormt een aanvulling op een meer volledige *close-coupling* berekening bekend uit de literatuur.

Een verslag van de experimentele bepaling van de ionisatiesnelheden is te vinden in hoofdstuk 5. Door een meting van het deeltjesverlies in aanwezigheid van resonant licht te combineren met een relatieve meting van de ionisatiesnelheid in aanwezigheid van resonant licht ten opzichte van de snelheid in afwezigheid van resonant licht, worden de ionisatiesnelheidscoëfficiënten bepaald. In het geval van ^{3}He* is de coëfficiënt $1.9(3) \times 10^{-10}$ cm^3/s en voor ^{4}He* is de coëfficiënt $1.0(2) \times 10^{-10}$ cm^3/s. De coëfficiënten zijn gecorrigeerd voor polarisatie-effecten in de wolken en komen zeer goed overeen met de berekende waarden. Uit het model blijkt dat het verschil tussen de coëfficiënten het gevolg is van de verschillende kwantummechanische symmetrie van de isotopen en de

aanwezigheid van een kernspin in het geval van ^{3}He*.

Het onderwerp van hoofdstuk 6 is de eerste waarneming van een gelijktijdige opsluiting van ^{3}He* en ^{4}He* atomen in een magneto-optische val. Het behaalde aantal atomen in de val bedraagt ongeveer 1.5×10^8 bedraagt per isotoop en daarom vormen de opgesloten wolken een goed uitgangspunt voor experimenten gericht op kwantum ontaarding (*quantum degeneracy*) in een mengsel van spin-gepolariseerde ^{3}He* en ^{4}He* atomen. Het verlies van ^{3}He* atomen door optisch pompen komt uitgebreid aan de orde. Het blijkt dat dit deeltjesverlies, dat veroorzaakt wordt door een overgang van atomen naar een andere hyperfijntoestand, klein is en dat grote aantal atomen kunnen worden opgesloten.

Hoofdstuk 7 vormt de neerslag van een haalbaarheidsstudie naar een atoomklok gebaseerd op een lasergekoelde fontein van ^{3}He* atomen. Er wordt betoogd dat een dergelijke atoomklok aandacht verdiend op basis van de innovatieve onderzoeksmogelijkheden. Zo is het mogelijk de onderdrukking van de frequentieverschuiving door atomaire botsingen in het geval van fermionen te onderzoeken. Tevens biedt de klok door kleine atoommassa van ^{3}He mogelijkheden om eventuele variaties van de fijnstructuurconstante te bepalen. Uit een berekening van de verwachte stabiliteit, nauwkeurigheid en contrast van de *Ramsey fringes* blijkt echter dat een ^{3}He* atoomklok veel slechter presteert dan al bestaande fonteinklokken en dat een studie van de innovatieve aspecten daardoor niet mogelijk is. De conclusie is dan ook dat het op dit moment niet zinnig zou zijn om de ^{3}He* atoomklok experimenteel te onderzoeken.